Universidade de Aveiro Departamento de Engenharia de Materiais e Cerâmica
(2019)

Basam Abobaker Emhmed Ben Arfa

Novos métodos de robocasting e evaporador rotativo para a preparaçao de scaffold de vidro e vitrocerâmico por sol–gel

Novel robocasting and rotary evaporator routes for the preparation of sol–gel derived glass & glass ceramic scaffolds

Universidade de Aveiro Departamento de Engenharia de Materiais e Cerâmica
(2019)

Basam Abobaker Emhmed Ben Arfa

Novos métodos de robocasting e evaporador rotativo para a preparaçao de scaffold de vidro e vitrocerâmico por sol–gel

Novel robocasting and rotary evaporator routes for the preparation of sol–gel derived glass & glass ceramic scaffolds

Dissertação apresentada à Universidade de Aveiro para cumprimento dos requisitos necessários à obtenção do grau de Doutor em Ciência e Engenharia de Materiais, realizada sob a orientação científica da Doutora Isabel Margarida Miranda Salvado, Professora Associada do Departamento de Engenharia de Materiais e Cerâmica da Universidade de Aveiro e do Doutor Robert Pullar, investigador principal do mesmo departamento.

Dissertation presented to the University of Aveiro to fulfill the requirements necessary to obtain a PhD degree in Materials Science and Engineering, carried out under the scientific guidance of Dr. Isabel Margarida Miranda Salvado, Associate Professor of the Department of Materials and Ceramics Engineering the University of Aveiro and Dr. Robert Pullar, principal investigator at the same department

This work is dedicated to the memory of my father, and to my mother, my wife and my kids (Omar, Rayan & Maria) for their unconditional love and support.

o júri

presidente

Prof. Doutor Nelson Fernando Pacheco da Rocha
professor Catedrático, Universidade de Aveiro

Prof. Doutora Maria Clara Henriques Baptista Gonçalves
professora Auxiliar Com Agregação, Universidade de Lisboa

Prof. Doutora Maria Ascensão Ferreira da Silva Lopes
professora Auxiliar, Universidade do Poro

Doutor Luis Miguel Monteiro Mafra
Investigador Principal em Regime Laboral, Universidade de Aveiro

Doutor Robert Carlyle Pullar
Equiparado a Investigador Principal, Universidade de Aveiro

Doutor Luís Miguel Mota Ferreira
Investigador, Centro de Clências e Tecnologias Nucleares - Instituto Superior Técnico

acknowledgment

First of all, I am very thankful to Allah for providing me with all the strength and ability to be capable of overcoming the challenges and eliminating difficulties during a long four years of hard work.

Special appreciation and sincere gratitude goes to my supervisor Professor Isabel Salvado, for the support and advice. Her trust and belief in me gave me tremendous capability and encouragement to overcome all those challenges.

I am very thankful to my supervisor Dr Robert Pullar. Without his advice and enormous support I would not have been able to finish my PhD. Those sharp, precise comments were all very valuable advice for me, many thanks for all of that.

Besides my supervisors, special thanks to Professor José Maria, for his insightful comments and advice. His office door was always open for me, all the time, and he was clarifying my doubts with a simple smile, many thanks for all the support you have given to me.

My sincere thanks also go to Professor Jorge Frade, who provided me with an opportunity to have his contribution to some other scientific works not included in this thesis.

My deep thanks to my wife and kids, Omar, Rayan and Maria, for their support, sacrifices and patience. My deep thanks also go to my mother and father in law for their enormous support.

Special thanks to my colleague Sofia Neto, from the laboratory of Prof Jose Maria, who helped print the scaffolds, and made the rheology measurements.

Also many thanks to Dr Ilaria E. Palamá, from CNR Nanotec, Lecce, Italy, for her contribution in performing the cytotoxicity analysis.

I am extremely grateful to Dr Clara Piccirillo, Escola Superior Biotecnologia, Universidade Católica Portuguesa – Porto, for her valuable suggestions and advice in some of the publications within the scope of this work.

Thank you to all who are left without mention, but have, both directly and indirectly, contributed to the development and implementation of this work.

palavras-chave Sol–gel, vidro bioativo, evaporador rotativo, alta sílica, scaffold, rbocasting, biomateriais, lantânio, cobre. .

resumo

A obtenção de vidros bioactivos amorfos por sol–gel a partir de um sistema quaternário contendo sódio é extremamente difícil, uma vez que são propensos a sofrerem cristalização durante o tratamento térmico. Além disso, é provável que ocorra segregação de fase e cristalização irreversível de fases indesejáveis durante o processo de preparação. As consequências são a redução da homogeneidade, tempo excessivo de processamento e consumo de energia durante as fases de envelhecimento e secagem lenta.

Um dos principais objetivos desta tese é desenvolver um novo e rápido processo de síntese por sol–gel de vidros bioativos quaternários com alto teor em sílica. Modificações são incorporadas ao procedimento convencional de síntese por sol–gel para minimizar os tempos de envelhecimento e secagem, preservando a microestrutura e propriedades típicas e aumentando o grau de homogeneidade. Os esforços realizados levaram ao desenvolvimento de um método inovador e rápido para a produção de vidros bioactivos por sol–gel, evitando o processo de envelhecimento. Foi realizado um estudo comparativo entre os vidros sintetizados pelo método de secagem convencional (CD) e a nova secagem rápida (FD). Os resultados revelaram que ambos permitem obter bio–vidros estabilizados com comportamento e propriedades praticamente idênticos; mas o processo designado por FD é 100 vezes mais rápido em comparação com o processo CD. Além disso, os vidros FD exibiram bioatividade melhorada em testes em que se usou fluido corporal simulado (SBF).

Os efeitos de alguns parâmetros de processamento, tais como a concentração de cálcio, relação Ca / P, tipos de precursores de sais metálicos, tipos e concentrações de catalisadores, foram investigados para uma compreensão profunda dos seus papéis nas propriedades. A influência da velocidade de agitação na bio–mineralização ao imergir as amostras em fluido corporal simulado (SBF) também foi estudada.

Observou–se ainda, que a bioactividade aumenta quando no método de preparação se usaram precursores de sal nitrato e ácido cítrico como catalisador, e quando ocorreu um aumento da concentração de Ca até um dado teor.

Outro objetivo foi dopar ou co–dopar o vidro preparado por sol–gel de elevado teor em sílica (HSSGG) seletivamente com Cu e La. Os efeitos individuais e combinados desses elementos de dopagem na estrutura do vidro, cristalização, porosidade, área superficial específica, tamanho de partícula, densidade , capacidade de sinterização, resistência à compressão e citotoxicidade foram estudados. Verificou–se que o Cu e o La isoladamente desempenham papéis opostos em algumas propriedades relevantes. Por outro lado, benefícios sinérgicos poderiam ser obtidos pela combinação dos dois dopantes.

A citotoxicidade foi significativamente melhorada para algumas combinações de dopagem, enquanto a biomineralização das amostras dopadas foi sempre muito semelhante à da composição HSSGG.

A fracção de porosidade intrínseca dos pós de vidro preparados por sol–gel e a consequente absorção de qualquer meio líquido dispersante, tornam–nos inapropriados para processamento coloidal. Essas características impediram até agora a fabricação de “scaffolds” por técnicas de manufatura aditiva, como o robocasting. A superação desse grande desafio é de suma importância para explorar plenamente as vantagens específicas dos vidros preparados por sol–gel. Assim, a compreensão dos efeitos de cada variável de processamento experimental nas propriedades dos pós é essencial para alcançar condições otimizadas de processamento para a fabricação de “scaffolds” por robocasting. Assim, os efeitos da temperatura de tratamento térmico (HTT), razão bolas / pó (BPR), e carga sólida no comportamento do fluxo e nas propriedades viscoelásticas das suspensões / pastas foram sistematicamente avaliados. Suspensões com cargas sólidas de até 40% em volume podem ser preparadas a partir de vidros HSSGG dopados com Cu–La e usadas para fabricar com sucesso “scaffolds” por robocasting. A formação de hidroxiapatite nas superfícies do “scaffold” foi observada após 72 h de imersão em SBF para o vidro HSSGG.

Essas características tornam os “scaffolds” candidatos promissores para aplicações em regeneração óssea e engenharia de tecidos e merecem posterior investigação in vivo.

keywords Sol–gel, bioactive glass, rotary evaporator, high silica, scaffold, robocasting, biomaterials, lanthanum, copper.

abstract

Producing pure amorphous bioactive glasses by sol–gel from a quaternary system containing sodium is extremely difficult as they are prone to undergo readily crystallisation during heat treatment. Moreover, phase segregations and irreversible crystallisation of unwanted phases are likely to occur during the conventional xerogel process. The consequences are reduced homogeneity, excessive time and energy consumptions during the aging and slow drying steps of sol–gel derived bioglasses.

A main objective of this thesis is to develop a new and expedite sol–gel synthesis process to prepare high silica quaternary bioactive glasses. Additional concepts are incorporated in the conventional sol–gel synthesis procedure to minimise the aging and drying times, while preserving the typical microstructure and properties and enhancing the degree of homogeneity. The efforts made led to the development of an innovative and rapid sol–gel method for producing bioactive glasses, which skips the ageing process. A comparative study was made between the glasses synthesised by the conventional drying method (CD) and the novel fast drying (FD). The results revealed that both methods produce stabilised bio–glasses with virtually identical behaviour and properties, but FD is 100 times faster in comparison to CD. Moreover, FD glasses exhibited improved bioactivity in simulated body fluid (SBF).

The effects of some processing parameters such as calcium concentration, Ca/P ratio, types of metal salts precursors, types and concentrations of catalysts, were investigated to gain an in–depth understanding of their roles in the overall properties. The influence of agitation rate on the extent of bio–mineralisation upon immersing the samples in simulated body fluid (SBF) was also studied. The results revealed that bioactivity was enhanced by using nitrate salt precursors and citric acid as catalyst, and by increasing Ca concentration to some extent.

Another aim was doping or co–doping the high silica sol–gel glass (HSSGG) selectively with Cu and La. The individual and combined effects of these doping elements on the glass structure, crystallisation, porosity, specific surface area, particle sizes, density, sintering ability, compressive strength and cytotoxicity were studied. As individual doping elements, Cu and La were found to play opposite roles in some relevant properties. On the other hand, synergistic benefits could be obtained by combining the two dopants. Cytotoxicity was significantly improved for some doping combinations, while the bio–mineralisation activity of doped samples was always very similar to that of the parent HSSGG composition.

The significant intrinsic porosity fraction of sol–gel derived glass powders and the consequent uptake of any dispersing liquid medium, which will not be available for dispersion and flow, make them inappropriate for colloidal processing. These features have hindered so far the fabrication of porous scaffolds by additive manufacturing techniques such as robocasting. Overcoming this big challenge is of paramount importance for fully exploiting the specific advantages of the sol–gel derived glasses. Therefore, understanding the effects of each experimental processing variable on the properties of the powders is essential towards achieving optimised processing conditions for the fabrication of scaffolds by robocasting. Accordingly, the effects of heat treatment temperature (HTT), balls to powder ratio (BPR), and solid loading on the flow behaviour and on the viscoelastic properties of the suspensions/pastes were systematically evaluated. Suspensions with solid loadings up to 40 vol.% could be prepared from both HSSGG and Cu–La doped glasses and used to successfully fabricate scaffolds by robocasting. The formation of hydroxyapatite on the scaffold surfaces was observed after 72 h of immersion in SBF for HSSGG.

These features make the scaffolds promising candidates for bone regeneration and tissue engineering applications and worthy for further in vivo investigations.

Table of contents

List of Figures

List of Tables

List of Acronyms and Abbreviations

a.u.	Arbitrary Units
BPR	Balls to powder ratio
BPC	Biphasic calcium phosphates
BO	Bridging Oxygen
BET	Brunauer–Emmett–Teller method
CT	Calcination temperature
CN	Calcium nitrate tetrahydrate
Ca/P	Calcium/Phosphate ratio
CHAp	Carbonated hydroxyapatite
CMC	Carboxymethyl cellulose
ca.	Circa
CA	Citric acid
CAD–CAM	Computer-Aided Design/Computer-Aided Manufacturing
Dc	Condensation degree
CD	Conventional drying
CuN	Copper nitrate
Tc	Crystallization temperature.
DTA	Differential Thermal Analysis
ESRD	End stage renal disease
EDS	Energy dispersive X–Ray Spectroscopy
EtOH	Ethanol
EPR	Ethanol to powder mass ratio
FD	Fast Drying
FTIR	Fourier Transform Infrared Spectroscopy
Tg	Glass transition temperature
HTT	Heat treatment temperature
HSSGG	High Silica Sol Gel Glass
HAp	Hydroxyapatite
ICP	Inductively coupled plasma
ISO	International Organization for Standardization
JCPDS	Joint committee on powder diffraction standards
lbl	Layer by layer

LVR	Linear viscoelastic regions
LPR	Liquid to powder ratio
MAS	Magic angle spinning
NMR	Nuclear magnetic resonance
MPS	Mean Particle sizes
NPs	Nano paricles
Nc	Network connectivity
NBO	Non-Bridging Oxygen
OA	Orthogonal array
ppm	parts–per–million
T_p	Peak temperature of crystallisation
PA	Pore area
PV	Pore volume
pH	Potential of Hydrogen
PDF card	Powder diffraction file database
rpm	Revolution per minute
RT	Room temperature
SEM	Scanning electron microscopy
S/N	Signal to noise ratio
SBF	Simulated body fluid
SSA	Specific surface area
SD	Standard deviation
TG	Thermogravimetry
3D	Three–dimensional
TE	Tissue engineering
TO	Transverse optical
UV	Ultraviolet
XRD	X–Ray Diffraction
ZSV	Zero–Shear–Viscosity
β–TCP	β–tricalcium phosphate
T	Tesla (magnetic flux density)
DNA	Deoxyribonucleic acid

List of Symbols

δ_a	Bending (asymmetric) vibrational mode
δ_s	Bending (symmetric) vibrational mode
G’	Elastic modulus
n	Number of bridging oxygen atoms surrounding Si
ν_a	Stretching (asymmetric) vibrational mode
ν_s	Stretching (symmetric) vibrational mode
ζ	Zeta potential

List of publications directly related to this thesis

1. **Ben-Arfa BAE**, Fernandes HR, Salvado IMM, Ferreira JMF, Pullar RC. Effects of catalysts on polymerization and microstructure of sol-gel derived bioglasses. *J. Am. Ceram. Soc.* 2018;101(7):2831-2839. doi:10.1111/jace.15450.

2. **Ben-Arfa BAE**, Salvado IMM, Ferreira JMF, Pullar RC. Enhanced bioactivity of a rapidly-dried sol-gel derived quaternary bioglass. *Mater. Sci. Eng. C* 2018;91(October 2017):36-43. doi:10.1016/j.msec.2018.05.016.

3. **Ben-Arfa BAE**, Fernandes HR, Miranda Salvado IM, Ferreira JMF, Pullar RC. Synthesis and bioactivity assessment of high silica content quaternary glasses with Ca: P ratios of 1.5 and 1.67, made by a rapid sol-gel process. *J. Biomed. Mater. Res. - Part A* 2018;106(2):510-520. doi:10.1002/jbm.a.36239.

4. **Ben-Arfa BAE**, Miranda Salvado IM, Pullar RC, Ferreira JMF. The influence of processing parameters on morphology and granulometry of a wet-milled sol-gel glass powder. *Ceram. Int.* 2018;44(11):12754-12762. doi:10.1016/j.ceramint.2018.04.080.

5. **Ben-Arfa BAE** and Robert C. Pullar, Chapter 4 in Advances in Materials Science Research: Volume 34, editor Maryann C. Wythers, Nova, New York, NY, 2018, pp. 171-200. ISBN 978-1-53613-329-5.

6. **Ben-Arfa BAE**, Salvado IMM, Ferreira JMF, Pullar RC. Novel route for rapid sol-gel synthesis of hydroxyapatite, avoiding ageing and using fast drying with a 50-fold to 200-fold reduction in process time. *Mater. Sci. Eng. C* 2017;70:796-804. doi:10.1016/j.msec.2016.09.054.

7. **Ben-Arfa BAE**, Miranda Salvado IM, Ferreira JMF, Pullar RC. A hundred times faster: Novel, rapid sol-gel synthesis of bio-glass nanopowders (Si-Na-Ca-P system, Ca:P = 1.67) without aging. *Int. J. Appl. Glas. Sci.* 2017;8(3):337-343. doi:10.1111/ijag.12255.

8. **Ben-Arfa BAE**, Ana S. Neto, Miranda Salvado IM, Ferreira JMF, Pullar RC. Robocasting: Prediction of ink printability in solgel bioactive glass. *J. Am. Ceram. Soc. 2018;:1-11. doi: 10.1111/jace.16092.*

9. **Ben-Arfa BAE**, Ilaria E. Palamá, Isabel M. Miranda Salvado, José M. F. Ferreira and Robert C. Pullar. The role of calcium (source & content) on the in–vitro behaviour of sol–gel quaternary glass series. *Journal of the American Ceramic Society (under review).*

10. **Ben-Arfa BAE**, Ilaria E. Palamá, Isabel M. Miranda Salvado, José M. F. Ferreira and Robert C. Pullar. Cytotoxicity and bioactivity assessments for Cu^{2+} and La^{3+} doped high silica sol–gel derived glasses. Materials Science & Engineering C (submitted).

11. **Ben-Arfa BAE**, Isabel M. Miranda Salvado, José M. F. Ferreira and Robert C. Pullar. The effects of Cu^{2+} and La^{3+} doping on the sintering ability of sol–gel derived high silica glasses. *Journal of the European Ceram. Soc.2019; doi: 10.1016/j.ceramint.2019.02.081.*

12. **Ben-Arfa BAE**, Ana S. Neto, Isabel M. Miranda Salvado, José M. F. Ferreira and Robert C. Pullar. Robocasting of ceramic glass scaffolds: Sol–gel glass, new horizons . Journal of the European Ceramic Society . *J. European. Ceram. Soc. 2018;:39-04. doi: 10.1016/j.jeurceramsoc.2018.11.019.*

13. **Ben-Arfa BAE**, Ana S. Neto, Isabel M. Miranda Salvado, José M. F. Ferreira and Robert C. Pullar. Robocasting of Cu^{2+} & La^{3+} doped sol–gel glass scaffolds with enhanced mechanical properties. *Acta Biomaterialia. (online)2019;. doi: 10.1016/j.actbio.2019.01.048* .

Others

14. **Ben-Arfa BAE**, Miranda Salvado IM, Ferreira JMF, Pullar RC. The Influence of Cu^{2+} and Mn^{2+} Ions on the Structure and Crystallization of Diopside-Calcium Pyrophosphate Bioglasses. *Int. J. Appl. Glas. Sci.* 2016;7(3):345-354.

15. **Ben-Arfa BAE**, Salvado IMM, Ferreira JMF, Pullar RC. The effect of functional ions (Y^{3+}, F^{-}, Ti^{4+}) on the structure, sintering and crystallization of diopside-calcium pyrophosphate bioglasses. *J. Non. Cryst. Solids* 2016;443(July):162-171.

16. **Ben-Arfa BAE**, Salvado IMM, Frade JR, Pullar RC. Fast route for synthesis of stoichiometric hydroxyapatite by employing the Taguchi method. *Mater. Des.* 2016;109(November):547-555. doi:10.1016/j.matdes.2016.07.083.

17. **Ben-Arfa BAE**, Salvado IMM, Frade JR, Pullar RC. Guidelines to adjust particle size distributions by wet comminution of a bioactive glass determined by Taguchi and multivariate analysis, *Ceram. Int.* 2019;45(3): 3857-3863. doi: 10.1016/j.ceramint.2018.11.057.

18. **Ben-Arfa BAE**, Salvado IMM, Ferreira JMF, Pullar RC. Clove & cinnamon: Novel anti-oxidant eco-fuels for preparing magnetic iron oxide particles by the sol-gel auto-ignition method. Journal of Alloys and Compounds, 786 (2019) 71-76. doi: 10.1016/j.jallcom.2019.01.306

19. P R Moreira, N Silva, R Pullar, **Ben-Arfa BAE**, J G Abreu, F Henriques, M pintado, Vieira E Vieira. BIONANOSCULP, an ongoing project in biotechnology applications for preventive conservation of outdoor sculptures. IOP Conf. Series: Materials Science and Engineering; 364, 2018, doi:10.1088/1757-899X/364/1/012075.

Preface

Preface

More than 6.2 million accidental bone fractures occur each year in USA, yet ~10% fail to recover due to poor bone union. Osteoporosis, another growing problem, affects a further ~10 million people in USA, and it is expected to increase, resulting in extra costs of over $25 billion/year **[1]**. In bone resections **[2]**, the body is not able to regrow large volumes (e.g. hip joints), thus bone substitution is required, either via metallic implants **[3]**, or scaffolds **[4]** to avoid rapid pathological transmission **[5]** and the risk of transferring viral diseases **[5]**, which arise from autografts and allografts, respectively. Although metallic implants are capable of withstanding bearing loads, they promote bone resorption (mass loss) as a result of stress shielding **[6]**, which contributes to an increasing occurrence of fractures **[7,8]**. Therefore, scaffolds in general are promising candidates as implants to help the body to heal itself and resume normal function.

Many methods were developed to fabricate scaffolds: polymer foam replication **[9]**, freeze casting **[10]**, solid freeform fabrication **[11]** or lithography–based additive manufacturing **[12]**. However, amongst all, robocasting is a promising technique as it is capable of optimising scaffold morphology to mimic the trabecular bone structure **[13]** with improved mechanical properties **[14]**. Robocasting is an extrusion based direct writing technique that enables the construction of three dimensional (3D) structures layer by layer (lbl) according to a computer aided design (CAD) model. **[15]**. The ink with the required viscoelastic properties is extruded through a nozzle to form constructs with suitable pore sizes to enable bone ingrowth, and help the body to heal itself. Scaffolds should be fabricated from bioactive & bioresorpable materials (third generation biomaterials) **[16]** that will degrade and be integrated in the new bone tissue, preventing further surgical interventions. Bioactive glasses and glass ceramics are typical examples of the third generation of biomaterials **[5]**. Glasses and glass ceramics exhibit better bone bonding and anchorage than bioceramics **[5]**. The first bioactive glass (45S5; Bioglass®) was reported in 1969 **[17]**. Despite the great success of 45S5, it presents poor mechanical properties **[18],** and high dissolution rates **[19]**. To some extent, mechanical properties can be improved by doping the glasses with some functional ions **[20,21]**, or by combining them in composites **[22,23]**. Composites have relatively lower bioactivity in comparison to bioactive glasses.

The bioactive glasses are usually synthesised by two methods: sol–gel **[24]** and melt–quenching **[25]**. Sol–gel provides many advantages over melt–quenching, such as: (i) high degree of homogeneity; (ii) lower processing temperatures **[26]**; (iii) higher specific surface area **[25]**. However, the by–products are toxic and require a high temperature (typically >500 ºC) to be eliminated **[27]**. Moreover, a long aging processing step is usually required **[28,29]**. Increasing aging time often leads to some segregation that tends to induce early crystallisation and decreases bioactivity **[28]**.

The precursors used in the sol–gel process are very important in deciding the final properties. Tetraethyl orthosilicate (TEOS) and triethyl phosphate (TEP) are usually used as precursors for silica and phosphorus oxide. Organic acid salts such as acetates and citrates have the potential to be used as precursors for calcium and sodium **[30]** The major problem when using acetates is the basicity of the solutions, which demands a relatively high amount of acid to decrease the pH of the solution, leaving carbonaceous residues. Inorganic salts, such as nitrates salts, are commonly used **[30]**. Nevertheless, metal nitrate salts are prone to promote sudden crystallisation during the calcination step.

The type of catalyst used affects the structure and the final properties, such as porosity **[31]**. Inorganic acids such as sulphuric, hydrochloric and nitric are the most used catalysts. They trigger fast hydrolysis reaction **[32]**. The increase in inorganic acids concentration to catalyse the acetate salt precursors makes the elimination of their by–products from the samples more difficult.

Dry / wet milling can be used to reduce the particle size of the powders. Wet milling is recommended when high surface energy induces agglomeration between particles **[33]**. To achieve high green density **[34]**, particle size)PS), particle size distribution (PSD), particle morphology and all the relevant processing parameters need to be optimised **[35]**. All these reasons justify a renewed importance on the powder milling procedure.

There is still a lack of research aimed at fabricating scaffolds by robocasting from bioactive sol–gel derived glasses. This can be attributed to the high specific surface area and porous structure of the resulting powders that leads to the up–take of a significant portion of the dispersing liquid, hindering the formulation of suitable inks. Such features of sol–gel derived glasses are advantageous in terms of bioactivity, but supposedly constituted the main barriers towards using them in robocasting so far.

Accordingly, the objectives of the current doctoral thesis are: (i) to prepare a new high silica bioactive glass based on the quaternary (Si–Ca–Na–P) system using sol–gel; (ii) to develop a novel sol–gel technique to overcome the problems associated with the long aging time; (iii) to enhance the properties of the prime glass by using Cu and La functional ions; (iv) to gain an in–depth understanding about the effect of processing parameters, precursors and catalyst types, and concentrations; (v) to undertake a deep investigation to disclose the relation between calcination temperature and wet–milling parameters to achieve better rheological properties suitable for robocasting; (vi) to be able to predict ink printability in earlier stages of ink design; (vii) to fabricate scaffolds by robocasting using the developed sol–gel bioactive glasses; (viii) to disclose and report bioactivity, biocompatibility, mechanical & physical properties of the scaffolds fabricated from different glasses.

Considering the above perspective, this thesis comprises thirteen chapters. **Chapter 1** presents the state of the art; **Chapter 2** provides the solution to the long ageing in conventionally dried sol–gel (CD) and reports on a novel fast sol–gel synthesis (FD). **Chapter 3** demonstrates bioactivity assessments for FD and CD glasses to show the positive impacts of the novel sol–gel method on the glass bioactivity. After confirming the improved results of the novel sol–gel synthesis route, it was always adopted in the subsequent chapters. The main idea explored in **Chapter 4** was the preparation of high silica glass with Ca/P ratios mimicking those of stoichiometric hydroxyapatite (1.67) and β–tricalcium phosphate (1.5), as an attempt to obtain strong network structures and good bioactive glasses. The results revealed that bioactivity of the high silica glasses increases with increasing Ca/P ratio. Inspired by the findings of Chapter 4, **Chapter 5** aimed at investigating if bioactivity could be increased by further increasing the Ca/P ratio up to 12, and switching between acetate and nitrate metal salts, aiming to investigate their effect on biocompatibility, and bioactivity of glasses. **Chapter 6** is especially devoted to investigate the effects of using different metal salts and different catalyst types and concentrations on the preparation of high silica content glasses on the glass structure, to confirm the results obtained in Chapter 5. **Chapter 7** addresses the effects of doping the parent glass with Cu^{2+} and La^{3+} on cytotoxicity and bioactivity. Encouraged by the reasonable bioactivity & cytotoxicity results of the doped glasses, **Chapter 8** further investigates the influence of (Cu^{2+} & La^{3+}) co–doping on crystallisation, sintering–ability and sintered density, aiming at improving the mechanical properties of scaffolds fabricated thereof. **Chapter 9** reports a preliminary study aiming at

evaluating the effects of calcination temperature and milling parameters on the powder properties, including their dispersion ability and on the rheological properties of the resulting pastes. The findings are of high relevance for setting the suitable experimental conditions for the fabrication of scaffolds by robocasting. **Chapter 10** builds on the findings of Chapter 9, and aims at a better understanding of the effect of different parameters and their interactions on the rheological properties of the pastes prepared from the sol–gel derived glasses. **Chapter 11** is a follow up of the developments made in the frame of Chapters 9 & 10, reporting for the first time the successful fabrication of scaffolds by robocasting from sol–gel derived glass powders. **Chapter 12** reports on the fabrication of scaffolds from doped glasses with improved mechanical properties. **Chapter 13** provides the concluding remarks and summarises the main achievements, and points out future research directions towards enhancing materials properties and functionalities.

This work has taken entire four years full of challenges. It is hoped that this dissertation will be a good contribution in the field of Materials Science & Engineering, particularly in biomaterials and regenerative medicine.

References

[1] Q. Fu, E. Saiz, M.N. Rahaman, A.P. Tomsia, Bioactive glass scaffolds for bone tissue engineering : state of the art and future perspectives, Mater. Sci. Eng. C. 31 (2011) 1245–1256.

[2] V. Levašič, I. Milošev, V. Zadnik, Risk of cancer after primary total hip replacement: The influence of bearings, cementation and the material of the stem, Acta Orthop. 89 (2018) 234–239.

[3] R. Agarwal, A.J. García, Biomaterial strategies for engineering implants for enhanced osseointegration and bone repair, Adv. Drug Deliv. Rev. 1 (2015) 53–62.

[4] R.C. Richard, R.N. Oliveira, G.D.A. Soares, R.M.S.M. Thiré, Direct–write assembly of 3D scaffolds using colloidal calcium phosphates inks, Rev. Mater. 19 (2014) 61–67.

[5] D.G. Poitout, Biomechanics and Biomaterials in Orthopedics, London, 2004.

[6] K. Prasad, O. Bazaka, M. Chua, M. Rochford, L. Fedrick, J. Spoor, et al., Metallic biomaterials: Current challenges and opportunities, Materials (Basel). 10 (2017).

[7] B.R.A. Martin, S. Yue, J.V. Hanna, P.D. Lee, R.J.Newport, M.E. Smith, et al., Characterizing the hierarchical structures of bioactive sol – gel silicate glass and hybrid scaffolds for bone regeneration, (2012) 1422–1443.

[8] T.S. Wik, O.A. Foss, S. Havik, L. Persen, A. Aamodt, E. Witsø, Periprosthetic fracture caused by stress shielding after implantation of a femoral condyle endoprosthesis in a transfemoral amputee–a case report, Acta Orthop. 81 (2010) 765–767.

[9] Q. Fu, M.N. Rahaman, B. Sonny Bal, R.F. Brown, D.E. Day, Mechanical and in vitro performance of 13–93 bioactive glass scaffolds prepared by a polymer foam replication technique, Acta Biomater. 4 (2008) 1854–1864.

[10] S. Deville, E. Saiz, A.P. Tomsia, Freeze casting of hydroxyapatite scaffolds for bone tissue engineering, Biomaterials. 27 (2006) 5480–5489.

[11] K.F. Leong, C.M. Cheah, C.K. Chua, Solid freeform fabrication of three–dimensional scaffolds for engineering replacement tissues and organs,

Biomaterials. 24 (2003) 2363–2378.

[12] R. Felzmann, S. Gruber, G. Mitteramskogler, P. Tesavibul, A.R. Boccaccini, R. Liska, et al., Lithography–based additive manufacturing of cellular ceramic structures, Adv. Eng. Mater. 14 (2012) 1052–1058.

[13] Q.L. Loh, C. Choong, Three–Dimensional Scaffolds for Tissue Engineering Applications: Role of Porosity and Pore Size, Tissue Eng. Part B Rev. 19 (2013) 485–502.

[14] A. Entezari, Z. Zhang, J. Chen, Q. Li, Optimization of bone tissue scaffolds fabricated by robocasting technique, in: 11th World Congr. Struct. Multidiscip. Optim., Sydney, 2015: pp. 1–6.

[15] J.A. Lewis, J.E. Smay, J. Stuecker, J. Cesarano, Direct ink writing of three–dimensional ceramic structures, J. Am. Ceram. Soc. 89 (2006) 3599–3609.

[16] L.L. Hench, Third–Generation Biomedical Materials, Science (80–.). 295 (2002) 1014–1017.

[17] L.L. Hench, The story of Bioglass®, J. Mater. Sci. Mater. Med. 17 (2006) 967–978.

[18] I.D. Thompson, L.L. Hcnch, Mechanical properties of bioactive glasses, glass–ceramics and composites, Proc. Inst. Mech. Eng. Part H J. Eng. Med. 212 (1998) 127–136.

[19] D.M. Calandra, D. Di Mauro, F. Cutugno, S. Di Martino, Navigating wall–sized displays with the gaze: A proposal for cultural heritage, CEUR Workshop Proc. 1621 (2016) 36–43.

[20] M.N. Rahamana, D.E. Daya, S. Bal, Q. Fu, S.J. B., L.F. Bonewalde, et al., Bioactive glass in tissue engineering, Acta Biomater. 7 (2011) 2355–2373.

[21] W.D. Wong–ángel, L. Téllez–jurado, J.F. Chávez–alcalá, E. Chavira–martínez, V.F. Verduzco–cedeño, Effect of copper on the mechanical properties of alloys formed by powder metallurgy, Masterials Des. 58 (2014) 12–18.

[22] M. Rizwan, M. Hamdi, W.J. Basirun, Bioglass 45S5–based composites for bone tissue engineering and Bioglass V functional applications, J. Biomed. Mater. Part A. 105A (2017) 3197–3223.

[23] R.A. Pérez, J. Won, J.C. Knowles, H. Kim, Naturally and synthetic smart composite biomaterials for tissue regeneration ☆, Adv. Drug Deliv. Rev. 65 (2013) 471–496.

[24] M. Guglielmi, P. Barboux, The sol–gel method for the synthesis of glasses, ceramics and hybrid materials, Radiat. Eff. Defects Solids. 134 (1995) 31–37.

[25] B.A.E. Ben–Arfa, I.M.M. Salvado, J.M.F. Ferreira, R.C. Pullar, The effect of functional ions (Y3 +, F–, Ti4 +) on the structure, sintering and crystallization of diopside–calcium pyrophosphate bioglasses, J. Non. Cryst. Solids. 443 (2016) 162–171.

[26] C.S. Chai, K.A. Gross, B. Ben–Nissan, Critical ageing of hydroxyapatite sol–gel solutions, Biomaterials. 19 (1998) 2291–2296.

[27] J.D. Mackenzie, Applications of the sol–gel process, J. Non. Cryst. Solids. 100 (1988) 162–168.

[28] K. Zheng, A. Solodovnyk, W. Li, O.M. Goudouri, C. Stähli, S.N. Nazhat, et al., Aging time and temperature effects on the structure and bioactivity of gel–derived 45S5 glass–ceramics, J. Am. Ceram. Soc. 98 (2015) 30–38.

[29] D. Liu, T. Troczynski, W.J. Tseng, Aging effect on the phase evolution of water–based sol – gel hydroxyapatite, Biomaterials. 23 (2002) 1227–1236.

[30] L.C. Klein, Sol–gel technology for thin films, fibres, preforms, electronics, and specialty shapes, Noyes Publications, New Jersey, 1988.

[31] M. a. Fardad, Catalysts and the structure of SiO2 sol–gel films, J. Mater. Sci. 35 (2000) 1835–1841.

[32] Q.–Z. Chen, Y. Li, L.–Y. Jin, J.M.W. Quinn, P.A. Komesaroff, A new sol–gel process for producing Na2O–containing bioactive glass ceramics, Acta Biomater. 6 (2010) 4143–4153.

[33] M.I.L.L. Oliveira, K. Chen, M.F. Ferreira, J.M.F. Ferreira, Influence of thedeagglomeration procedure on aqueous dispersion , slip casting and sintering of Si3N4 –based ceramics, J. Eur. Ceram. Soc. 22 (2002) 1601–1607.

[34] H.N. Chia, B.M. Wu, Recent advances in 3D printing of biomaterials, J. Biol. Eng. 9 (2015) 1–14.

[35] E. Feilden, E.G.T. Blanca, F. Giuliani, E. Saiz, L. Vandeperre, Robocasting of structural ceramic parts with hydrogel inks, J. Eur. Ceram. Soc. 36 (2016) 2525–2533.

Chapter 1

1. State of the art

1.1. Biomaterials

Biomaterials have been used as implants since the ancient Greek, Egyptian and Hindu civilisations, with heterogeneous grafts being employed since the 19th century. The first used bioceramic was plaster of Paris in the form of calcium and/or phosphate, reported in 1892 by Dreesman **[1]**.

1.1.1. Classification according to biodegradability

The *1st generation* of biomaterials developed in 1963 was intended to be bio–inert (exhibits no/minimal response with the surrounding tissue), as the case of alumina **[1]**. The *2nd generation* biomaterials exhibit relatively low bioactivity and slow biodegradability, as in the case of β–tricalcium phosphate and hydroxyapatite, while the *3rd generation* are materials which stimulate cellular response at molecular level, inducing bone formation, and exhibiting faster bioactivity and biodegradability than bioceramics **[2]**.

1.1.2. Classification according to the type of material

i) Bioceramics: a family of biomaterials based on calcium phosphate (CP), such as hydroxapaptite and β–tricalcium phosphate, or a mixture between these two materials (biphasic calcium phosphates (BCP)) **[3]**. These materials are stiff and exhibit slow degradability. They are often used in combinations with polymers (composites) to enhance their mechanical and biological responses **[4]**. Nevertheless, composites lacks good bioactivity and biodegradability in comparison with bioactive glasses **[4]**.

ii) Polymers: include a wide group such as polylactic acid, polyglycolic acid, polyurethane, polyanhydrides, and polyorthoester. They lack sufficient mechanical properties, and they exhibit hydrophobic behaviour when implanted in the body providing low pH environments, which in turn tends to promote bone degradation **[5]**.

iii) Bioactive glasses: bioactive glasses and glass ceramics are typical examples of the third generation of biomaterials that can be gradually dissolved and replaced by bone **[6]**. The

paradigm changed in the late 1960s with the discovery of Bioglass® (BG) by Hench and collaborators in their pioneering work **[7]**.

1.2. Bioactive glass

Bioglass®, BG, is a silica–based glass synthesised in the (Si–Ca–Na–P) quaternary system usually prepared by the traditional melt–quenching technique. Bioactive glasses in general are biodegradable, with special responses when coming into contact with biological fluids, leading to the formation of a bone–like layer of hydroxyapatite (HA) at their surface. HA provides strong bonding between BG and the host living tissues.

Besides being non–cytotoxic and either bioactive or resorbable, modern biomaterials are aimed at adding other features to stimulate gene activation and enhance their performances in vitro and in vivo, including: (i) Non–genotoxicity (causing no damage to genes within a cell or DNA mutations); (ii) Osteoconductivity (bone readily grows on its surface); (iii) Osteoinduction (ability to recruit immature cells and to stimulate them towards developing into pre–osteoblasts, essential in any bone healing process); (iv) Osseo integration (establish a stable implant anchorage through its direct bone–to–implant contact) **[8]**.

Bioactive glasses and glass ceramics have gained particular interest in recent decades **[8,9]**. They show superior bioactivity properties to bioceramics **[10]**. The major advantages of bioactive glasses over bioceramics are: i) higher capability for bone re–generation; b) the possibility to provoke gene activation; c) they bond firmly to the bones in a faster manner than bioceramics **[6,11]** Moreover, bioactive glasses offer other advantages in the treatment of many disorders of several biological systems, and proved to help resume normal function, such as: osteomyelitis (destructive bony lesions) **[12,13]**; treating dentin hypersensitivity **[14]**; repairing injured cardiac & pulmonary tissues **[15]**; treatment of aneurysmal bone cysts (bone tumours) **[16]**.

Bioactive glasses have been synthesised in many systems, such as ternary and quaternary systems. Typical examples of bioactive glasses in quaternary systems are 45S5 and S53P4. 45S5 is probably the most well–known bioactive glass, containing 26.9 mol% CaO and with Ca/P ~5 **[7]**, while S53P4 is another famous bioactive glass with 20 mol% CaO and Ca/P = 5 **[17]**. The most common sol–gel bioactive glasses in the ternary system are 58S,

which contains 36 mol% CaO and Ca/P = 4.5 **[18]**, and 77S with 16 mol% CaO and Ca/P = 2 **[19]**.

1.2.1. Choice of glass composition

Yan and co–workers **[20]** prepared bioactive glasses by sol–gel in the three–component SiO_2–CaO–P_2O_5 (Si–Ca–P) system within the range of (100–x–y)SiO_2–xCaO–yP_2O_5 molar compositions. They found the best in–vitro bioactivity for the 80SiO_2–15CaO–5P_2O_5 composition. Saiz et al. **[21]** prepared silicate glass with different silica contents up to (67.7 wt. %), in addition to Na_2O, K_2O, CaO, MgO and P_2O_5 (Si–Na–K–Ca–Mg–P), with (56.5–67.7)SiO_2–(8.3–11)Na_2O–(2.2–3)K_2O–(10.1–15)CaO–(5.7–8.5)MgO, and P_2O_5 kept fixed at 6 wt%. They observed good mechanical properties, and a low rate of bioactivity because of the high silica content. Peitl et al. **[22]** concluded that the tendency of glasses in the (Si–Na–Ca–P) system to crystallise decreased, and the bioactivity was enhanced, with decreased P_2O_5 content. In turn, the in vitro bioactivity of bioactive glasses can be favoured by using low P_2O_5 contents (< 10 mol%), as under these conditions phosphorus acts as network modifier instead of network former. Consistently, greater P_2O_5 contents increase the network connectivity, and exert an opposite and deteriorating effect on bioactivity **[23]**. This can be attributed to the high affinity of the modifiers such as calcium and sodium to coordinate with phosphorus, thus enhancing its structural role **[24]**. This will result in a lower bio–mineralisation rate **[25]**. Pereira et al. **[26]** synthesised silica glass compositions in a three component (Si–Ca–P) system, and concluded that the compositions with higher silica contents [(80–x)SiO_2–xCaO–4P_2O_5] exhibited better bioactivity. However these results contradict the results obtaind bySaiz et al. **[21].**

The inclusion of calcium and phosphate in the glass system facilitates apatite formation **[27]**. The Ca/P ratio is known to play an important role in modifying and tailoring the bioactivity of glasses. Compositions that enhance the non–bridging oxygens/bridging oxygens (NBO/BO) ratio reduce the glass network's structure and connectivity.

It has been referred to that the inclusion of Na_2O in bioactive glasses induces a more accentuated glass network disrupting effect, and maintains a good bioactivity rate, while the mechanical properties of glasses and glass ceramics may be improved **[28]**.

1.2.2. Glass functionalisation

Bioactive glasses experience poor mechanical properties which limit their use in load bearing devices **[29,30]**. Enormous efforts were made to improve the mechanical properties of bioactive glasses **[31–34]**. The mechanical properties could be improved by increasing the fracture toughness for bioactive glasses. This target can be accomplished by doping a parent glass with some functional ions **[35,36]**, or by impregnating ceramic/metal/polymer particles or fibres in the bioactive glass matrix to produce composites **[19,37]**. Accordingly, attention is required to tune the degradation rates between all the constituent composite components **[38]**. Nevertheless, composites are known to exhibit lower bioactivity compared with bioactive glasses **[39]**. The difficulty in governing biodegradability, and the low bioactivity of composites, prevents their use when a rapid bioactive response with highly controlled biodegradation is required.

The research frontiers are still far from the optimum needed design in terms of mechanical properties and tuned bioactivity. There are many functional ions that, although existing in trace quantities in the human body, play many important and different roles, and are vital for a good body metabolism. Doping bioactive glasses with some functional ions is likely to give room for enhancing the harmony between the desired levels of bioactivity and mechanical properties **[40]**. In this regard, many investigations reported on the role of different functional ions in binary **[41,42]**, ternary **[43,44]** and quaternary glass systems **[44,45]**.

i) Copper (Cu) is found throughout the tissues of the human body in total trace quantities of ~75–100 mg of this quantity, 50% of the Cu is stored in the muscles and bones **[46]**. Cu is an antioxidant, also a vital component in gene–expression **[47]**, and it serves as a cofactor **[48]** stimulating ~30 enzymes to provide their proper functions **[49]**. Moreover, Cu is an essential element for keeping blood vessels, connective tissues and skin in a healthy condition **[49]**. Cu deficiency may lead to inappropriate bone formation, and bone's fracture, particularly in children. In patients with bone fractures, it is found that Cu supplements reduce the healing time **[50]**.

Cu has been extensively reported to significantly enhance the mechanical properties and sintering ability in metal alloys **[51,52]**. It forms a liquid phase that tends to reduce the

overall porosity and enhance the diffusion during sintering. Moreover, it enhances the mechanical properties of Ca–Zn–Mg bulk metallic glass **[53]** and of borate glass **[54]**.

ii) Lanthanum (La) is a rare earth element, which has no biological role in humans, and its bioavailability in the human body is extremely low, at 0.00127% (± 0.00080%) **[55]**. Commonly La does not exist in animal and plants tissue; nevertheless, traces are found in drinking water **[56]**, and in elevated quantities (up to 16 times higher than nonexposed controls), with amounts up to ~0.5 μg g^{-1} in the bones and lungs of refinery and smeltery workers **[57]**. Despite this, it has a wide range of applications in treatments to repair disorders in the human body, such as playing an important role in treating atherosclerotic cardiovascular disease when taken as a lanthanum chloride supplement **[58]**. Furthermore, if taken as supplement in the form of lanthanum carbonate it can partially replace the calcium–based phosphate which occurs in hypercalcemia, leading to reduce the risk of cardiovascular calcification **[56]**, or the case of hyperphosphatemia in patients with end stage renal disease (ESRD) **[59]**. La was found to increase the density of strontium borate glasses **[60]**. Nevertheless a literature overview revealed that very scarce information is available about the effects of these two ions on the density, sintering ability and crystallisation kinetics of bioactive glasses. Therefore, the combination of these ions and their interaction with the glassy matrix still needs to be addressed.

A novel bioactive glass exhibiting better mechanical properties as well as competitive bioactivity needs to be developed. Increasing the silica content in the glass matrix, and doping the developed glass with some functional ions, could both provide a good solution.

1.2.3. Glass synthesis methods

Bioactive glasses are synthesised mainly by two methods; sol–gel **[61–63]** and melt–quenching methods **[35,36]**. Hench was a pioneer in employing these two methods in bioactive glass synthesis, he prepared BG using the melt–quenching technique in 1969 **[7]**. After almost 2 decades, he prepared the same glass by the sol–gel technique to improve surface morphology and bioactivity **[64]**.

i) Melt quenching technique

In the melt quenching technique, glass is obtained by fusing precursors such as oxides or carbonates at an elevated temperature. To inhibit crystallisation, the melt is quenched in cold water to obtain a frit glass, or cast to obtain bulk glasses **[35]**.

ii) Sol–gel technique

In the sol–gel technique, a mixture of the precursor solution (alkoxides and/or metal salts) is kept under stirring for a certain interval of time, for the hydrolysis and condensation process and a clear sol is obtained, followed by aging, drying and calcination to form a glass powder or monolithic shapes **[65]**.

1.3. Sol–gel glass

The synthesis of silicate glasses by the sol–gel method involves the hydrolysis and condensation process of silicon alkoxide (usually tetra–ethyl ortho–silicate, TEOS, $C_8H_{20}O_4Si$), in water **[66]**. The beginning of sol–gel can be assigned to Ebelmen **[67]**, who in 1845 successfully synthesised an inorganic product in the form of silica, from the hydrolysis of TEOS. Roy et al. prepared multicomponent sol–gel glasses in 1950 **[68]**, and Schott Glaswerke in Germany started using sol–gel commercially in 1953 **[67]**. The chemical basis of multi–component–oxides preparation was elaborated first in 1969 by Dislich and Hinz **[69]**.

The sol–gel method provides numerous advantages over the conventional melt quenching technique: (i) a molecular–level mixing of the batch components which enhance the homogeneity of the glasses **[70]**; (ii) it can produce compositions unattainable by the melt–quenching method **[65]**; sol–gel requires lower processing temperatures **[71]** that prevent preferential volatilisation of certain components such as phosphorus; (iii) for the same composition, sol–gel glasses exhibit higher specific surface area (SSA) and lower network connectivity than those produced by the melt quenching method, which leads to higher dissolution rates and higher bioactivity **[65]**.

1.3.1. Effects of precursor and processing parameters on sol–gel derived glasses

It is well known that alkoxides are often used as precursors for oxides in sol–gel synthesis. The problems are the unavailability of some metal alkoxides, and/or the complexity in dealing with some alkoxides, as in the case of group I and II elements where the alkoxides are often air–sensitive, are sometimes in the solid state, can have unreliable purity, and they do not dissolve easily. The alternative to overcome this problem is by using organic or inorganic acid salts.

i) Organic acid salts – have the potential to be used as precursors, as in the case of acetates and citrates **[72]**. The disadvantages of using acetate metal salts are: (a) the carbonaceous residues in the final products; (b) the high pH of the solution, which may lead precipitation and to a fast gelation process; (c) the large amount of acid required to promote hydrolysis, which tends to remain in the residues in the final product and need elevated temperatures to be eliminated.

ii) Inorganic acid salts – are the most commonly used in sol–gel, namely in the nitrates form, as they dissolve easily, and their by–products decompose at relatively moderate temperatures in comparison with sulphates and chlorides, which need higher decomposition temperatures **[72]**. The major disadvantage of using metal nitrate salts is their tendency to crystallise in an uncontrollable manner during the aging and drying processes, which negatively affects the homogeneity and the microstructure of the final product. The effective solution to this problem is to extract a large portion of water content in an early stage during sol preparation, i.e. before gelling. The fast elimination of water can be performed by evaporation **[72]**, which in turn tends to supress the crystallisation.

iii) Catalyst – the type of catalyst used dramatically affects the final properties, such as porosity, optical, and structural properties. The selection of the catalyst depends on the desired properties of the final product **[73]**. The catalyst facilitates the hydrolysis of alkoxides. The hydrolysis and condensation process are extensively explained and addressed by Brinker and co–workers **[74]**. They reported on hydrolysis reactions catalysed by acids or bases. These reactions can be promoted by increasing the H_2O/Si ratio to some extent under acidic conditions. Also, they stated that pH plays crucial role in hydrolysis and condensation. Cihlar **[75]** reported that hydrolysis and condensation

reactions do not depend on the type of catalyst, but are strongly dependent on the pH of the solution. Both acid and base catalysts could be used. Many authors suggest that using a certain amount of inorganic acid is a more effective catalyst than an equivalent amount of base **[74]**.The mineral (inorganic) acids such as sulphuric acid, hydrochloric acid and nitric acid are strong, being the most commonly used as catalysts. They trigger the hydrolysis reaction in a very short time (a few minutes) **[28]**.

The increase in inorganic acids concentration in the sample is the major drawback of using them as catalysts, because they need higher temperatures for the elimination of their by–products. However, the increase in the calcination temperature to eliminate these residuals readily converts glasses into glass ceramics **[72,76].** As a trial to reduce the inorganic acid concentration in the sol–gel glass, Faure et al. replaced the strong inorganic acids (~0.5–2 mol L^{-1}) with much lower quantities of weak organic acids (0.5–50 mmol L^{-1}) **[72]**, and they successfully used citric acid as acatalyst for thesynthesis of 45S5 bioactive glass ceramic.

iv) Aging and drying – the sol–gel method requires extra–long drying and aging times, extended beyond a month in some cases. Aging and drying procedures are the most time consuming stages and the major disadvantages in the sol–gel process, which limits its use in both research and commercial applications. Many attempts have been made to produce glasses using different aging and drying times. For example, Chen et al. **[28]** used a relatively quick process to synthesise bioactive glass ceramics by aging the sol for 72 h at 60 °C, followed by drying for 40 h at 200 °C. Shirong et al. dried the sol at 70 °C for 3 days after aging for 3 days at 60 °C **[77]**. Bellucci et al. kept the sol at ambient temperature for 4 h, and they used 3 days aging time at 35 °C, followed by 6 days for drying at a constant temperature of 50°C, and then elevating the temperature to 110 °C for 3 more days to make a bioglass **[70]**. Ageing at 70 °C for 3 days, followed by drying at 150 °C for 52 h was utilised by Mami et al. **[78]**. In a similar regime, Siqueira et al. **[79]** aged the sol at 70 °C for 7 days and then dried at 130 °C for 2 days. A four–component bioactive glass (Si–Ca–P–Zn) was synthesised by Balamurugan et al., where the sol was aged at room temperature for 10 days, followed with 2–stage drying at 70 °C for 3 days, and 120 °C for 2 days **[80]**. Zheng et al. used longer aging times, where they aged the sample at room temperature for 15 days, followed by 24 h drying time **[81]**. In the synthesis of silica–based glass powder

by Nariyal et al. **[82]**, they aged the sol for one entire month at room temperature. Out of all these cases, the fastest aging and drying process took about 5 entire days (120 h).

It was reportedthat increasing aging times are often accompanied by a noticeable increase in crystallisation and a decrease in bioactivity **[72,81]**.

In regard to the problems associated with long drying and aging procedures, a new specific technique capable of eliminating the liquid part at the early stage of sol–gel preparation, reducing the drying and aging times by about 100 times was developed and implemented in the frame of this PhD.

1.4. Bone disorder and substitution

Bone diseases or trauma may result in bone disorders that need special treatment procedures to resume normal bone function **[83]**. This includes replacing the affected bone with an implant device, which must be one of the three possibilities: i) *autograft* (bone graft harvested from the same patient); ii) *allograft* (bone graft harvested from another donor); iii) *artificial implant.* An *autograft* does not provide optimum substitute for bone cancer patients to avoid fast spread of the tumour, and when large bone segments are needed **[6]**. Meanwhile, the lack of donors and the risk of transferring viral diseases limit the use of *allografts* **[84]**. Therefore, an *artificial implant* is more suitable. The *artificial implant* can be metallic or bioglass/bioceramic tissue engineering scaffolds **[85]**. Although metallic implants are capable of withstanding bearing loads, they promote bone resorption (mass loss) due to the effect of stress shielding (osteopenia, reduction of bone density) **[86]**, which causes bone fracture over time **[87,88]**. Accordingly, scaffolds are the most promising candidates.

1.5. Scaffolds for tissue engineering (regenerative medicine)

Tissue engineering (TE) was introduced a long time ago with great success. In the 16th century, Professor Gasparo Tagliacozzi (1546–1599) successfully replaced a damaged nose from the forearm flap **[89]**. Eventhough, TE procedures was formally introduced in the 1980's **[90]**. TE is an emerging interdisciplinary field of research combining engineering and life science, aiming to develop new methods and procedures to repair damaged tissues **[91]**. This includes impregnating the scaffold with harvested cells. The scaffold is a three

dimensional (3D) structure fabricated to serve temporarily as a template to guide and support new tissue growth, and restore the tissue's normal function. After implantation and during the healing process, the scaffold must degrade while the cells grow and proliferate to regenerate new tissue **[89]**.

1.5.1. Scaffold requirements

i) Biocompatible: The scaffold's products must not exhibit any harmful/inflammatory effect on the cells and tissue around. The degraded products are removed from the body without any side–effects.

ii) Biodegradable: The scaffold must degrade overtime, and be gradually replaced by new generative tissue, stimulating the body to heal itself.

iii) Morphological: The scaffolds have large interconnected pores, and a hierarchical degree of porosity to permit vascularisation, with macro–pore sizes >50 μm to enable the cells to penetrate easily into the scaffold, and also to allow the waste to diffuse out of the scaffold, and micro pores within the size range of 1–50 μm to facilitate cell anchorage and proliferation.

iv) Mechanical properties: The scaffold must exhibit very similar mechanical properties with the replaced tissue, to be able to withstand the exerted loads and ensure there is no stress shielding effect to the bones. They must also maintain overall mechanical integrity during the remodelling (bone formation and resorption) process [**92,93]**.

1.5.2. Scaffold fabrication methods

Many methods were used to fabricate scaffolds for TE such, as polymer foam replication **[94]**, freeze casting **[95]**, solid freeform fabrication **[96]** or lithography–based additive manufacturing **[97]**. However, amongst all, robocasting is a promising technique in scaffold synthesis, as it opens new avenues for optimising scaffold morphology to mimic specific human bone morphology by a computer aided design (CAD), with improved mechanical properties compared to older fabrication techniques **[98]**.

1.6. Robocasting

Robocasting has been used for two decades as an innovative tool for casting complex shaped ceramic and composite components, without the need for moulds **[99]**. It is related to direct writing and additive manufacturing techniques. In robocasting, the ink is extruded from a nozzle to construct three dimensional (3D) structures layer by layer **[100]**. The structure's shape and size are controlled by a CAD model.

1.6.1. Ink/paste preparation

The ink is made by mixing a powder with water and small percentages of processing additives, including dispersants, binders, thickening agents and coagulants, in order to obtain the desired rheological properties. A suitable ink for robocasting should flow steadily, and become thinner under the applied shear stress (i.e., exhibit a shear thinning flow behaviour) to facilitate extrusion, without blocking the nozzle. It should then exhibit a fast recovering of the internal structure to maintain the shape, and offer mechanical support to the subsequent layers **[101]**. It is a challenge to set the suitable viscoelastic behaviour of the pastes, depending on many experimental factors. The most relevant factors determining the rheological behaviour of the starting suspensions include particles size (PS), particle size distribution (PSD)] **[102–104]**, particle shape and density **[105]**, and the solid/liquid interactions **[106–108]**. Maximising the solid loading is an important issue for minimising the dimensional variations during the drying and sintering steps **[106,108]**. However, an obvious consequence of incrementing the dispersed solids volume fraction of a powder is the increase in viscosity of the resulting suspension **[106,107]**. Therefore, the optimal solids volume fraction has to be a balance achieved between these two desirable, but incompatible, features (a maximum solid loading and a relatively low viscosity that determines the ease of preparation, handling and casting of the suspensions) **[107,108]**.

Repulsive interparticle forces are required to overcome the attractive Van der Walls forces for preparing dense and homogeneous suspensions with good flow properties for colloidal processing **[106–114]**. Repulsive forces can be of electrostatic origin, or be created by steric hindrance of polymeric species specifically adsorbed at the surface of the particles,

or be achieved by a mixed electrosteric stabilisation mechanism when polyelectrolytes are used as dispersants [**102,111**].

The solid/liquid interactions can be manipulated by selecting suitable processing additives for the specific system **[106,109]**.

The particle packing density can be greatly improved by mixing suitable volume fractions of different sized particles having adequate mean size ratios. Filling the interstitial spaces left between the coarser particles with finer particles has a further advantage of releasing dispersion media from those interstices, which becomes available for flow, lowering the viscosity and enabling further increments in solids loading.

Hard agglomerates tend to confer poor flow properties (shear thickening behaviour) to the suspensions, implying the use of low shear rate processes **[115]**. The efficient destruction of hard agglomerates is of outstanding importance for improving the flow behaviour of the suspensions, and the homogeneity and the sintering ability of the green bodies. The homogeneity of green bodies, with small particle and pore sizes that shorten the diffusion paths, enable full densification, sub–micrometre grain sizes and transparent ceramics to be achieved at relatively low sintering temperatures, as the best proof of this concept **[116–118]**.

1.6.2. Material used for robocasting

Many materials were used to robocast scaffolds for tissue engineering, including calcium phosphate (CP) and its derivatives **[119–121]**, and ceramic/polymer composites **[122,123]**. However, the fabrication of bioactive glass scaffolds by robocasting has proven to be more complicated, even from non–porous melt–quenched glass frits. The typical porous features of sol–gel derived bioactive glass powders bring further processing difficulties, as the dispersing liquid portion absorbed by the porous structure will not be available for flowing. This explains why the fabrication of bioactive glass scaffolds by robocasting has been scarcely reported, and only for glass compositions prepared by melt–quenching **[101,124]**. The most important requirements for successful fabrication of scaffolds by robocasting include the ease of ink preparation and the aptitude of the glass composition for sintering **[124]**. These requirements are not satisfactorily met by the most popular 45S5 Bioglass® composition. The excessive leaching of Na^+ and the concomitant increase in pH

hinders an efficient dispersion. The ink preparation challenge for melt quenched glasses could only be overcome recently **[101,124]**.

However, the sintered scaffolds exhibited poor mechanical properties. Therefore, in the robocasting of scaffolds, preference has been given to less soluble glasses that exhibit broader sintering windows, such as the (13–93) composition **[125]**. Nevertheless, the enhanced sintering ability and the gains in mechanical properties are in this case achieved at the expense of lower bio–mineralisation and degradation rates, as expected from the relatively high network connectivity of the (13–93) glass **[126]**.

Nevertheless, there is still a lack of bioactive sol–gel glasses suitable for formulating inks for robocasting. This can be attributed to their high specific surface area and porous structure, responsible for up–taking a significant portion of the dispersing liquid. Although these features of sol–gel derived glasses are advantageous in terms of bioactivity, such features supposedly constitute the main barriers towards using them in robocasting.

1.7. Powder milling

Powder milling is a very important segment to ensure successful robocasting. The difficulty experienced in robocasting bioactive glasses, and in particular sol–gel derived glasses, justifies a renewed emphasis on the powder milling process. Powder milling can be conducted as wet or dry milling. The former is more effective, being commonly recommended when agglomeration between particles can be induced by high surface energy **[115]**.

The reduction in particle size occurring during milling results from the accumulated stresses inside the particles due to the applied mechanical energy, which induces cracks that propagate, leading to particle breakage **[127]**.

1.7.1. Parameters effecting wet milling

Many important parameters should be taken into consideration while performing wet ball milling, such as solids loading (liquid to powder ratio (LPR)), and the speed and type of milling machine **[128]**. High heat treatment temperatures may lead to the formation of hard

agglomerates that are difficult to destroy with milling. The individual and mutual influences of heat treatment temperature and of the balls to powder ratio (BPR) on the wet milling performance, and morphology of the powders produced, still need to be better investigated and reported. Therefore, the control and understanding of wet milling parameters may lead to a prediction of the printing ability of the subsequent ink.

The robocasting of sol–gel glasses has not been investigated so far. A literature survey revealed that no work has been carried out to demonstrate the combined effects of porosity and particle/agglomerate size on the rheological properties of the suspensions prepared from sol–gel derived bioactive glass powders.

In this work, a novel sol–gel route will be used to synthesis new quaternary glass system (Si–Ca–Na–P) with high silica, and low Na and P contents. The use of organic and inorganic metal salts as precursors for Ca and Na will be deeply studied to understand the impact of these precursors on the glass's final properties. Tuning the bioactivity by modifying the catalyst and its concentration will be evaluated and disclosed. Powder milling will be used to control different parameters to facilitate the early prediction of ink printability by robocasting. The obtained information will be used as a base formula to print scaffolds from sol–gel glass for the first time.

1.8. Outline of the Research Programme

Bone fracture can be provoked by accidents and trauma, or it can be stimulated by an increase in osteoporosis or bone cancers. Thus, the need for scaffolds fabricated by smart modern methods such as robocasting is increasing progressively. This can be attributed to the high control over the pore size and shape.

Therefore, the outline of the research program is as follows:

1- Development of a novel fast sol–gel synthesis route to synthesise a new sol–gel glass in only one hour, avoiding the associated problems with long aging time, which is explained in chapters 2, 3 and 4.

2- The new sol–gel glass was designed with high silica and low sodium contents, to increase the mechanical properties and reduce the high dissolution rate, and detailed information on this is available in chapter 5. In Chapter 6 is presented the role of catalysts on the final microstructure of the sol-gel derived bioglass.

3- Studies were also made into the doping of the bioactive sol-gel glass with Cu^{2+} and La^{3+} ions. The cytotoxicity and bioactivity for Cu and La doped high silica sol-gel glasses is described in chapter 7. The effects of a range of quantities of La and Cu co-doping on the structure, crystallisation and sinterability of the bioglass was investigated in detail in chapter 8.

4- The high specific area of the sol–gel glass is considered as the main obstacle for the use of these glasses as an ink for robocasting of the scaffolds. Therefore, the morphology parameters of the powder need to be well monitored and controlled to meet the requirements for scaffold fabrication by robocasting. The effect of powder milling on the morphology is explained in detail in chapter 9, and the rheology properties to meet an ink requirement for printing / robocasting is investigated in chapter 10.

5- Bioactive glass scaffolds were robocast from sol-gel precursors for the first time. The robocasting of the glass scaffolds and their characterisation is reported in chapter 11. The robocasting of La and Cu doped bioactive glass scaffolds is finally detailed in chapter 12, and is was found that while doping the sol–gel glass with La led to slight increase in the mechanical properties, the mechanical properties were increased significantly by Cu doping, leading to a very high compressive strength of 14 MPa.

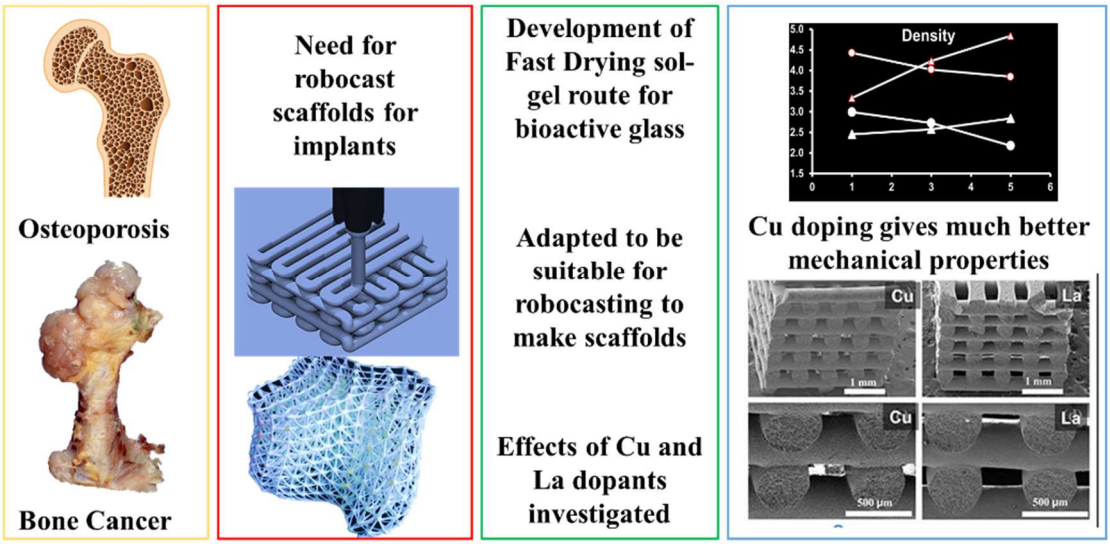

Fig. 1.1: General outline of the Research Programme

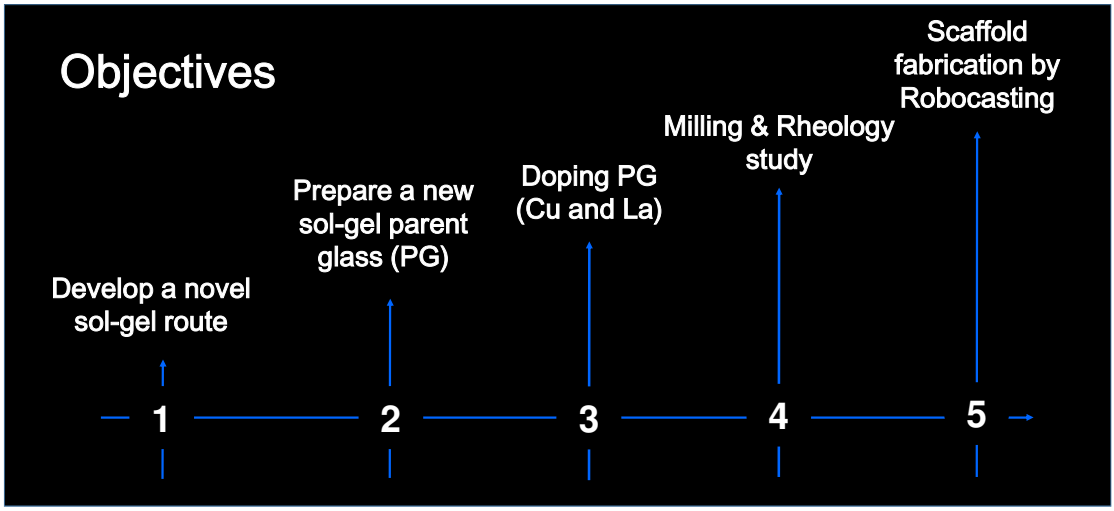

Fig. 1.2: The five stages of the Research Programme

References

[1] S.F. Hulbert, L.L. Hench, D. Forbers, L.S. Bowman, History of bioceramics, Ceram. Int. 8 (1982) 131–140.

[2] M. Navarro, A. Michiardi, O. Castaño, J.A. Planell, Biomaterials in orthopaedics, J. R. Soc. Interface. 5 (2008) 1137–1158.

[3] E.J. Lee, F.K. Kasper, A.G. Mikos, Biomaterials for tissue engineering, Ann Biomed. Eng. 42 (2014) 323–337.

[4] M. Rizwan, M. Hamdi, W.J. Basirun, Bioglass 45S5–based composites for bone tissue engineering and Bioglass V functional applications, J. Biomed. Mater. Part A. 105A (2017) 3197–3223.

[5] S. Oh, N. Oh, M. Appleford, J.L. Ong, Bioceramics for tissue engineering applications – A Review, Am. J. Biochem. Biotechnol. 2 (2006) 49–56.

[6] D.G. Poitout, Biomechanics and Biomaterials in Orthopedics, London, 2004.

[7] L.L. Hench, The story of Bioglass®, J. Mater. Sci. Mater. Med. 17 (2006) 967–978.

[8] L.L. Hench, N. Roki, M.B. Fenn, Bioactive glasses: Importance of structure and properties in bone regeneration, J. Mol. Struct. 1073 (2014) 24–30.

[9] M.N. Rahamana, D.E. Daya, S. Bal, Q. Fu, S.J. B., L.F. Bonewalde, et al., Bioactive glass in tissue engineering, Acta Biomater. 7 (2011) 2355–2373.

[10] L.L. Hench, Bioceramics: From Concept to Clinic, J. Am. Ceram. Soc. 74 (1991) 1487–1510.

[11] V. Krishnan, T. Lakshmi, Bioglass: A novel biocompatible innovation, J. Adv. Pharm. Technol. Res. 4 (2013) 78–83.

[12] J. McAndrew, C. Efrimescu, E. Sheehan, D. Niall, Through the looking glass; Bioactive glass S53P4 (BonAlive®) in the treatment of chronic osteomyelitis, Ir. J. Med. Sci. 182 (2013) 509–511.

[13] L. Drago, D. Romanò, E. De Vecchi, C. Vassena, N. Logoluso, R. Mattina, et al., Bioactive glass BAG–S53P4 for the adjunctive treatment of chronic osteomyelitis of the long bones: an in vitro and prospective clinical study., BMC Infect. Dis. 13 (2013) 1–8.

[14] C. Tirapelli, H. Panzeri, R.G. Soares, O. Peitl, E.D. Zanotto, A novel bioactive glass–ceramic for treating dentin hypersensitivity., Braz. Oral Res. 24 (2010) 381–7.

[15] S. Kargozar, S. Hamzehlou, F. Baino, Potential of bioactive glasses for cardiac and pulmonary tissue engineering, Materials (Basel). 10 (2017) 1–17.

[16] J. Syvänen, Y. Nietosvaara, I. Kohonen, E. Koskimies, M. Haara, J. Korhonen, et al., Treatment of Aneurysmal Bone Cysts with Bioactive Glass in Children, Scand. J. Surg. 107 (2018) 76–81.

[17] I. Kinnunen, K. Aitasalo, M. Pöllönen, M. Varpula, Reconstruction of orbital floor fractures using bioactive glass, J. Cranio–Maxillofacial Surg. 28 (2000) 229–234.

[18] P. Saravanapavan, J.R. Jones, R.S. Pryce, L.L. Hench, Bioactivity of gel – glass powders in the CaO–SiO2 system : A comparison with ternary (CaO–P2O5–SiO2) and quaternary glasses (SiO2 –CaO–P2O5 –Na2O), J. Biomed. Mater. Res. A. 66 (2003) 110–119.

[19] J.R. Jones, Reprint of: Review of bioactive glass: From Hench to hybrids, Acta Biomater. 23 (2015) S53–S82.

[20] X. Yan, X. Huang, C. Yu, H. Deng, Y. Wang, Z. Zhang, et al., The in–vitro bioactivity of mesoporous bioactive glasses, Biomaterials. 27 (2006) 3396–3403.

[21] E. Saiz, M. Goldman, J.M. Gomez–Vega, A.P. Tomsia, G.W. Marshall, S.J. Marshall, In vitro behavior of silicate glass coatings on Ti6Al4V, Biomaterials. 23 (2002) 3749–3756.

[22] O. Peitl, E.D. Zanotto, L.L. Hench, Highly bioactive P2O5–Na2O–CaO–SiO2 glass–ceramics, Non–Crystalline Solids. 292 (2001) 115–126.

[23] P. Kiran, V. Ramakrishna, M. Trebbin, N.K. Udayashankar, H.D. Shashikala, Effective role of CaO / P2O5 ratio on SiO2 –CaO–P2O5 glass system, J. Adv. Res. 8 (2017) 279–288.

[24] A. Tilocca, A.N. Cormack, Structural Effects of Phosphorus Inclusion in Bioactive Silicate Glasses, J. Phys. Chem. B. 111 (2007) 14256–14264.

[25] M.D. O'Donnell, S.J. Watts, R.G. Hill, The effect of phosphate content on the bioactivity of soda–lime–phosphosilicate glasses, J. Mater. Sci. Mater. Med. 20

(2009) 1611–1618.

[26] M.M. Pereira, A.E. Clark, L.L. Hench, Calcium Phosphate Formation on Sol Gel Derived Bioactive Glasses in Vitro, J Biomed Mater Res. 28 (1994) 693–698.

[27] A. Martınez, I. Izquierdo–Barba, M. Vallet–Regı, Bioactivity of a CaO–SiO2 Binary Glasses System, Chem. Mater. 12 (2000) 3080–3088.

[28] Q.Z. Chen, Y. Li, L.Y. Jin, J.M.W. Quinn, P.A. Komesaroff, A new sol–gel process for producing Na2O–containing bioactive glass ceramics, Acta Biomater. 6 (2010) 4143–4153.

[29] Q. Fu, E. Saiz, M.N. Rahaman, A.P. Tomsia, Bioactive glass scaffolds for bone tissue engineering: state of the art and future perspectives, Mater Sci Eng C Mater Biol Appl. 31 (2012) 1245–1256.

[30] E. Fiume, J. Barberi, E. Verné, F. Baino, Bioactive glasses: From parent 45S5 Composition to Scaffold–Assisted Tissue–Healing Therapies, J. Funct. Biomater. 9 (2018) 1–33.

[31] V.K. Vyas, A.S. Kumar, S. Prasad, S.P. Singh, R. Pyare, Bioactivity and Mechanical behavior of cobalt oxide doped bioactive glass, Bull. Mater. Sci.,. 38 (2015) 957–964.

[32] V.K. Vyas, A. Sampath Kumar, S.P. Singh, R. Pyare, Effect of nickel oxide substitution on bioactivity and mechanical properties of bioactive glass, Bull. Mater. Sci. 39 (2016) 1355–1361.

[33] J.. Wang, C.K.; Ju, C.P.; Chern Lin, Effect of doped bioactive glass on structure and properties of sintered hydroxyapatite, Mater. Chem. Phys. 53 (1998) 138–149.

[34] R. Moonesi Rad, A.Z. Alshemary, Z. Evis, D. Keskin, K. Altunbaş, A. Tezcaner, Structural and biological assessment of boron doped bioactive glass nanoparticles for dental tissue applications, Ceram. Int. 44 (2018) 9854–9864.

[35] B.A.E. Ben–Arfa, I.M. Miranda Salvado, J.M.F. Ferreira, R.C. Pullar, The Influence of Cu2+ and Mn2+ Ions on the Structure and Crystallization of Diopside–Calcium Pyrophosphate Bioglasses, Int. J. Appl. Glas. Sci. 7 (2016) 345–354.

[36] B.A.E. Ben–Arfa, I.M.M. Salvado, J.M.F. Ferreira, R.C. Pullar, The effect of

functional ions (Y3+, F−, Ti4+) on the structure, sintering and crystallization of diopside–calcium pyrophosphate bioglasses, J. Non. Cryst. Solids. 443 (2016) 162–171.

[37] I.D. Thompson, L.L. Hcnch, Mechanical properties of bioactive glasses, glass–ceramics and composites, Proc. Inst. Mech. Eng. Part H J. Eng. Med. 212 (1998) 127–136.

[38] R.A. Pérez, J. Won, J.C. Knowles, H. Kim, Naturally and synthetic smart composite biomaterials for tissue regeneration ☆, Adv. Drug Deliv. Rev. 65 (2013) 471–496.

[39] M. Par, Z. Tarle, R. Hickel, N. Ilie, Polymerization kinetics of experimental bioactive composites containing bioactive glass, J. Dent. 76 (2018) 83–88.

[40] L.L. Hench, J. Julian, Bioactive Glasses : Frontiers and Challenges, Frontiers (Boulder). 3 (2015) 1–12.

[41] L. Courthéoux, J. Lao, J. Nedelec, E. Jallot, Controlled Bioactivity in Zinc–Doped Sol – Gel–Derived Binary Bioactive Glasses, J. Phys. Chem. C. 112 (2008) 13663–13667.

[42] J. Soulie, J.M. Nedeleccd, E. Jallot, Influence of Mg doping on the early steps of physico–chemical reactivity of sol – gel derived bioactive glasses in biological medium, Phys. Chem. Chem. Phys. 11 (2009) 10473–10483.

[43] A. Philippart, N. Gómez–cerezo, D. Arcos, A.J. Salinas, E. Boccardi, M. Vallet–regi, et al., Novel ion–doped mesoporous glasses for bone tissue engineering : Study of their structural characteristics in fl uenced by the presence of phosphorous oxide, J. Non. Cryst. Solids. 455 (2017) 90–97.

[44] J. Bejarano, P. Caviedes, H. Palza, Sol–gel synthesis and in vitro bioactivity of copper and zinc–doped silicate bioactive glasses and glass–ceramics, Biomed. Mater. 10 (2015) 1–13.

[45] N.J. Lakhkar, E.A.A. Neel, V. Salih, Strontium oxide doped quaternary glasses : effect on structure, degradation and cytocompatibility, J. Mater. Sci. Mater. Med. 20 (2009) 1339–1346.

[46] M. Angelova, S. Asenova, V. Nedkova, Copper in the human organism, Trakia J.

Sci. 9 (2011) 88–98.

[47] R. Uauy, M. Olivares, M. Gonzalez, Essentiality of Copper in Humans, Am J Clin Nutr. 67 (1998) 9525–98.

[48] V. Culotta, Cell Biology of copper, J. Biol. Inorg. Chem. 15 (2010) 1–2.

[49] J. Osredkar, N. Sustar, Copper and Zinc, Biological Role and Significance of Copper/Zinc Imbalance, J. Clin. Toxicol. s3 (2011) 1–18.

[50] H.H.A. Dollwet, J.R.J. Sorenson, Roles of copper in bone maintenance and healing, Biol. Trace Elem. Res. 18 (1988) 39–48.

[51] M. V Kostina, M.M. Perkas, A.E. Shelest, V.S. Yusupov, Effect of Copper Additions on the Mechanical Properties of Iron 1, Metally. 2011 (2011) 454–458.

[52] W.D. Wong–ángel, L. Téllez–jurado, J.F. Chávez–alcalá, E. Chavira–martínez, V.F. Verduzco–cedeño, Effect of copper on the mechanical properties of alloys formed by powder metallurgy, Masterials Des. 58 (2014) 12–18.

[53] Y. Zhao, J. Zhu, L. Chang, J. Song, X. Chen, X. Hui, Influence of Cu content on the mechanical properties and corrosion resistance of Mg–Zn–Ca bulk metallic glasses, Int. J. Miner. Metall. Mater. 21 (2014) 487–493.

[54] Z. Yao, P. Houizot, F. Célarié, D. Möncke, L. Wondraczek, T. Rouxel, et al., The influence of Cu content on the mechanical properties of copper–borate glasses, Key Eng. Mater. 702 (2016) 71–76.

[55] D.M. Taylor, R.W. Leggett, A generic biokinetic model for predicting the behaviour of the lanthanide elements in the human body, Radiat. Prot. Dosimetry. 105 (2003) 193–198.

[56] F. Bronner, Metals in Bone. Aluminum, Boron, Cadmium, Chromium, Lanthanum, Lead, Silicon, and Strontium, in: Princ. Bone Biol., 3rd editio, Academic Press, Inc., Farmington, 2008: pp. 515–531.

[57] T. Das, A. Sharma, G. Talukder, Effects of lanthanum in cellular systems – A review, Biol. Trace Elem. Res. 18 (1988) 201–228.

[58] D.M. Kramsch, A.J. Aspen, C.S. Apstein, Suppression of experimental atherosclerosis by the Ca++–antagonist lanthanum. Possible role of calcium in

atherogenesis, J. Clin. Invest. 65 (1980) 967–981.

[59] D.M. Weekes, Lanthanum Complexes as Therapeutic Agents for the Treatment, Britsh Columbia, 2016.

[60] S. V Smiljanic, S.R. Grujic, M.B. Tošic, Vladimir Živanovic, S.D. Matijaševic, J.D. Nikolic, et al., Effect of La2O3 on the structure and the properties of strontium borate glasses, Chem. Ind. Eng. Qual. 22 (2016) 111–115.

[61] S.K. Sarkar, B.T. Lee, Synthesis of Bioactive Glass by Microwave Energy Irradiation and Its In–Vitro Biocompatibility, Bioceram. Dev. Appl. 1 (2011) 1–3.

[62] B.A.E. Ben–Arfa, H.R. Fernandes, I.M. Miranda Salvado, J.M.F. Ferreira, R.C. Pullar, Synthesis and bioactivity assessment of high silica content quaternary glasses with Ca: P ratios of 1.5 and 1.67, made by a rapid sol–gel process, J. Biomed. Mater. Res. – Part A. 106 (2018) 510–520.

[63] M. Guglielmi, P. Barboux, The sol–gel method for the synthesis of glasses, ceramics and hybrid materials, Radiat. Eff. Defects Solids. 134 (1995) 31–37.

[64] R. Li, A.E. Clark, L.L. Hench, An Investigation of Bioactive Glass Powders by Sol–Gel Processing, J. Appl. Biomater. 2 (1991) 231–239.

[65] G. Kaur, G. Pickrell, N. Sriranganathan, V. Kumar, D. Homa, Review and the state of the art: Sol–gel and melt quenched bioactive glasses for tissue engineering, J. Biomed. Mater. Res. – Part B Appl. Biomater. 104 (2016) 1248–1275.

[66] R.A. Assink, B.D. Kay, Sol–gel kinetics III. Test of the statistical reaction model, J. Non. Cryst. Solids. 107 (1988) 35–40.

[67] T. Coradin, J. Livage, Sol–Gel Synthesis of Solids, Encycl. Inorg. Chem. (2006) 1–11.

[68] D.M. Roy, R. Roy, Synthesis and stability of minerals in the system MgO–Al2O3–SiO2–H2O., Am. Mineral. 40 (1955) 1–32.

[69] H. Dislich, P. Hinz, History and principles of the sol–gel process, and some new multicomponent oxide coatings. J. Non. Cryst. Solids. 48 (1982) 11–16.

[70] D. Bellucci, A. Sola, R. Salvatori, A. Anesi, L. Chiarini, V. Cannillo, Sol–gel derived bioactive glasses with low tendency to crystallize: Synthesis, post–sintering

bioactivity and possible application for the production of porous scaffolds, Mater. Sci. Eng. C. 43 (2014) 573–586.

[71] C.S. Chai, K.A. Gross, B. Ben–Nissan, Critical ageing of hydroxyapatite sol–gel solutions, Biomaterials. 19 (1998) 2291–2296.

[72] L.C. Klein, Sol–gel technology for thin films, fibres, preforms, electronics, and specialty shapes, Noyes Publications, New Jersey, 1988.

[73] M. a. Fardad, Catalysts and the structure of SiO2 sol–gel films, J. Mater. Sci. 35 (2000) 1835–1841.

[74] C.J. Brinker, Hydrolysis and condensation of silicates: Effects on structure, J. Non. Cryst. Solids. 100 (1988) 31–50.

[75] J. Cihlar, Hydrolysis and polycondebsation of ethyl silicate. 1. Effect of pH and catalyst on the hydrolysis and polycondensation of tetraethoxysilane (TEOS), Colloid Surf. A. 70 (1993) 239–251.

[76] J.D. Mackenzie, Applications of the sol–gel process, J. Non. Cryst. Solids. 100 (1988) 162–168.

[77] S. Ni, R. Du, S. Ni, The influence of Na and Ti on the in vitro degradation and bioactivity in 58S sol–gel bioactive glass, Adv. Mater. Sci. Eng. 2012 (2012).

[78] M. Mami, A. Lucas–Girot, H. Oudadesse, R. Dorbez–Sridi, F. Mezahi, E. Dietrich, Investigation of the surface reactivity of a sol–gel derived glass in the ternary system SiO2–CaO–P2O5, Appl. Surf. Sci. 254 (2008) 7386–7393.

[79] R.L. Siqueira, O. Peitl, E.D. Zanotto, Gel–derived SiO2–CaO–Na2O–P2O5bioactive powders: Synthesis and in vitro bioactivity, Mater. Sci. Eng. C. 31 (2011) 983–991.

[80] A. Balamurugan, G. Balossier, S. Kannan, J. Michel, A.H.S. Rebelo, J.M.F. Ferreira, Development and in vitro characterization of sol–gel derived CaO–P2O5–SiO2–ZnO bioglass, Acta Biomater. 3 (2007) 255–262.

[81] K. Zheng, A. Solodovnyk, W. Li, O.M. Goudouri, C. Stähli, S.N. Nazhat, et al., Aging time and temperature effects on the structure and bioactivity of gel–derived 45S5 glass–ceramics, J. Am. Ceram. Soc. 98 (2015) 30–38.

[82] R.K. Nariyal, P. Kothari, B. Bisht, FTIR Measurements of SiO2 Glass Prepared by Sol–Gel Technique, Chem. Sci. Trans. 3 (2014) 1064–1066.

[83] V. Levašič, I. Milošev, V. Zadnik, Risk of cancer after primary total hip replacement: The influence of bearings, cementation and the material of the stem, Acta Orthop. 89 (2018) 234–239.

[84] V.Y. Ng, Risk of Disease Transmission With Bone Allograft, Orthopedics. 35 (2012) 679–681.

[85] R. Agarwal, A.J. García, Biomaterial strategies for engineering implants for enhanced osseointegration and bone repair, Adv. Drug Deliv. Rev. 1 (2015) 53–62.

[86] K. Prasad, O. Bazaka, M. Chua, M. Rochford, L. Fedrick, J. Spoor, et al., Metallic biomaterials: Current challenges and opportunities, Materials (Basel). 10 (2017).

[87] B.R.A. Martin, S. Yue, J.V. Hanna, P.D. Lee, R.J.Newport, M.E. Smith, et al., Characterizing the hierarchical structures of bioactive sol – gel silicate glass and hybrid scaffolds for bone regeneration, (2012) 1422–1443.

[88] T.S. Wik, O.A. Foss, S. Havik, L. Persen, A. Aamodt, E. Witsø, Periprosthetic fracture caused by stress shielding after implantation of a femoral condyle endoprosthesis in a transfemoral amputee–a case report, Acta Orthop. 81 (2010) 765–767.

[89] F.J. O'Brien, Biomaterials & scaffolds for tissue engineering, Mater. Today. 14 (2011) 88–95.

[90] B.P. Chan, K.W. Leong, Scaffolding in tissue engineering : general approaches and tissue–specific considerations, Eur. Spine J. 17 (2008) S467–S479.

[91] F.J. O'Brien, Biomaterials & scaffolds for tissue engineering, Mater. Today. 14 (2011) 88–95.

[92] M. Houmard, Q. Fu, E. Saiz, A.P. Tomsia, Sol–gel method to fabricate CaP scaffolds by robocasting for tissue engineering, J. Mater. Sci. Mater. Med. 23 (2012) 921–930.

[93] J.M. Karp, P.D. Dalton, M.S. Shoichet, F. Cahn, Scaffolds for tissue engineering, clinical use of porous scaffolds for tissue engineering of skin, MRS Bull. (2003)

301–306.

[94] Q. Fu, M.N. Rahaman, B. Sonny Bal, R.F. Brown, D.E. Day, Mechanical and in vitro performance of 13–93 bioactive glass scaffolds prepared by a polymer foam replication technique, Acta Biomater. 4 (2008) 1854–1864.

[95] S. Deville, E. Saiz, A.P. Tomsia, Freeze casting of hydroxyapatite scaffolds for bone tissue engineering, Biomaterials. 27 (2006) 5480–5489.

[96] K.F. Leong, C.M. Cheah, C.K. Chua, Solid freeform fabrication of three–dimensional scaffolds for engineering replacement tissues and organs, Biomaterials. 24 (2003) 2363–2378.

[97] R. Felzmann, S. Gruber, G. Mitteramskogler, P. Tesavibul, A.R. Boccaccini, R. Liska, et al., Lithography–based additive manufacturing of cellular ceramic structures, Adv. Eng. Mater. 14 (2012) 1052–1058.

[98] A. Entezari, Z. Zhang, J. Chen, Q. Li, Optimization of bone tissue scaffolds fabricated by robocasting technique, in: 11th World Congr. Struct. Multidiscip. Optim., Sydney, 2015: pp. 1–6.

[99] J. Cesarano III, A Review of Robocasting Technology, in: MRS Proc., 1998: pp. 133–139.

[100] J.A. Lewis, J.E. Smay, J. Stuecker, J. Cesarano, Direct ink writing of three–dimensional ceramic structures, J. Am. Ceram. Soc. 89 (2006) 3599–3609.

[101] S. Eqtesadi, A. Motealleh, P. Miranda, A. Pajares, A. Lemos, J.M.F. Ferreira, Robocasting of 45S5 bioactive glass scaffolds for bone tissue engineering, J. Eur. Ceram. Soc. 34 (2014) 107–118.

[102] G. Tarì, J.M.F. Ferreira, A.T. Fonseca, O. Lyckfeldt, Influence of particle size distribution on colloidal processing of alumina, J. Eur. Ceram. Soc. 18 (1998) 249–253.

[103] S.M. Olhero, J.M.F. Ferreira, Influence of particle size distribution on rheology and particle packing of silica–based suspensions, Powder Technol. 139 (2004) 69–75.

[104] G. Tari, J.M.F. Ferreira, A.T. Fonseca, Infuence of particle size and particle size distribution on drying–shrinkage behaviour of alumina slip cast bodies, Ceram. Int.

25 (1999) 577–580.

[105] J.V. Milewski, Efficient Use of Whiskers in the Reinforcement of Ceramics, Adv. Ceram. Mater. 1 (1986) 36–41.

[106] G. Tarì, J.M.F. Ferreira, O. Lyckfeldt, Influence of the Stabilising Mechanism and Solid Loading on Slip Casting of Alumina, J. Eur. Ceram. Soc. 18 (1998) 479–486.

[107] A. Kaushal, S.M. Olhero, J.M.F. Ferreira, Lead–free 0.5Ba(Zr0.2Ti0.8)O3–0.5(Ba0.7Ca0.3)TiO3 powder surface treated against hydrolysis – a key for a successful aqueous processing, J. Mater. Chem. C. 1 (2013) 4846–4853.

[108] J.M.F. Ferreira, O. SM, Drying Induced Forming from Highly Concentrated Alumina Slips, Am. Ceram. Soc. 112 (2001) 483–488.

[109] G. Tarì, J.M.F. Ferreira, Influence of Solid Loading on Drying–Shrinkage Behaviour of Slip Cast Bodies, J. Eur. Ceram. Soc. 18 (1998) 487–493.

[110] J.M.F. Ferreira, H.M.M. Diz, Effect of Solids Loading on Slip–Casting Performance of Silicon Carbide Slurries, J. Am. Ceram. Soc. 82 (1993) 1993–2000.

[111] B. V. Velamakanni, F.F. Lange, Effect of Interparticle Potentials and Sedimentation on Particle Packing Density of Bimodal Particle Distributions During Pressure Filtration, J. Am. Ceram. Soc. 74 (1991) 166–172.

[112] Pugh, R. J. & Bergstrom, L., Surface and colloid chemistry in advanced ceramic processing, Surfactant science series vol. 51, Marcel Dekker, New York, 1994.

[113] C.T. Nguyen, F. Desgranges, G. Roy, N. Galanis, T. Maré, S. Boucher, et al., Temperature and particle–size dependent viscosity data for water–based nanofluids – Hysteresis phenomenon, Int. J. Heat Fluid Flow. 28 (2007) 1492–1506.

[114] C. Furnas, The relation between specific volume, voids and size composition in systems of broken solids of mixed sizes, Dep. of commerce, Bureau of mines, RI 2894, 1928.

[115] M.I.L.L. Oliveira, K. Chen, M.F. Ferreira, J.M.F. Ferreira, Influence of thedeagglomeration procedure on aqueous dispersion , slip casting and sintering of Si3N4 –based ceramics, J. Eur. Ceram. Soc. 22 (2002) 1601–1607.

[116] A. Krell, P. Blank, M. Honggwei, T. Hutzler, Transparent Sintered Corundum with

High Hardness and Strength, J. Am. Ceram. Soc. 86 (2003) 12–18.

[117] A. Krell, J. Klimke, Effects of the homogeneity of particle coordination on solid–state sintering of transparent alumina, J. Am. Ceram. Soc. 89 (2006) 1985–1992.

[118] A. Krell, J. Klimke, T. Hutzler, Advanced spinel and sub–μm Al2O3for transparent armour applications, J. Eur. Ceram. Soc. 29 (2009) 275–281.

[119] P. Miranda, A. Pajares, E. Saiz, A.P. Tomsia, F. Guiberteau, Mechanical properties of calcium phosphate scaffolds fabricated by robocasting, J. Biomed. Res. Part A. 85 (2008) 218–227.

[120] R.C. Richard, M.S. Sader, J. Dai, R.M.S.M. Thiré, G.D.A. Soares, Beta–type calcium phosphates with and without magnesium: From hydrolysis of brushite powder to robocasting of periodic scaffolds, J. Biomed. Mater. Res. – Part A. 102 (2014) 3685–3692.

[121] Y. Maazouz, E.B. Montufar, J. Guillem–Marti, I. Fleps, C. Öhman, C. Persson, et al., Robocasting of biomimetic hydroxyapatite scaffolds using self–setting inks, J. Mater. Chem. B. 2 (2014) 5378–5386.

[122] E. Feilden, C. Ferraro, Q. Zhang, E. García–Tuñón, E. D'Elia, F. Giuliani, et al., 3D Printing Bioinspired Ceramic Composites, Sci. Rep. 7 (2017) 1–9.

[123] A.P.T. J. Russias, E. Saiz, S. Deville, K. Gryn, G. Liu, R.K. Nalla, Fabrication and in vitro characterization of three– dimensional organic/inorganic scaffolds by robocasting, J. Biomed. Mater. Res. Part A. 38A (2006) 434–445.

[124] S. Eqtesadi, A. Motealleh, P. Miranda, A. Lemos, A. Rebelo, J.M.F.F. Ferreira, A simple recipe for direct writing complex 45S5 Bioglass®3D scaffolds, Mater. Lett. 93 (2013) 68–71.

[125] X. Liu, M.N. Rahaman, G.E. Hilmas, B.S. Bal, Mechanical properties of bioactive glass (13–93) scaffolds fabricated by robotic deposition for structural bone repair, Acta Biomater. 9 (2013) 7025–7034.

[126] A. Nommeots–Nomm, P.D. Lee, J.R. Jones, Direct ink writing of highly bioactive glasses, J. Eur. Ceram. Soc. 38 (2018) 837–844.

[127] Z.H. Loh, A.K. Samanta, P.W. Sia Heng, Overview of milling techniques for improving the solubility of poorly water–soluble drugs, Asian J. Pharm. Sci. 10 (2014) 255–274.

[128] M.D. Bentzon, L.O. Andersen, J. Goul, P. Bodin, P. Vase, Influence of the Powder Calcination Temperature on the Microstructure in Bi (Pb) –2223 Tapes, IEEE Trans. Appl. Supercond. 7 (1997) 1411–1414.

Chapter 2

The present chapter was published on:
International Journal of Applied Glass Science;
Volume 8, Issue 3,
21 December 2016,
Pages 337–343.
Doi:10.1111/ijag.12255

A hundred times faster: novel, rapid sol–gel synthesis of bio–glass nanopowders (Si–Na–Ca–P system, Ca:P = 1.67) without ageing

Basam A. E. Ben–Arfa, Isabel M. Miranda Salvado*, José M. F. Ferreira and Robert C. Pullar*

Department of Materials and Ceramic Engineering / CICECO – Aveiro Institute of Materials, University of Aveiro, 3810–193 Aveiro, Portugal

*To whom correspondence should be addressed: isabelmsalvado@ua.pt, rpullar@ua.pt

Keywords: oxide; Glass Forming Systems; phosphate; Glass Forming Systems; crystallisation; bioglass; bioactivity.

Abstract

Synthesis of sol–gel glass with incorporation of Na_2O is extremely difficult, as such glasses have a great tendency to crystallise. Slow drying and ageing over several days or weeks is usually required in sol–gel preparation procedures. This work reports a fast, novel route for the synthesis of bioglass powders in a considerably shortened period of 1 h. A comparative study of sol–gel derived glasses made by this novel route using rotary evaporator drying, and a conventional route using oven drying and ageing, revealed that the two methods produce stabilised (devitrified) bio–glasses with virtually identical behaviour and properties. Indeed, the rapidly dried powder exhibited slightly enhanced properties that should result in improved bioactivity. Fourier–transform infrared spectroscopy (FTIR) was used to understand the structures of the synthesised powders, and MAS–NMR was used to look at the degree of polymerisation. This innovative, rapid route was successfully demonstrated to produce glass and devitrified glass nanopowders more than one hundred times quicker than the quickest reported standard drying methods.

1. Introduction

Glasses are considered as very important materials in many industrial sectors, as well as in daily human life. Melt quenching is a well–known and commonly used method for glass synthesis. The glass end product is produced as a result of inhibiting crystallization by rapid quenching from the melt. Sol–gel methods are another important route for glass synthesis, where the glass can be produced at low temperatures with high homogeneity. The end products produced by sol–gel, with all forms such as powder and bulk, have high porosity in comparison with the end products synthesized by melt quenching methods. A problem with sol–gel methods is that a small extent of crystallization of one or more of the components can occur during the stabilization and aging/curing process of the gel, and such crystalline precursors are particularly important to avoid in bioglasses, which usually contain Ca, P, Si, and often Na **[1]**. To overcome such problems, the sol–gel method for bio–glasses often involves very long aging and drying periods, which can last for weeks or even months, which is an obvious disadvantage, and a rate limiting step in research and production. For example, Nariyal et al. **[2]** aged the sol for 1 month at room temperature to synthesize SiO_2–based glass powder. Zheng et al. **[3]** aged the samples at room temperature for 15 days, after which the formed gels were dried at 120°C for 24 h to create a bioglass. Balamurugan et al. synthesized bioglass in a four–component Si–Ca–P–Na system, where the sol was kept at room temperature for 10 days for aging, then dried at 70°C for 3 days, and120°C for two more days **[4–6]**. In other work, Siqueira et al. aged the sol for 7 days at 70°C and then dried it at 130°C for 2 days for SiO_2–CaO–Na_2O–P_2O_5 bioglasses **[7,8]**, and a similar regime (aging at 70°C/3 days, then drying at 150°C/52 h) was employed by Mami et al. **[9]** Bellucci et al. **[10]** kept their sol at room temperature for 4 h after adding the last reagent, and then aged it at 35°C for 3 days to obtain a gel, which was subsequently dried at 50°C for 6 days, and then 110°C for three more days to make a bioglass. Shirong et al. aged their sol at 60°C for 3 days and then dried it at 70°C for more 3 days **[11]**, and in a particularly quick process Chen et al. **[12]** synthesized bioactive glass–ceramics containing Na_2O by aging the sol at only 60°C for 72 h, followed by drying at 200°C for 40 h. It can be seen that even the most rapid of these processes took around 5 entire days (>100 h).

This work intends to surpass the problems of long aging and drying times using a rotary evaporator to dry the sol to an amorphous bioglass precursor gel in only 1 h. This novel, fast method suppresses crystallization in the gel forming phase. To the best of the

authors' knowledge, no such work has been reported before concerning the synthesis of glass nanopowder by sol–gel using a rotary evaporator.

2. Experimental

2.1. Glass synthesis

The glass was synthesized using the sol–gel method. Tetra–ethyl orthosilicate (TEOS, $C_8H_{20}O_4Si$, 98%) supplied from Sigma–Aldrich was used as a precursor for silica, orthophosphoric acid (H_3PO_4, 85%) supplied from VWR was used as a precursor for phosphorus, and calcium nitrate tetrahydrate ($Ca(NO_3)_2.4H_2O$, 99%, Sigma–Aldrich) and sodium nitrate ($NaNO_3$, 99%, Sigma–Aldrich) were used as precursors for calcium, and sodium, respectively. Concentrated nitric acid (HNO_3, ≥65%, Sigma–Aldrich) and deionized water were also used. The four–component Si–Na–Ca–P glass was prepared with the mole percentages of 76 mol% Si, 8 mol% Na, 10 mol% Ca, and 6 mol% P (to prepare 10 g of end product), hereafter referred to as 76S10.

Sodium nitrate was added to a solution of 0.1 M nitric acid in 22 mL of water in a glass beaker. After the solution became clear, the calcium, phosphorus and silica precursors were added one after the other, in that order, without adding any more water. Each subsequent precursor was added only after a clear solution/sol was obtained, ensuring complete dissolution of the previously added precursors. After adding the last precursor, the sol was stirred for 1 h as shown in the flowchart diagram in **Fig. 2.1**. The silica/water molar ratio was 1:10 with the 22 mL used. The clear sol produced was divided into two parts. One part was poured into a glass petri dish, having a 120 mm outside diameter and a height of 20 mm, to be dried in the oven (conventional drying, CD), and the other part was dried by the rotary evaporator (fast drying, FD). The rotary evaporator used was a Buchi 210 Rotavapor with V–850 vacuum controller and V–700 diaphragm vacuum pump (Buchi Labortechnik AG, Flawil, Switzerland), and the sols were dried in a 500 mL pear–shaped flask while rotating in a water bath at 55°C and under a pressure of 50 mbar for 1 h. One hour was chosen as this was approximately the time required to complete the drying process under these conditions and form a gel, but even shorter periods could be sufficient. In the oven, the sample was aged at room temperature for 4 h, followed by drying in the oven at 35°C/3 days, then 50°C/6 days, and finally 100°C/3 days (12 days in total) **[10]**. This process

is summarized in **Fig. 2.1** and **Table 2.1**. After drying, all dried gels were stabilized at 550°C for 1 h. The heating rate was 2°C/min up to 300°C, and then 10°C/min up to 550°C.

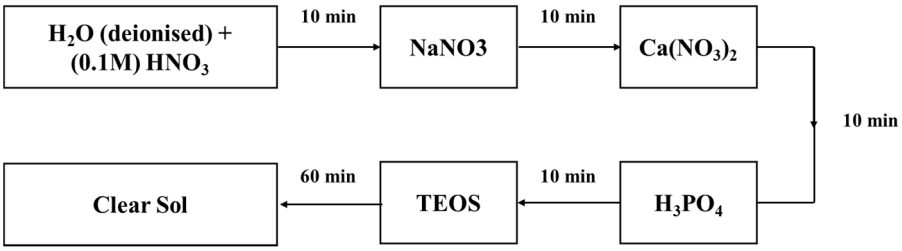

Fig. 2.1: Flowchart scheme of the sol–gel synthesis

Table 2.1: Sample designation

Sample	Drying method	Salt precursor
CD	Oven drying	Nitrate precursors
FD	Rotary evaporator	Nitrate precursors

2.2. Characterization of glass

For all characterization techniques, samples were used as a powder sieved through a 45 μm mesh, after having first been pulverized using an agate mortar and pestle.

The microstructure of the as–dried samples, as well as stabilized glass–ceramics, were observed by scanning electron microscope (SEM, S–4100, Hitachi, Japan), with samples coated in carbon.

Thermal behaviour of the samples was determined by differential thermal analysis (DTA) and thermogravimetry (TG) carried out in air (DTA–TG; Labsys Setaram, Caluire, France) from room temperature to 1200°C at a heating rate of 2 K/min), with calcined α–alumina as the reference material.

Crystalline phase content in the samples was determined by X–ray diffraction (XRD, Rigaku Geigerflex D/Mac, C Series, Tokyo, Japan) using Cu Kα radiation with 2h varying

from 6–70° in steps of 0.02° s^{-1}. The diffraction patterns were compared with joint committee on powder diffraction standards (JCPDS).

^{29}Si MAS–NMR spectra was recorded for glass powders prepared from the stabilised glass on an ASX 400 spectrometer (Bruker, Karlsruhe, Germany) operating at 79.52 MHz (9.4 T) using a 7 mm probe at a spinning rate of 5 kHz. The pulse length was 2 µs with 60 s delay time, and kaolinite was used as a chemical shift reference.

Infrared transmittance spectra of glass powders before and after stabilization at 700°C, were obtained using a Fourier Transform Infrared Spectrometer (FTIR; Tensor 27, Bruker, Germany) in the range of 350 – 4000 cm^{-1}, with 128 Scans and 4 cm^{-1} resolution. Samples for FTIR analysis were prepared by mixing a 1/150 (by weight) portion of the sample with KBr, and pressing this to obtain pellets.

The specific surface areas (SSA) of the powders were computed using the Brunauer–Emmett–Teller (BET) method using a Gemini M–2380 (Micrometrics, Norcross, GA) with N_2 as the adsorbate. Particle size was measured by laser diffraction particle size analyzer (Coulter LS particle size analyzer; Beckman Coulter, CA).

3. Results and discussion

3.1. Thermal properties

DTA–TG measurement of the as–synthesized fast–dried (FD) gel is shown in **Fig. 2.2**. A large endothermic peak at ~120 °C, accompanied by ~50% of weight loss, is due to the evaporation of water.

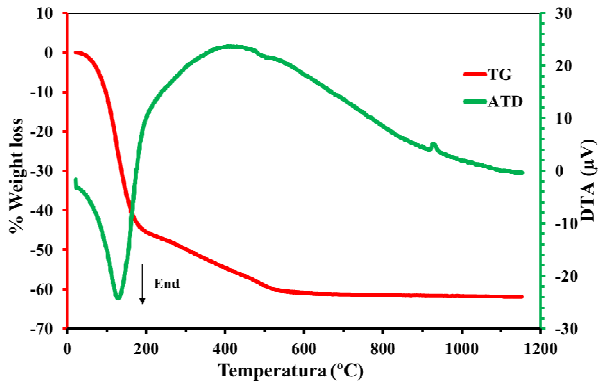

Fig. 2.2: DTA and TGA curves for the as–dried gel produced by the novel fast drying process (FD).

A second TG weight loss of ~14% occurred between temperatures of 175–500 °C, and this is attributed to the pyrolysis of residual organic groups. The DTA exhibited a significant change in the slope at ~500 °C which is attributed to the glass transition temperature (Tg), and small exothermic peak at ~930°C represents the crystallization temperature (Tc). This small Tc peak could be attributed to the devitrification process for the glass during calcination **[13]**.

3.2. Structure of glasses

Fig. 2.3 shows the XRD difractograms of the as–dried powder (a), and the stabilized powder heat–treated at 550°C/1 h in air inside an electric furnace (b), for samples CD and FD.

Fig. 2.3 demonstrates that both drying methods produce materials with similar profiles. Both are amorphous after drying, and have a mostly amorphous structure overlaid with a small amount of crystalline sodium calcium phosphate (Buchwaldite, $NaCa(PO_4)$, PDF card # 01–076–1456) after heat treatment at 550°C. If anything, the pattern of the conventionally dried materials appears to be slightly more crystalline after stabilizing at 550°C.

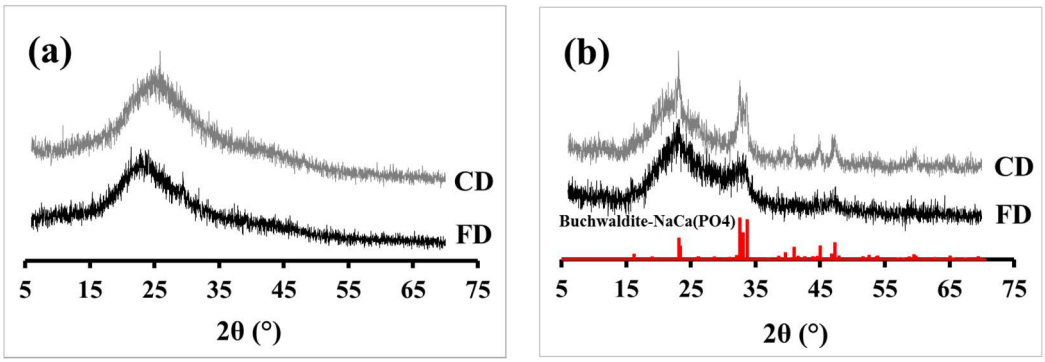

Fig. 2.3: XRD patterns for (a) as–dried gels, and (b) stabilized powders after heating to 550°C/1 h. The standard pattern used is JCPDF No. 01–076–1456.

In a good agreement between NMR, FTIR, and XRD, the CD devitrified glass exhibited more crystallinity than FD, which was attributed to the longer aging and drying time involved in the CD process than that of FD. Fast drying while in the rotary evaporator diminished the opportunity for crystallization (both processes being thermodynamically equivalent as they occur at similar temperatures), and had the effect of effectively "freezing" the microstructure in a less reorganized state, resulting in less crystallization **[14,15]**.

The room–temperature FTIR spectra of all the investigated glasses are presented in **Fig. 2.4**. In the FTIR spectra of the as–dried powders **Fig. 2.4 (a)**, those produced by the novel rapid route (FD) are very similar to those obtained for the conventional method (CD).

The Si–O–Si bending mode causes the absorption band observed at ~460 cm **[1,16,17]** and a doublet with small intensity at around 530–600 cm^{-1} can also been observed, which is attributed to crystalline calcium phosphate **[18]**. These are both stronger in CD than FD.

Both spectra exhibit bands at ~790 cm^{-1} which are assigned to (Si–O) symmetric stretching, thus showing the characteristic band peaks of trialkoxylsilyl functional groups **[19]**, and this appears stronger in CD. The P–O symmetric stretching peak is centred at 960 cm^{-1} **[20]**, whereas the silicate absorption bands observed at about 1070–1090 cm^{-1}, together with a shoulder at ~1200 cm^{-1}, are ascribed to asymmetric stretching (Si–O) bonds **[12,16,17,21,22]**. These bands are all stronger in the CD sample. There is also a small band at 1012–1014 cm^{-1}, also assigned to Si–O asymmetric stretching vibrations **[23]** which is also stronger in CD than FD, and all together this evidence suggests that there is a significantly greater presence of these Si–O bonds in the conventionally dried sample, CD. The 1384 cm^{-1} peak is due to N–O stretching of residual nitrate anions resulting from the HNO_3 used as a catalyst in the synthesis, and it is a very sharp peak in the as–synthesized products **[6,16,17,24]** which is stronger in FD, indicating the slower CD process may result in greater loss of these nitrate groups. The band at ~1635 cm^{-1}, assigned to the deformation vibration of the H–O–H bond, and the υ(O–H) vibration around ~3450 cm^{-1}, both indicate the existence of water (H_2O) which is probably mostly absorbed in the hygroscopic KBr disk used for the measurements **[25]**, although some may be present in the samples as well.

The FTIR spectra of the stabilized glasses **Fig. 2.4 (b)**, show the evolution of the structure after thermal stabilization of the dried powders: The much stronger band centred at 1090

cm^{-1} can be assigned to a greater occurrence of asymmetric stretching Si–O groups, as well as the increased bands at 460, 795, 1012, 1090, and 1207 cm^{-1} **[5,26]**. Additional bands at wavenumbers 570–580 cm^{-1} are due to the presence of a sodium calcium silicate crystalline phase **[27]**, which is confirmed by XRD **Fig. 2.3 (b)**, The band at 820 cm^{-1} is a characteristic of NO_3 residues from the synthesis, disappears after the calcination/stabilization process **[28]**, showing these have been removed or greatly reduced with heating. In general, more pronounced bands are observed for both synthesized samples FD and CD after stabilization, except for the bands due to nitrate residues, with the disappearance of the band at 820 cm^{-1} and a great reduction in the one at 1384 cm^{-1} to very small peak.

With the regime of aging and drying over an extended time for CD, it can be observed that this sample contains less nitrate residues than FD, which is one way in which the conventional drying process may be superior to our new method. On the other hand, the FD sample has weaker silica bonds, and a lower degree of polymerization, which can also be confirmed by the MAS–NMR results in **Table 2.2**. The greater degree of sharpness of the peaks for CD than FD, in the peaks at 790 cm^{-1} and 1070–1090 cm^{-1} (corresponding to Si–O bonds) and also around 570–580 cm^{-1} (P–O groups), demonstrates the higher degree of crystallinity of the CD sample, which can also be confirmed from the XRD patterns **Fig. 2.3 (b)**.

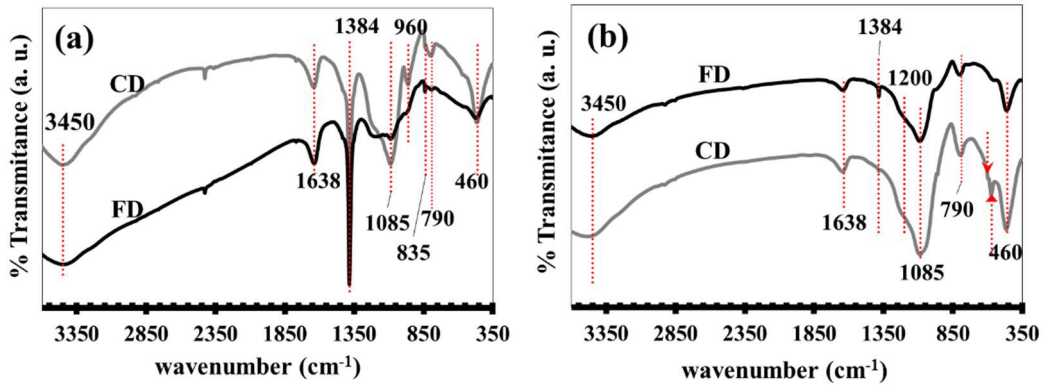

Fig. 2.4: FTIR spectra of (a) as–dried gel and (b) stabilized glass after heating to 550°C/1 h

3.3. MAS– NMR analysis of stabilized powders heat–treated at 550°C

The ^{29}Si NMR analysis allows us to examine the environment of the Si atom, and once more it can be seen that the stabilized glass samples made by the two methods are virtually identical. The main peak at –111 ppm and the shoulder at –100 ppm, as observed in **Fig. 2.5**, can be attributed to Si atoms connected to four bridging oxygens (BO) and arranged in a Q^4 environment, and a Q^3 environment with one nonbridging oxygen (NBO), respectively **[29–31]**. The lack of Q^2, Q^1, or Q^0 environments can be attributed to the relatively low levels of modifiers present in this composition, which leads to less disruption of the silica network **[32]**.

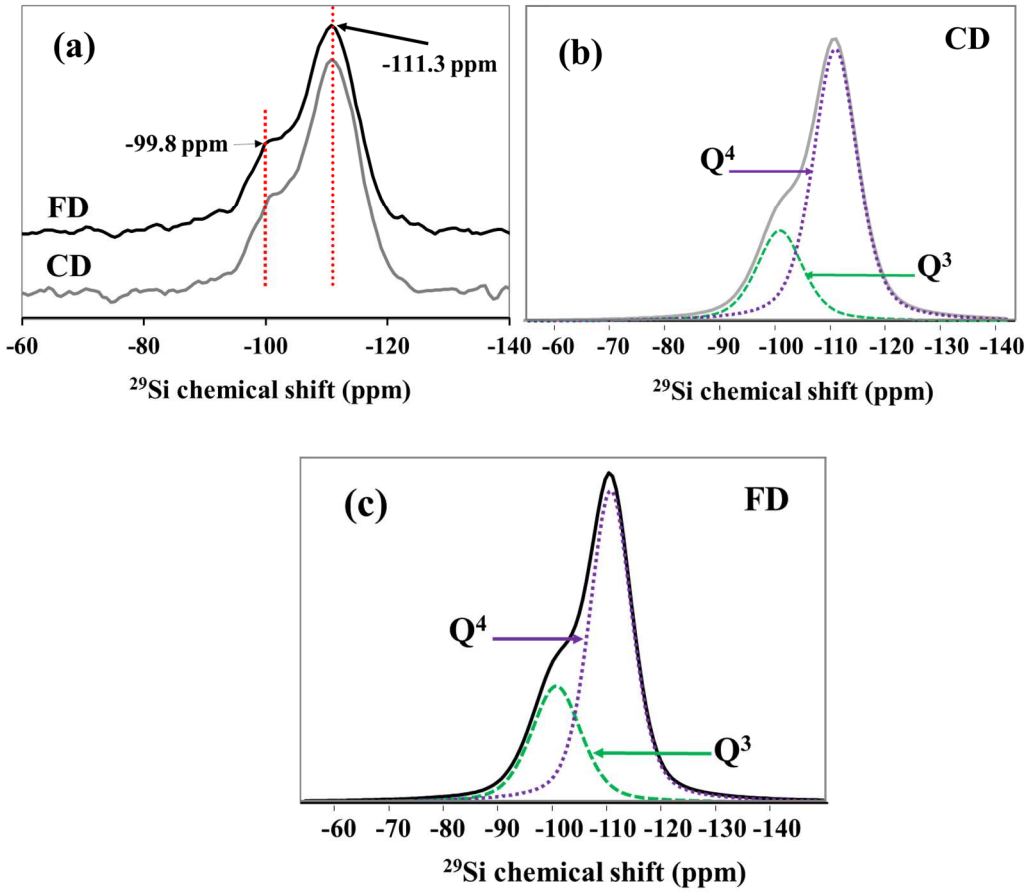

Fig. 2.5: (a) ^{29}Si MAS–NMR spectra of as–synthesized powders of FD and CD. Deconvoluted ^{29}Si MAS–NMR spectra are shown for (b) CD and (c) FD.

Table 2.2 shows that for CD and FD the positions of the peaks of Q^4 and Q^3 are virtually identical. However, the integral % values for FD glasses exhibit a higher percentage of Q^3 (30.5% vs 25.6% for CD), and a lower percentage of Q^4, than CD, meaning a higher degree of disruption and less network connectivity, and hence probably greater bioactivity **[33]**, in the rapidly dried sample, FD, after stabilization. Nevertheless, both glasses exhibit almost the same degree of polymerization, which demonstrates that the same structure was obtained by the two different drying methods.

Table 2.2: Q^n (Si) distribution for devitrified glasses CD, and FD obtained by NMR deconvolution.

Sample	Q^n			
	Q^3		Q^4	
	Peak position (ppm)	% Integral	Peak position (ppm)	% Integral
CD	–100.95	25.62	–110.96	74.38
FD	–100.75	30.52	–110.76	69.48

3.4. Morphology of stabilized powders

From the observations of **Table 2.3**, it can be seen that the particle size of FD is reduced to a slightly smaller size than that of CD, whereas FD also exhibits a slightly greater SSA than CD, which is another good attribute for higher service reactivity and bioactivity **[34]**. However, once again, both samples are extremely similar in size and SSA.

Very similar microstructures were obtained for the stabilized glasses produced by both the rotary evaporator route FD, **Fig. 2.6(a,d,f)** and by the conventional drying route CD, **Fig. 2.6(a,c,e)**. This is demonstrated by **Fig. 2.6(a,b)** in which there is almost no difference between CD and FD. Agglomerations of nanoparticles with sizes between 120–300 nm can be seen in **Fig. 2.6(c–f)**, where irregular clusters of similar size and shape can be clearly observed in the products of both routes.

Table 2.3: Particle size and BET SSA for FD, & CD glasses

Sample code	Network connectivity (NC)	Particle size		BET SSA(m^2g^{-1})
		d_{50}(mμ)	D(mμ)	
CD	4	21.53±0.05	24.56±0.34	115.0784
FD	4	20.68±0.11	24.19±0.19	121.3693

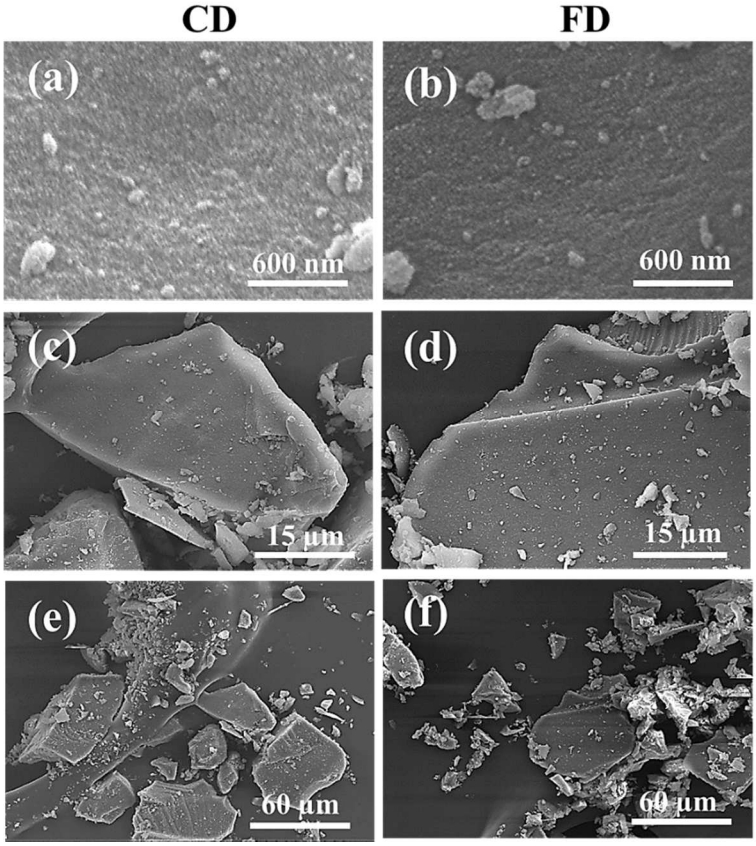

Fig. 2.6: SEM images of the stabilized glasses (A, C, E) CD and (B, D, F) FD, after heating to 550°C/1 h.

4. Conclusions

Fine nanopowders of sodium–containing stabilized (devitrified) glasses were synthesized successfully, using a novel, rapid sol–gel technique. This involved drying the gels rapidly on a rotary evaporator in 1 h, as opposed to conventionally slow drying for >100 h, a process one hundred times faster. Comparison the synthesis of a Na_2O–containing glass using the conventional and new rapid routes, results showed very similar final products could be obtained by the use of either method. In fact, the new rapid route exhibited even slightly smaller particle sizes, larger surface areas, and a greater degree of network disruption (equal to less polymerization), which should result in higher bioactivity. The new route presented in this work can be considered as a new way to rapidly synthesize glasses and glass–ceramics by sol–gel, and is the first study using a rotary evaporator to synthesize and dry a sol–gel–derived bioglass. This novel method greatly decreases the time required to form stable bioglass nanopowders by factor of >100, requiring just 1 h instead of aging for at least 5 days (over 100 h).

Acknowledgments

R.C. Pullar wishes to thank the FCT Grant SFRH/BPD/ 97115/2013 for supporting this work. This work was developed in the scope of the project CICECO Aveiro Institute of Materials (Ref. FCT UID /CTM /50011/2013), financed by national funds through the FCT/MEC and when applicable co–financed by FEDER under the PT2020 Partnership Agreement.

References

[1] L.L. Hench, An introduction to bioceramics, Second edi, Imperical College Press, London, 2015.

[2] R.K. Nariyal, P. Kothari, B. Bisht, FTIR Measurements of SiO2 Glass Prepared by Sol–Gel Technique, Chem. Sci. Trans. 3 (2014) 1064–1066.

[3] K. Zheng, A. Solodovnyk, W. Li, O.M. Goudouri, C. Stähli, S.N. Nazhat, et al., Aging time and temperature effects on the structure and bioactivity of gel–derived 45S5 glass–ceramics, J. Am. Ceram. Soc. 98 (2015) 30–38.

[4] A. Balamurugan, G. Balossier, S. Kannan, J. Michel, A.H.S. Rebelo, J.M.F. Ferreira, Development and in vitro characterization of sol–gel derived CaO–P2O5–SiO2–ZnO bioglass, Acta Biomater. 3 (2007) 255–262.

[5] I. Cacciotti, M. Lombardi, A. Bianco, A. Ravaglioli, L. Montanaro, Sol–gel derived 45S5 bioglass: Synthesis, microstructural evolution and thermal behaviour, J. Mater. Sci. Mater. Med. 23 (2012) 1849–1866.

[6] M. Montazerian, J.F. Schneider, B.E. Yekta, V.K. Marghussian, A.M. Rodrigues, E.D. Zanotto, Sol–gel synthesis, structure, sintering and properties of bioactive and inert nano–apatite–zirconia glass–ceramics, Ceram. Int. 41 (2015) 11024–11045.

[7] R.L. Siqueira, O. Peitl, E.D. Zanotto, Gel–derived SiO2–CaO–Na2O–P2O5 bioactive powders: Synthesis and in vitro bioactivity, Mater. Sci. Eng. C. 31 (2011) 983–991.

[8] M. Mozafari, F. Moztarzadeh, M. Tahriri, Investigation of the physico–chemical reactivity of a mesoporous bioactive SiO2–CaO–P2O5glass in simulated body fluid, J. Non. Cryst. Solids. 356 (2010) 1470–1478.

[9] M. Mami, A. Lucas–Girot, H. Oudadesse, R. Dorbez–Sridi, F. Mezahi, E. Dietrich, Investigation of the surface reactivity of a sol–gel derived glass in the ternary system SiO2–CaO–P2O5, Appl. Surf. Sci. 254 (2008) 7386–7393.

[10] D. Bellucci, A. Sola, R. Salvatori, A. Anesi, L. Chiarini, V. Cannillo, Sol–gel derived bioactive glasses with low tendency to crystallize: Synthesis, post–sintering bioactivity and possible application for the production of porous scaffolds, Mater.

Sci. Eng. C. 43 (2014) 573–586.

[11] S. Ni, R. Du, S. Ni, The influence of Na and Ti on the in vitro degradation and bioactivity in 58S sol–gel bioactive glass, Adv. Mater. Sci. Eng. 2012 (2012) 1–7.

[12] Q.Z. Chen, Y. Li, L.Y. Jin, J.M.W. Quinn, P.A. Komesaroff, A new sol–gel process for producing Na2O–containing bioactive glass ceramics, Acta Biomater. 6 (2010) 4143–4153.

[13] M. Catauro, M.G. Raucci, F. De Gaetano, A. Marotta, Antibacterial and bioactive silver–containing Na2O.CaO.2SiO2 glass prepared by sol–gel method, J. Mater. Sci. Mater. Med. 15 (2004) 831–837.

[14] S. Alfaro, C. Rodríguez, M.A. Valenzuela, P. Bosch, Aging time effect on the synthesis of small crystal LTA zeolites in the absence of organic template, Mater. Lett. 61 (2007) 4655–4658.

[15] H.I. Hsiang, S.C. Lin, Effects of aging on the phase transformation and sintering properties of TiO2 gels, Mater. Sci. Eng. A. 380 (2004) 67–72.

[16] M. Catauro, F. Bollino, F. Papale, M. Gallicchio, S. Pacifico, Influence of the polymer amount on bioactivity and biocompatibility of SiO2/PEG hybrid materials synthesized by sol–gel technique, Mater. Sci. Eng. C. 48 (2015) 548–555.

[17] G. Hernández, P. Robles, Vidrios SiO2 nanocompuestos preparados por sol–gel: revisión, Superf. y Vacio. 11 (2000) 1–16.

[18] L. Radev, Influence of thermal treatment on the structure and in vitro bioactivity of sol–gel prepared CaO–SiO2–P2O5 glass–ceramics, Process. Appl. Ceram. 8 (2014) 155–166.

[19] Z. Sun, D. Guo, L. Zhang, H. Li, B. Yang, S. Yan, Multifunctional fibrous silica composite with high optical sensing performance and effective removal ability toward Hg 2+ ions, J. Mater. Chem. B. 3 (2015) 3201–3210.

[20] I. Notingher, J.R. Jones, S. Verrier, I. Bisson, P. Embanga, P. Edwards, et al., Application of FTIR and Raman Spectroscopy to Characterisation of Bioactive Materials and Living Cells, Spectrosc. Int. J. 17 (2003) 275–288.

[21] H. Aguiar, J. Serra, P. González, B. León, Structural study of sol–gel silicate glasses

by IR and Raman spectroscopies, J. Non. Cryst. Solids. 355 (2009) 475–480.

[22] Y. Dimitriev, M. Krupchanska, Y. Ivanova, A. Staneva, Sol–Gel Synthesis of Materials in the system Bi2O3 – SiO2, J. Univ. Chem. Technol. Metall. 45 (2010) 39–42.

[23] V.P. Reddy, T.G.V.M. Rao, A.R. Kumar, K. Neeraja, K.K. Chakravarthi, M.R. Reddy, Optical and Structural Analysis of Ho3+ Ion Doped Sodium zirconium Silicate Gasses, Int. J. Curr. Eng. Technol. 4 (2014) 873–878.

[24] J. Simitzis, D.E. Baciu, In vitro bioactivity investigation of porous calcium silicate bioactive glasses prepared by sol–gel using PEG beads as template, Dig. J. Nanomater. Biostructure. 7 (2012) 1719–1725.

[25] B.A. Sava, T. Vişan, Raman and FTIR studies of some sol–gel based glasses in the ZnO–TiO2–SiO2 system, UPB Sci. Bull. Ser. B Chem. Mater. Sci. 69 (2007) 11–24.

[26] J. Serra, P. González, S. Liste, C. Serra, S. Chiussi, B. León, et al., FTIR and XPS studies of bioactive silica based glasses, J. Non. Cryst. Solids. 332 (2003) 20–27.

[27] S. Chajri, S. Bouhazma, S. Herradi, H. Barkai, S. Elabed, S.I. Koraichi, et al., Studies on preparation and characterization of SiO2–CaO–P2O5 and SiO2–CaO–P2O5–Na2O bioglasses subtituted with ZnO, J. Mater. Environ. Sci. 6 (2015) 1882–1897.

[28] L. Berzina–Cimdina, N. Borodajenko, Research of Calcium Phosphates Using Fourier Transform Infrared Spectroscopy, in: T. Prof. Theophile (Ed.), Infrared Spectrosc. – Mater. Sci. Eng. Technol., InTech, 2012: pp. 123–148.

[29] G.Q. Silveira, C.M. Ronconi, M.D. Vargas, R.A.S. San Gil, A. Magalhães, Modified silica nanoparticles with an Aminonaphthoquinone, J. Braz. Chem. Soc. 22 (2011) 961–967.

[30] E.M. Valliant, C.A. Turdean–Ionescu, J. V. Hanna, M.E. Smith, J.R. Jones, Role of pH and temperature on silica network formation and calcium incorporation into sol–gel derived bioactive glasses, J. Mater. Chem. 22 (2012) 1613–1619.

[31] S.K. Young, W.L. Jarrett, K.A. Mauritz, Studies of the aging of Nafion/silicate nanocomposites using Si–29 solid state NMR spectroscopy, Polym. Eng. Sci. 41

(2001) 1529–1539.

[32] P. González, J. Serra, S. Liste, S. Chiussi, B. León, M. Pérez–Amor, Raman spectroscopic study of bioactive silica based glasses, J. Non. Cryst. Solids. 320 (2003) 92–99.

[33] R.G. Hill, D.S. Brauer, Predicting the bioactivity of glasses using the network connectivity or split network models, J. Non. Cryst. Solids. 357 (2011) 3884–3887.

[34] L.M. Mukundan, R. Nirmal, D. Vaikkath, P.D. Nair, A new synthesis route to high surface area sol gel bioactive glass through alcohol washing A preliminary study, Biomatter. 2 (2013) 1–10.

Chapter 3

The present chapter was published on:
Materials Science and Engineering: C;
Volume 91, Issue -,
1 October 2018,
Pages 36–43.
Doi: 10.1016/j.msec.2018.05.016

Enhanced bioactivity of a rapidly–dried sol–gel derived quaternary bioglass

Basam A.E. Ben–Arfa, Isabel M. Miranda Salvado , José M.F. Ferreira, Robert C. Pullar

Department of Materials and Ceramic Engineering / CICECO – Aveiro Institute of Materials, University of Aveiro, 3810–193 Aveiro, Portugal

*To whom correspondence should be addressed: isabelmsalvado@ua.pt, rpullar@ua.pt

Keywords: Glass; Glass ceramics; Crystallisation; Bioactivity; Hydroxyapatite.

Abstract

Novel quaternary (67Si–24Ca–10Na–8P) glass powders were successfully synthesised by sol–gel followed by two alternative drying schedules, conventional drying (CD) and an innovative fast drying (FD) process (200 times quicker). The glasses were thermally stabilised at 550 °C, and then characterised by different complementary techniques. The samples showed very similar silica network structures, with the FD one having slightly lower degree of polymerisation than the CD sample. This less polymerised, more open, network structure exhibited an improved bioactivity in simulated body fluid (SBF), probably also due to the apparent presence of poorly crystalline HAp in the stabilised glass powder. In contrast, the CD glass exhibited an unwanted secondary crystalline silica phase. Both glasses showed excellent biomineralisation upon immersion in SBF, being more pronounced in the case of FD with clear evidence of HAp formation after 4 h, while equivalent signs in the CD samples were only noticed after longer immersion periods between 8 h and 1 week.

1. Introduction

Glasses find applications in many modern technologies and industries **[1]**. These materials can be prepared by the traditional melting route or via sol–gel **[2]**. Sol–gel offers several advantages, including an atomic level mixing of the batch components at room temperature (RT), lower processing temperatures **[3]** that prevent preferential volatilisation of certain components, and an enhanced homogeneity of the glasses **[4]**. This synthesis route attracted increasing attention from the research community after the first sol–gel preparation of a multi–component glass in 1950 **[2]**, being considered a promising technique for producing bioactive glasses and glass ceramics. The high surface area of sol–gel derived materials, the presence of micro pores and of residual hydroxyl ions confer them enhanced bioactivity **[1]**. However, a long aging processing step is usually required to harden the sol net–work **[4]**, which affects the final microstructure and the mineralisation ability of sol–gel bioglasses **[5]**. Increasing aging times are often accompanied by a noticeable decreases in bioactivity **[4]**. Therefore, the aim of this work is to improve the bioactivity of a four–component bioglass and overcoming the problem of long aging stages in sol–gel processing by following a new rapid sol–gel synthesis method developed by the authors **[6]**. This rapid approach uses a rotary evaporator to dry the sol to a near amorphous bioglass gel in 1 h and has been already tested for bioglasses with Ca and P contents equivalent to stoichiometric hydroxyapatite (HAp, Ca/P = 1.67) **[7]**.

Typical examples of bioactive glasses in quaternary systems are 45S5 and S53P4. 45S5 is probably the most well–known bioactive glass, containing 26.9 mol% CaO and with Ca/P ~5 **[8]**, while S53P4 is another famous bioactive glass with 20 mol% CaO and Ca/P = 5 **[9]**. The most common sol–gel bioactive glasses in this ternary system are 58S, which contains 36 mol% CaO and Ca/P = 4.5 **[10]**, and 77S with 16 mol% CaO and Ca/P = 2 **[11]**.

In terms of network structure, melt derived 45S5 bioglass consists of 69% chains and rings of Q^2, with 31% of Q^3 units providing some cross–linking **[12]**. It has been suggested that bioglasses with network connectivity (N_c) > 2.6 lack bioactivity **[13]**. However, sol–gel glasses often do not obey the N_c calculations, as H^+ can also be considered as a network modifier, which increases the glass's dissolution rate **[14]**.

In the present work, a quaternary bioglass composition enriched in calcium (Ca/P = 3: $67SiO_2 – 5Na_2O – 24CaO – 4P_2O_5$) was selected to investigate the effect of a larger amount

of modifier on the network structure and HAp formation in–vitro. The high silica content is justified by its role as primary nucleation centre for apatite formation **[15]** and to foster mechanical strength. The content of phosphate was kept intentionally low as its role in the glass is only to aid the nucleation of calcium phosphate **[16]**. The presence of Na_2O (5 mol%) in the glass compositions aims at enhancing the degradation rate **[17]**, stimulate bone formation and differentiation **[18,19]**, and the apatite–forming ability in–vitro **[19]**.

2. Experimental

2.1. Glass synthesis

Tetra–ethyl–ortho–silicate (TEOS, $C_8H_{20}O_4Si$, 98%), calcium nitrate tetrahydrate (CaN, $Ca(NO_3)_2{\cdot}4H_2O$, ≥99%), sodium nitrate (NaN, $NaNO_3$, ≥99%) and triethyl phosphate (TEP, $C_6H_{15}O_4P$, ≥99.8%) were used as precursors for silica, calcium oxide, sodium oxide and phosphorus oxide, respectively. All four precursors were supplied from Sigma–Aldrich. Distilled water was used as solvent and citric acid monohydrate (CA, $C_6H_8O_7{\cdot}H_2O$, 99.5−102%, Sigma–Aldrich) was added to catalyse the sol–gel hydration and polymerisation reactions.

The four–component composition was selected in the (Si−Na−Ca−P) system: $67SiO_2$ – $5Na_2O$ – $24CaO$ – $4P_2O_5$ (mol%, Ca/P = 3), as shown in **Table 3.1**.

Table 3.1: Composition, drying schedules and sample codes.

Composition (mol%)	Drying schedule	Sample code
$67SiO_2$ – $5Na_2O$ – $24CaO$ – $4P_2O_5$ (67Si – 5Na – 24Ca – 4P)	Conventional drying (CD)	67S24C–CD
	Rotary evaporator (FD)	67S24C–FD

20 ml of 0.15 M aqueous solution of CA was poured in 150 ml glass beaker, and 24 ml TEOS and 2.2 ml TEP were sequentially added quickly to this solution. After a clear sol was formed, 1.3616 g of NaN was dissolved separately in 10 ml 0.15 M aqueous solution of CA, stirred for 10 min, and then added quickly to the beaker containing the TEOS and TEP. 9.0798 g of CaN was dissolved separately in 50 ml 0.15 M aqueous solution of CA and added

quickly to the beaker containing the other three components. This solution was then stirred for 1 h, at RT as schematised the flow chart diagram of **Fig. 3.1**. The resulting sol was divided into two equal parts. One half was poured into a glass petri dish (120 mm diameter, 20 mm high) to be aged and dried by conventional drying (CD). The sample was aged at RT for 4 h, followed by drying in an oven at 35 °C/3 days, then at 50 °C/6 days, and finally at 100 °C/3 days, making a total of 12 days (288 h) **[19]** for the sample 67S24C–CD.

The second half was rapidly dried in a Buchi 210 Rotavapor (rotary evaporator) with V–850 vacuum controller and V–700 diaphragm vacuum pump (Buchi Labortechnik AG, Flawil, Switzerland). The sols were dried in a 500 ml pear–shaped flask while rotating in a water bath at 55 °C and under a pressure of 50 mbar for 1 h **[19]**. This drying process was 288 times quicker, and the as–obtained sample was designated as 67S24C–FD (with FD standing for fast drying). Both processes are summarised in **Fig. 3.1** and **Table 3.1**.

Both dried gels were thermally stabilised at 550 °C in air for 1 h. The heating rate was 1 °C/min up to 300 °C for 1 h, and then increased to 10 °C/min up to 550 °C, holding for 1 h at this temperature, followed by natural cooling. The heat–treated samples were ground using a mortar and pestle to obtain glass powders, which were sieved through a 40–63 μm mesh and then used for all the subsequent characterisations.

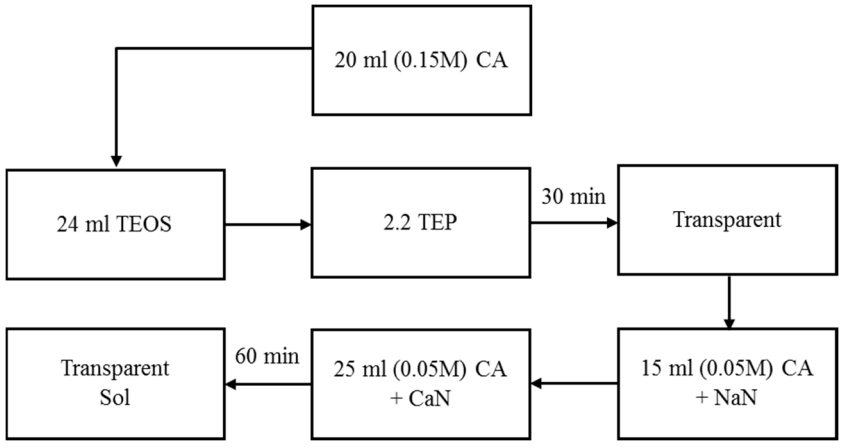

Fig. 3.1: Flow chart scheme of the sol gel synthesis.

2.2. Characterization of glass

The specific surface areas (SSA) of the powders were estimated using the Brunauer–Emmett–Teller (BET) method using a Gemini M–2380 (Micrometrics, Norcross, GA) with N_2 as the adsorbate. Samples were degassed at 200 °C before performing the analysis.

Skeletal density was determined by helium pycnometry. The particle size was measured using a laser diffraction particle size analyser (Coulter LS particle size analyser; Beckman Coulter, CA).

The crystalline phase analysis of the samples before and after immersion in simulated body fluid (SBF) was performed by X–ray diffraction (XRD, PANalytical XPERT–PRO Diffractometer system), using Cu Kα radiation (Kα = 1.54059 Å) with 2θ varying from 6 to 70° in steps of 0.026 s−1. The diffraction patterns were compared with JCPDS standards **[20,21]**.

The ^{29}Si MAS–NMR spectra were recorded in a ASX 400 spectrometer (Brucker, Germany) operating at 79.52 MHz (9.4 T), using a 7 mm probe at a spinning rate of 5 kHz. The pulse length was 2 μs with 60 s delay time. The aim was to investigate the silica environments and the degree of silica polymerisation of the stabilised glass samples. Kaolinite was used as a chemical shift reference. ^{29}Si MAS NMR spectra were deconvoluted using dimFit software.

Infrared transmittance spectra of the glasses, before and after immersion in SBF, were obtained using a Fourier Transform Infrared Spectrometer (FTIR, Tensor 27, Brucker, Germany) in the range of 350–4000 cm^{-1}, with 128 Scans and 4 cm^{-1} resolution. The pellets were prepared by pressing a mixture of KBr and glass powder with ratio of 1/150 (by weight) and pressed into a pellet using a hand press.

2.3. Bioactivity tests

The in–vitro bioactivity in simulated body fluid (SBF) was assessed by immersion of 75 mg of glass powders from samples in 50 mL of SBF solution at 37 °C following a unified approach recommended elsewhere **[22]**. The ionic concentrations of the SBF (in mmol L^{-1}: Na^+ = 142.0, K^+ = 5.0, Ca^{2+} = 2.5, Mg^{2+} = 1.5, CI^- = 125.0, HPO_4^{2-} = 1.0, HCO_3^- = 27.0

and SO_4^{2-} = 0.5) are virtually equivalent to those of human plasma **[23]**. The powder–SBF mixtures were immediately sealed into plastic flasks and placed in an incubator at 37 ± 0.5 °C on an orbital shaker set at 120 rpm. The sampling took place for 7 different times: (4 h, 8 h, 72 h, 1 week, 2 weeks, 3 weeks and 4 weeks) **[22]**. At the end of each time period, the sample was removed from the incubator and the solids were collected by centrifuging the mixture at 10,000 rpm under vacuum for 30 min, using a Beckman model LB–70 M ultracentrifuge. The pH of the separated solution was measured directly, while the separated particles were washed with deionised water and subsequently with acetone to terminate the reaction, and after separation for the second time, dried in an oven overnight at 37 °C. The experiments were performed in triplicate in order to ensure the accuracy of results. The apatite–forming ability of the glass powders was followed by XRD, FTIR, and SEM analysis, and pH measurement.

3. Results and discussion

3.1. Surface area and density measurements

Table 3.2 shows the data of density, particle size and specific surface area measured for the thermally stabilised glass powders obtained by the two drying schedules. As can be seen, the protocol used for drying and aging drastically affects the physical properties of the resulting materials. The density of 67S24C–CD is only slightly lower in comparison to that of 67S24C–FD, but the SSA of 67S24C–CD glass powder is > 1.4 times greater than that of 67S24C–FD sample.

Table 3.2: Physical properties (density, particle size, and specific surface area) of 67S24C– CD and 67S24C–FD glasses.

Sample code	Density	Particle size	BET SSA
	(g/cm^3)	d_{50} (μm)	m^2/g
67S24C–CD	2.3 ± 0.03	34	99.5
67S24C–FD	2.5 ± 0.03	16	68.1

The higher SSA value of 67S24C–CD can be attributed to the fine porous network formed during the long and undisturbed sol–gel transition followed by solvent evaporation from the pores. The impacts on the in vitro bioactivity will depend not only on the extent of surface area exposed to SBF, but also on the degree of glass network connectivity and how it is affected by the drying schedule, as will be discussed below.

3.2. Structure of stabilised glasses

3.2.1. MAS–NMR analysis

The measured and deconvoluted ^{29}Si MAS NMR spectra for 67S24C–FD and 67S24C–CD routes are shown in **Fig. 3.2**. Deconvolution enabled identifying the various Q^n species, where n denotes the number of bridging oxygens and can assume the values of 1, 2, 3 or 4. The condensation degree (D_c) values calculated by using the Eq. (3.1) below **[24]** are presented in **Table 3.3**

$$D_c = \frac{1\times Q^1+2\times Q^2+3\times Q^3+4\times Q^4}{4} \times 100\% \quad (3.1)$$

The network connectivity N_c can be calculated from the % integral of Q^n acquired from the NMR deconvolution by dimFit using Eq. (3.2) **[25]**:

$$Nc = 4\left(\frac{Q^4}{100}\right) + 3\left(\frac{Q^3}{100}\right) + 2\left(\frac{Q^2}{100}\right) + 1\left(\frac{Q^1}{100}\right) \quad (3.2)$$

The chemical shifts at ~ −100.2 and ~−100.7 ppm are assigned to Q^3 species for 67S24C–FD and 67S24C–CD samples, respectively, while Q^4 species are observed around −110 ppm for the two glasses. Both glasses also contain significant populations of Q^2 and Q^1 species as well, between −94.4 to −96.4 ppm, and −86.5 and −88.2 ppm, respectively **Table 3.3**. Although the two samples have the same composition, the proportions of the Q^n species are significantly different. 67S24C–FD has fewer Q^4 species than 67S24C–CD, but a greater number of Q^2 and Q^1 species, with the difference of ~10% in Q^2 species between the FD and

CD routes being particularly significant. 67S24C–FD also has consistently lower chemical shift values as a result of less extensive polymerisation. This means that 67S24C–FD has a smaller Dc value (71.8%) than 67S24C–CD (78.4%), which also translates in lower calculated network connectivity (N_c = 3.0) for 67S24C–FD in comparison to 67S24C–CD (N_c = 3.2). These results are shown in **Table 3.3**.

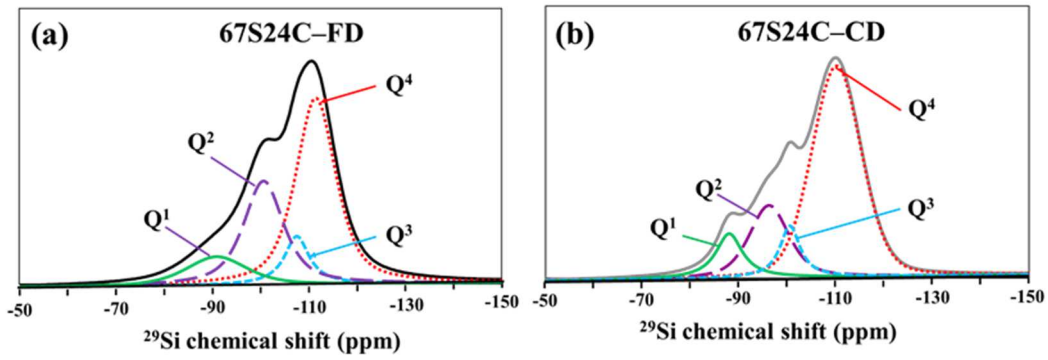

Fig. 3.2: Deconvoluted ^{29}Si NMR spectra for stabilised glass powders obtained through a) fast drying (FD) and b) conventional drying (CD) routes.

Table 3.3: Q^n (Si) distribution for 67S24C–CD and 67S24C–FD glasses obtained by NMR deconvolution, and calculated degrees of condensation (D_c) and network connectivity (N_c).

Sample code	Q^n								D_c (%)	N_c from ^{29}Si MAS NMR
	Q1		Q^2		Q^3		Q^4			
	Peak position (ppm)	Integral %	Peak position (ppm)	Integral %	Peak position (ppm)	Integral %	Peak position (ppm)	Integral %		
67S24C–FD	–86.5	11.3	–94.4	29.0	–100.2	9.4	–110.4	50.3	71.8	3.0
67S24C–CD	–88.2	9.8	–96.4	19.4	–100.7	8.5	–110.3	62.3	78.4	3.2

Different drying protocols for the same proportions of modifiers results in different extents of silica network disruption. The 67S24C–FD sample exhibits a lower degree of network connectivity compared with 67S24C–CD and is likely to be more readily mineralised upon

immersion in SBF. This result is consistent with our previous observations made for FD bioglasses of the same Si–Ca–Na–P system but containing lower amounts of Ca modifier bioglasses with Si/Ca ratios of 76/10 **[26]** and 76/9 **[7,26]**. These CD bioglasses only showed Q^4 and Q^3 silica species; with ~70–75% being fully connected Q^4. The FD method produced glasses with a slightly lower degree of connectivity (D_c = 91.8% for FD vs. 93.8% for CD) **[16]**. Moreover, all these glasses with lower contents of Ca modifier exhibited greater extents of network connectivity (Nc = ~3.7) than the present calcium–rich bioglasses with a Si/Ca ratio of 67/24 (approximately 3 times less than in refs **[7,26]**. The higher amount of modifier used in this work resulted in a much less polymerised glass network structure, which is expected to have positive impacts on its in vitro bioactivity in SBF.

3.2.2. X–ray diffraction (XRD)

Fig. 3.3(a) shows the XRD patterns of the stabilised glasses. Both have some traces of crystallinity in a highly amorphous glass matrix, but it is apparent that 67S24C–FD is less crystalline than 67S24C–CD. This result is in a good agreement with our previous findings for a different glass system showing that the FD method could to some extent suppress crystallisation **[26]**. 67S24C–CD contains crystalline silica (coesite SiO_2, PDF card #04–015–7166) **[20]**. This phase was not formed in FD sample, a feature that favours the 67S24C–FD process.

Avery poorly crystalline HAp [$Ca_{10.12}(H_{1.26}P_{5.99}O_{23.88})(OH)_{2.05}$, PDF card #01–080–3956] **[21]** is a common secondary phase in both samples. The corresponding broad XRD peaks suggest that crystals are at nanoscale, which may act as seeds for the crystallisation for HAp formation and growth upon immersion in SBF.

In our previous compositions **[7,26]** with Ca/P ratios corresponding to stoichiometric HAp (Ca/P = 1.67) and tri-calcium phosphate (TCP, Ca/P = 1.5), the stabilised glasses never exhibited the formation of crystalline HAp. Instead, the crystalline phases observed in both FD and CD produced glasses were $NaCa(PO_4)$ **[26]** and $CaNa_4Si_3O_9$ **[7]**. Therefore, it seems that the much higher ratio of Ca/P used here (Ca/ P = 3) enables squeezing sufficient calcium from the glass network to form nanocrystalline HAp. This should also assist the formation and growth of HAp from these bioglasses in body fluids. Further manipulation of

the Ca/P ratio in the glass composition may enable control over the exact calcium phosphate phase which can be crystallised **[27]**.

3.2.3. FTIR spectra

The FTIR spectra of the two stabilised glasses are presented in **Fig. 3.3(b)**. They are typically dominated by a broad band between 900 and 1300 cm^{-1}, assigned to asymmetric stretching for Si–O–Si centred at ~1080 cm^{-1} **[28]**, which represents the transverse optical (TO_1) Si–O–Si stretching mode. Moreover, a shoulder at ~1225 cm^{-1} represents the Si–O–Si (TO_2) stretching mode **[29]**, as a result of the introduction of P_2O_5 into silica glass **[30]**. The longitudinal optical (LO) vibration can be observed at 1170 cm^{-1} **[29]**. The very faint bands around 880 cm^{-1} and 1425–1460 cm^{-1} are assigned to C–O bonds (probably small amounts of carbonate) **[24,31,32]**. The main signal in 67S24C–CD is divided into two peaks; one appears at 1092 cm^{-1} and the other at 1045 cm^{-1}.

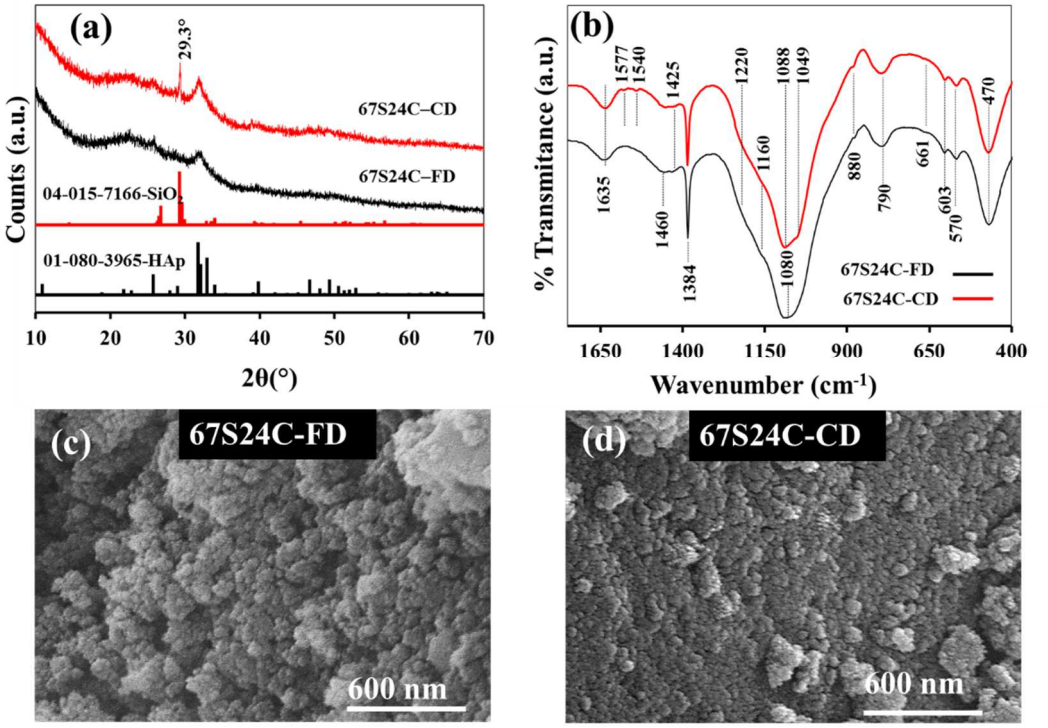

Fig. 3.3: Structural and morphological features of the 67S24C–FD and 67S24C–CD stabilised glass powders before immersion in SBF: (a) XRD patterns; (b) FTIR spectra; (c) and (d) SEM micrographs.

The appearance of the twin peaks at ~570 and ~603 cm^{-1} for the two glasses can be attributed to phosphate group PO_4^{3-}, being usually considered an evidence for the presence of HAp. The other characteristic phosphate peaks for HAp appear at around 962, 1034 and 1092 cm^{-1} **[33]** and considering their low intensities, they are probably masked by the strong and broad silica peaks in these glasses. Representative HAp peaks were not observed in our previously reported stabilised glasses with stoichiometric Ca/P ratios corresponding to HAp and TCP **[7,26]**. Bands characteristic of (COO^-) group, maybe from the catalyst citric acid species, can be seen as twin peaks at 1540 cm^{-1} and at 1571 cm^{-1}, assigned respectively to $\upsilon_{as}(COO^-)$ and $\upsilon_s(COO^-)$ vibration modes **[34]**. The peak observed at ~1635 cm^{-1} can be assigned to the bending vibration of molecular water **[35]**. These peaks, along with the two shoulders at 1170 cm^{-1} and 1225 cm^{-1}, are assigned to Si–O stretching modes for tetrahedral coesite (a less common form of SiO_2), and the 796 cm^{-1} peak is also assigned to Si–O–Si stretching frequencies of various silica phases, including coesite **[27,28]**. This splitting is much less apparent in FD suggesting it may not contain the coesite phase, but instead quartz with a peak at 1080 cm^{-1}.

3.2.4. Scanning electron microscope (SEM) images

The SEM images of the stabilised glasses are sown in **Fig. 3.3(c)**. It can be seen that both glass powders consist of agglomerated primary nanoparticles (NPs) with approximate dimensions of 30–50 nm. These approximately spherical NPs associate to form submitter agglomerates. No significant morphological differences can be observed between 67S24C–FD and 67S24C–CD samples. Their appearances resemble the morphologies observed for the corresponding stabilised glass powders prepared by the same FD and CD routes reported previously by the authors **[7,26]**.

3.3. Bioactivity assessment

3.3.1. XRD after immersion in simulated body fluid (SBF)

Fig. 3.4(a) displays the XRD patterns of the 67S24C–FD and 67S24C–CD samples, respectively, after immersion in SBF for different periods of time up to 4 weeks. The crystalline SiO_2 phase seen in CD (Coesite, PDF card #04–015–7166) has apparently disappeared, being probably hidden by the poorly–crystalline HAp surface layer.

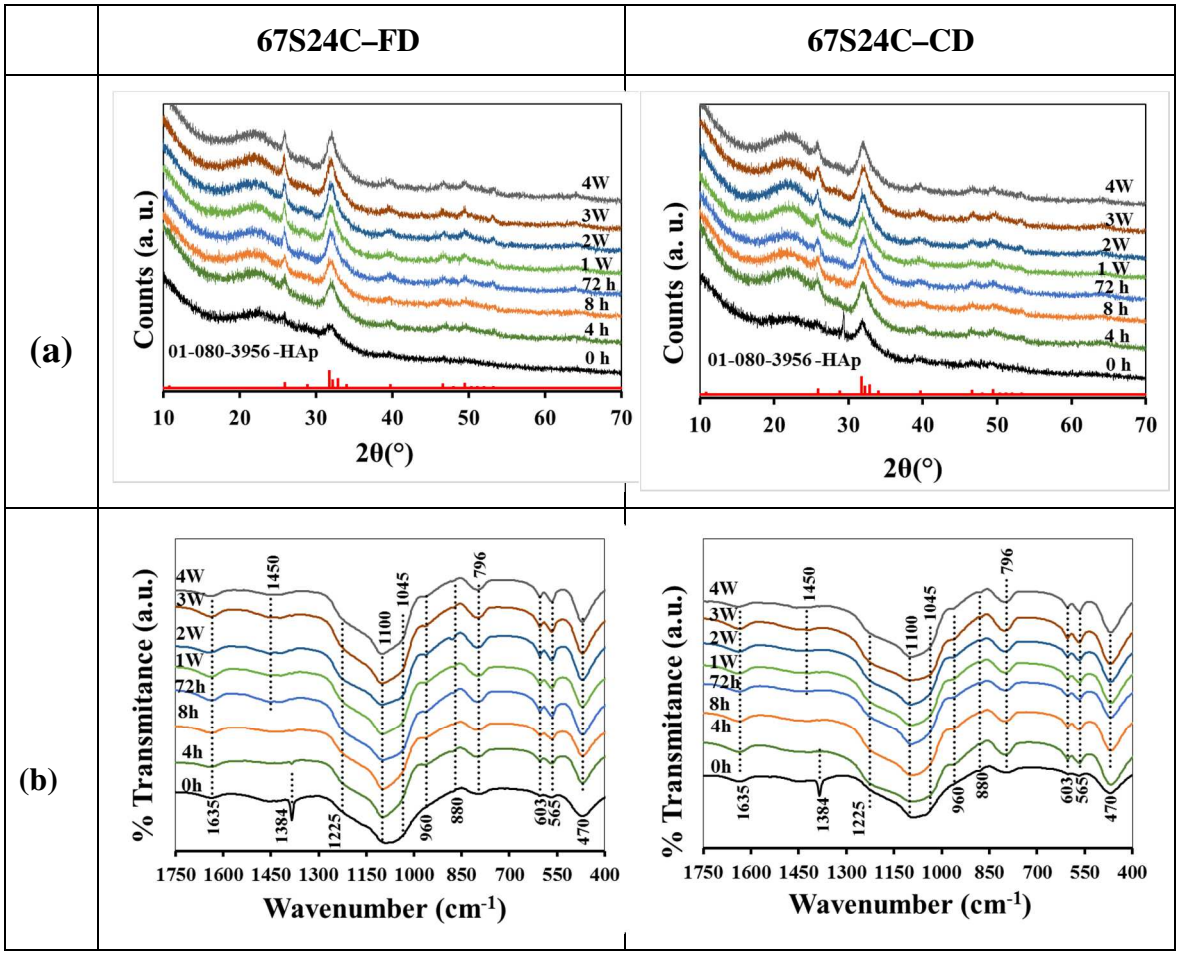

Fig. 3.4: Structural evolutions undergone by the FD and CD stabilised glass powders after immersion in SBF for different periods of time (4 h, and 4 w) assessed by: (a); XRD; (b) FTIR.

This hypothesis is consistent with the observed gradual intensification of the HAp peaks (PDF # 01–080–3956) already identified in the stabilised glasses. There major changes in the degree of crystallinity were observed between 4 h and 4 weeks of immersion. Within the period from 72 h to 4 weeks, 67S24C–FD with sharper and better defined major peaks seems to have undergone a slightly more extensive biomineralisation process in comparison to 67S24C–CD. This supports the hypothesis that the FD method fosters the in vitro bioactivity (the ability to deposit a surface layer of HAp), attributed to the less polymerised silica network structure of 67S24C–FD (50.3% Q^4, 29.0% Q^2) in comparison to 67S24C–CD (62.3% Q^4, 19.4% Q^2).

The earlier tested bioglass powders with Ca/P ratios corresponding to stoichiometric HAp and TCP phases did not show the formation of crystalline HAp until after 3–4 weeks of

immersion in SBF, and even then, only for the powder with Ca/P = 1.67 and under shaking at 120 rpm **[7]**.

3.3.2. FTIR spectra after immersion in SBF

Fig. 3.4(b) shows the evolution of the FTIR bands upon immersion in SBF over different time periods. The major HAp band at around 1034 cm^{-1} is still masked by the large silica band, but the two characteristic phosphate peaks of HAp at around 560 and 600 cm^{-1} are clearly present and sharp after just 4 h of immersion for both samples, and the weak–but–sharp 962 cm^{-1} peak is faintly visible **[36]**. This may confirm the dissolution of HAp and the evolution of a new HAp phase, as suggested by XRD. As observed by XRD, there are little changes over time with HAp peaks becoming better defined and sharper after 72 h, with the changes being slightly more noticeable for 67S24C–FD than for 67S24C–CD between 72 h and 4 weeks. The FTIR data also support the superior bioactivity of the present composition and of the FD method in comparison the lower Ca/P ratio and CD reported in our previous studies **[7]**. Here, the presence of existing HAp NPs in the stabilised powders and the less polymerised network structure seem to be the reasons for the enhanced bioactivity.

The two tiny non–HAp related peaks at 1425−1460 cm^{-1} were replaced by wide band centred at ~1450 cm^{-1}, which is assigned to the C–O group. Also the evolution of the peak at 880 cm^{-1} evidences the presence of carbonated hydroxyapatite formation (CHAp). It can be classified as type A due to the band being centred at 1450 cm^{-1} and the peak at 880 cm^{-1} **[33,37]**. The band at 1045 cm^{-1} belongs to a more linear silica structure. The shifting of the main bands from 1080−1092 to 1100 cm^{-1} for the two glass samples could also be attributed to transformation of the silica structure to a less cross linked and more linear structure due to SBF immersion **[38]**. The appearance of a new band at ~960 cm^{-1} could be assigned to stretching vibrational mode of Si–OH **[39–41]**, although as stated above there is a weak HAp peak at 962 cm^{-1}, and it is also reported that a peak at about 960 cm^{-1} could be assigned to P–O symmetric stretching in the formed layer of CHAp layer on the powder surface **[42]**. This may show the occurrence of the 5 stages of hydroxycarbonated apatite CHAp layer formation as proposed by Hench et al. **[42]** during the initial hours of immersion in SBF. Although the FTIR spectra of both glasses are very similar, after 72 h 67S24C–

FD shows sharper and better defined peaks supporting its enhanced bioactivity in comparison to 67S24C–CD. Interestingly, sharpness of FTIR HAp peaks can only be noticed after 4 h in the 67S24C–CD sample.

The morphological evolution of the HAp layer deposited onto the surface of 67S24C–FD and 67S24C–CD along the immersion time in SBF is shown in the SEM images displayed in **Fig. 3.6**. A network of poorly crystalline platy flakes has been deposited after only 4 h for both glasses, with relatively higher deposition of HAp on the surface of 67S24C–CD as shown in **Fig. 4.6(a)**. After 8 h of SBF immersion **Fig. 4.6(b)**, HAp deposition increased intensively in both glasses, maintaining a higher bioactivity for 67S24C–CD, with a denser HAp deposited layer. At 1 week, **Fig. 4.6(c)**, it can be observed that the higher bioactivity favours the 67S24C–FD glass, as shown by highly uniform layer covering the glass surface. The bioactivity exhibits similar behaviour after 4 w of SBF immersion with almost similar morphology, as can be seen in **Fig. 4.6(d)**.

3.3.3. pH behaviour in SBF

The pH variations along the immersion time in SBF for the 67S24C–FD and 67S24C–CD samples exhibit almost identical trends as shown in **Fig. 3.5**. The pH variations for both samples run in parallel within the 7.40–7.75 range, being slightly smaller for 67S24C–FD. A rapid initial increase in pH values from the starting value of 7.4 was registered for both samples after just 4 h, attributed to the leaching of alkaline Na and alkaline earth Ca from the surface of the glass particles. This increasing step is then followed by a gradual reversal trend starting between 4 h to 8 h, which might be due to the partial dissolution of acidic glass former species such as Si^{4+} and phosphate ions; and to the precipitation of HAp, as confirmed by XRD and FTIR spectra. The two samples then underwent a gradual increase in pH reaching plateaux values within 3−14 days, followed by slow general decreasing trends with the accomplishment of the surface HAp coating layer. Seemingly, the in vitro biomineralisation occurred through three–stages: (i) initial fast ionic exchanges, saturation of the SBF solution and surface precipitation of poorly crystalline HAp (4−8 h); (ii) the continuation of the dissolution–precipitation reactions but at a slower pace (3−14 day□); followed by (iii) a trend towards stabilisation due to the gradual depletion of Ca and

P species in the SBF solution and the completeness of the surface HAp coating layer. The observed pH changes are consistent with the previous results obtained by XRD and FTIR.

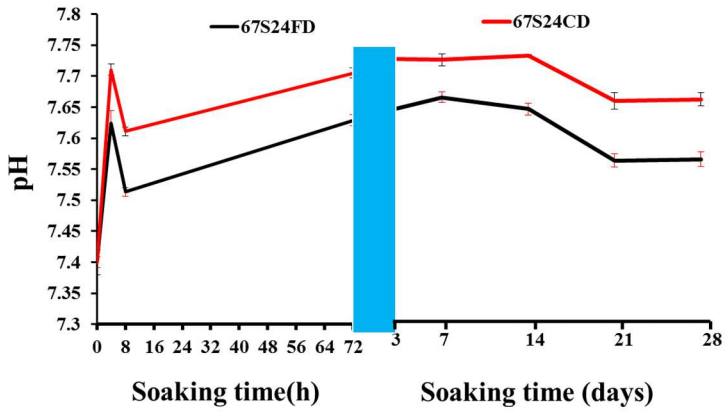

Fig. 3.5: Evolution of solution pH with immersion time in SBF for the 67S24C–FD and 67S24C–CD samples

3.3.4. SEM images after immersion in SBF

The SEM micrographs of the 67S24C–FD and 67S24C–CD samples immersed in SBF for different time periods (4 h, and 4 w) are shown in **Fig. 3.6(a, b)**. After just 4 h the microstructure has already evolved significantly from that observed before immersion in SBF with nanosize HAp formations covering most of the available surface, as can be deduced from the evidences gathered by XRD and FTIR **Fig. 3.4(a, b)**. With the immersion time increasing to 8 h, the individual NPs tended to group in clusters of larger sizes. These features resemble the micro–structure of HAp precipitated on pure HAp ceramics after 1 week in SBF **[37]**. This is supported by the gradual intensification of FTIR peaks of HAp seen in the spectra of 67S24C–FD and 67S24C–CD samples **Fig. 3.4(a, b)**.

The HAp surface layer continued to develop between 1 and 4 weeks becoming gradually more crystalline as seen in **Fig. 3.4(a)**, and **3.6**. After immersion for 4 weeks, the particles of both 67S24C–CD and 67S24C–FD exhibit a dense coverage of crystalline flakes or plates, but with the same morphological features as those observed in 67S24C–FD after 8 h. This refinement of the surface morphology is probably due to the local continuous and slowly dissolution/precipitation reactions that occur when the system approaches

equilibrium conditions. This nanotextured surface may offer favourable conditions for cell adhesion.

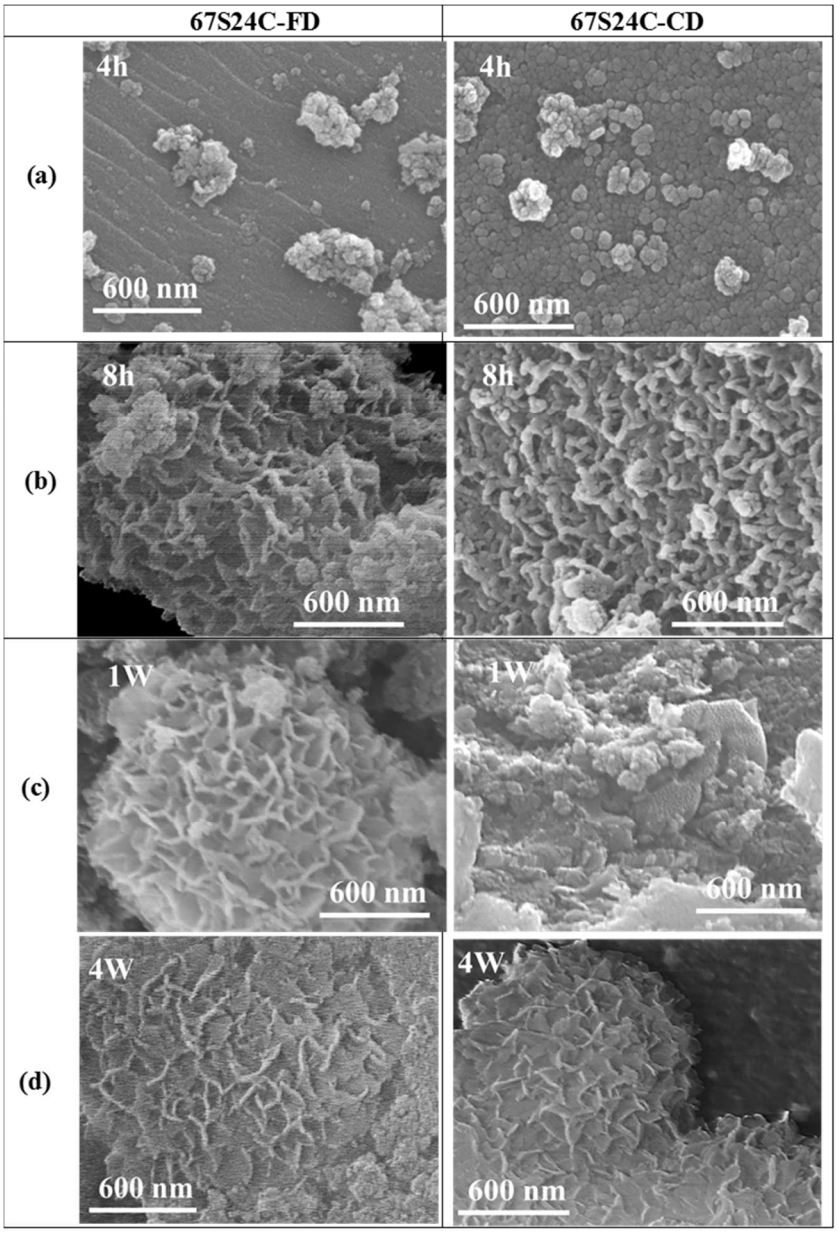

Fig. 3.6: SEM images for 67S24C–FD and 67S24C–CD glass powders after immersion in SBF for (a) 4 h, (b) 8 h, (c) 1 w, and (d) 4 w.

Other reports on rapid glass preparation routes, such as those by Yan et al. (a gel calcined at 800 °C) **[32]** and by Peitl et al. (from a glass melt quenching route) **[43]**, indicate the appearance of the phosphate peaks at around 560–600 cm^{-1} in the FTIR spectra only after

24 h and 20 h of immersion in SBF, respectively – much longer periods than 4 h reported here. Furthermore, these and many other publications do not show XRD data or SEM images of the microstructures hindering any well supported comparison with our bioglasses concerning the bio–mineralization extents after a given immersion time period.

4. Conclusions

Quaternary (67Si–24Ca–10Na–8P) glass powders were successfully synthesised by sol–gel technique using both conventional drying (67S24C–CD) and an innovative fast drying (67S24C–FD) process. The two samples were thermally stabilised at 550 °C and characterised for their physical properties, and their biomineralisation capabilities assessed upon immersion in SBF. The relatively high Ca content favoured the depolymerisation of the silica matrix resulting in a network connectivity value of ~3. Although the network structures of the two samples were very similar, the degree of polymerisation of the rapidly dried sample 67S24C–FD was slightly lower than that of the conventionally dried sample 67S24C–CD. Both stabilised glasses contained poorly crystalline HAp. Crystalline silica was also identified as secondary phase in the 67S24C–CD sample. Although both samples exhibited good biomineralisation responses upon immersion in SBF, the rapidly dried one (67S24C–FD) showed an improved growth of crystalline HAp, especially at exended periods of contact with SBF. This study confirms the superiority of the FD rapid drying method in terms of the overall performance of the sol–gel derived bioactive glasses.

Acknowledgments

R.C. Pullar wishes to thank the FCT (Fundação para a Ciência e a Tecnologia) Grant IF/00681/2015 for supporting this work. This work was developed in the scope of the project CICECO–Aveiro Institute of Materials (Ref. FCT UID/CTM/50011/2013), financed by national funds through the FCT/MEC and when applicable co–financed by FEDER under the PT2020 Partnership Agreement

References

[1] A. Balamurugan, G. Sockalingum, J. Michel, J. Fauré, V. Banchet, L. Wortham, et al., Synthesis and characterisation of sol gel derived bioactive glass for biomedical applications, Mater. Lett. 60 (2006) 3752–3757.

[2] L.C. Klein, Sol–gel technology for thin films. fibers, preforms, electronics, and specialty shapes, Noyes Publications, New Jersey, 1988.

[3] C.S. Chai, K.A. Gross, B. Ben–Nissan, Critical ageing of hydroxyapatite sol–gel solutions, Biomaterials. 19 (1998) 2291–2296.

[4] K. Zheng, A. Solodovnyk, W. Li, O.M. Goudouri, C. Stähli, S.N. Nazhat, et al., Aging time and temperature effects on the structure and bioactivity of gel–derived 45S5 glass–ceramics, J. Am. Ceram. Soc. 98 (2015) 30–38.

[5] D. Liu, T. Troczynski, W.J. Tseng, Aging effect on the phase evolution of water–based sol – gel hydroxyapatite, Biomaterials. 23 (2002) 1227–1236.

[6] B.A.E. Ben–Arfa, I.M.M. Salvado, J.M.F. Ferreira, R.C. Pullar, Novel route for rapid sol–gel synthesis of hydroxyapatite, avoiding ageing and using fast drying with a 50–fold to 200–fold reduction in process time, Mater. Sci. Eng. C. 70 (2017) 796–804.

[7] B.A.E. Ben–Arfa, H.R. Fernandes, I.M. Miranda Salvado, J.M.F. Ferreira, R.C. Pullar, Synthesis and bioactivity assessment of high silica content quaternary glasses with Ca: P ratios of 1.5 and 1.67, made by a rapid sol–gel process, J. Biomed. Mater. Res. – Part A. 106 (2018) 510–520.

[8] L.L. Hench, The story of Bioglass®, J. Mater. Sci. Mater. Med. 17 (2006) 967–978.

[9] I. Kinnunen, K. Aitasalo, M. Pöllönen, M. Varpula, Reconstruction of orbital floor fractures using bioactive glass, J. Cranio–Maxillofacial Surg. 28 (2000) 229–234.

[10] P. Saravanapavan, J.R. Jones, R.S. Pryce, L.L. Hench, Bioactivity of gel – glass powders in the CaO–SiO2 system : A comparison with ternary (CaO–P2O5–SiO2) and quaternary glasses (SiO2 –CaO–P2O5 –Na2O), J. Biomed. Mater. Res. A. 66 (2003) 110–119.

[11] J.R. Jones, Reprint of: Review of bioactive glass: From Hench to hybrids, Acta

Biomater. 23 (2015) S53–S82.

[12] A. Pedone, T. Charpentier, G. Malavasi, M.C. Menziani, New insights into the atomic structure of 45S5 bioglass by means of solid–state NMR spectroscopy and accurate first–principles simulations, Chem. Mater. 22 (2010) 5644–5652.

[13] M. Edén, P. Sundberg, C. Stålhandske, The split network analysis for exploring composition–structure correlations in multi–component glasses: II. Multinuclear NMR studies of alumino–borosilicates and glass–wool fibers, J. Non. Cryst. Solids. 357 (2011) 1587–1594.

[14] S. Lin, C. Ionescu, K.J. Pike, M.E. Smith, J.R. Jones, Nanostructure evolution and calcium distribution in sol–gel derived bioactive glass, J. Mater. Chem. 19 (2009) 1276–1282.

[15] B.A.E. Ben–Arfa, I.M. Miranda Salvado, J.M.F. Ferreira, R.C. Pullar, The Influence of Cu2+ and Mn2+ Ions on the Structure and Crystallization of Diopside–Calcium Pyrophosphate Bioglasses, Int. J. Appl. Glas. Sci. 7 (2016) 345–354.

[16] B.A.E. Ben–Arfa, I.M.M. Salvado, J.M.F. Ferreira, R.C. Pullar, The effect of functional ions (Y3 +, F–, Ti4 +) on the structure, sintering and crystallization of diopside–calcium pyrophosphate bioglasses, J. Non. Cryst. Solids. 443 (2016) 162–171.

[17] A. Patel, J.C. Knowles, Investigation of silica–iron–phosphate glasses for tissue engineering, J. Mater. Sci. Mater. Med. 17 (2006) 937–944.

[18] F. Foroutan, N.J. Walters, G.J. Owens, N.J. Mordan, H.–W. Kim, N.H. de Leeuw, et al., Sol–gel synthesis of quaternary (P2O5) 55–(CaO)25 –(Na2O)(20−x) –(TiO2)x bioresorbable glasses for bone tissue engineering applications (x = 0, 5, 10, or 15), Biomed. Mater. 10 (2015) 1–10.

[19] G. Kaur, G. Pickrell, N. Sriranganathan, V. Kumar, D. Homa, Review and the state of the art: Sol–gel and melt quenched bioactive glasses for tissue engineering, J. Biomed. Mater. Res. – Part B Appl. Biomater. 104 (2016) 1248–1275.

[20] R.J. Angel, C.S.J. Shaw, G. V. Gibbs, Compression mechanisms of coesite, Phys. Chem. Miner. 30 (2003) 167–176.

[21] C. Mochales, R.M. Wilson, S.E.P. Dowker, M.P. Ginebra, Dry mechanosynthesis of nanocrystalline calcium deficient hydroxyapatite: Structural characterisation, J. Alloys Compd. 509 (2011) 7389–7394.

[22] A.L.B. Maçon, T.B. Kim, E.M. Valliant, K. Goetschius, R.K. Brow, D.E. Day, et al., A unified in vitro evaluation for apatite–forming ability of bioactive glasses and their variants, J. Mater. Sci. Mater. Med. 26 (2015) 1–10.

[23] A. Oyane, H.M. Kim, T. Furuya, T. Kokubo, T. Miyazaki, T. Nakamura, Preparation and assessment of revised simulated body fluids, J. Biomed. Mater. Res. – Part A. 65 (2003) 188–195.

[24] G. Poologasundarampillai, D. Wang, S. Li, J. Nakamura, R. Bradley, P.D. Lee, et al., Cotton–wool–like bioactive glasses for bone regeneration, Acta Biomater. 10 (2014) 3733–3746.

[25] Z. Lin, J.R. Jones, J. V. Hanna, M.E. Smith, A multinuclear solid state NMR spectroscopic study of the structural evolution of disordered calcium silicate sol–gel biomaterials, Phys. Chem. Chem. Phys. 17 (2015) 2540–2549.

[26] B.A.E. Ben–Arfa, I.M. Miranda Salvado, J.M.F. Ferreira, R.C. Pullar, A hundred times faster: Novel, rapid sol–gel synthesis of bio–glass nanopowders (Si–Na–Ca–P system, Ca:P = 1.67) without aging, Int. J. Appl. Glas. Sci. 8 (2017) 337–343.

[27] M. Araújo, M. Miola, G. Baldi, J. Perez, E. Verné, Bioactive glasses with low Ca/P ratio and enhanced bioactivity, Materials (Basel). 9 (2016).

[28] P. Innocenzi, Infrared spectroscopy of sol–gel derived silica–based films: a spectra–microstructure overview, J. Non. Cryst. Solids. 316 (2003) 309–319.

[29] H. Aguiar, J. Serra, P. González, B. León, Structural study of sol–gel silicate glasses by IR and Raman spectroscopies, J. Non. Cryst. Solids. 355 (2009) 475–480.

[30] L. Stoch, M. Sroda, Infrared spectroscopy in the investigation of oxide glasses structure, J. Mol. Struct. 512 (1999) 77–84.

[31] M. Taherian, R. Rojaee, M. Fathi, M. Tamizifar, Effect of different sol–gel synthesis processes on microstructural and morphological characteristics of hydroxyapatite–bioactive glass composite nanopowders, J. Adv. Ceram. 3 (2014)

207–214.

[32] A. a Ignatius, M. Ohnmacht, L.E. Claes, J. Kreidler, F. Palm, A Composite Polymer / Tricalcium Phosphate Membrane for Guided Bone Regeneration in Maxillofacial Surgery, J. Biomed. Mater. Res. 58 (2001) 564–569.

[33] A. Ślósarczyk, Z. Paszkiewicz, C. Paluszkiewicz, FTIR and XRD evaluation of carbonated hydroxyapatite powders synthesized by wet methods, J. Mol. Struct. 744–747 (2005) 657–661.

[34] G. Lefèvre, T. Preo, J. Lützenkirchen, Attenuated Total Reflection – Infrared Spectroscopy Applied to the Study of Mineral – Aqueous Electrolyte Solution Interfaces : A General Overview and a Case Study, in: P.T. Theophile (Ed.), Infrared Spectrosc. Sci. Eng. Technol., In Tech, 2012: pp. 97–122.

[35] A. Beganskiene, V. Sirutkaitis, M. Kurtinaitiene, R. Juskenas, A. Kareiva, FTIR, TEM and NMR Iinvestigations of Stöber Silica Nanoparticles, Mater. Sci. 10 (2004) 287–290.

[36] C. Piccirillo, R.C. Pullar, E. Costa, A. Santos–Silva, M.M.E. Pintado, P.M.L. Castro, Hydroxyapatite–based materials of marine origin: A bioactivity and sintering study, Mater. Sci. Eng. C. 51 (2015) 309–315.

[37] E. Landi, G. Celotti, G. Logroscino, A. Tampieri, Carbonated hydroxyapatite as bone substitute, J. Eur. Ceram. Soc. 23 (2003) 2931–2937.

[38] R.F.S. Lenza, W.L. Vasconcelos, Structural evolution of silica sols modified with formamide, Mater. Res. 4 (2001) 175–179.

[39] R.F.S. Lenza, W.L. Vasconcelos, Preparation of silica by sol–gel method using formamide, Mater. Res. 4 (2001) 189–194.

[40] D. Scarano, A. Zecchina, S. Bordiga, F. Geobaldo, G. Spoto, G. Petrini, et al., Fourier–transform infrared and Raman spectra of pure and Al–, B–, Ti–and Fe–substituted silicalites: stretching–mode region, J. Chem. Soc. Faraday Trans. 89 (1993) 4123–4130.

[41] T. Kamiya, K., Oka, A., Nasu, H., Hashimoto, Comparative study of structure of silica gels from different sources, J. Sol–Gel Sci. Technol. 19 (2000) 495–499.

[42] I. Notingher, J.R. Jones, S. Verrier, I. Bisson, P. Embanga, P. Edwards, et al., Application of FTIR and Raman Spectroscopy to Characterisation of Bioactive Materials and Living Cells, Spectrosc. Int. J. 17 (2003) 275–288.

[43] O. Peitl, E.D. Zanotto, L.L. Hench, Highly bioactive P2O5–Na2O–CaO–SiO2 glass–ceramics, J. Non. Cryst. Solids. 292 (2000) 115–126.

Chapter 4

The present chapter was published on:
Journal of Biomedical Matrials Research: Part A;
Volume 106, Issue 2,
16 Sebetember 2017,
Pages 510–520.
Doi: 10.1002/jbm.a.36239

Synthesis and bioactivity assessment of high silica content quaternary glasses with Ca:P ratios of 1.5 and 1.67, made by a rapid sol–gel process

Basam A. E. Ben–Arfa, Hugo R. Fernandes, Isabel M. Miranda Salvado*, José M. F. Ferreira and Robert C. Pullar*

Department of Materials and Ceramic Engineering / CICECO – Aveiro Institute of Materials, University of Aveiro, 3810–193 Aveiro, Portugal

*To whom correspondence should be addressed: isabelmsalvado@ua.pt, rpullar@ua.pt

Keywords: Glass; Glass–ceramics; Crystallisation; Bioactivity; Hydroxyapatite

Abstract

Sol–gel glasses in quaternary silica–sodium–calcium–phosphorous systems have been synthesized using a rotary evaporator for rapid drying without ageing. This novel fast drying method drastically decreases the total drying and ageing time from several weeks to only 1 hour, thus overcoming a serious drawback in sol–gel preparation procedures for bioglasses. This work investigates the bioactivity behavior of two glasses synthesized by this fast method, with Ca:P ratios of 1.5, and 1.67. X–ray diffraction (XRD), Inductive coupled plasma, Fourier–transform infrared, and Raman spectroscopy were used to confirm the bioactivity of the synthesized powders. MAS–NMR was also used to assess the degree of silica polymerization. The composition with higher Ca:P = 1.67 ratio showed better bioactivity in comparison to the one with Ca:P = 1.5, which exhibited little bioresponse with up to 4 weeks of immersion in SBF (simulated body fluid). It was also found that an orbital agitation rate of 120 rpm favors the interfacial bio–mineralization reactions, promoting the formation of a crystalline hydroxyapatite (HAp) layer at the surface of the (Ca:P = 1.67) composition after 2 weeks immersion in SBF.

1. Introduction

The importance of glass is demonstrated by its use in many aspects of human life, for instance buildings, transport, house–hold items and appliances, as well as in many industries and advanced technologies **[1]**. Medical, biotechnology, life sciences, and optical technologies are all important applications of glasses, and glasses were introduced as a biomaterial after the discovery of bioactive glass by Hench **[2]**. Since then, tremendous progress has been made using different compositions **[3–6]**, or by using various dopant ions **[7,8]**. Different preparation techniques have been used to synthesis glass **[9]**, but melt quenching and sol–gel are the most common techniques to synthesize glass for tissue engineering **[10]**. Although melt quenching is probably the most commonly used method to synthesize glass, sol–gel is considered another important route as it can eliminate the problem of needing a high melting temperature for glass synthesis, offering glass products at low temperatures with high homogeneity **[11]**.

Yan and co–workers **[12]** prepared bioactive glass by sol–gel in the three–component SiO_2–CaO–$P2O_5$ (Si–Ca–P) system within the range of (100–x–y)SiO_2–xCaO–yP_2O_5 molar compositions. The best in vitro bioactivity was found for the 80SiO_2–15CaO–5P_2O_5 composition. Saiz et al. **[13]** prepared silicate glass with different silica contents up to (67.7 wt. %), in addition to Na_2O, K_2O, CaO, MgO, and P_2O_5 (Si–Na–K–Ca– Mg–P), with (56.5–67.7)SiO_2–(8.3–11)Na_2O–(2.2–3)K_2O–(10.1–15)CaO– (5.7–8.5)MgO, and P_2O_5 kept fixed at 6 wt%. They observed good mechanical properties, and a low rate of bioactivity because of the high silica content. Peitl et al. **[14]** concluded that the tendency of glasses in the (Si–Na–Ca–P) system to crystallize decreased with decreasing P_2O_5 content, therefore enhancing bioactivity. Pereira et al. **[15]** synthesized silica glass compositions in a three component (Si–Ca–P) system and concluded that the compositions with higher silica contents [(80–x)SiO_2–x CaO–4P_2O_5] exhibited better bioactivity.

The low solubility of hydroxyapatite (HAp, $Ca_{10}(PO_4)_6$ $(OH)_2$) under physiological conditions is well known, making its resorption rate in–vivo slower than would be desired for a resorbable bone graft material. In contrast, tricalcium phosphate (β–TCP, $Ca_3(PO_4)_2$) dissolves much faster under the same physiological conditions. This explains why temporary (resorbable) calcium phosphate based bone grafts commonly consist of biphasic calcium phosphates (HAp + β–TCP). Bioactivity depends on the solubility of the material

in simulated body fluid (SBF). β–TCP tends to gradually dissolve in SBF, but its low Ca:P ratio is less prone to lead to the precipitation/crystallization of HAp. As a trial to combine the advantages of the two phases, Cho et al. **[16]** synthesized biphasic calcium phosphates (HAp + β–TCP) with Ca:P mol ratios between 1.5 and 1.67. They concluded that the biphasic calcium phosphate exhibited better osteoconductivity than pure HAp. Yu et al. **[17]** synthesized bone cement by combining calcium phosphate and bioactive glass, and they reported improved injectability, prolonged setting times and enhanced mechanical properties over the calcium phosphate cement alone. Other researchers have explored the combined advantages of using bioactive glasses with calcium phosphate phases by synthesizing glass–calcium phosphate composites. For instance, Ning et al. **[18]**, studied silica–calcium–phosphate composites (20–80 wt % silica) and suggested that the silica–rich compositions were more bioactive than calcium phosphate ceramics alone, because of the incorporation of silica.

The aim of this work is to synthesize bioglass powders in a four–component system (Si–Na–Ca–P) by a novel rapid sol–gel method and test their bioactivity. The authors have been investigating the rapid sol–gel synthesis of HAp using approaches such as the Taguchi experimental design method **[19]**, and have published a highly innovative technique which can produce HAp powders 50–200 times quicker than other reported sol–gel techniques, avoiding the lengthy ageing and drying processes usually required **[20]**. These powders were produced by drying the precursor sol for only 1 h on a rotary evaporator, and produced HAp materials virtually physically/structurally identical to, if not slightly better than, those produced by conventional routes. Recently they have also published this rapid approach using a rotary evaporator to dry the sol for the first time to an amorphous bioglass precursor gel in only 1 hour **[21]**, 100 times quicker than the standard long aging and drying times required to avoid crystallization in the glass product. The advantages of this process, and comparison with many reported conventionally dried sol–gel bioglasses, were discussed in this publication **[21]**. In this article we now compare for the first time different glass compositions made by this method, and examine their bioactivity and ability to promote the formation of HAp in SBF. Compositions with high silica content and Ca:P ratios of 1.67 and 1.5 were selected, in an attempt to combine the benefits of silica mentioned in the literature with the stoichiometric Ca/P ratios corresponding to pure HAp (Ca:P = 1.67) and β–TCP (Ca:P = 1.5). The selected high silica content (76 mol %) was intended for high

mechanical strength, and for the important role silica plays in bone formation, acting as a primary nucleation center for apatite formation **[22]**. The content of phosphate in the designed glasses was kept intentionally low (6 mol %), as its role in the glass is to aid the nucleation of calcium phosphates **[23]**. The presence of NaO_2 in the glass compositions was to enhance the degradation rate **[24]** and the apatite–forming ability in vitro **[25]**.

2. Materials and methods

2.1. Glass synthesis

The two glass samples were synthesized using the sol–gel method. Tetraethyl orthosilicate (TEOS, $C_8H_{20}O_4Si$, 98%), calcium acetate monohydrate [$Ca(CH_3CO_2)_2$ H_2O, 99%] and sodium acetate ($C_2H_3NaO_2$, 99%) were used as precursors for silica, calcium oxide, and sodium oxide, respectively, all three precursors being supplied from Sigma–Aldrich. Ortho–phosphoric acid (H_3PO_4, 85%) supplied from VWR was used as the precursor for phosphorus. Concentrated HNO_3 (65%, Sigma–Aldrich) was used as a catalyst, and deionised water as the solvent.

The selected compositions are within the four–component (SiO_2–CaO–Na_2O–P_2O_5) system. This was prepared with a stoichiometry of 76Si–10Ca–8Na–6P (in mol %) with a calcium–phosphorous molar ratio set at Ca:P = 1.67, hereafter designated as 1.67, and 76Si–9Ca–9Na–6P stoichiometry, with a calcium–phosphorous molar ratio set at Ca:P = 1.5, here after designated as 1.5 **Table 4.1**.

Table 4.1: Sample designation

Sample	Composition (mol%)	Ratio of ions
1.5	$76SiO_2 – 4.5Na_2O – 9CaO – 3P_2O_5$	76Ca:9Na:9Ca:6P
1.67	$76SiO_2 – 4Na_2O – 10CaO – 3P_2O_5$	76Ca:8Na:10Ca:6P

Sodium acetate was added to a solution of 0.1M nitric acid in deionised water in a glass beaker, in order to have a silica: water molar ratio of 1:10 to obtain a clear sol. Calcium, phosphorus, and silica precursors were then added in this order, one after the other.

Each subsequent precursor was added only after a clear solution/sol was obtained, ensuring complete dissolution of the previously added precursors. After adding the last precursor, the sol was stirred for 1 h as shown in the flow chart diagram in **Fig. 4.1**. The clear sol produced was then rapidly dried using a rotary evaporator (Buchi 210 Rotavapor with V–850 vacuum controller and V–700 diaphragm vacuum pump), in a 500 mL pear–shaped flask while rotating in a water bath at 550 ºC and under a negative pressure of 50 mbar for 1 h. All dried gels were stabilized by heating at 550 ºC for 1 h in air. The heating rate was 1 ºC min^{-1} up to 300 ºC, and then 10 ºC min^{-1} up to 550 ºC, with natural cooling. The heat treated powders were ground using a mortar and pestle, sieved through a 40–63 µm mesh and then used for all the characterization techniques.

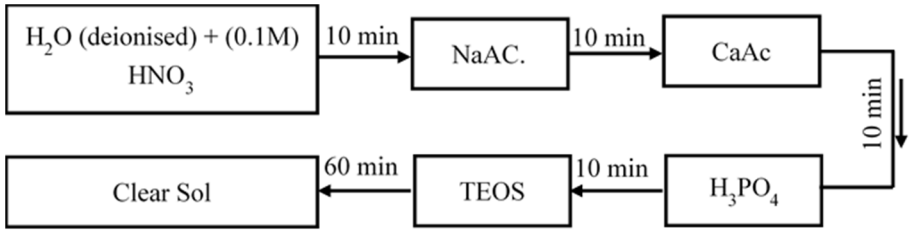

Fig. 4.1: Flow chart scheme of the sol gel synthesis

2.2. Glass Characterization

The morphology of the stabilized glass particles coated with carbon was observed by scanning electron microscope (SEM, SU–70, Hitachi, Japan).

The crystalline phase analysis of the samples before and after immersion in SBF was determined by X–ray diffraction (XRD, PANalytical XPERT–PRO Diffractometer system), using Cu Kα radiation (Kα = 1.54059 Å) with 2Θ varying from 6º to 70º in steps of 0.026 s^{-1}. The diffraction patterns were compared with JCPDS standards.

The 29Si MAS–NMR spectra were measured to investigate the silica environments and degree of silica polymerization of the stabilized glass samples, on an ASX 400 spectrometer (Bruker, Germany) operating at 79.52 MHz (9.4 T), using a 7 mm probe at a spinning rate of 5 kHz. The pulse length was 2 µs with 60 s delay time. Kaolinite was used as a chemical shift reference. ^{1}H MAS–NMR spectra were also measured. The ^{1}H, and ^{29}Si MAS–NMR spectra were deconvoluted using dimFit software.

Infrared transmittance spectra of the glasses, before and after immersion in SBF, were obtained using a Fourier Transform Infrared Spectrometer (FTIR, Tensor 27, Brucker, Germany) in the range of 350–4000 cm^{-1}, with 128 Scans and 4 cm^{-1} resolution. The pellets were prepared by pressing a mixture of KBr and glass powder with ratio of 150:1 of KBr: glass by weight.

The *in vitro* bioactivity in SBF was assessed by immersion of 58.5 and 59.2 mg of glass powders from samples 1.5 and 1.67, respectively, in 50 mL of SBF solution at 37 ºC following a unified approach recommended elsewhere **[26]**. The ionic concentrations of the SBF (Na^+ = 142.0, K^+ = 5.0, Ca^{2+} = 2.5, Mg^{2+} = 1.5, CI^- = 125.0, HPO_4^{2-} = 1.0, HCO_3^- = 27.0 and SO_4^{2-} = 0.5 mmol L^{-1}) are virtually equivalent to those of human plasma **[27]**. The mixtures were immediately sealed in plastic flasks and placed in an incubator at 37 ± 0.5 ºC on an orbital shaker. Two sets of tests were carried out, with the shaker using agitation of 60 or 120 rpm. The sampling took place for eight different times: (4, 8, 24, 72 h, 1, 2, 3, and 4 weeks) **[28]**. At the end of each time period, a sample was removed from the incubator and the solids were collected by centrifuging the mixture at 10,000 rpm under vacuum for 30 min, using a Beckman model LB–70M ultracentrifuge. The pH of the separated solution was measured directly, while the separated particles were washed with deionised water and subsequently with acetone to terminate the reaction, and after separation for the second time, dried in an oven overnight at 37 ºC. The experiments were performed in triplicate in order to ensure the accuracy of results. The apatite–forming ability of the glass powders was followed by XRD, FTIR, Inductively coupled plasma (ICP), and SEM–EDS analysis.

3. Results

3.1. MAS–NMR analysis of stabilized powders heat–treated at 550 ºC

Fig. 4.2 shows the ^1H MAS NMR spectra of the sol–gel derived glass stabilized at 550 ºC. The small peak at the chemical shift of 3.95–6 ppm seen in both samples can be attributed to the presence of H_2O on the glass surface **[29]**. The peak at 5.25–5.42 ppm can be attributed to molecular H_2 of silica glasses, and the broadening of the peak in sample 1.5 is a measure of a stronger interaction between the hydrogen species **[30]**. The highly intense peak around 2.11–12 ppm for both samples is assigned to isolated (nonhydrogen–bonded) OH groups

[30]. The peak at 1.06–7 ppm could also be related to the water content in the glass **[31]**, with a higher quantity in 1.67.

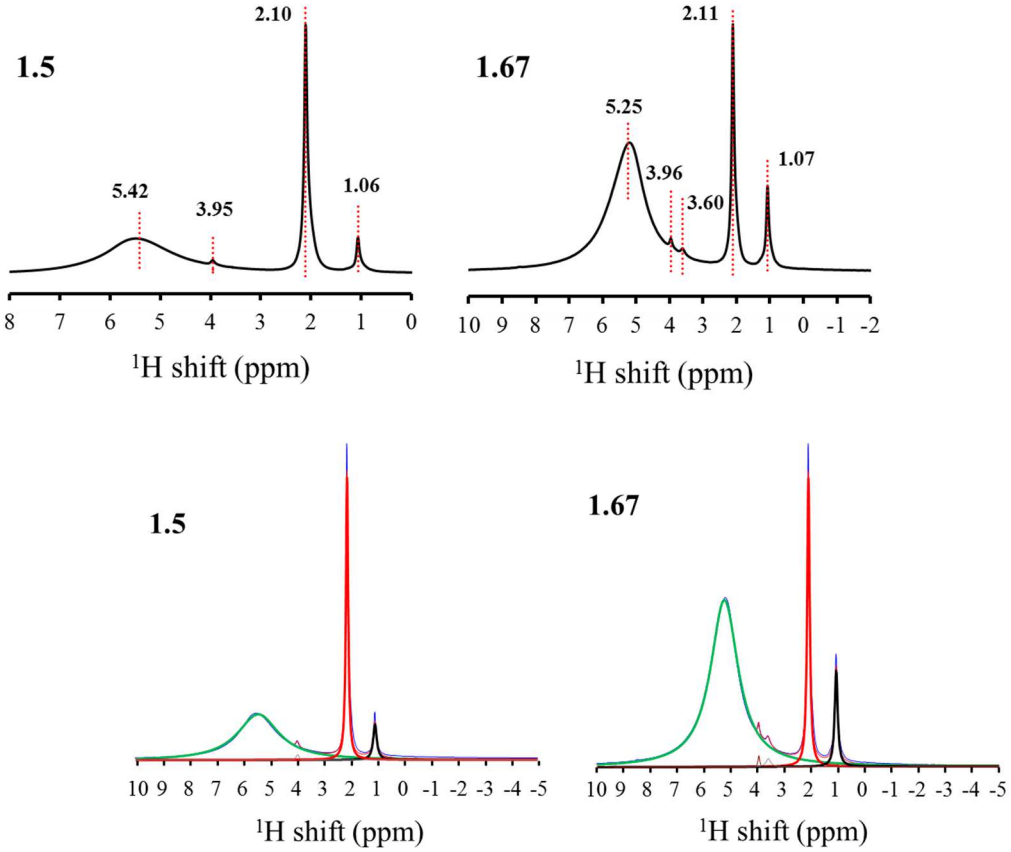

Fig. 4.2: ^{1}H–NMR spectra for 1.50, and 1.67 stabilised glass powders.

Fig. 4.3 shows the ^{29}Si MAS NMR spectra of the sol–gel derived glass stabilized at 550 ºC. The deconvoluted proportions of the ^{29}Si MAS NMR spectra enabled identification of Q^n species, where n denotes the number of oxygens bridging to silica, and Q^n can be 0, 1, 2, 3, or 4. The degree of condensation, D_c, can be calculated using the below equation **[32]**. Calculated values are presented in **Table 4.2**:

$$D_c = \frac{1\times Q^1 + 2\times Q^2 + 3\times Q^3 + 4\times Q^4}{4} \times 100\% \qquad (4.1)$$

The chemical shifts at 101–2 ppm were assigned to Q^3 species for 1.5 and 1.67, respectively, while Q^4 species were observed around 111 ppm for the two glasses. Both glasses have a large proportion of Q^4 (>67%) and a lower amount of Q^3 species, with Dc values of 93.8 and 91.8, respectively, which translate to a calculated network connectivity (N_c) of 3.75 for 1.5, and 3.67 for 1.67. These results are shown in **Table 4.2**.

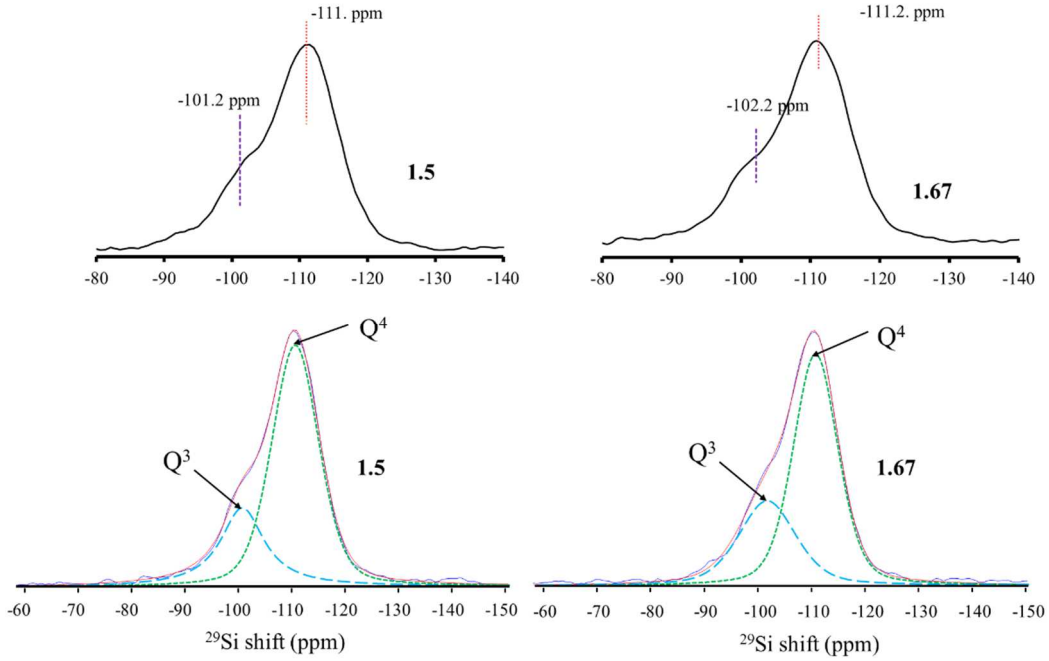

Fig. 4.3: ^{29}Si NMR spectra for 1.50, and 1.67 stabilised glass powders.

Table 4.2: Q^n (Si) distribution for devitrified glasses **1.5**, and **1.67** obtained by NMR deconvolution

Glass	Q^n				D_c (%)	N_c Via ^{29}Si NMR
	Q^3		Q^4			
	Peak position (ppm)	% Integral	Peak position (ppm)	% Integral		
1.5	–101.2	24.57	–111	75.42	93.8	3.75
1.67	–102.17	32.67	–111.2	67.32	91.82	3.67

The small proportions of modifiers in these two samples result in low degrees of silica network rupture. The sample 1.67 having a slightly lower N_c value is likely to be more easily

mineralized upon immersion in SBF in comparison to the sample 1.5, as will be confirmed in the following sections.

3.2. X–ray diffraction

Fig. 4.4 shows the X–ray diffraction (XRD) patterns for both samples, before and after immersion in SBF, and at orbital agitation rates of 60 and 120 rpm.

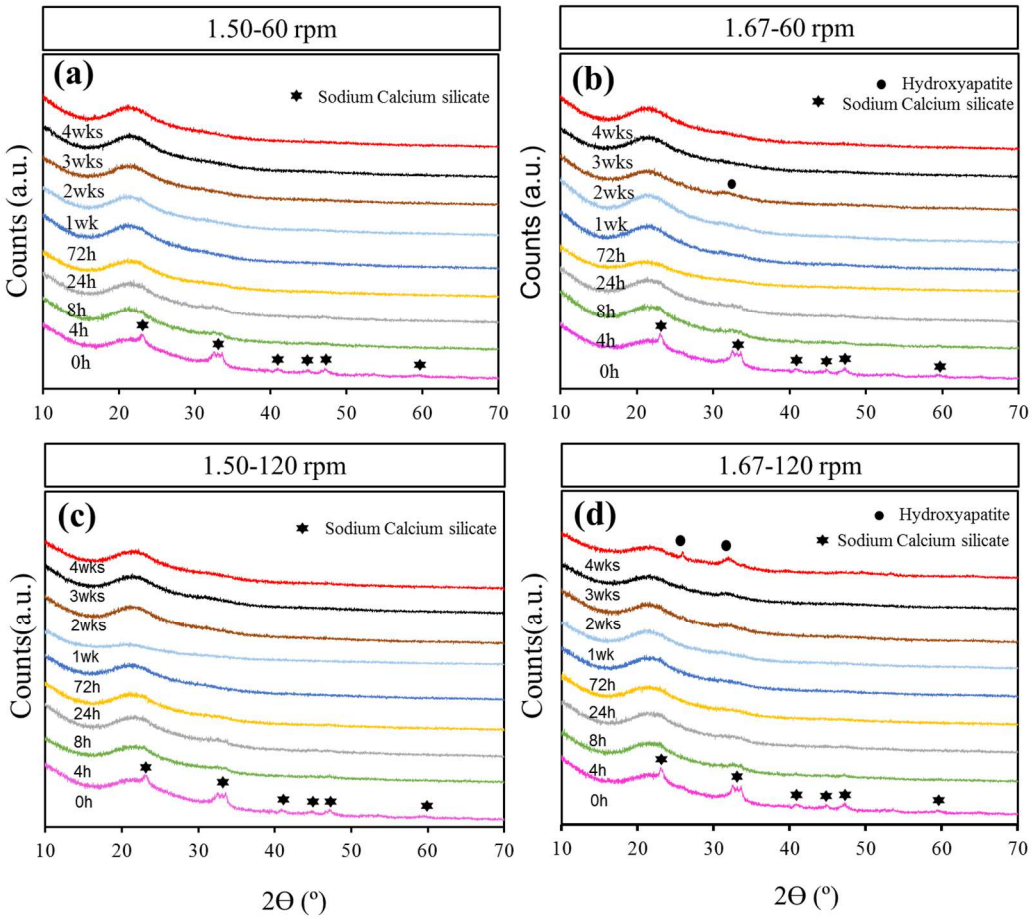

Fig. 4.4: show x–ray difractogram for 1.50, and 1.67 glass powder at 60 rpm (a,b), and 120 rpm (c,d) before and after SBF immersion.

The stabilized glasses have some traces of crystalline sodium calcium silicate ($CaNa_4O_9Si_3$) as the sole crystallized phase (PDF card #00–012–0670). It can be seen at low agitation speed of 60 rpm **Fig. 4.4(a, b)**, both samples 1.5 and 1.67 did not show any evidence of apatite or calcium phosphate formation, indicating a lack of bioactivity. The mineralization

extent was somewhat improved at the higher agitation speed of 120 rpm and weak signals of hydroxyapatite (PDF card # 01–080–3956) deposited onto the surface of 1.67 sample started to be noticed after 2 weeks. The intensity of XRD peaks of HAp noticeably increased with further extending to 4 weeks the immersion period in SBF **Fig. 4.4(d)**.

It should be noted that no other calcium phosphate phases were detected in these samples, particularly in the sample 1.5 that has the same Ca:P ratio as stoichiometric β–TCP. This demonstrates that the development of crystalline phases from these sol–gel glasses follows a very different path in comparison to the calcium phosphate ceramics.

3.3. FTIR analysis of glass powder

The FTIR spectra of the investigated glasses are presented in **Fig. 4.5**. The IR spectra of sol–gel glasses are typically dominated by a broad band between 1000 and 1250 cm^{-1}, centred at 1090 cm^{-1}, which represents the transverse optical (TO_1) Si–O–Si stretching mode. Moreover, a shoulder at 1220 cm^{-1} represents the Si–O–Si (TO_2) stretching mode **[33]**, as a result of the introduction of P_2O_5 to silica glass **[34]**. The shoulder observed at 1020 cm^{-1} is a common feature of sol–gel derived silicate glasses and can be attributed to Si–O–NBO (NBO = nonbridging oxygen). Its broadness and low intensity may be a result of the relatively small network modifier content present in the samples, therefore favouring the extent of glass polymerization with low amounts of NBOs. The broad band at 790 cm^{-1} can be identified as the bending vibration of Si–O–Si because of the ring structures in the glass matrix **[35,36]**, and this band could also arise from Si–O–P bonds **[34]**. The small band at 960 cm^{-1} is assigned to surface silanol groups **[37]**. The appearance of the twin peaks at 565 cm^{-1} and 601 cm^{-1} for the two glasses before SBF immersion can be attributed to the phosphate group PO_4^{3-}, as the compositions include 6 mol% P. There is a well–known intense phosphate band from HAp which also occurs at around 1090 cm^{-1}, which overlaps with the silicate bands noted above. Previous work by the authors on sol–gel phosphate–containing biolgasses also identified a significant shoulder around 1050 cm^{-1}, attributed to terminal PO_3 end groups, and this may also contribute to the significant broadening of this peak **[7]**. The small band at ~870 cm^{-1} is attributed to a carbonate substitution at a phosphate site **[32,38]**. These two peaks at around 560 and 600 cm^{-1} tend to disappear after immersing the samples in SBF for short time periods up to one week.

However, they clearly begin to appear again after 2 weeks in the case of sample 1.67 under agitation of 120 rpm and gain in intensity as immersing time increases **Fig. 4.5(d)**. This initial disappearance is as a result of leaching phosphate groups from the glass matrix in all samples. Its re–appearance after 2 weeks in the sample 1.67 kept under stirring at 120 rpm, coinciding with the crystallization of HAp **Fig. 4.4(d)** is evidence of the mineralization process.

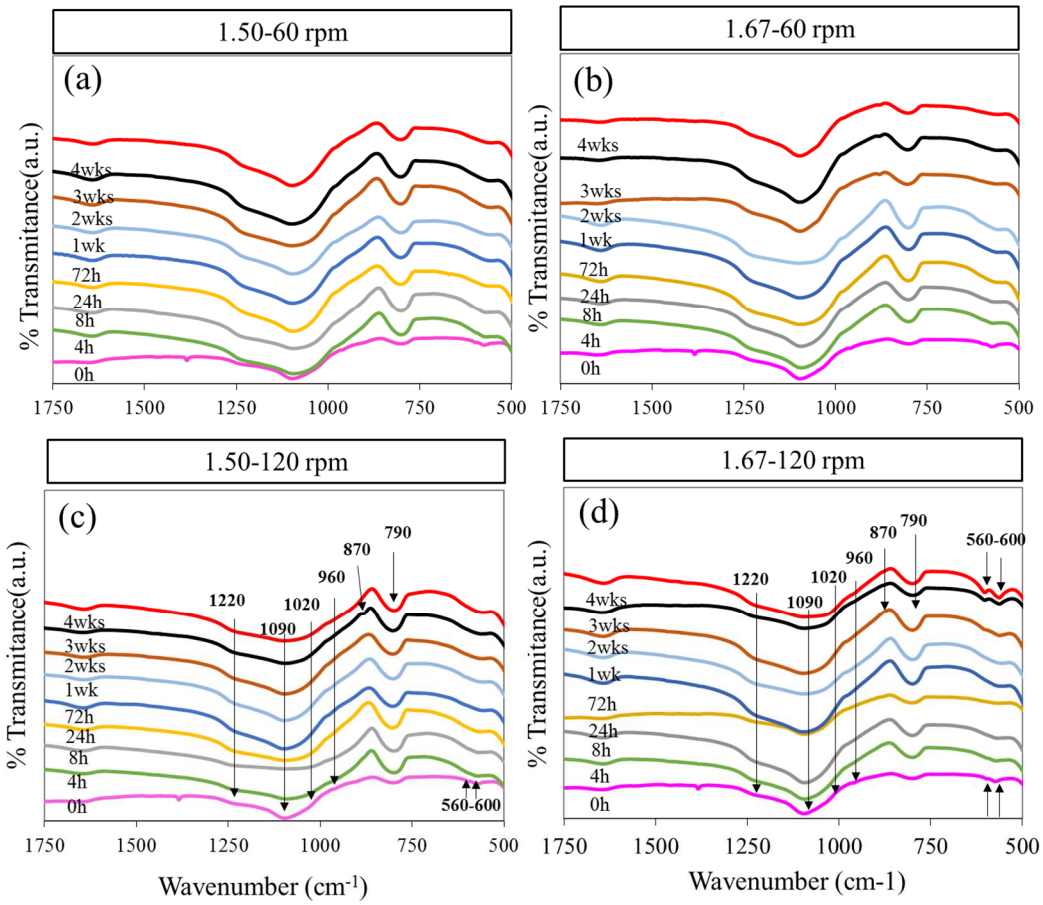

Fig. 4.5: FTIR spectra for 1.50, and 1.67 glass powder before and after SBF immersion in SBF under stirring at 60 rpm (a,b), and at 120 rpm (c,d).

Other works in rapid glass preparation routes, such as those by Yan et al. (a gel calcined at 800 ºC) **[12]** and Peitl et al. (from a glass melt route) **[14]** indicate the appearance of the phosphate peaks around 560–600 cm^{-1} in the FTIR spectra after only 24 and 20 h immersion in the SBF, respectively, as opposed to the 2 weeks needed for 1.67 agitated at 120 rpm. However, they do not note an initial presence of these peaks, which we see before

immersion, and which we then see disappear as part of the slower dissolution–recrystallization process observed here. Similarly, with Raman spectroscopy we observe the presence of phosphate groups throughout, and evidence of a dissolution/recrystallization process over time (see Raman analysis of glass powder section). Furthermore, although we observe direct evidence of crystalline HAp/calcium phosphate formation via XRD and SEM evidence after 2 weeks, in these previous sol–gel bioactivity reports, any crystallinity is inferred merely from some IR peaks and leaching of ions into the SBF, with no actual XRD or SEM evidence of crystalline material formation in such a short time span. Therefore, although it initially seems that HAp formation is considerably slower in our rapidly produced sol–gel materials, this may be misleading, as the levels of Ca and P ions measured in the solution are Similar, or superior, to those seen in Ref. 12 (see Inductively coupled plasma (ICP) and pH section below), and we show direct evidence of crystalline HAp growth after 2 weeks in SBF, unlike these other papers.

3.4. Raman analysis of glass powder

Raman is a very powerful tool and can be used to monitor Si–O–Si vibrational modes, and probe (Si–NBO) groups of silicate glasses **[39]**. It is able to detect the changes in glass microstructure that may happen as a result of adding different modifiers, and is, therefore, useful to assess the bioactivity evolution in the early stages of in vitro testing and tuning glass design and processing **[39]**. The Raman spectra of samples 1.5 and 1.67 immersed in SBF and kept under agitation at 60 and 120 rpm are shown in **Fig. 4.6**.

The presence of a sharp peak with great intensity at 960 cm^{-1} in the as–produced samples is attributed to the presence of PO_4^{3-} in the glass composition, and the small shoulder at about 920 cm^{-1} is attributed to nonbridging silicon bonds because of a disruption of the silica net–work **[33,39,40]**. The very weak peak around 750–800 cm^{-1} is attributed to a bond bending vibration **[40]**, and the bands between 500 and 620 cm^{-1} are assigned to a rocking vibration of the Si–O–Si group **[39]**. Peaks in this region can also be attributed to a very small addition of Na_2O **[41]**. The bands for Q^4 tectosilicate species, the most abundant silica species in the two samples, are present at around 430, 1060, and 1190 cm^{-1} **[42]**, although the latter two are rather weak and typical of amorphous silica–rich matrices such as these. The intensity of the PO_4^{3-} peak at 960 cm^{-1} tends to initially decrease with immersion time

in SBF because of demineralization of phosphorus, but following different evolution in the two samples, and depending on the stirring speed. While a steady decrease is observed along the entire period of 4 weeks for the samples stirred at 60 rpm, a recovery is clearly observed after 2 weeks for 1.67 kept under agitation at 120 rpm, and a stabiliziation of this peak (it does not get any smaller) after 2 weeks for 1.5. This indicates the gradual formation of new phosphate groups on the surface of the glass particles, especially in sample 1.67, as an initially amorphous HAp layer then tends to crystallize, as can be observed for 1.67 at 120 rpm **Fig. 4.6(b) [43]**.

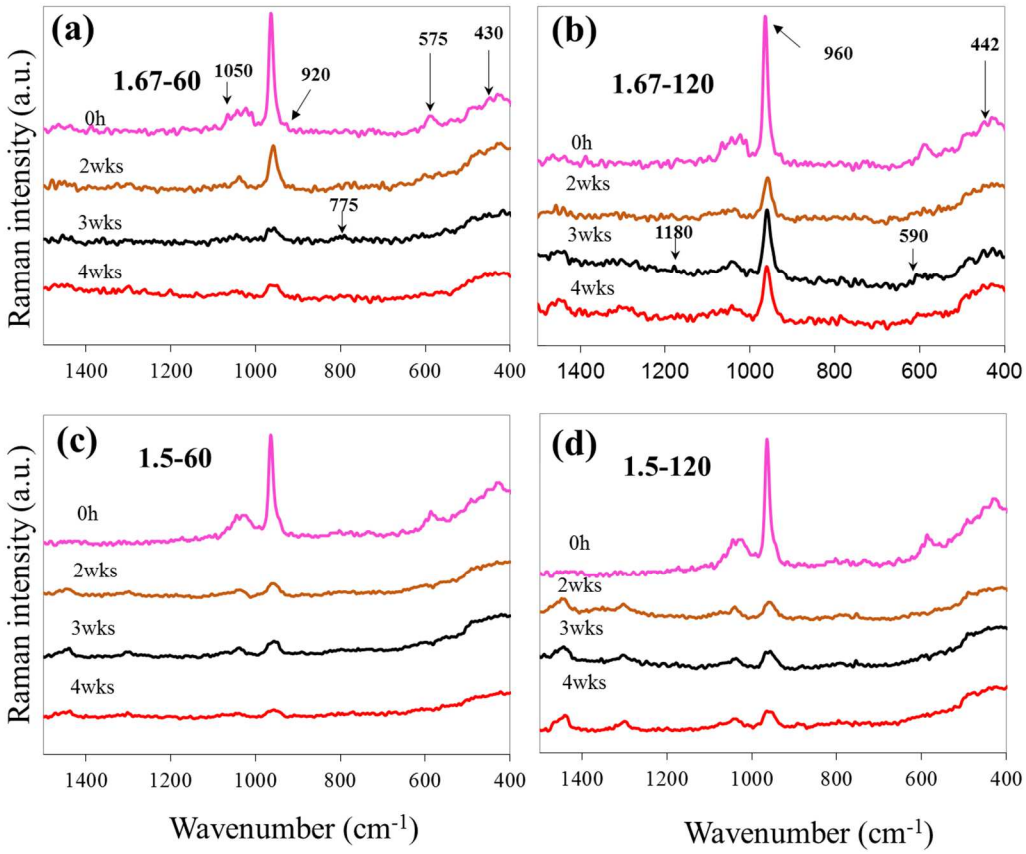

Fig. 4.6: Raman spectra for 1.67 (a–b) and 1.5 (c–d) glass powders before and after immersion in SBF, under stirring at 60 rpm (a & c) and at 120 rpm (b & d) for different periods of time between 2 and 4 weeks.

These results demonstrate that the kinetics of leaching and mineralization processes are faster when the sample is agitated at the higher speed. In fact, the peak at 960 cm^{-1} is the major peak seen in Raman spectra of HAp, and this result is in good agreement with the XRD and FTIR results shown previously.

Other minor peaks observed in Raman spectra displayed in **Fig. 4.6(b, d)** around 1050 cm^{-1}, and the peak at 590 cm^{-1} observed only in **Fig. 4.6(b)**, can also be ascribed to phosphate groups in HAp **[44]**. The bands at 1000–1050 cm^{-1} are attributed to Si–O– stretching in Q^3 silica polymerization species **[45]**. The gradual disappearance of these peaks along the immersion period in SBF could be attributed to the on–going hydrolysis and demineralization of the Si–O bonds. Similarly, the disappearance of the peak at 575 cm^{-1} can be attributed to the dissolution of NaO_2.

3.5. Inductively coupled plasma (ICP) and pH

The changes in pH and in Si, Ca, and P ion concentrations measured in the SBF solution after soaking the samples 1.50 and 1.67 (both agitated at 120 rpm, the optimum for HAp formation) for up to 4 weeks, are presented in **Fig. 4.7**. The pH values show an initial fast increase **Fig. 4.7(a)** that can be attributed to the rapid leaching of alkaline (Na) and alkaline earth (Ca) ions from the surface of glass particles, followed by a small reversing trend and a recover to finally stabilize within the range of pH 7.5–7.6. These mean that the overall pH changes were minor for both glasses (only around 4% after 4 weeks immersion). The Si concentrations in SBF increased greatly at the beginning of the soaking time for both samples, but then levelled off after the first week **Fig. 4.7(b)**. Similarly, Ca and P ionic concentrations exhibit almost the same initial trend, increasing greatly along the initial couple of days. However, after a peak at around 1 week for Ca **Fig.** 4.**7(c)** and 2 weeks for P **Fig. 4.7(d)**, the concentrations of these ions begin to slowly decrease again, indicating the precipitation of calcium phosphate species on the surface the glass for both samples. Although the loss of Ca and P ions from the SBF to form calcium phosphates is much greater for 1.67, the possibility of formation of an amorphous apatitic layer onto the surface of 1.5 glass particles cannot be excluded, although at a slower pace. What seems apparent is that because of the early shortage of phosphorus, the first deposits of HAp onto the surface of glass particles become gradually more Ca–deficient after 1 week. The continuous precipitation and recrystallization process of Ca–deficient HAp after 2 weeks leads to a gradual depletion in the SBF solution of the Ca and P building species that tend to equilibrium concentrations after 3 weeks **Fig. 4.7(d)**. These overall observations are in good agreement with the previous results obtained by FTIR, Raman, and XRD. The final

ratio of Ca:P observed by ICP in the SBF is almost exactly 1.67 (that of pure HAp) for 1.67, and a slightly lower ratio of 1.62 for 1.5. This compares well with results from sol–gel bioglasses prepared by standard slow ageing and drying processes, such as the ratio of 1.67 found for the 80% Si—15% Ca—5% P glass reported by Yan et al. **[12]**. The levels of calcium observed here after just a few hours (100–115 mg mL^{-1}) compared well with those of Peitl et al. **[14]** despite them having a much greater calcium content of 23–31 wt % CaO, and the phosphorous levels (60–70 mg mL^{-1}) are much higher than theirs, although they had similar phosphorous content (up to 6 wt % P_2O_5).

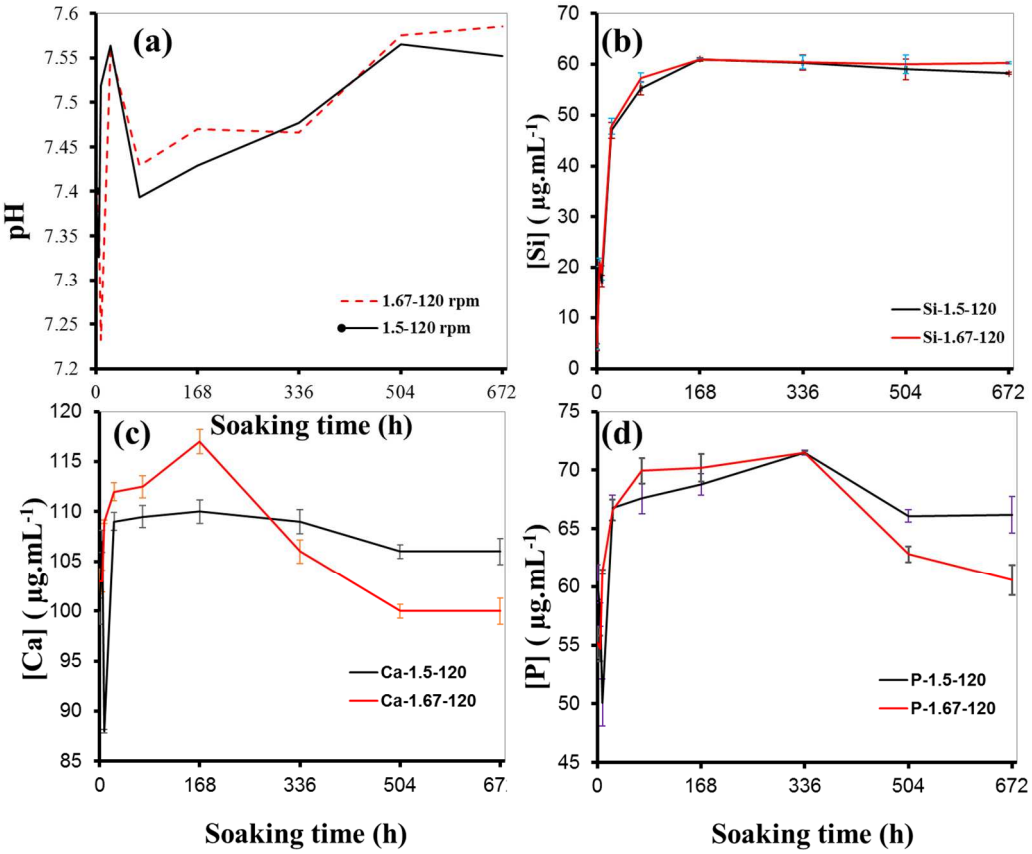

Fig. 4.7: Evolution of pH of SBF and of Si, Ca, and P contents leached out in SBF solution for the 1.50 and 1.67) glass powders along the immersion period of 4 weeks under stirring at 120 rpm.

3.6. Scanning electron microscopy (SEM) and energy dispersive spectroscopy (EDS)

The SEM micrographs of the thermally stabilized 1.50 and 1.67 glasses before and after immersion in SBF for different time periods are shown in **Fig. 4.8**. As can be seen, the particles of both glasses exhibit similar morphological features and sizes, showing large particles with adsorbed small clusters to their surfaces, which likely derive from the milling process, **Fig. 4.8** (0 h). These small clusters were apparently left behind upon immersion in SBF and after 4 h soaking, they do not appear. The surface of the particles seems relatively smooth and the formation of any calcium phosphate layer can hardly be inferred at this early stage. This is not surprising as this short period of time corresponds to the quick demineralization step with ionic species being leached out from the glass particles, as already shown in **Fig. 4.7(c, d)**. The demineralization process continued but at slower rate from 8 h to one week (not shown). Then, the calcium phosphate deposits gradually developed and appear clearly visible in the SEM micrographs gathered after 3 and 4 weeks, being particularly obvious in the case of the 1.67 glass sample. The calcium phosphate formations onto the surface of the 1.50 samples are much less evident. These microstructural observations are in good accordance with the results collected by using the other characterization techniques discussed above.

Although, as we noted above, many bioactivity tests for the growth of HAp in SBF in similar bioglasses do not actually present hard evidence of crystallization of HAp through XRD or SEM images, one of the authors has published an article previously on the crystallization and growth of HAp in SBF on sintered pellets of HAp derived from marine wastes **[46]**. These showed a clear growth of HAp between 3 and 7 days, much less than the 2–4 weeks required with these materials, although it also must be stressed that these were pure HAp ceramics, which were themselves highly crystalline after being sintered at 700 ºC. In comparison, our samples are mostly amorphous, any crystalline phase which does exist is a sodium calcium silicate, not HAp or a calcium phosphate, and the calcium and phosphorous together make >16 mol % of the silica–based bioglass. Therefore, it is not entirely surprising that the Ca/P dissolution and subsequent HAp crystallization process is considerably slower in these non–HAp bioglass materials.

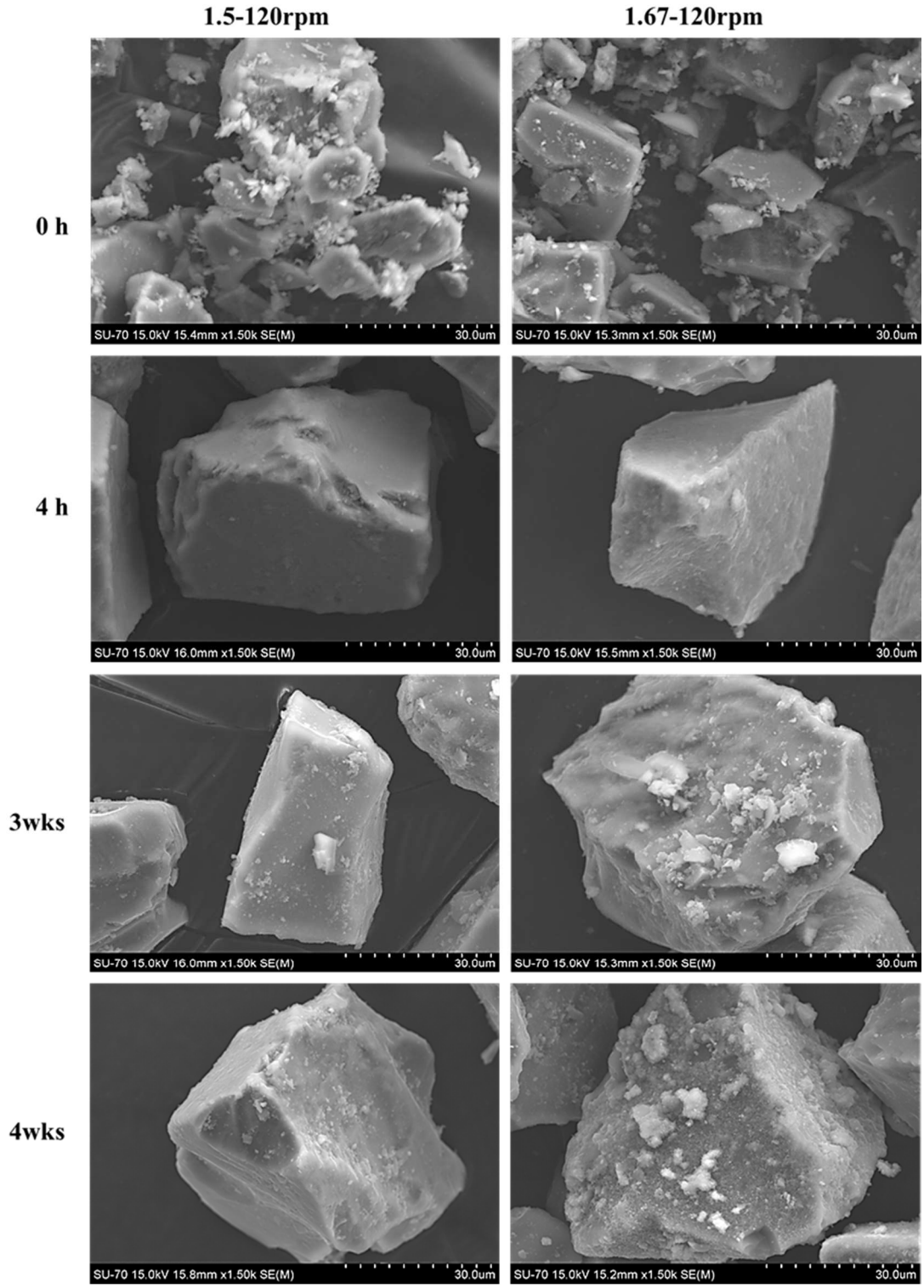

Fig. 4.8: SEM images for 1.50 and 1.67 glass powders before and after immersion in SBF for different time periods under stirring at 120 rpm.

4. Conclusions

Quaternary glass (Si–Na–Ca–P) powders of were successfully synthesized using a novel rapid sol–gel technique. Two samples, 1.50 and 1.67 (the numbers representing their Ca:P ratios), were produced, stabilized at 550 ºC, and then immersed in SBF to evaluate their bioactivity and biomineralization capabilities. The two samples showed similar microstructures, with a strong amorphous silica network (>67% Q^4), a high network connectivity (N_c 3.7), and the presence of phosphate groups and crystalline $CaNa_2Si_3O_9$. The speed of orbital agitation appeared to be crucial in accelerating the biomineralization process in SBF. The lower agitation speed (60 rpm) was ineffective in promoting the clear formation of calcium phosphate layer at the surface or both glass particles. However, when kept under agitation at 120 rpm, sample 1.67 exhibited bioactivity after two weeks of immersion, with precipitation of calcium phosphate deposits and the crystallization of HAp on the glass particle surfaces. We conclude from this work that bioactivity is affected by the content of modifiers in the glass network, and an increase in the content of modifiers in the glass matrix will likely lead to an increase in bioactivity. Direct evidence of crystalline HAp formation was observed in 1.67 after agitation at 120 rpm for 2 weeks or more in SBF.

Acknowledgments

This work was developed in the scope of the project CICECO– Aveiro Institute of Materials (Ref. FCT UID/CTM/50011/ 2013), financed by national funds through the FCT/MEC and when applicable co–financed by FEDER under the PT2020 Partnership Agreement.

References

[1] J. Savic, D. Djuric–Mijovic, V. Bogdanovic, Architectural glass: Types, performance and legislation, Facta Univ. – Ser. Archit. Civ. Eng. 11 (2013) 35–45.

[2] L.L. Hench, The story of Bioglass®, J. Mater. Sci. Mater. Med. 17 (2006) 967–978.

[3] G. Malavasi, L. Menabue, M.C. Menziani, A. Pedone, A.J. Salinas, M. Vallet–Regí, New insights into the bioactivity of SiO2–CaO and SiO2–CaO–P2O5 sol–gel glasses by molecular dynamics simulations, J. Sol–Gel Sci. Technol. 67 (2011) 208–219.

[4] X. Chen, X. Liao, Z. Huang, P. You, C. Chen, Y. Kang, et al., Synthesis and characterization of novel multiphase bioactive glass–ceramics in the CaO–MgO–SiO2 system, J. Biomed. Mater. Res. – Part B Appl. Biomater. 93 (2010) 194–202.

[5] Y. Ebisawa, T. Kokubo, O. K., T. Yamamuro, Bioactivity of CaO . Si02–based glasses: in vitro evaluation, J. Mater. Sci. Mater. Med. 1 (1990) 239–244.

[6] P. Sepulvda, J.R. Jones, L.L. Hench, Bioactive sol–gel foams for tissue repair, J. Biomed. Mater. Res. 59 (2002) 340–348.

[7] B.A.E. Ben–arfa, I.M.M. Salvado, J.M.F. Ferreira, R.C. Pullar, The Influence of Cu2+ and Mn2+ Ions on the Structure and Crystallization of Diopside –Calcium Pyrophosphate Bioglasses, Int. J. Appl. Glas. Sci. 354 (2016) 345–354.

[8] B.A.E. Ben–Arfa, I.M.M. Salvado, J.M.F. Ferreira, R.C. Pullar, The effect of functional ions (Y3+, F–, Ti4+) on the structure, sintering and crystallization of diopside–calcium pyrophosphate bioglasses, J. Non. Cryst. Solids. 443 (2016) 162–171.

[9] S.K. Sarkar, B.T. Lee, Synthesis of Bioactive Glass by Microwave Energy Irradiation and Its In–Vitro Biocompatibility, Bioceram. Dev. Appl. 1 (2011) 1–3.

[10] G. Kaur, G. Pickrell, N. Sriranganathan, V. Kumar, D. Homa, Review and the state of the art: Sol–gel and melt quenched bioactive glasses for tissue engineering, J. Biomed. Mater. Res. – Part B Appl. Biomater. 4803 (2015) 1248–1275.

[11] S. Sakka, Handbook of sol–gel science and technology (volume 1), Kluwer academic publishers, Osaka, 2005.

[12] X. Yan, X. Huang, C. Yu, H. Deng, Y. Wang, Z. Zhang, et al., The in–vitro bioactivity of mesoporous bioactive glasses, Biomaterials. 27 (2006) 3396–3403.

[13] E. Saiz, M. Goldman, J.. Gomez–Vega, A.. Tomsia, G.. Marshall, S.. Marshall, In vitro behavior of silicate glass coatings on Ti6Al4V, Biomaterials. 23 (2002) 3749–3756.

[14] O. Peitl, E.D. Zanotto, L.L. Hench, Highly bioactive P2O5–Na2O–CaO–SiO2 glass–ceramics, Non–Crystalline Solids. 292 (2001) 115–126.

[15] M.M. Pereira, A.E. Clark, L.L. Hench, Calcium Phosphate Formation on Sol Gel Derived Bioactive Glasses in Vitro, J Biomed Mater Res. 28 (1994) 693–698.

[16] J.S. Cho, C.–P. Chung, S.–H. Rhee, Bioactivity and Osteoconductivity of Biphasic Calcium Phosphates, Bioceram. Dev. Appl. 1 (2011) 1–3.

[17] L. Yu, Y. Li, K. Zhao, Y. Tang, Z. Cheng, J. Chen, et al., A Novel Injectable Calcium Phosphate Cement–Bioactive Glass Composite for Bone Regeneration, PLoS One. 8 (2013) e62570.

[18] C.Q. Ning, J. Mehta, A. El–Ghannam, Effects of silica on the bioactivity of calcium phosphate composites in vitro, J. Mater. Sci. Mater. Med. 16 (2005) 355–360.

[19] B.A.E.E. Ben–Arfa, I.M.M.M. Salvado, J.R. Frade, R.C. Pullar, Fast route for synthesis of stoichiometric hydroxyapatite by employing the Taguchi method, Mater. Des. 109 (2016) 547–555.

[20] B.A.E. Ben–Arfa, I.M.M. Salvado, J.M.F.J.M.F. Ferreira, R.C. Pullar, Novel route for rapid sol–gel synthesis of hydroxyapatite, avoiding ageing and using fast drying with a 50–fold to 200–fold reduction in process time, Mater. Sci. Eng. C. 70 (2017) 796–804.

[21] B.A.E. Ben–Arfa, I.M. Miranda Salvado, J.M.F. Ferreira, R.C. Pullar, A hundred times faster: Novel, rapid sol–gel synthesis of bio–glass nanopowders (Si–Na–Ca–P system, Ca:P = 1.67) without aging, Int. J. Appl. Glas. Sci. 8 (2017) 337–343.

[22] H.O. Ylanen, Bioactive glasses materials, properties and applications, woodhead publishing limited, Cambridge, 2011.

[23] A.N.I. Hench, Larry L.To, An introduction to bioceramics, second edi, Imperical College Press, London, 2013.

[24] A.P.J.C. Knowles, Investigation of silica–iron–phosphate glasses for tissue engineering, J. Mater. Sci. Mater. Med. 17 (2006) 937–944.

[25] S. Ni, R. Du, S. Ni, The Influence of Na and Ti on the In Vitro Degradation and Bioactivity in 58S Sol–Gel Bioactive Glass, Adv. Mater. Sci. Eng. 2012 (2012) 7.

[26] A.C. Popa, G.E. Stan, M.A. Husanu, I. Mercioniu, L.F. Santos, H.R. Fernandes, et al., Bioglass implant–coating interactions in synthetic physiological fluids with varying degrees of biomimicry, Int. J. Nanomedicine. 12 (2017) 683–707.

[27] A. Oyane, H.–M. Kim, T. Furuya, T. Kokubo, T. Miyazaki, T. Nakamura, Preparation and assessment of revised simulated body fluids, J Biomed Mater Res. 65 (2003) 188–195.

[28] A.L.B. Maçon, T.B. Kim, E.M. Valliant, K. Goetschius, R.K. Brow, D.E. Day, et al., A unified in vitro evaluation for apatite–forming ability of bioactive glasses and their variants, J. Mater. Sci. Mater. Med. 26 (2015) 1–10.

[29] J. Trébosc, J.W. Wiench, S. Huh, V.S.–Y. Lin, M. Pruski, Solid–state NMR study of MCM–41–type mesoporous silica nanoparticles., J. Am. Chem. Soc. 127 (2005) 3057–3068.

[30] Y. Zhou, Q. Zeng, Speciation of hydrogen in silica glass by 1 H MAS NMR, J. Non. Cryst. Solids. 355 (2009) 1212–1214.

[31] H. Eckert, J.P. Yesinowski, L.A. Silver, E.M. Stolper, Water in silicate glasses: quantitation and structural studies by proton solid echo and magic angle spinning NMR methods, J. Phys. Chem. 92 (1988) 2055–2064.

[32] G. Poologasundarampillai, D. Wang, S. Li, J. Nakamura, R. Bradley, P.D. Lee, et al., Cotton–wool–like bioactive glasses for bone regeneration, Acta Biomater. 10 (2014) 3733–3746.

[33] H. Aguiar, J. Serra, P. González, B. León, Structural study of sol–gel silicate glasses by IR and Raman spectroscopies, J. Non. Cryst. Solids. 355 (2009) 475–480.

[34] L. Stoch, M. Sroda, Infrared spectroscopy in the investigation of oxide glasses structure, J. Mol. Struct. 512 (1999) 77–84.

[35] M. Sitarz, M. Handke, W. Mozgawa, Calculations of silicooxygen ring vibration frequencies, Spectrochim. Acta – Part A Mol. Biomol. Spectrosc. 55 (1999) 2831–2837.

[36] C.J. Brinker, G.W. Sherer, Sol–Gel Science The physics and chemistry of sol–Gel processing, Academic Press, Inc., London, 1990.

[37] K. Kamiya, A.I. Oka, H. Nasu, T. Hashimoto, Comparative Study of Structure of Silica Gels from Different Sources, J. Sol–Gel Sci. Technol. 19 (2000) 495–499.

[38] A. a Ignatius, M. Ohnmacht, L.E. Claes, J. Kreidler, F. Palm, A Composite Polymer / Tricalcium Phosphate Membrane for Guided Bone Regeneration in Maxillofacial Surgery, J Biomed Mater Res. 58 (2001) 564–569.

[39] P. Gonzáles, J. Serra, S. Liste, S. Chiussi, B. León, M. Pérez–Amor, Raman spectroscopic study of bioactive silica based glasses, J. Non. Cryst. Solids. 320 (2003) 92–99.

[40] L. Marsich, L. Moimas, V. Sergo, C. Schmid, Raman spectroscopic study of bioactive silica–based glasses : The role of the alkali / alkali earth ratio on the Non–Bridging Oxygen / Bridging Oxygen (NBO / BO) ratio, Spectroscopy. 23 (2009) 227–232.

[41] P.F. McMillan, Structural Studies of Silicate Glasses and Melts–Applications and Limitations of Raman Spectroscopy, Am. Mineral. 69 (1984) 622–644.

[42] C.C. Lin, L.C. Huang, P. Shen, Na2CaSi2O6–P2O5 based bioactive glasses. Part 1: Elasticity and structure, J. Non. Cryst. Solids. 351 (2005) 3195–3203.

[43] D.C. Clupper, J.E. Gough, P.M. Embanga, I. Notingher, L.L. Hench, M.M. Hall, Bioactive evaluation of 45S5 bioactive glass fibres and preliminary study of human osteoblast attachement, J. Mater. Sci. Mater. Med. 15 (2004) 803–808.

[44] C.S. Ciobanu, F. Massuyeau, L.V. Constantin, D. Predoi, Structural and physical properties of antibacterial Ag–doped nano–hydroxyapatite synthesized at 100°C, Nanoscale Res. Lett. 6 (2011) 613.

[45] D.R. Neuville, L. Cormier, Structure of Na2O–CaO–Al2O3–SiO2 glasses using Raman spectroscopy, in: 70th Conf. Glas. Probl. Proc. Glas. Odyssey, Ohio, 2009: pp. 2–6.

[46] C. Piccirillo, R.C. Pullar, E. Costa, A. Santos–silva, M.M.E. Pintado, P.M.L. Castro, Hydroxyapatite–based materials of marine origin : A bioactivity and sintering study, Mater. Sci. Eng. C. 51 (2015) 309–315.

Chapter 5

The present chapter was submitted to:
Journal of the American Ceramic Society;
10 Sebtemper 2018,
ID is JACERS-42719

The role of calcium (source & content) on the in–vitro behaviour of sol–gel quaternary glass series

Basam A. E. Ben–Arfa [a], Ilaria E. Palamá [b], Isabel M. Miranda Salvado [a*], José M. F. Ferreira [a] and Robert C. Pullar [a*]

[a] *Department of Materials and Ceramic Engineering / CICECO – Aveiro Institute of Materials, University of Aveiro, 3810–193 Aveiro, Portugal*

[b] *CNR NANOTEC – Istituto di Nanotecnologia, Campus Ecotekne, Via Monteroni, 73100 Lecce, Italy*

*To whom correspondence should be addressed: isabelmsalvado@ua.pt, rpullar@ua.pt

Keywords: Bioactive glasses; biocompatibility; Ca/P ratio; high silica content; sol–gel derived glass; in–vitro MTT tests

Abstract

Five quaternary (Si–Ca–P–Na) glass compositions were successfully prepared through two distinct rapid sol–gel routes; one using acetate salt precursors (A) catalysed by nitric acid, and the other using nitrate salts (N) and citric acid as a catalyst. On a cationic basis, the Ca contents varied from 24–48 at% at the expenses of Si contents. Interestingly, besides a common amorphous structure, the as synthesized products also revealed the presence of small amounts of HAp, crystalline (A–glasses) or crystalline/amorphous (N–glasses), which is likely to foster bioactivity. The ability to form a surface layer of HAp was also initially enhanced by increasing Ca contents, but the highest levels of calcium favoured the formation of calcite upon immersion in simulated body fluid (SBF). The chemical surface modifications could be early noticed after only 4 h, being more evident in the case of N–glasses that exposed higher specific surface areas to the SBF solution in comparison to A–glasses. In contrast, the in–vitro biocompatibility assays carried out using two human cell lines (osteoblasts, and lymphoblasts) revealed that this biological property is favoured for the highest silica contents. This trend was particularly evident in the case of osteoblasts, being likely related to the lower pH values developed in the culture medium under those conditions.

1. Introduction

The release of calcium ions (Ca^{2+}) from bioactive glasses during the in vitro bioactivity assessment in simulated body fluid (SBF) may increase the degree of super saturation of the SBF solution and favour the nucleation of apatite onto the silica gel layer initially formed at the glass surface **[1]**. To some extent, increasing the calcium (Ca) content in glass composition tends to enhance porosity (pore volume and diameter) while significantly increasing the skeletal density **[2]**. However, it was also demonstrated that very high Ca contents stimulate the preferential formation of calcite ($CaCO_3$) over HAp during the SBF immersion tests **[3]**.

In turn, the in vitro bioactivity of bioactive glasses can be favoured by using low P_2O_5 contents (< 10 mol%) as under these conditions phosphorus acts as network modifier instead of network former. Consistently, greater P_2O_5 contents increase the network connectivity and exert an opposite and deteriorating effect on bioactivity **[4]**. This can be attributed to the high affinity of the modifiers such as calcium and sodium to coordinate with phosphorus, thus enhancing its structural role **[5]**. This will result in a lower bio–mineralization rate **[6]**.

The inclusion of calcium and phosphate in the glass system facilitates the apatite formation **[3]**. The Ca/P ratio is known to play an important role in modifying and tailoring the bioactivity of glasses. Compositions that enhance the non–bridging oxygens/bridging oxygens (NBO/BO) ratio reduce the glass network structure and connectivity. It has been referred to the inclusion of Na_2O in bioactive glasses induces a more accentuated glass network disrupting effect and maintaining a good bioactivity rate, while the mechanical properties of glasses and glass ceramics may be improved **[7]**.

Recently, organic acids were successfully used as catalysts for the hydrolysis and condensation of sol–gel glasses, and with a minimal concentration of citric acid, the reaction has been catalysed to synthesize the bioglass created by Hench **[8]**. The use of hydrochloric acid (HCl) as a catalyst was shown to aid the formation of NaCl at low temperatures, as sodium from the glass composition has a high affinity to chlorine from HCl **[9]**.

The aim of this work is to synthesise two series of five glass compositions. In the 1st route, acetate salts are used as precursors for Ca and Na, and nitric acid served as catalyst. In the 2nd route, nitrate salts were used as precursors for Ca and Na, and citric acid was used as catalyst. In both routes, the amounts of calcium were increased at the expenses of silica

contents with Ca/P ratios varying from 6–15. The molar content of the sodium was intentionally kept low, because Na^+ exhibits a very fast exchange with the H^+ from SBF, which can lead to an abrupt increase of dissolution rate, and concomitantly to an increase in pH and a decrease in silica gel re–polymerisation **[10]**. Increasing Ca contents in glasses while using acetate or nitrate salts as alternative Na and Ca precursors were systematically explored in this work in an attempt to shed light on their effects induced on the network structure, bioactivity and biocompatibility of the resulting sol–gel derived bioactive glasses. As far as we are aware, no such systematic study on the synthesis of quaternary bioactive glasses for biomedical applications has been performed previously.

2. Materials and methods

2.1. Glass synthesis

The rapid sol–gel synthesis method developed by the authors **[11]** was adopted in this work to produce two series of glasses each one with five different compositions **Table 5.1**.

Table 5.1: Nominal compositions of the sol–gel derived glass.

№	Designation		Composition		Ca/P
	Acetate	Nitrate	Oxide molar ratios	Cationic ratios	
1 & 6	S67C24–A	S67C24–N	$67SiO_2$–$2.5Na_2O$–$24CaO$–$2P_2O_5$	67Si – 5Na – 24Ca – 4P	6
2 & 7	S59C32–A	S59C32–N	$59SiO_2$–$2.5Na_2O$–$32CaO$–$2P_2O_5$	59Si – 5Na – 32Ca – 4P	8
3 & 8	S51C40–A	S51C40–N	$51SiO_2$–$2.5Na_2O$–$40CaO$–$2P_2O_5$	51Si – 5Na – 40Ca – 4P	10
4 & 9	S49C45–A	S49C45–N	$49SiO_2$–$1.5Na_2O$–$45CaO$–$1.5P_2O_5$	49Si – 3Na – 45Ca – 3P	15
5 & 10	S44C48–A	S44C48–N	$44SiO_2$ –$2Na_2O$–$48CaO$–$2P_2O_5$	44Si – 4Na – 48Ca – 4P	12

The two different series only differ in the precursor salts for sodium and calcium and in the catalyst used. In the acetate route, acetate salts [calcium acetate monohydrate ($Ca(C_2H_3O_2)_2.H_2O$, ≥99.0%) and sodium acetate ($Na(C_2H_3O_2)$, ≥99.0%)] were selected as precursors and nitric acid (HNO_3, ≥68.0%, Sigma–Aldrich) was used as catalysts). In the nitrate route, nitrate salts [calcium nitrate tetrahydrate (CaN, $Ca(NO_3)_2.4H_2O$, ≥ 99%) and

sodium nitrate (NaN, $NaNO_3$, ≥ 99%)] were adopted as precursors and citric acid monohydrate (CA, $C_6H_8O_7.H_2O$, 99.5–102%) was utilised as catalyst. Distilled water was used as the solvent. Aqueous stock solutions of the network formers were prepared by dissolving the precursors [tetraethyl ortho silicate (TEOS, $C_8H_{20}O_4Si$, 98%) and triethyl phosphate (TEP, $C_6H_{15}O_4P$, ≥ 99.8%), both supplied from Sigma–Aldrich] in the acidic solutions of above referred catalysts. The preparation of each TEOS–TEP solution started with the sequential adding TEOS and TEP to the catalyst solution under stirring for 30 min to obtaining a clear sol, as schematised in **Fig. 5.1** and **Table 5.2**.

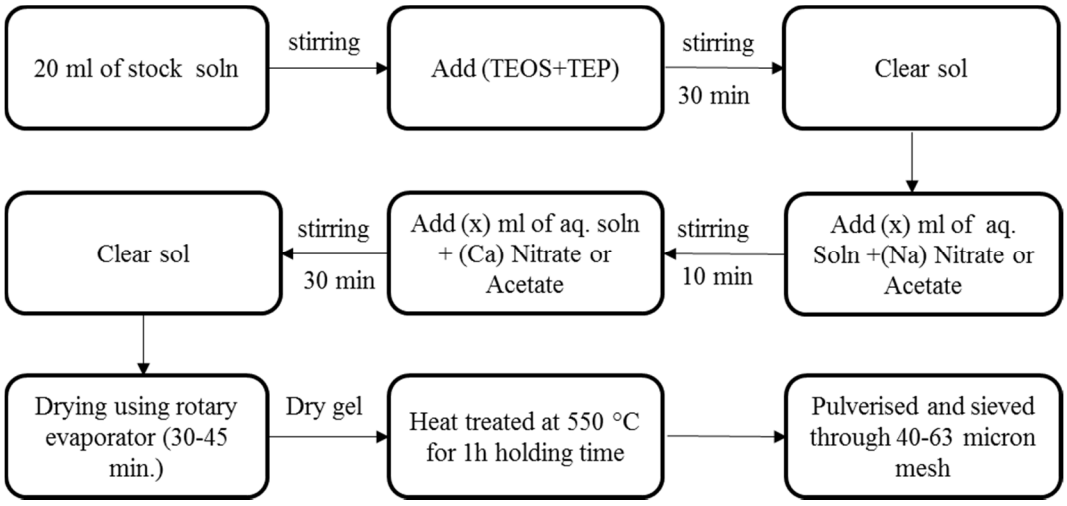

Fig. 5.1: General basic flow chart of the sol–gel glass synthesis process.

Both sodium and calcium salts were separately dissolved according to the concentrations reported in **Table 5.2**. The Na–precursor solution was firstly added to the TEOS–TEP solution and after 10 min the Ca–precursor solution was also adjoined. The overall mixtures were stirred for a further 30 min after adding the last precursor (Ca), as illustrated in **Fig. 5.1**. The quaternary (Si–Na–Ca–P) compositions and their corresponding Ca/P molar ratios are shown in **Table 5.1**.

The resulting sols were dried using a Buchi 210 Rotavapor evaporator with V–850 vacuum controller and V–700 diaphragm vacuum pump (Buchi Labortechnik AG, Flawil, Switzerland). The sols were dried in a 500 mL flask rotating in a water bath at 55ºC under a

vacuum pressure of 50 mbar for 30 to 45 minutes **[11–13]**. After this rapid drying/condensation, the sols were converted into dry gels.

The letters (A, for acetate) & (N, for nitrate) were added to the sample codes in **Table 5.1** to identify the synthesis routes. The dried gels were thermally stabilised at 550ºC in air for 1 h. The heating rate was 1ºC min^{-1} up to 300ºC for 1 h, and then increased to 10ºC min^{-1} up to 550ºC with a holding time of 1 h, followed by natural cooling to room temperature. The heat–treated samples were ground using a mortar and pestle and the obtained glass powders were sieved through 63 and 40 micron meshes. The powder retained in the finer sieve, having particles comprised in this size range (40–63 microns) were used in the bio–mineralization experiments in SBF according to a unified procedure disclosed elsewhere **[14]**.

Table 5.2: Concentrations of precursors and acid catalysts in the starting aqueous solutions for each composition.

№	Designation	Precursors aqueous solutions (mL)			Catalyst concentration		Molar ratio of H_2O/total reactants
		TEOS+TEP	Na	Ca	HNO_3	$C_6H_8O_7.H_2O$	
1	S67C24–A	20	15	35	1.3 M	–	~ 22
2	S59C32–A	20	15	40	1.6 M	–	~ 24
3	S51C40–A	20	15	55	1.35 M	–	~ 28
4	S49C45–A	20	15	65	1.7 M	–	~ 32
5	S44C48–A	20	15	60	1.5 M	–	~ 30
6	S67C24–N	20	10	50	–	0.25 M	~ 25
7	S59C32–N	20	10	55	–	0.25 M	~ 27
8	S51C40–N	20	10	60	–	0.25 M	~ 30
9	S49C45–N	20	10	70	—	0.26 M	~ 31
10	S44C48–N	20	10	70	—	0.26 M	~ 31

2.2. Glass Characterization

The specific surface area (SSA) of the powders was measured by the Brunauer – Emmett–Teller (BET) method using a Gemini M–2380 instrument (Micrometrics, Norcross, GA, USA) with N_2 as the adsorbate. The samples were previously degassed at a slightly elevated temperature (200ºC).

Skeletal density was estimated by helium pycnometry after overnight drying the powder samples at 60ºC to eliminate any absorbed humidity and grating the accuracy of the results.

The particle size distributions were measured using a laser diffraction particle size analyser (Coulter LS particle size analyser; Beckman Coulter, CA). Triplicate measurements were performed for each sample.

X–ray diffraction (XRD) was used to analyse the crystalline phases of the samples before and after immersion in simulated body fluid (SBF). The analyses were performed using a PANalytical XPERT–PRO Diffractometer system, utilising Cu Kα radiation (Kα =1.54059 Å) with 2θ varying from 6–70º in steps of 0.026 s^{-1}. The diffraction patterns were compared with the Joint Committee on Powder Diffraction Standards (JCPDS).

Silica environments and the degree of silica polymerisation of the stabilised glass samples were investigated by ^{29}Si MAS–NMR. The spectra were recorded on ASX 400 spectrometer (Brucker, Germany) operating at 79.52 MHz (9.4 T), using a 7 mm probe at a spinning rate of 5 kHz. The pulse length was 2 µs with 60 s delay time. Kaolinite was used as a chemical shift reference.

Infrared transmittance spectra of the glasses, before and after immersion in SBF, were obtained using a Fourier Transform Infrared Spectrometer (FTIR, Tensor 27, Brucker, Germany) in the range of 350–4000 cm^{-1}, with 128 Scans and 4 cm^{-1} resolution. The pellets were prepared by pressing a mixture of glass powder and KBr with a ratio of 1:150 (by weight) into a pellet.

The compositional surface modifications of the glasses after immersion in SBF were assessed by energy dispersive spectroscopy (EDX Bruker Nano GmbH Berlin, Germany) on a scanning electron microscope (SEM, S–4100, Hitachi, Japan) using carbon coated samples.

2.3. Bioactivity tests

The in–vitro bioactivity assessment in simulated body fluid (SBF) was performed by immersion of 75 mg of glass powders in 50 mL of SBF solution at 37ºC, using sealed plastic flasks **[14]**. The flasks were immediately placed in an incubator at 37 ± 0.5ºC in an orbital shaker agitating at 120 rpm for 4 different time periods: 4 h, 24 h, 1 week, and 3 weeks **[14]**.

At the end of each time period, each sample was removed from the incubator and the powder was collected by centrifuging the mixture under vacuum at 10,000 rpm for 30 min, using a Beckman model LB–70M ultracentrifuge. The pH of the separated solution was measured directly, while the separated powders were washed with deionised water. Subsequently, the powders were washed with acetone to terminate the reaction and then separated again from the liquid, following by drying overnight in an oven at 37ºC. The experiments were performed in triplicate in order to ensure the accuracy of results. The apatite–forming ability of the glass powders was followed by XRD, FTIR, EDX and pH measurements.

2.4. Biocompatibility tests

The in–vitro cytotoxicity tests were performed according to the International Organization for Standardization (ISO) guidelines (ISO 10993–5) (International Organization for Standardization 2009) **[15]**. Only some N–glasses (S67C24N, S59C32N and S51C40N) were selected because of their lower contents of nitrate residues and the absence of calcite, as will be discussed later. The samples were sterilized by UV–radiation prior to testing them in cell cultures. Two cell lines, MG63 (ATCC CRL–1427, Human osteosarcoma) and C13589 (ATCC CRL–2704, Human B lymphoblasts) were used to determine the materials cytotoxicity through MTT assay, by measuring the metabolic activity of living cells via mitochondrial dehydrogenase activity, whose key component is 3–[4,5–dimethylthiazol–2–yl]–2,5–diphenyl tetrazolium bromide.

MG63 cells were maintained in Dulbecco's Modified Eagle Medium (DMEM, Sigma Aldrich) supplemented with 10% (v/v) of foetal bovine serum (FBS, Sigma Aldrich), penicillin (100 U mL^{-1} culture medium, Sigma Aldrich), streptomycin (100 µg mL^{-1} culture medium, Sigma Aldrich), L–glutamine (5%, Sigma Aldrich) and sodium pyruvate (5%, Sigma Aldrich). C13589 cells were maintained in Roswell Park Memorial Institute 1640 (RPMI, Sigma Aldrich) supplemented with 10% (v/v) of foetal bovine serum (FBS, Sigma Aldrich), penicillin (100 U mL^{-1} culture medium, Sigma Aldrich), streptomycin (100 µg mL^{-1} culture medium, Sigma Aldrich), L–glutamine (5%, Sigma Aldrich). All cell lines were grown in a humidified incubator at 37ºC, 5% CO_2, and 95% relative humidity.

To determine the viability of cells when exposed to bioglass samples, all cell lines tested were seeded into 24 well plates, at $1*10^5$ cells per well, and cultured in cell media

supplemented with 0 (CTR), 0.05, 0.15, 0.30 and 0.75 mg mL^{-1} of each bioglass material for 24, 48 and 72 h. The control (CTR) was a complete culture medium. In–vitro cytotoxicity of the bioglass was evaluated via MTT assay, according to the manufacturer's instructions (Sigma–Aldrich). The absorbance was spectrophotometrically measured at a wavelength of 570 nm, and the background absorbance measured at 690 nm was subtracted.

The percentage of cell viability was expressed as the relative growth rate (RGR) by the equation:

$$RGR\ (\%) = \frac{D_{\text{sample}}}{D_{\text{control}}} \times 100 \qquad (5.1)$$

where D_{sample} and $D_{control}$ were the absorbance of the sample and the negative control, respectively. Levels of cells incubated with 0 mg mL^{-1} of bioglass were taken as 100%, and cell viability calculated as a percentage of these control values. Each experiment was triplicated.

3. Results and discussion

3.1. XRD for the stabilised glasses/ vitrified glasses

Fig. 5.2(a–b) shows the XRD patterns of the samples synthesised through both routes and thermally stabilised at 550ºC. The A–glasses **Fig. 5.2(a)** exhibit clear crystalline HAp for all calcium contents, along with the formation of small amounts of a silica phase [Coesite (SiO_2), PDF card #04–015–7166] in some cases. These results clearly suggest that the components have been partially segregated along the process probably due to a faster sol–gel transition induced by the higher pH values of the starting sols. The N–glasses exhibit an amorphous glassy structure for all compositions except for that with the highest Ca content (S44C48N), which showed as well some traces of hydroxyapatite (HAp) [($Ca_{10}(PO_4)_6(OH)_2$, PDF card #01–080–3956] **Fig. 5.2(b)**.

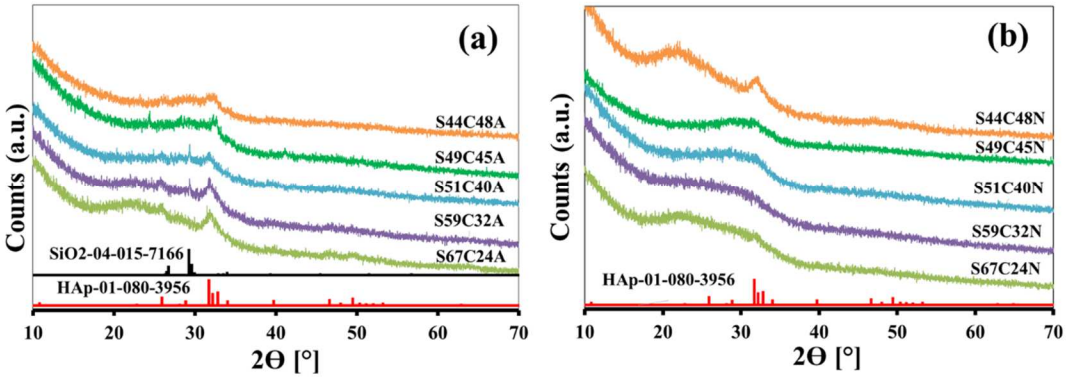

Fig. 5.2: XRD patterns of the glasses synthesized through different routes and thermally stabilised at 550ºC: (a) A−glasses; (b) N−glasses.

3.2. MAS–NMR analysis

The measured ^{29}Si MAS NMR spectra for A−glasses and N−glasses are shown in **Fig. 5.3**. Only the compositions containing 24, 32, and 40 Ca were chosen for NMR analysis for two reasons: Firstly, higher Ca contents were found to readily induce the precipitation of the undesired calcite phase during SBF immersion. Secondly, the acquired signal became gradually noisier as the amount of silica decreased and an accurate extraction of the information was increasing difficult. The structural Q^n speciation (where n denotes the number of bridging oxygens (BO) and may acquire the values of 1, 2, 3 or 4 can be inferred from NMR spectra. The A−glasses show chemical shift towards lower degrees of polymerisation (i.e. lower network connectivity). The highest silica content glasses (67S24C) exhibit the highest degrees of polymerisation, with a significant fraction of Q^4 species at ~ −111 ppm, and fewer Q^3 species at ~ −100.7 ppm as shown in **Fig. 5.3(a)**. The Q^4 band was slightly shifted to less negative values (~ −110 ppm), upon increasing Ca content at the expenses of silica (S59C32) as seen in **Fig. 5.3(b)**, denoting a lower polymerisation degree. This depolymerisation trend became more obvious upon further increasing the Ca content (S51C40) as shown in **Fig. 5.3(c)**, with the Q^4 band appearing at lower chemical shift (~ −108.5 ppm).

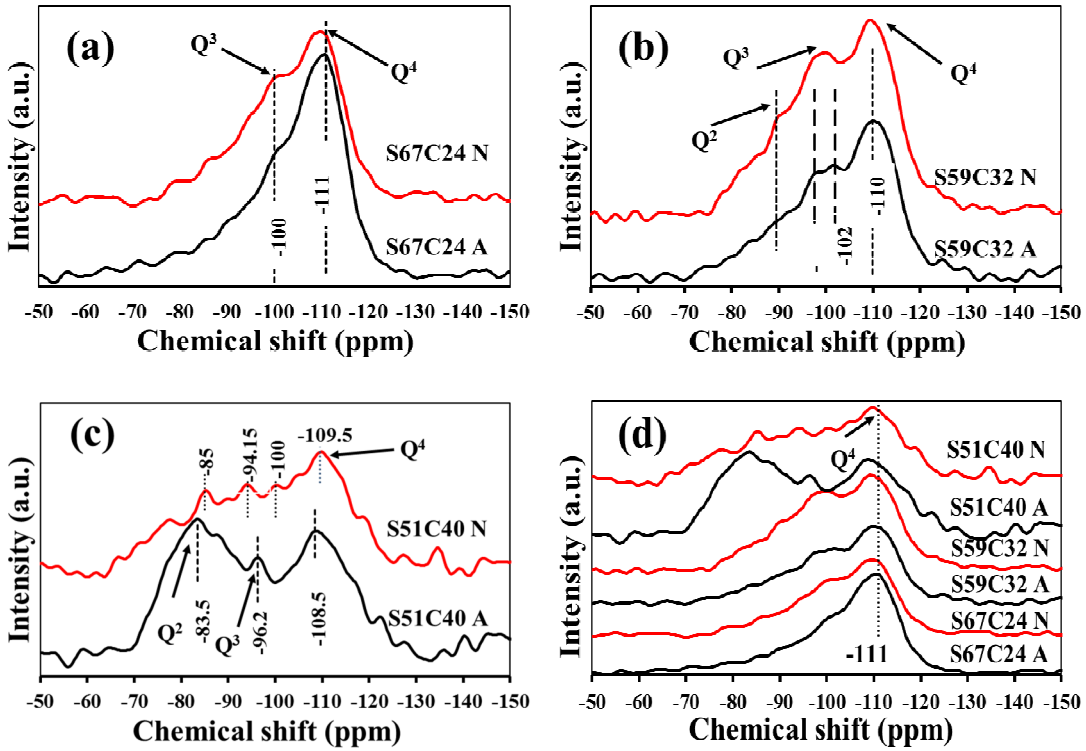

Fig. 5.3: ^{29}Si MAS–NMR of A–glasses (black) and N–glasses (red) thermally stabilised at 550ºC for selected compositions: (a) S67C24;(b) S59C32; (c) S51C40; (d) comparison of the three compositions.

This gradual deviation trend of Q^4 towards lower chemical shifts with decreasing Si contents from 67 to 51 is also accompanied by: (i) the appearance a band at −100 ppm corresponding to Q^3; (ii) the broadening of this band and its apparent deviation to less negative chemical shifts towards the onset of Q^2 species. What is more certain is the clear depolymerisation trend when Ca content increases at the expenses of Si content, leading to significant populations of Q^2 and even Q^1 species, between −97 to −85 ppm **Fig. 5.3(c)**. The accurate identification and quantification of these species is difficult because the spectra become noisier as with decreasing Si content. Although the glasses prepared through the different routes have the same nominal compositions, A–glasses exhibit slightly lower degrees of polymerisation in comparison to N–glasses. These results are in a good agreement with results published earlier by the authors **[16]**.

3.3. FTIR spectra for stabilised glasses

The FTIR spectra of the thermally stabilised A–glasses and N–glasses are displayed in **Fig. 5.4(a)**, and **Fig. 5.4(b)**, respectively. All the spectra are dominated by a broad band between 800 and 1300 cm^{-1}, assigned to asymmetric stretching for Si–O–Si, which becomes gradually shallower as Si content decreases.

Both routes provide glasses with almost similar features. The broad band centred at ~1090–1100 cm^{-1} is attributed to the Si–O–Si transverse optical stretching mode (TO_1). This peak is shifted to a lower wavenumber ~1040 cm^{-1} by increasing the Ca content (S51C40, S49C45, and S44C48) due to higher contributions of Q^3 species **[17]**. The appearance of relatively small band at 1640 cm^{-1} in all glasses is related to the presence of H_2O molecules **[18]**. The band at 1460 cm^{-1} in N–glasses is divided into two separate peaks at 1490, and 1420 cm^{-1} that can be assigned to amorphous calcite **[19,20]**. The presence of a sharp peak around 1385 cm^{-1} can be attributed to the NO_3^- group **[21]**. This peak is of higher intensity in the case of A–glasses. These results are consistent with the fuel role of citric acid towards nitrates **[22]** with self–propagation combustion reactions being favoured at proper molar ratios of metal salts/citric acid **[23]**.

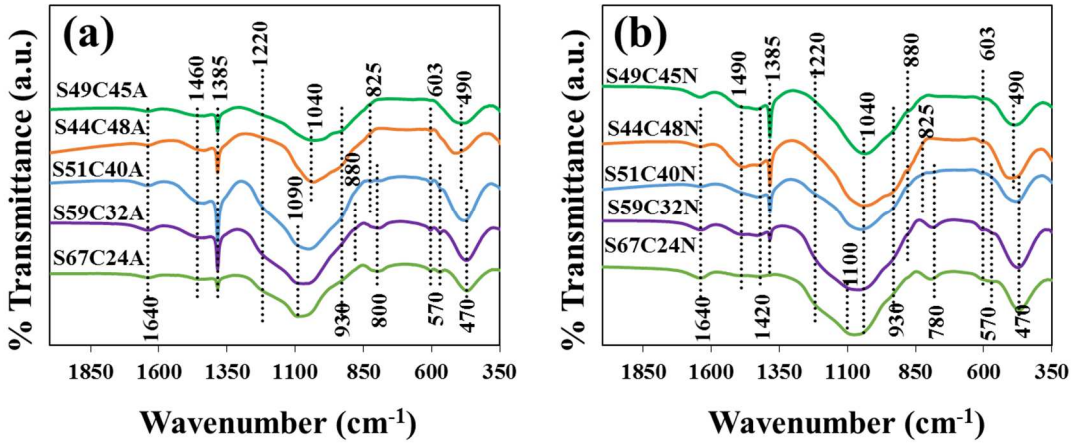

Fig. 5.4: FTIR spectra of all glass compositions thermally stabilised at 550ºC: (a) A–glasses; (b) N–glasses.

Therefore, higher amounts of nitrate residues will be eliminated from the as prepared N–glasses in comparison to A–glasses. Further, acetate precursors are highly basic salts,

being often used as buffers **[24]**. To reduce the pH of acetate salt solutions a high amount of nitric acid has to be added, which serves two functions: (i) as catalyst; (ii) pH reducer of the sol to prevent the fast gelation, which may occur immediately after adding one or both acetate metal salts.

The shoulder positioned at ~1220 cm^{-1} in **Fig. 5.4(a–b)** may represent the Si–O–Si (TO_2) stretching mode **[24]**, or be also assigned to P–O stretch vibration **[25]**. The band at 930 cm^{-1} intensified with increasing Ca contents, and can be attributed to the Si–O–Si stretching vibration mode of non–bridging oxygens (NBO) **[26]**. The very small peaks at around 880 cm^{-1} **[27]** along with the band at around 1460 cm^{-1} **[28]**, are assigned to C–O. The two tiny peaks around 825 and 800 cm^{-1} are related to TO symmetric stretching of Si–O–Si **[29]**. The twin sharp peaks at 603 and 570 cm^{-1} correspond to the P–O bending vibration of PO_4^{-3} tetrahedra. The presence of these two peaks indicates the formation of HAp **[26,29]**. The low wavenumber band at ~490 cm^{-1} for high calcium content glasses can be assigned to the symmetric vibration of Si–O–Si. In the low calcium content glasses, this band shifted to about ~470 cm^{-1}, and can be assigned to the bending vibrating mode of P–O–P bonds of the HAp phosphate groups **[30]**.

3.4. Density, particle size and specific surface area (SSA)

Table 5.3 shows the density, diameter (d_{50}) and SSA for the 10 prepared glasses. Density values varied within the ranges of 2.24–2.56 g cm^{-3} and 2.30–2.61 g cm^{-3} for A–glasses and N–glasses, respectively. The two different synthesis routes do not induce significant density differences. The average particle sizes (after sieving through a 40 µm mesh) varied within the ranges of 15.1–24.5 µm, and 16.6–25.60 µm, for A–glasses and N–glasses, respectively. The smaller particle sizes were measured for the lower Ca contents, S51C40 and S44C48, irrespective of the synthesis route. The A–glasses exhibited SSA values in the range 28.4–53.5 m^2 g^{-1}, lower than those of N–glasses that varied within the range of 32.4–99.5 m^2 g^{-1}.

From these results it can be concluded that N–glasses tend to exhibit higher skeletal densities, slightly coarser particles, and higher specific surface areas. This last feature is likely to favour the *in–vitro* bio–mineralisation rate of N–glasses in comparison to A–glasses.

Table 5.3: Density, particle size and SSA for the glasses heat–treated for 1 h at 550ºC.

Designation	Density ± SD ($g\ cm^{-3}$)	Particle size ± SD d50 (µm)	SSA ($m^2\ g^{-1}$)
S67C24–A	2.25± 0.04	19.2± 0.04	35.0
S67C24–N	2.31± 0.06	23.3± 0.11	99.5
S59C32–A	2.34± 0.08	23.6± 0.16	53.5
S59C32–N	2.37± 0.05	23.7± 0.11	72.5
S51C40–A	2.24± 0.08	15.1± 0.51	28.4
S51C40–N	2.30± 0.04	16.6± 0.06	32.4
S49C45–A	2.42± 0.02	24.5± 0.11	51.1
S49C45–N	2.49± 0.04	25.6± 0.23	56.8
S44C48–A	2.56± 0.03	15.3± 0.40	53.1
S44C48–N	2.61± 0.04	17.8± 0.31	58.7

3.5. Bioactivity assessment

3.5.1. XRD after immersion in simulated body fluid (SBF)

Figs. 5.5(a–e) displays the XRD patterns of A−glasses and N−glasses after immersion in SBF for different time periods up to 3 weeks. The presence of crystalline (A−glasses) and semi crystalline or amorphous HAp (N−glasses) identified even before immersion (0 h) is not a commonly reported feature.

This early formation of HAp during sol–gel synthesis can be considered as a good attribute, as it can act as seeding for the new HAp formation upon SBF immersion. The crystalline SiO_2 phase (Coesite, PDF card #04–015–7166) seen in some A−glasses in **Fig. 5.2(a)** has apparently disappeared just after 4 h. Such apparent disappearance can only be attributed to: (i) its dissolution in the SBF solution; (ii) a masking effect caused by the deposition of a HAp (PDF # 01–080–3956) surface layer. The intensity of XRD peaks of HAp gradually increases between 4 h and 3 weeks of immersion. The higher crystallinity of HAp in A−glasses noticed for shorter immersion periods is an apparent heritage of the faster sol–gel transition that induced a more extensive segregation, as discussed for **Fig. 5.2(a)**. Although initially revealing less crystalline HAp and enhanced homogeneity **Fig. 5.2(b)**, N−glasses

have undergone a more extensive bio–mineralisation process as deduced from the intensification of HAp XRD peaks after 3 weeks of immersion.

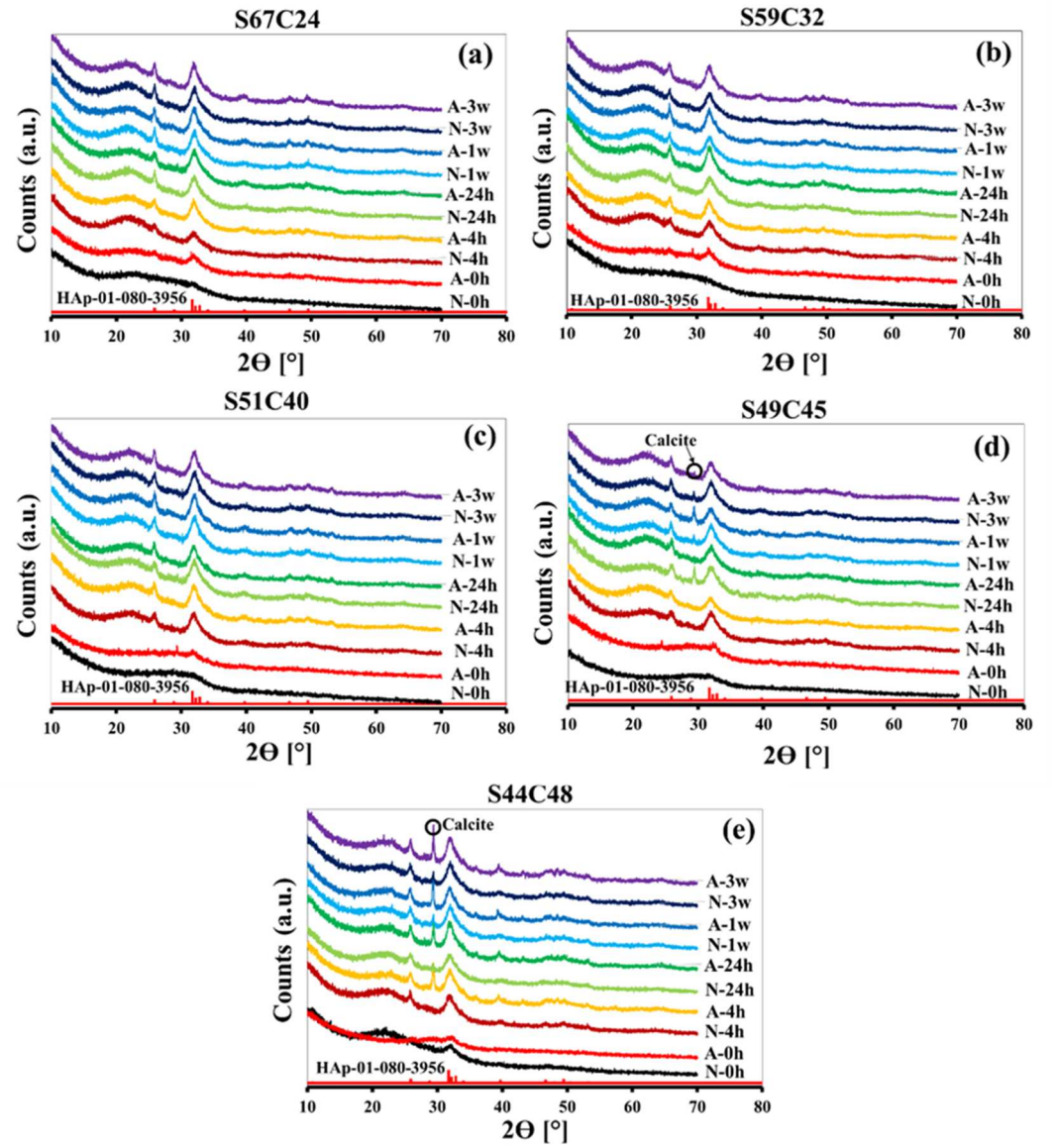

Fig. 5.5: XRD patterns of the A–glasses and N–glasses thermally stabilised at 550ºC after immersion in SBF for different periods from 4 h to 3 weeks: (a) 67S24C; (b) 59S32C; (c) 51S40C; (d) 49S45C; (e) 44S48C.

This observation supports the hypothesis admitted at the end of section 3.3 that higher SSA of N–glasses could favour the *in–vitro* bio–mineralisation rate.

Calcite phase ($CaCO_3$, PDF #00–005–0586) was identified at the early stage of SBF immersion in the S44C48 and S49C45 glasses, being more evident in A−glasses and with increasing Ca contents, in a good agreement with results reported elsewhere **[31]**. This can be understood considering that higher concentrations of Ca^{2+} released into the SBF solution **[31]** and the concomitant increase in pH favour the precipitation of calcite from the reaction between Ca^{2+} and CO_3^{2-} available in air **[32]**. The early appearance (after 4 h of immersion) of calcite in A−glasses can be attributed to their less polymerised network structures favouring the release of Ca^{2+} and the cascade of associated leading to the formation of calcite **[32]**. The same reasoning also explains why calcite was formed for longer immersion time periods, even in the case of N−glasses.

3.5.2. FTIR spectra after immersion in SBF

Fig. 5.6 shows the evolution of FTIR peaks/bands of glasses over different immersion time periods in SBF. The wide band centred at ~1450 cm^{-1} is assigned to the C–O group. Also the evolution of the peak at 870–880 cm^{-1} confirms the presence of type–A carbonated hydroxyapatite formation (CHAp).

The band centred at 1450 cm^{-1} and the peak at 880 cm^{-1} support this hypothesis. The type–A CHAp results from the CO_3 substituting for OH into apatite lattice **[33]**.

Two sharp phosphate peaks characteristic of HAp at around 560 and 600 cm^{-1} are clearly present after just 4 h of immersion for both A−glasses and N−glasses.

A peak observed at 960 cm^{-1} could be also assigned to P–O symmetric stretching in the CHAp layer formed onto the surface of the powders **[34]**. This may show the occurrence of the 5 stages of carbonated hydroxyapatite CHAp layer formation as proposed by Hench *et al.* **[34]** for the initial hours of immersion. As observed by XRD, there are little changes over time with HAp peaks becoming better defined and sharper as immersing time increases. Although the FTIR spectra of both series of glasses look very similar, N−glasses show sharper and better defined peaks supporting its enhanced bioactivity in comparison to A−glasses.

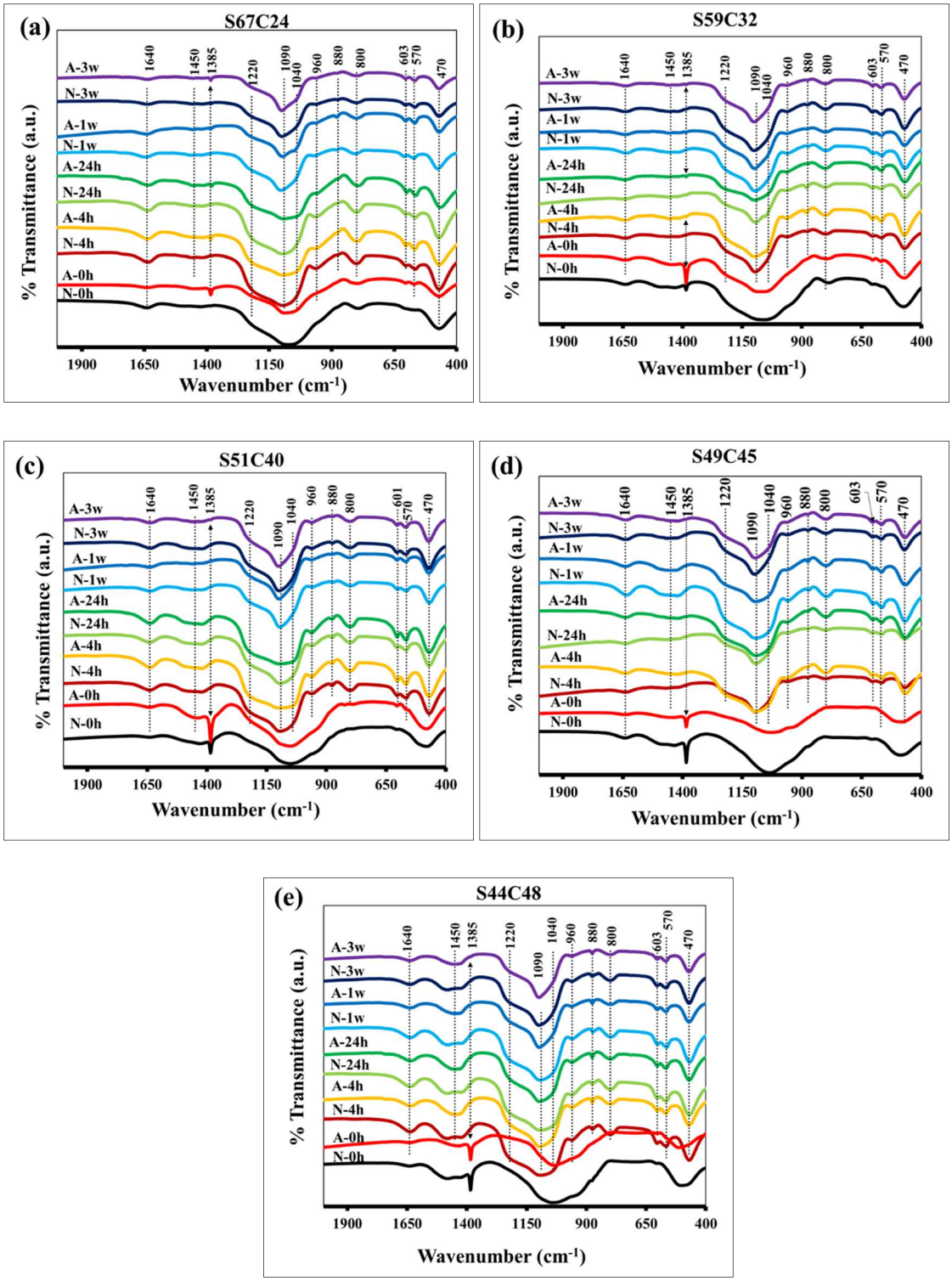

Fig. 5.6: FTIR spectra of the A−glasses and N−glasses thermally stabilised at 550ºC after immersion in SBF for different periods from 4 h to 3 weeks: (a) S67C24; (b) S67C24; (c) S51C40; (d) S49C45; (e) S44C48.

3.5.3. pH behaviour in SBF

The pH variations along the immersion time in SBF for the 67SC24, S59C32 and 51SC40 glass samples synthesised from both routes exhibit almost identical trends as shown in **Fig. 5.7**. The pH curves for N−glasses appear always above, a feature that can be attributed to their higher SSA. A rapid initial raise in pH from the starting value of 7.4 was registered at 4 h time point for both A−glasses and N−glasses, attributed to the sudden leaching of alkaline Na and alkaline earth Ca from the surface of the glass particles. This is then followed by an overall gradual reversal trend between 4 h to 24 h, probably due to the consumption of Ca^{2+} ions in the calcium containing phases HAp and calcite. The pH variations are systematically less noticeable for A−glasses and for compositions with the lowest calcium contents **Fig. 5.7**. This is consistent with the early precipitation of calcite in A−glasses **Fig. 5.5**, particularly noticeable for **Fig. 5.5(e)**. The decrease in pH value for A−glasses and N−glasses tend to approach as Ca content increase, appearing almost superimposed for the S51SC40 composition. The apparent overall pH decreasing trend after 1 week of immersion might be due to the continuous dissolution of acidic glass former species such as Si^{4+} and phosphate ions; and to the depletion of Ca ions from the solution due to the precipitation of HAp and calcite, as confirmed by XRD patterns **Fig. 5.5** and FTIR spectra **Fig. 5.6**.

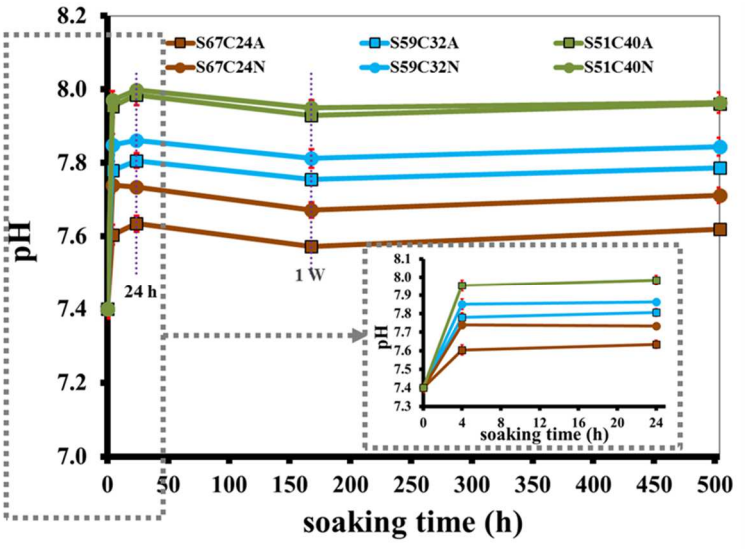

Fig. 5.7: pH values measured in the supernatant SBF liquids remaining after the indicated immersion time points for selected compositions (S67C24, S59C32, S51C40) of A−glasses and N−glasses thermally stabilised at 550ºC.

3.5.4. EDX results after SBF immersion

The atomic surface concentrations of Ca and P species as measured by EDX for A–glasses and N–glasses immersed in SBF for different time periods are presented in **Fig. 5.8**. A first abrupt decrease in Ca content is observed for all samples up to 4 h. This Ca surface depletion can be attributed to the leaching of Ca^{2+} ions into the SBF solution. The excess ions in the solution then tend to precipitate and form surface Ca–containing phases such as calcite and HAp upon further prolonging the immersion time.

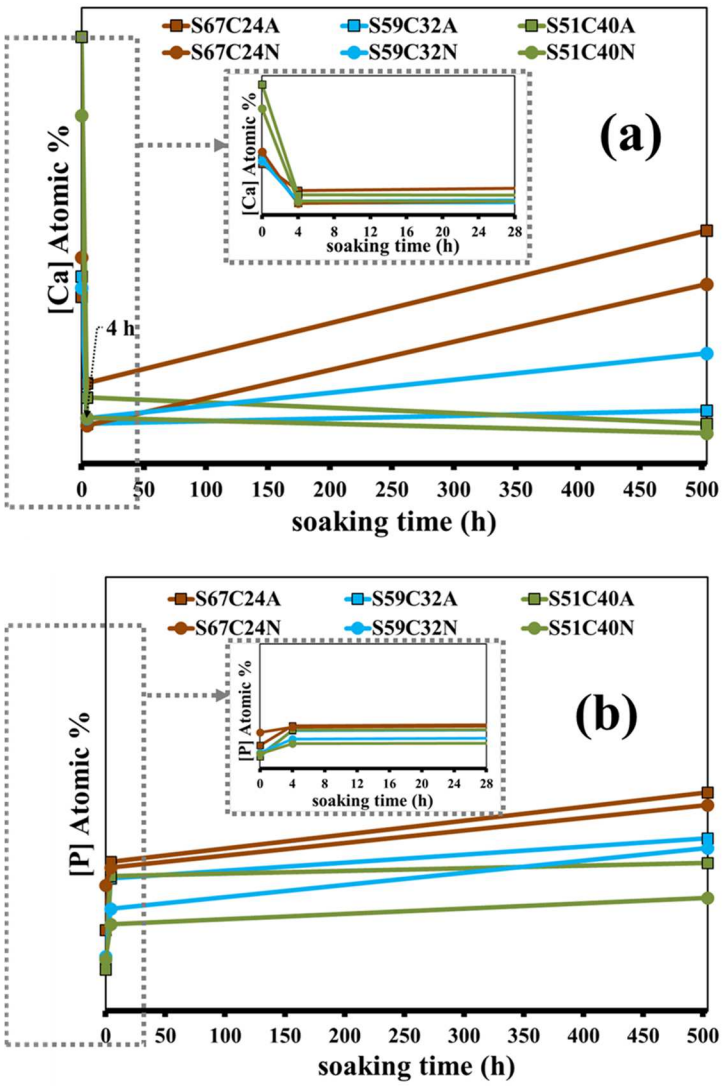

Fig. 5.8: Atomic surface concentrations of Ca (a) and P (b) species measured by EDX after the indicated immersion time points for selected compositions (S67C24, S59C32, S51C40) of A–glasses and N–glasses thermally stabilised at 550ºC and immersed in SBF for different time periods.

The surface contents of P show faster initial steps up to 4 h, followed by slower steady state increasing trends as the immersion time further increases, being also consistent with the gradual precipitation of HAp as supported by the XRD, FTIR and pH results reported above.

3.5. Biocompatibility assessment

The compositions (67SC24, S59C32 and 51SC40) and testing conditions selected for the *in–vitro* biocompatibility cytotoxicity assessment are detailed described in the section 2.4. The results displayed in **Fig. 5.9(a–f)** reveal that MG63 cells show the highest degree of cytocompatibility towards S67C24N glass **Fig. 5.9(a,b**). For concentration levels of up to 0.30 mg mL^{-1} result in cell viability of at least 70 % over all the three tested time periods, especially for the sample thermally stabilised at 800 ºC **Fig. 5.9(b**). High concentration levels tend to become cytotoxic. Similar scenarios concerning the effects of thermal stabilization temperature can be observed for the other calcium richer compositions **Figs. 5.9(c–d)**, and **Figs. 5.9(e–f**).

The responses of lymphoblast C13895 **Figs. 5.10(a–f)** to the tested glasses reveal that these cells are more sensitive to the presence of nitrate residues as deduced from the high degrees of cytotoxicity of the samples thermally stabilised at 550 ºC **Figs. 5.10(a,c,e)**. The lower degree of cytotoxicity observed for the composition S67C24N **Fig. 5.10(a)** also points out to the increased cytotoxicity of glasses with increasing Ca contents.

No similar MTT assays have been carried out previously for bioglasses synthesised by rapid sol–gel route. Only a single study **[35]** was found reporting about cytotoxicity tests of sol–gel derived 45S5® Bioglass composition thermally stabilised at 600 ºC towards human dental pulp stem cells, with cytotoxic effects being observed for concentration levels > 0.4 mg mL^{-1} after between 1–7 days **[35]**.

The enhanced biocompatibility of the Si–richer composition S67C24N is not surprising as silica is well–known to play an important role in enhancing biocompatibility of the bioactive glasses **[36,37]**.

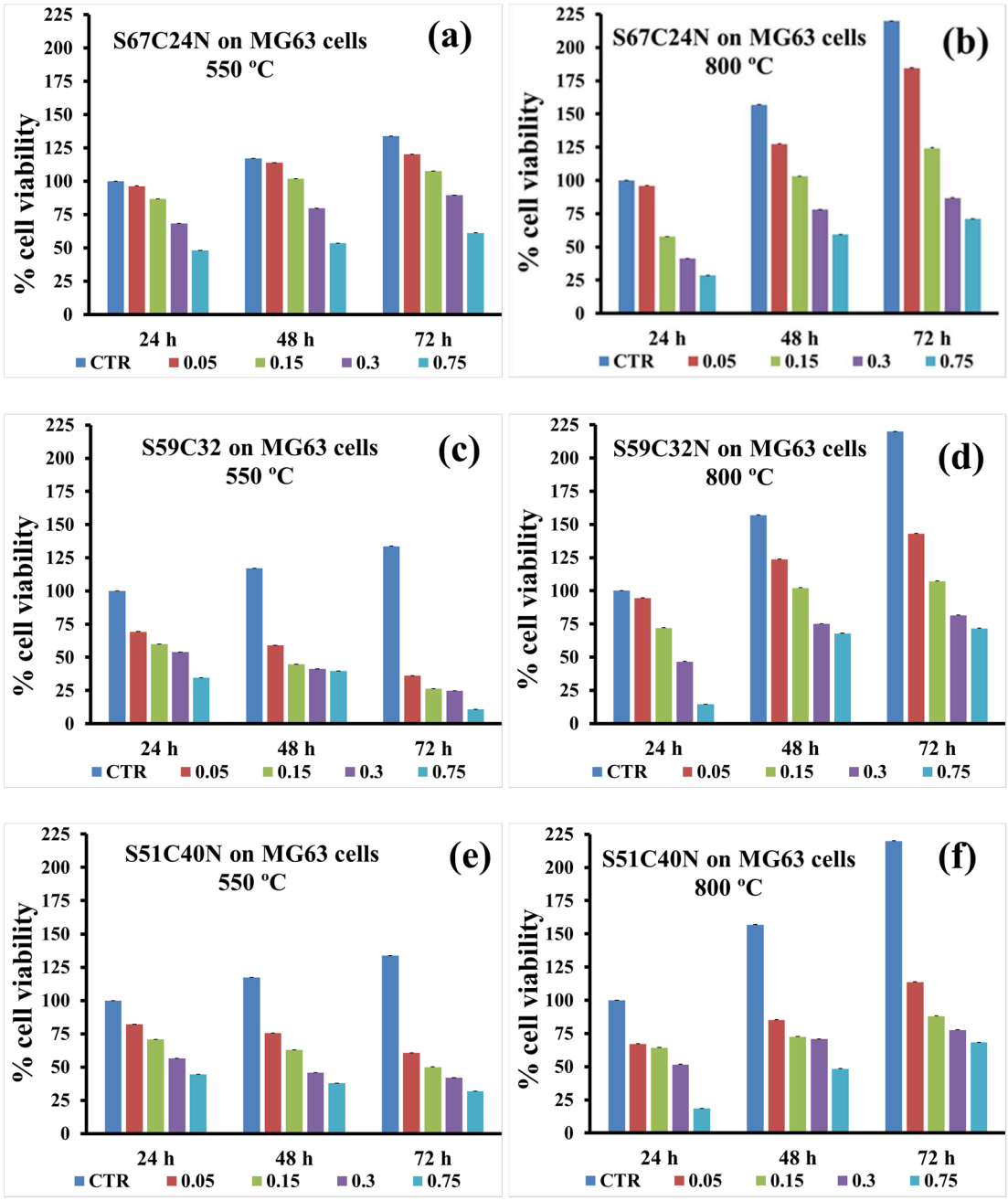

Fig. 5.9: MTT biocompatibility assays of S67C24N, S59C32N and S51C40N glasses stabilised at 550ºC (a, c, e) and at 800ºC (b, d, f) with MG63 human osteosarcoma (osteoblasts). The material is considered non–cytotoxic if the percentage of viable cell is equal to or greater than 70% of the untreated control. The tested glass powder concentrations (0.05, 0.1, 0.3, and 0.75) are in mg mL^{-1}.

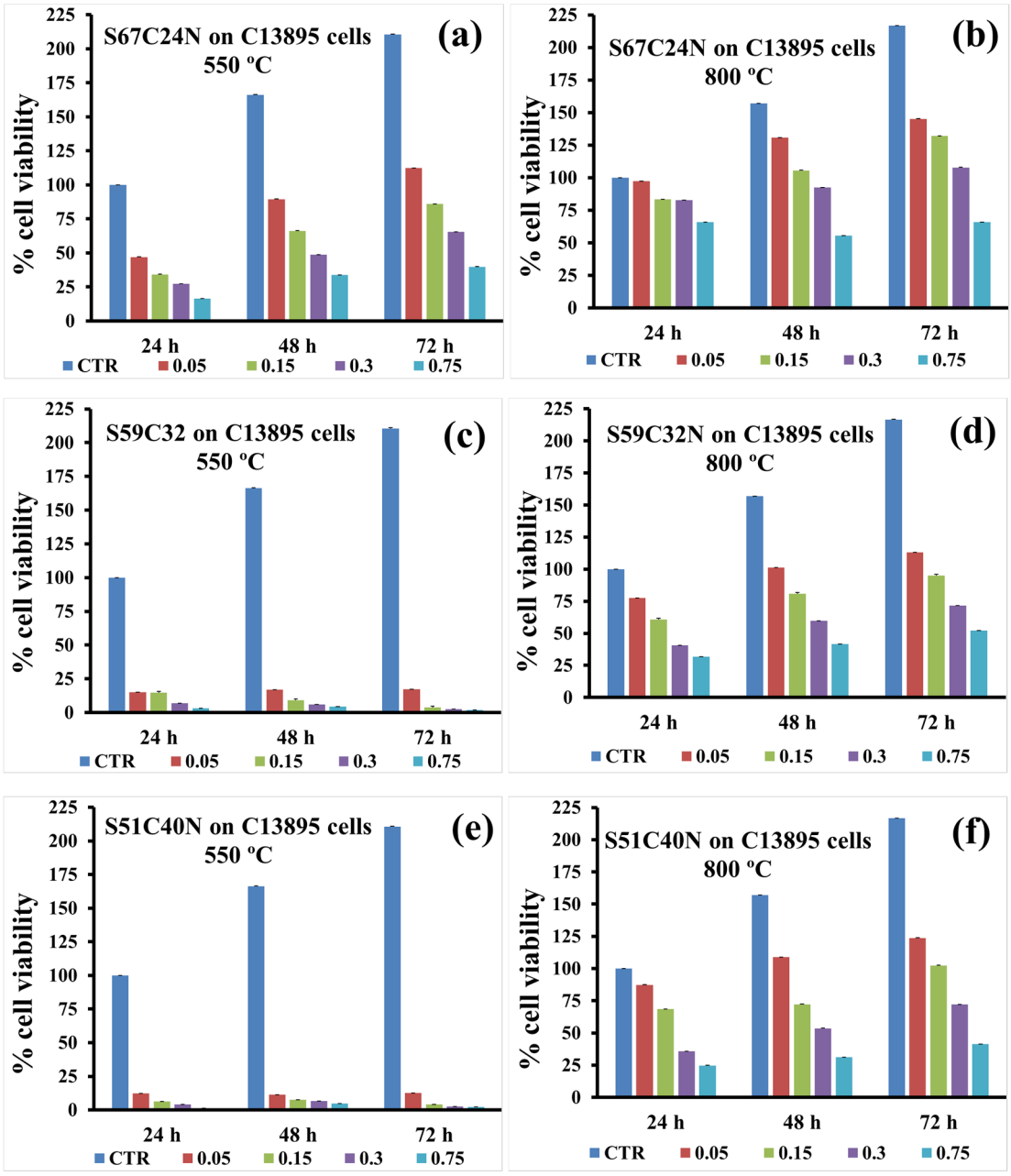

Fig. 5.10: MTT biocompatibility assays of S67C24N, S59C32N and S51C40N glasses stabilised at 550ºC (a, c, e) and at 800ºC (b, d, f) with C13895 osteosarcoma C13589 B lymphoblasts. The material is considered non–cytotoxic if the percentage of viable cell is equal to or greater than 70% of the untreated control. The tested glass powder concentrations (0.05, 0.1, 0.3, and 0.75) are in mg mL^{-1}.

4. Conclusions

The synthesis from nitrate precursors under lower pH environments results in slower condensation reactions, favouring the obtaining of amorphous glass structures with higher degree of polymerisation, skeletal density, and SSA values that favour the *in–vitro* bio–mineralization rate;

Besides being mostly amorphous, A–glasses also contain small amounts of crystallise phases such HAp and silica (Coesite). The components' segregation is stimulated by the higher pH environment and the consequent faster condensation reactions, resulting in lower degrees of network polymerisation, higher agglomeration of the forming primary particles, closed porosity and lower SSA values. These features favoured the *in–vitro* formation of unwanted calcite ($CaCO_3$) phase;

The poor extraction of nitrate residues derived from the high concentrations of nitric acid used as catalyst and its interaction with acetate species is the main drawback of A–glasses. The thermal stabilisation at 550ºC is insufficient to get rid of nitrate residues;

The biocompatibility is enhanced for samples thermally stabilised at higher temperature (800ºC) and especially for glass compositions richer in silica. The composition S67C24N is biocompatible with MG63 osteoblasts up to concentration levels of 0.3 mg mL^{-1}.

Acknowledgments

Rob C. Pullar wishes to thank the FCT Grant IF/00681/2015 for supporting this work. B. A. E. Ben –Arfa thanks FCT grant BIONANOSCULP PTDC/EPH–PAT/6281/2014 for supporting him during this work. I.E. Palamà thanks the Italian Association for Cancer Research (AIRC) through the grant MFAG n. 16803 and Tecnomed (FIRS project of nanotechnology, photonics and precision medicine) for partially supporting this work. This work was developed in the scope of the project CICECO–Aveiro Institute of Materials (Ref. FCT UID /CTM /50011/2013), financed by national funds through the FCT/MEC and when applicable co–financed by FEDER

References

[1] C. Ohtsuki, T. Kokubo, T. Yamamuro, Mechanism of apatite formation on CaO–SiO2–P205 glasses in in a simulated body fluid, J. Non. Cryst. Solids. 143 (1992) 84–92.

[2] N.J. Coleman, M. Bellantone, J.W. Nicholson, A.P. Mendham, TEXTURAL AND STRUCTURAL PROPERTIES OF BIOACTIVE GLASSES IN THE SYSTEM CaO–SiO2, Ceram. – Silikaty. 51 (2007) 1–8.

[3] A. Martınez, I. Izquierdo–Barba, M. Vallet–Regı, Bioactivity of a CaO – SiO2 Binary Glasses System, Chem. Mater. 12 (2000) 3080–3088.

[4] P. Kiran, V. Ramakrishna, M. Trebbin, N.K. Udayashankar, H.D. Shashikala, Effective role of CaO / P2O5 ratio on SiO2 –CaO–P2O5 glass system, J. Adv. Res. 8 (2017) 279–288.

[5] A. Tilocca, A.N. Cormack, Structural Effects of Phosphorus Inclusion in Bioactive Silicate Glasses, J. Phys. Chem. B. 111 (2007) 14256–14264.

[6] M.D. O'Donnell, S.J. Watts, R.G. Hill, The effect of phosphate content on the bioactivity of soda–lime–phosphosilicate glasses, J. Mater. Sci. Mater. Med. 20 (2009) 1611–1618.

[7] Q. Chen, Y. Li, L. Jin, J.M.W. Quinn, P.A. Komesaroff, A new sol–gel process for producing Na 2O–containing bioactive glass ceramics, Acta Biomater. 6 (2010) 4143–4153.

[8] J. Faure, R. Drevet, A. Lemelle, N. Ben Jaber, A. Tara, H. El Btaouri, et al., A new sol–gel synthesis of 45S5 bioactive glass using an organic acid as catalyst, Mater. Sci. Eng. C. 47 (2015) 407–412.

[9] R. Catteaux, I. Grattepanche–Lebecq, F. Désanglois, É. Chai, J.–C. Hornez, S. Hampshire, et al., Synthesis, characterization and bioactivity of bioglasses in the Na2O–CaO–P2O5–SiO2 system prepared via sol gel processing., Chem. Eng. Res. Des. Trans. Inst. Chem. Eng. Part A. 91 (2013) 2420–2426.

[10] F.D. I. Lebecq, A. Leriche, C. Follet–Houttemane, Compositional dependence on the in vitro bioactivity of invert or conventional bioglasses in the Si–Ca–Na–P

system, J. Biomed. Mater. Res. A. 38A (2007) 156–168.

[11] B.A.E. Ben–Arfa, I.M. Miranda Salvado, J.M.F. Ferreira, R.C. Pullar, A hundred times faster: Novel, rapid sol–gel synthesis of bio–glass nanopowders (Si–Na–Ca–P system, Ca:P = 1.67) without aging, Int. J. Appl. Glas. Sci. 8 (2017) 337–343.

[12] B.A.E. Ben–Arfa, I.M.M. Salvado, J.M.F. Ferreira, R.C. Pullar, Novel route for rapid sol–gel synthesis of hydroxyapatite, avoiding ageing and using fast drying with a 50–fold to 200–fold reduction in process time, Mater. Sci. Eng. C. 70 (2017) 796–804.

[13] B.A.E. Ben–Arfa, I.M.M. Salvado, J.R. Frade, R.C. Pullar, Fast route for synthesis of stoichiometric hydroxyapatite by employing the Taguchi method, Mater. Des. 109 (2016) 547–555.

[14] A.L.B. Maçon, T.B. Kim, E.M. Valliant, K. Goetschius, R.K. Brow, D.E. Day, et al., A unified in vitro evaluation for apatite–forming ability of bioactive glasses and their variants, J. Mater. Sci. Mater. Med. 26 (2015) 1–10.

[15] I.O. for Standardization, International Organization for Standardization (2009) ISO 10993–5. Biological evaluation of medical devices—part 5: tests for in vitro cytotoxicity., 2009.

[16] B.A.E. Ben–Arfa, H.R. Fernandes, I.M.M. Salvado, J.M.F. Ferreira, R.C. Pullar, Effects of catalysts on polymerization and microstructure of sol–gel derived bioglasses, J. Am. Ceram. Soc. 101 (2018) 2831–2839.

[17] J.L. Bass, G.L. Turner, Anion Distributions in Sodium Silicate Solutions. Characterization by 29Si NMR and Infrared Spectroscopies, and Vapor Phase Osmometry, J. Phys. Chem. B. 101 (1997) 10638–10644.

[18] V. Simon, D. Eniu, A. Gritco, S. Simon, Thermal and spectroscopic investigation of sol–gel derived aluminosilicate bioglass matrices, J. Optoelectron. Adv. Mater. 9 (2007) 3368–3371.

[19] V. Aina, G. Malavasi, A. Fiorio Pla, L. Munaron, C. Morterra, Zinc–containing bioactive glasses: Surface reactivity and behaviour towards endothelial cells, Acta Biomater. 5 (2009) 1211–1222.

[20] F.A. Anderson, L. Brecevic, Infrared spectra of amorphous and crystalline calcium carbonate, Acta Chem. Scand. 45 (1991) 1018–1024.

[21] X. Chatzistavrou, D. Esteve, E. Hatzistavrou, E. Kontonasaki, K.M. Paraskevopoulos, A.R. Boccaccini, Sol–Gel Fabrication of Glass–Ceramic Composite Materials for Dental Application, Bioceram. Dev. Appl. 1 (2011) 1–4.

[22] A.E. Danks, S.R. Hall, Z. Schnepp, The evolution of 'sol–gel' chemistry as a technique for materials synthesis, Mater. Horizons. 3 (2016) 91–112.

[23] A. Mali, A. Ataie, Influence of the metal nitrates to citric acid molar ratio on the combustion process and phase constitution of barium hexaferrite particles prepared by sol–gel combustion method, Ceram. Int. 30 (2004) 1979–1983.

[24] J.M. Miller, B. Dunn, J.S. Valentine, J.I. Zink, Synthesis conditions for encapsulating cytochrome c and catalase in SiO2 sol–gel materials, J. Non. Cryst. Solids. 202 (1996) 279–289.

[25] H. Aguiar, J. Serra, P. González, B. León, Structural study of sol–gel silicate glasses by IR and Raman spectroscopies, J. Non. Cryst. Solids. 355 (2009) 475–480.

[26] L.L. Sepulveda, P., Jones, J.R., Hench, In vitro dissolution of melt derived 45 S5 and sol–gel derived 58 S bioactive glasses., Biomed. Mater. Res. 61 (2002) 301–311.

[27] L.L.Diaz–Flores, G.Luna–Barcenas, J.GONZALEZ–HERNANDEZ, Yu.V.VOROBIEV, Preparation and Optical Properties of SiO2 Sol–Gel Made Glass Colored with Carminic Acid, J. Sol–Gel Sci. Technol. 33 (2005) 261–267.

[28] P. Innocenzi, Infrared spectroscopy of sol–gel derived silica–based films: A spectra–microstructure overview, J. Non. Cryst. Solids. 316 (2003) 309–319.

[29] R.S. Pryce, L.L. Hench, Tailoring of bioactive glasses for the release of nitric oxide as an osteogenic stimulus, J. Mater. Chem. 14 (2004) 2303.

[30] B. Sarker, W. Li, K. Zheng, R. Detsch, A.R. Boccaccini, Designing Porous Bone Tissue Engineering Scaffolds with Enhanced Mechanical Properties from Composite Hydrogels Composed of Modified Alginate, Gelatin, and Bioactive

Glass, ACS Biomater. Sci. Eng. 2 (2016) 2240–2254.

[31] D. Lukito, J.M. Xue, J. Wang, In vitro bioactivity assessment of 70 (wt.)% SiO2 – 30 (wt .)% CaO bioactive glasses in simulated body fluid, Mater. Lett. 59 (2005) 3267–3271.

[32] J.M.F. Ferreira, S.M. Olhero, A. Kaushal, Is the ubiquitous presence of barium carbonate responsible for the poor aqueous processing ability of barium titanate?, J. Eur. Ceram. Soc. 33 (2013) 2509–2517.

[33] F.Z. Ren, Y. Leng, Carbonated Apatite, Type–A or Type–B?, Key Eng. Mater. 493–494 (2012) 293–297.

[34] I. Notingher, J.R. Jones, S. Verrier, I. Bisson, P. Embanga, P. Edwards, et al., Application of FTIR and Raman Spectroscopy to Characterisation of Bioactive Materials and Living Cells, Spectrosc. Int. J. 17 (2003) 275–288.

[35] S.N.F.M. Noor, N.S.M. Zain, P.Y. Wei, N.S. Azizan, H. Mohamad, Development of sol–gel bioactive glass for hard tissue regeneration, AIP Conf. Proc. 1791 (2016) 020017–1–6.

[36] J. Ge, M. Li, Q. Zhang, C.Z. Yang, P.H. Wooley, X. Chen, et al., Silica Aerogel Improves the Biocompatibility in a Poly– –Caprolactone Composite Used as a Tissue Engineering Scaffold, Int. J. Polym. Sci. 2013 (2013) 1–7.

[37] S.H. Huang, Y.J. Chen, C.T. Kao, C.C. Lin, T.H. Huang, M.Y. Shie, Physicochemical properties and biocompatibility of silica doped β–tricalcium phosphate for bone cement, J. Dent. Sci. 10 (2015) 282–290.

Chapter 6

The present chapter was published on:
Journal of the American Ceramic Society;
Volume 101, Issue 7,
20 January2018,
Pages 2831-2839.
Doi: 10.1111/jace.15450

Effects of catalysts on polymerization and microstructure of sol–gel derived bioglasses

Basam A. E. Ben–Arfa, Hugo R. Fernandes, Isabel M. Miranda Salvado*, José M. F. Ferreira and Robert C. Pullar*

Department of Materials and Ceramic Engineering / CICECO – Aveiro Institute of Materials, University of Aveiro, 3810–193 Aveiro, Portugal

*To whom correspondence should be addressed: isabelmsalvado@ua.pt, rpullar@ua.pt

Keywords: Bioceramics; Catalysts/Catalysis; Glass–ceramics; Polymers/Polymerization; Sol–gel

Abstract

This work investigates the effects of the type and concentration of acid catalysts on the microstructural features of silica–rich bioactive glasses (75Si–16Ca–5Na–4P, in mol%) synthesized from acetate and nitrate precursor salts, using an innovative rapid sol–gel method, followed by thermal stabilization at 550 °C. The results of XRD, SEM, Fourier Transform Infrared Spectrometer (FTIR) and solid state MAS NMR analysis revealed that the lower degrees of polymerization and network connectivity were found for bioglass powders obtained in the presence of high acid concentrations. A low amount of citric acid gave a polymerization degree similar to that obtained in the absence of any catalyst, but the synthesis time was as short as that found for high acid concentrations. The XRD and FTIR results demonstrated amorphous glass powders free of any nitrate by–products. The microstructure and degree of polymerization could be modified by changing the type and concentration of acid catalyst, enabling one to tailor the bioactivity of glasses even without changing the starting composition.

1. Introduction

The synthesis of silicate glasses by sol–gel method is involving the hydrolysis and condensation process of silicon alkoxide (usually tetra–ethyl ortho–silicate, TEOS, $C_8H_{20}O_4Si$), where water is consumed partially or totally in a hydrolysis step, and extracted in a condensation step **[1]**. The hydrolysis and condensation of alkoxides is extensively explained and addressed by Brinker and co–workers **[2]**. They reported hydrolysis reactions catalyzed by acid or base can be promoted by increasing H_2O/Si to some extent under acidic conditions. Also, they stated that pH plays crucial role in hydrolysis and condensation. Cihlar **[3]** reported that hydrolysis and condensation reactions do not depend on the type of catalyst, but are strongly dependent on the pH of the solution.

The type of catalyst used affects dramatically the final properties, such as porosity, optical, and structural properties, and the selection of the catalyst depends on the desired properties of the final product **[4]**. Both acid and base catalysts could be used. Many authors suggest that using a certain amount of a mineral acid (inorganic acid) is a more effective catalyst than an equivalent amount of base **[2]**.The mineral (inorganic) acids such as sulfuric acid, hydrochloric acid, and nitric acid are strong, being the most commonly used as catalysts. They trigger the hydrolysis reaction in a very short time (a few minutes) **[5]**.

The increase in inorganic acids concentration in the sample is the major drawback of using them as catalysts, because of the problems associated with the elimination of their by–products. As a trial to reduce the inorganic acid concentration in the sol–gel glass, Faure et al. replaced the strong inorganic acids (~0.5–2 mol L^{-1}) with much lower quantities of weak organic acids (0.5–50 mmol L^{-1}) **[6]**, and they successfully used citric acid as catalyst for synthesis of 45S5 bioactive glass–ceramic.

Salts of organic acids, in particular acetates, are potential candidates as metal precursors for sol–gel glasses, while nitrates are the most commonly used inorganic salts. The advantage of using acetates instead of nitrates is to reduce the crystallization tendency of the glasses **[7]**, contrarily to nitrates that tend to induce crystallization during the dehydration process, leading to lower degrees of homogeneity as described by McCarthy **[8]**. The tendency to crystallize can be reduced by extracting as much water as possible from the sample by evaporation before gelling **[7]**. This problem has been recently addressed and solved by a novel rapid drying protocol using a rotary evaporator **[9]** developed by the authors. On the other hand, the major drawback of acetates is the higher temperatures required for

their thermal degradation in subsequent processing/stabilization, in comparison to nitrates, this being a potential source of carbonaceous residues. Also, acetate salts give sols with higher pH values which undergo gelation in shorter times **[7]**.

As described in the preceding paragraphs, Faure et al. **[6]**, made a good contribution using organic acid as catalyst to minimize the inorganic acid concentration in the final product. Nevertheless, the problem remained unsolved, since they obtained a highly crystallized glass ceramic.

Another process is TEOS hydrolysis in a solution of water and ethanol using different hydrated nitrate metal salts (crystallized metal nitrate molecules bonded loosely to a number of water molecules) **[10–14]**. Friberg and co–workers used hydrated copper nitrate to hydrolyse tetraethoxysilane, the copper ions exhibiting strongly acidic behaviour in ethanol, allowing the liberation of 2 protons for each copper ion **[10]**. Amran et al **[11]** used calcium nitrate tetrahydrate to catalyse tetraethoxysilane, where the water molecules attached to the calcium nitrate tended to hydrate tetraethoxysilane, and disperse evenly with the silica gel after extracting ethanol in drying process. Selle et al. **[13]** added hydrated metal nitrates to a solution of ethanol and TEOS, where they demonstrated that the hydrolysis of TEOS was achieved by the reaction of water molecules attached to the metal nitrates, without the need to add distilled water, which resulted in colloidal metals being incorporated into the silica gel matrix. This approach has not been used so far to synthesize bioactive glasses.

The aim of this work is to implement a novel sol–gel approach for preparing catalyst–free, and organic solvents–free, glass powders using nitrate salts and compare their microstructural properties with those of three other glass samples synthesized from the traditional nitrate and acetates salts.

From a literature overview on sol–gel biomaterials design, one becomes fully aware about the tremendous amount of work that has been performed aiming at disclosing the effects of catalysts on glass properties. However, little attention has been addressed so far to unveil their effects on the microstructure and the degree of glass polymerization, which are very important features in deciding the bioactivity of the glasses at early stages.

2. Materials and methods

2.1. Glass synthesis

The bioglass samples were synthesized using the sol–gel method by employing 4 different synthesis paths, combined with an innovative rapid drying protocol using a rotary evaporator, recently disclosed to be able to produce an amorphous gel in only 1 hour **[15]**. This is more than 100 times faster than the quickest reported standard drying methods, and avoids the need for the usual slow drying and aging of the gels. In all cases, the same basic formula was used for the glass, being a high–silica–content, 4–component (SiO_2–CaO–Na_2O–P_2O_5) system. This was prepared with a stoichiometry of 75Si–16Ca–5Na–4P (in mol%), with a calcium–phosphorous molar ratio set at 4 (Ca:P = 4) **Table 6.1**. This composition is referred to throughout as S75C16. To compare the catalyst effects, different combinations of reagents were used: nitric acid with acetate salts, citric acid with nitrate salts, and nitrate salts alone with the absence of any catalyst.

Table 6.1: The compositions and designations of synthesised glasses.

Designation	Composition (mol %)	Salt precursor	Catalyst
S75C16–1	$75SiO_2$–16CaO–$2.5Na_2O$–$2P_2O_5$ Si75–Ca16–Na5–P4	Acetate	1.2 mol L^{-1} nitric acid
S75C16–2		Nitrate	None
S75C16–3		Nitrate	0.05 mol L^{-1} citric acid
S75C16–4		Nitrate	0.15 mol L^{-1} citric acid

In the first route, S75C16–1, calcium acetate monohydrate ($Ca(C_2H_3O_2)_2$ H_2O, ≥ 99.0%) and sodium acetate (Na ($C_2H_3O_2$), ≥ 99.0%) were used as precursors for calcium and sodium. Nitric acid (HNO_3, ≥65.0%) was used as catalyst. The other 3 synthesis routes used calcium nitrate tetrahydrate ($Ca(NO_3)_2$ $4H_2O$, 99%) and sodium nitrate ($NaNO_3$, ≥99%) as precursors for calcium and sodium. The sample S75C16–2 was synthesized in the absence of any catalyst, whereas different amounts of citric acid ($C_6H_8O_7$, 99.5%–102%) were added in the preparation of the samples S75C16–3 and S75C16–4 as detailed in **Fig. 6.1**.

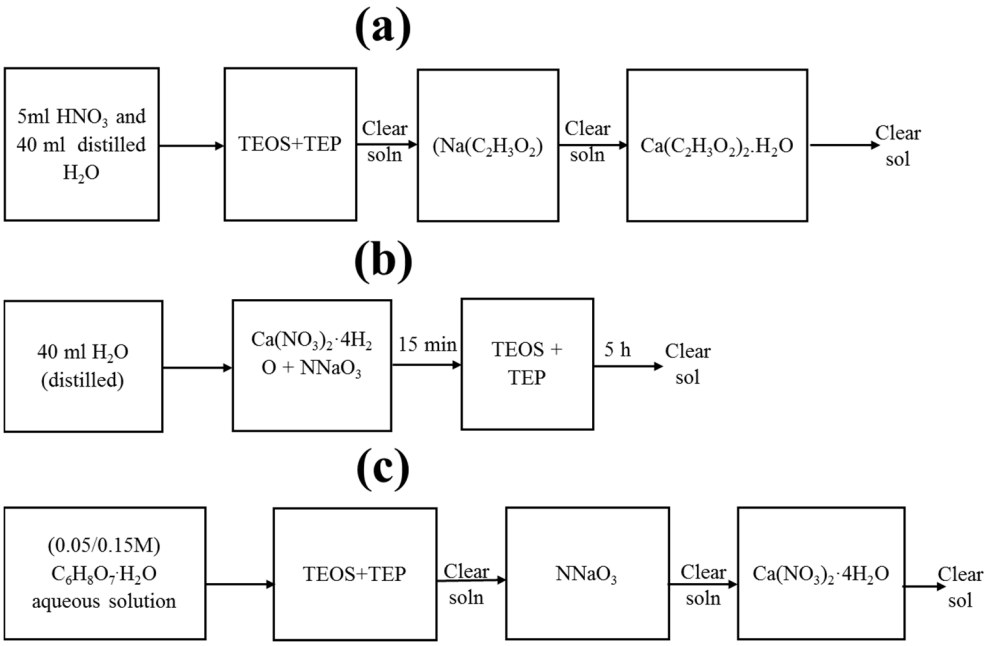

Fig. 6.1: Flowchart schemes for the sol–gel synthesis of glass samples: (a), S75C16–1; (b), S75C16–2; (c), S75C16–3/4

Distilled water was used as a solvent for all of the salts, and tetra–ethyl ortho–silicate (TEOS, $Si(C_2H_5O)_4$, 98%) and tri–ethyl phosphate (TEP, $PO_4(C_2H_5)_3$, ≥99.8%) were used as precursors for silica and phosphorous for all synthesis routes. All reagents were supplied by Sigma–Aldrich. To maintain a clear solution, the amount of water used was set to 13 times the total number of moles of all reactants for all synthesis routes.

2.1.1. Acetate salts and nitric acid route S75C16–1

An aqueous solution was prepared of 40 mL distilled water and 5 mL nitric acid. S75C16–1 was obtained by quickly adding to this aqueous solution TEOS and TEP, one after the other, while mixing using a magnetic stirrer at room temperature, resulting in a clear solution. Sodium acetate as solid salt was then immediately added to the solution, and stirred for 15 minutes to fully dissolve. Subsequently, calcium acetate was added in solid form and magnetic stirring (1100 rpm) was kept for a further 1 hour to complete dissolution, obtaining a clear transparent sol. The synthesis procedure is shown in the flow chart diagram of **Fig. 6.1(a)**.

2.1.2. Nitrate salts catalyst acid–free route S75C16–2

S75C16–2 was obtained employing a 2–step process. Calcium and sodium nitrates were added to 40 mL distilled water at room temperature, and stirred for 15 minutes until they fully dissolved to give a clear solution. TEOS and TEP were then quickly added, one after the other, while stirring. A transparent sol was obtained after 5 hours stirring at 1100 rpm. The synthesis procedure is shown in the flowchart diagram in **Fig. 6.1(b)**. The process without a catalyst acid is clearly slower, requiring 5 hours to produce a clear sol.

2.1.3. Nitrate salts and citric acid route S75C16–3 and S75C16–4

S75C16–3 and S75C16–4 were obtained by adding TEOS and TEP to aqueous solutions containing 0.42 and 1.26 g of citric acid (CA), respectively, in 40 mL of distilled H_2O (equivalent to a concentration of 0.05 and 0.15 mol L^{-1}, respectively), at room temperature under stirring for 30 minutes to obtain a clear solution. Although the higher catalyst concentration produced a clear sol in a shorter time and resulted in a faster hydrolysis, both samples were stirred for 30 minutes. Then sodium nitrate and calcium nitrate were quickly added, one after the other. After the last precursor was added, the solution was stirred for a further 30 minutes to obtain a clear transparent sol. The synthesis procedure is outlined in the flowchart diagram of **Fig. 6.1(c)**.

2.1.4. Drying and heating of precursor sols

For each glass synthesis route, the obtained clear sol was then rapidly dried using a rotary evaporator (Buchi 210 Rotavapor with V–850 vacuum controller and V–700 dia–phragm vacuum pump), in a 1000 mL pear–shaped flask while rotating in a water bath at 55°C and under a low pressure of 50 mbar for 15 minutes, as described else–where **[9]**. All dried gels were stabilized by heating at 550°C for 1 hour. The heating rate was 1°C/min up to 300°C, and then 10°C/min up to 550°C, with natural cooling **[15]**.

2.2. Glass Characterization

For all characterization techniques, the powder samples were sieved through a 40–63 µm mesh. The microstructure and morphology of the stabilized glasses were observed by scanning electron microscope (SEM, S–4100, Hitachi, Japan), with samples coated with carbon.

Crystalline and amorphous phases of the samples were determined by X–ray diffraction (XRD, PANalytical XPERT–PRO Diffractometer system), using Cu–Kα radiation (Kα = 1.54059), with 2θ varying from 6 to 70° in steps of 0.026 s^{-1}. The diffraction patterns were compared with JCPDS standards.

Solid–state nuclear magnetic resonance (NMR) analysis was carried out using magic angle spinning MAS–NMR for silicon. The ^{29}Si MAS–NMR spectra were measured, to investigate the silica environments and degree of silica polymerization of the stabilized glass samples, on an ASX 400 spectrometer (Bruker, Germany) operating at 79.52 MHz (9.4 T), using a 7 mm probe at a spinning rate of 5 kHz. The pulse length was 2 µs with 60 seconds delay time. Kaolinite was used as a chemical shift reference. ^{29}Si MAS NMR spectra were deconvoluted using dimFit software.

Infrared transmittance spectra of the glasses were obtained using a Fourier Transform Infrared Spectrometer (FTIR, Tensor 27, Brucker, Germany) in the range of 350–4000 cm^{-1}, with 128 Scans and 4 cm^{-1} resolution. The pellets were prepared by pressing a mixture of KBr and glass powder with ratio of 150:1 of KBr: glass by weight.

3. Results

3.1. Structure of the glasses

3.1.1. MAS–NMR analysis of stabilized powders

Fig. 6.2 shows the ^{29}Si MAS NMR spectra of all 4 sol–gel derived glasses stabilized at 550°C. The ^{29}Si NMR analysis allows us to monitor the environment of the Si atoms. Deconvoluted proportions of the ^{29}Si MAS NMR spectra enabled identification of Q^n species, where n denotes the number of oxygens bridging to silica, and n can be 0, 1, 2, 3 or 4 **[15]**. The degree of condensation (D_c) can be calculated using Equation 1 below.

$$D_c = \frac{1\times Q^1+2\times Q^2+3\times Q^3+4\times Q^4}{4} \times 100\% \quad (6.1)$$

The main peaks for the 4 glass samples lay in the chemical shift range between –109.9 and –110.5 ppm, which can be attributed to Si atoms connected to 4 bridging oxygens (BOs)

and arranged in a Q^4 environment. The Q^3 environment occurs between –99.4 and –99.9 ppm, denoting Si atoms connected to 3 BOs, where the network modifiers disrupt the chain by one non–bridging oxygen (NBO) **[16]**. Similarly, the Q^2 peak between –89.3 and –89.7 ppm denotes the portion of silica network having 2 BOs, and 2 NBOs. Network connectivity (N_c) is a value of how many BOs, on average, each Si atom is connected to.

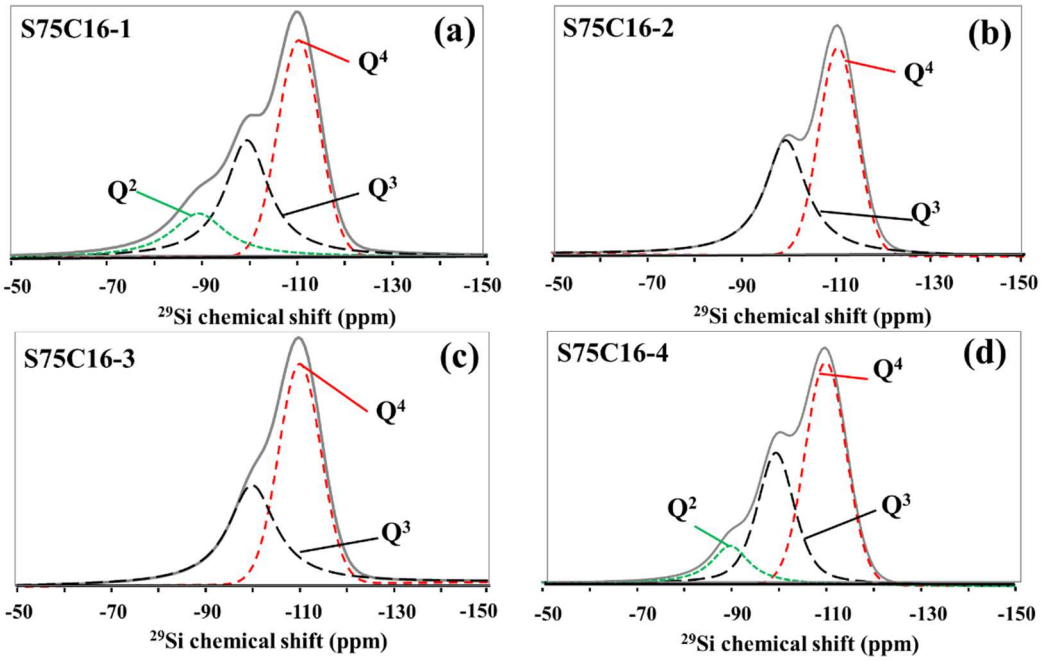

Fig. 6.2: Deconvoluted ^{29}Si MAS–NMR spectra of stabilized glass powders: (a), S75C16–1; (b), S75C16–2; (c), S75C16–3; (d), S75C16–4. MAS, magic angle spinning.

The proportions of these Q^n environments for each glass are shown in **Table 6.2** and **Figs. 6.2(a–d)**. It can be clearly observed that only S76C16–1 and S75C16–4 show any degree of Q^2 environment, and consequently they have fewer Q^3 and Q^4 environments, meaning they have a significantly greater number of NBOs than S76C16–2 and S75C16–3. The glass S76C16–1 synthesized in the presence of nitric acid as catalyst has the greatest number of NBOs, but both samples synthesized in the presence of the higher amounts of acid catalysts show significantly higher proportions of NBOs than those prepared in the absence or in the presence of a low amount of acid catalyst, and they are very similar in nature.

The quantitative NMR analysis spectra show that the glass samples have very different network structures. S75C16–1 has the lowest D_c and N_c values, of 81.6%, and 3.3,

respectively, followed by S75C16–4 with a D_c of 84.9% and N_c of 3.4. The other 2 samples, S75C16–2 and S75C16–3, both possess much higher, and very similar, D_c and N_c values of ~89% and ~3.55, respectively. Such discrepancies worth underlining, considering that the chemical composition is the same for all samples, which also underwent similar drying and stabilization conditions along the preparation steps.

Table 6.2: The structural parameters of the stabilized glasses assessed by ^{29}Si MAS–NMR spectroscopy, degree of polymerization (Q^n) degree of condensation (Dc), and network connectivity (Nc)

	Q^n							N_c
	Q^2		Q^3		Q^4		D_c	from ^{29}Si
Sample	**Peak position (ppm)**	**Integral %**	**Peak position (ppm)**	**Integral %**	**Peak position (ppm)**	**Integral %**	**(%)**	**MAS NMR**
S75C16–1	**–89.3**	**17.9**	**–99.5**	**37.9**	**–110.3**	**44.3**	**81.6**	**3.3**
S75C16–2	**–**		**– 99.5**	**47.8**	**–110.5**	**52.2**	**8.1**	**3.5**
S75C16–3	**–**		**–99.9**	**43.6**	**–110.0**	**56.4**	**89.1**	**3.6**
S75C16–4	**–89.7**	**12.6**	**–99.4**	**35.1**	**–109.9**	**52.3**	**84.9**	**3.4**

Therefore, the observed network structural differences derive only from the different types and concentrations of acid catalysts used in the synthesis. The network structures range from a more reactive material that is likely to exhibit a higher rate of dissolution in body fluids to a relatively inert material (S75C16–3). This can be attributed to the lower condensation rates that can be achieved at higher acid concentrations, and lower pH values around 1.5 to 2, as claimed by Cihlar **[3]**. The samples with lower network connectivity are likely to be more reactive upon immersion in SBF in comparison to the other glasses, since the lower network connectivity means a greater population of NBOs to disrupt the silica network, leading to an easier dissolution of glass components. Conversely, increasing the network connectivity increases the chemical durability of the whole structure **[17,18]**.

The acid concentration played the main role in the silica network polymerization, rather than the metal salts used. Plotting the 4 synthesized glasses in order from lower to higher pH, the silica network made with a lower pH resulted in a more disrupted network, with a higher

population of NBOs. It can be seen clearly that the strong inorganic acid (1.2 mol L^{-1} HNO_3) has the greatest effect on the final glass structure (S75C16–1), leading to the softest silica structure (the lowest D_c and N_c values, of 81.6%, and 3.3, respectively). This can be attributed to the faster hydrolysis and slower condensation that occurred in the more acidic medium. The second weakest structure was found in S75C16–4, with the highest concentration (0.15 mol L^{-1}) of organic acid used as a catalyst. In S75C16–2, the nitrates in the metal salt also have a strong acidic contribution, despite the absence of an added acid catalyst, leading to the third softest structure (Dc of 88.1% and N_c of 3.5). This D_c is almost identical to that of S75C16–3 (89.1%), which had a very low amount of organic acid catalyst, and these results suggest that the nitrate salts make a greater contribution that the added acid catalyst when it is at such low concentration (0.05 mol L^{-1}). When the hydrolysis and condensation occurs in a higher pH environment, it effectively delays the hydrolysis and fastens the condensation, leading to stronger, more connected silica structure. This confirms that the acid concentration plays the main role in the final network structure, when present in sufficient quantities.

From the above observations, it can be suggested that the acid concentration plays a key role in determining the polymerization degree of the glass, and this can be attributed to lower condensation rate that can be achieved at higher acid concentration and lower pH values. This may be considered as a useful tool to tailor the bioactivity of a certain material to fit into a desired application window, without the need to change its composition, especially in cases where it is important to keep the composition molar % fixed, as the case of commercial glasses such as 45S5.

3.1.2. X–ray diffraction (XRD)

Fig. 6.3 shows the XRD patterns for all glass samples after stabilization at 550°C for 1 hour. The XRD data depicts the highly amorphous character of all glasses, with a small reflection corresponding to calcium silicate (Ca_2O_4Si, PDF card # 01–077–0420) in samples S75C16–1 to S75C16–3. This peak is largest in S75C16–2 and S75C16–3, the 2 samples which also had the greatest levels of condensation and network connectivity. The sample S75C16–1 had only an extremely small crystalline peak. The S75C16–4 one having low degrees of polymerization and network connectivity is completely amorphous. Therefore,

the use of greater amounts of acid, and in particular citric acid, results in an amorphous glass, with no crystalline component at all.

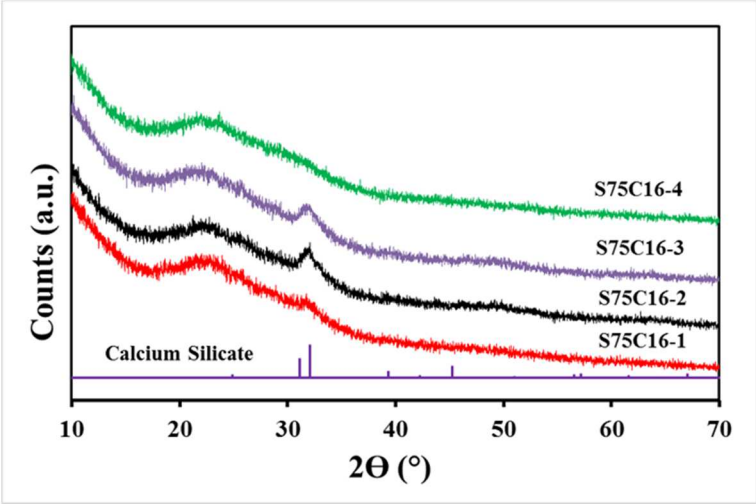

Fig. 6.3: X–ray diffractogram of glass compositions after stabilization at 550°C for 1 h.

3.1.3. FTIR analysis of glasses

The FTIR spectra of the investigated sol–gel glasses are presented in **Fig. 6.4**. They are typically dominated by a broad band between 1000 and 1300 cm^{-1} related to asymmetric stretching modes, centred on an intense peak at ~1085 cm^{-1}, which represents the transverse optical silica (TO_1) mode. This band in the glass S75C16–4 splits-into 2 distinct peaks at 1085 and 1049 cm^{1}, as a result of interaction of the carbon and silica **[19]**. This is accompanied by the evolution of the 880 (879) cm^{-1} peak, related to the CO_3^2 group, which could be attributed to the substitution of phosphate ions in B–type hydroxyapatite (HAp) **[20]**, which can even result in carbonate apatite. This is probably due to carbonate residues as this sample was synthesized with the higher amount of citric acid. Also, the peak at 1049 cm^{-1} can be assigned to asymmetric bending for P– O groups. The shoulder at ~1220 cm^{-1} represents the Si– O–Si (TO_2) stretching mode **[21]**. The stretching vibration band at ~950 cm^{1} is assigned to Si–OH **[22]**, and Si–O might also have a contribution to this vibration band **[23]**.

The broad band at ~790 cm^{-1} can be identified as the bending vibration of Si–O–Si **[22]**. The small notched peak at ~660 cm^{-1} can be assigned to the Si–O–Ca asymmetric bending mode

[24], becoming more defined as the calcium modifies the silica structure and starts to form the crystalline calcium silicate phase as depicted by XRD **Fig. 6.3**, and indeed these 2 peaks are strongest in S75C16–2 and S75C16–3. The small band near 860 cm^{-1} is a common feature for alkali silicate glass and assigned to Na, but it also may be attributed to the presence of Ca [**23**]. The appearance of the twin peaks at ~565 and ~601 cm^{-1} can be attributed to the presence of the phosphate group PO_4^3 **[25]**. The 1384 cm^{-1} peak is due to N–O stretching of residual nitrate anions resulting from the HNO_3 used as a catalyst or due to the nitrate salts residues from the synthesis **[15]**. Interestingly, this peak is strongest for the sample synthesized from just nitrate salts without any acid catalyst. It is also noticeable that this peak is weaker for the S75C16–3 sample with lower amount of citric acid, being absent in the sample S74C16–4 with higher added amount of citric acid, suggesting that citric acid also favours the removal of nitrates from the product after stabilizing at 550°C. The band at ~879 cm^{-1} belongs to a carbonate C– O vibration band **[22,23]** and is present in S75C16–4, the sample made with the larger amount of citric acid, suggesting this catalyst favours the formation of a carbonate compound.

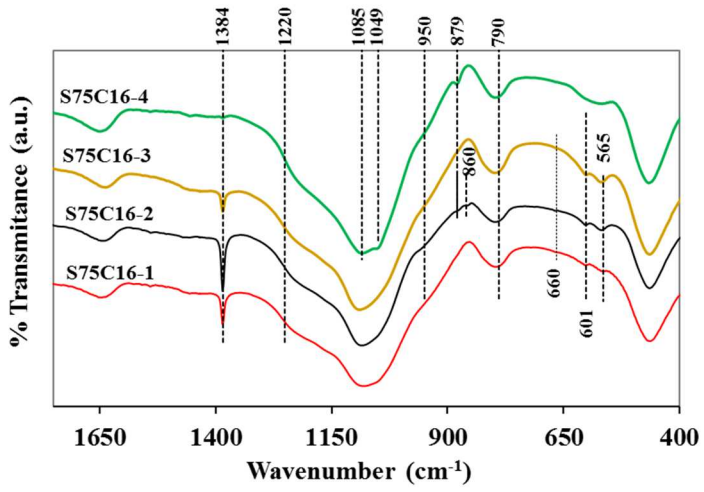

Fig. 6.4: FTIR spectra of glass powders after thermal stabilization at 550°C for 1 h. FTIR, Fourier Transform Infrared Spectrometer.

3.2. Scanning electron microscopy analysis

The morphological features of the 4 stabilized glass powders are shown in the micrographs of **Fig. 6.5**. As can be clearly seen, all of the samples consisted of sub–micrometer primary particles, agglomerated to form larger scale clusters up to 1–2 µm in size. It is quite clear that the type and concentration of the acid and precursors had a crucial effect on the morphology of the glass powder. For S75C16–1, synthesized in a medium of strong inorganic acid, the powder showed a compact microstructure evolved from small clusters of ~1 µm. S75C16–4, synthesized using the higher levels of organic acid catalyst, consisted of a smaller, looser particles, forming less compacted clusters, but with an overall morphology similar to that of S75C16–1. S75C16–3, made with a much lower acid concentration than the previous 2 samples, shows a different microstructure composed of several layers, each layer built of clusters of smaller particles with a size range of ~100–200 nm. It can be observed that as the acid concentration decreased, so did the individual particle size (down to ~100 nm in S75C16–3), and layers forming the microstructure become more apparent.

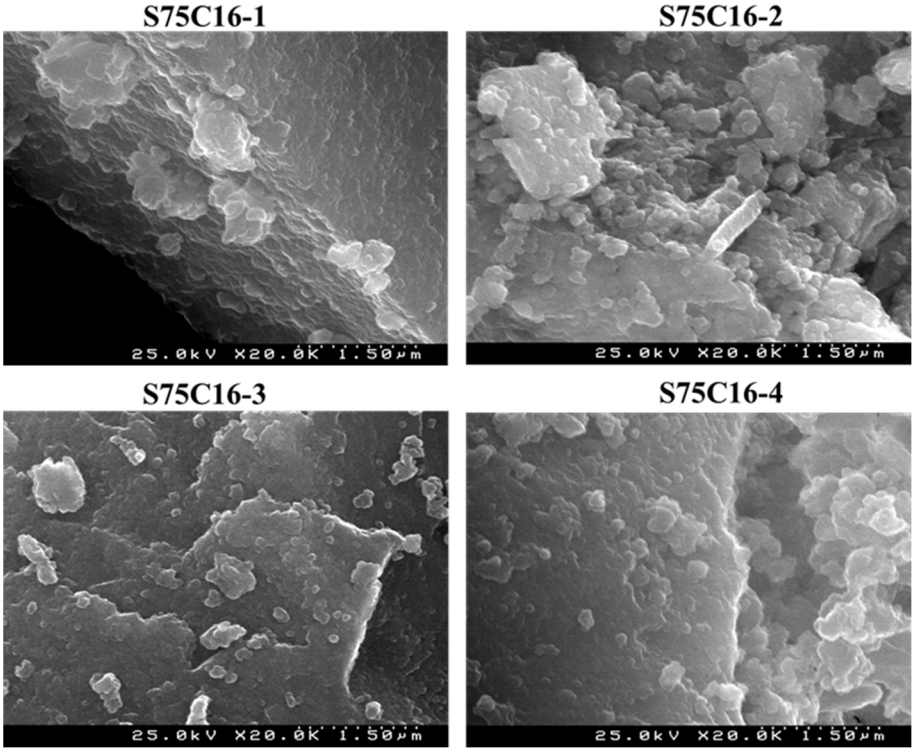

Fig. 6.5: SEM; scanning electron microscopy images at 20k magnification of the 4 glass samples after thermal stabilization at 550°C for 1 h.

The sample synthesized without any added acid catalyst (the self–catalysed S75C16–2) required a longer synthesis time compared to those using a catalyst (5 hours vs 1–1.5 hours for the others).

This has also resulted in a more disordered looking sample, with fewer layers combined with larger clusters, but built of small particles ~150 nm in size. It can be concluded that the acid concentration plays an important role in deciding the final microstructure of the synthesized sample. As the acid concentration decreased (i.e., pH increased), the basic particles became smaller, approaching 100 nm, but the overall microstructure became less ordered and less compact.

4. Conclusions

Quaternary (Si–Na–Ca–P) bioactive glass powders were successfully synthesized by sol–gel from acetate or nitrate precursor salts in the absence and in the presence of different types and concentrations of acid catalysts. Starting from the same chemical composition and adopting similar drying and stabilizing conditions, noticeable differences in the polymerization kinetics and network structures were obtained when following 4 different synthesis routes: 1) Acetate salts and nitric acid S75C16–1; 2) Nitrate salts in the absence of any acid catalyst S75C16–2; 3) Nitrate salts and low citric acid concentration (0.05 mol L^{-1}) as catalyst S75C16–3; 4) Nitrate salts and high citric acid concentration (0.15 mol L^{-1}) as catalyst S75C16–4. The use of acetate salts led to the lowest degrees of condensation (Dc) and network connectivity (N_c), but the thermally stabilized sample still exhibits considerable residual amounts of nitrogen coming from the high amount of catalyst. To the authors' knowledge, the preparation of biomedical glasses in the absence of any catalyst has never been reported so far. Interestingly, the catalyst–free sample S75C16–2 contains the highest amount of residual nitrogen combined with high D_c and Nc values. The highest extents of condensation and network connectivity were observed for the sample synthesized by route 3 (S75C16–3) in the presence of a low amount of citric acid. In contrast the sample S75C16–4 seems to be the most interesting one, since it contains a negligible amount of nitrogen residues and exhibits an amorphous structure with relatively low values of D_c and Nc after thermal stabilization at 550 °C. From the above results it can be concluded that the type and concentration of catalyst play major roles in determining the condensation rate and

the overall network connectivity. The possibility of tailoring the Nc without changing the composition is a very interesting feature of this synthesis route. Moreover, using citric acid as catalyst enables ensuring almost complete extraction of the nitrates as by–products after thermal stabilization at a relatively low temperature. These attractive features deserve to be further explored to better judge the appropriateness of the most commonly used nitrate salts as precursors in the sol–gel synthesis of glass.

Acknowledgments

R.C. Pullar wishes to thank the FCT Grant IF/00681/2015 for supporting this work. B. A. E. Ben–Arfa thanks FCT grant BIONANOSCULP PTDC/EPH–PAT/6281/2014 for supporting him during this work. This work was developed in the scope of the project CICECO Aveiro Institute of Materials (Ref. FCT UID/CTM/50011/2013), financed by national funds through the FCT/MEC and when applicable co–financed by FEDER under the PT2020 Partnership Agreement.

References

[1] R.A. Assink, B.D. Kay, Sol–gel kinetics, III. Test of the statistical reaction model, J. Non. Cryst. Solids. 107 (1988) 35–40.

[2] C.J. Brinker, Hydrolysis and condensation of silicates: Effects on structure, J. Non. 100 (1988) 31–50.

[3] J. Cihlar, Hydrolysis and polycondebsation of ethyl silicate. 1. Effect of pH and catalyst on the hydrolysis and polycondensation of tetraethoxysilane (TEOS), Colloid Surf. A. 70 (1993) 239–251.

[4] M. a. Fardad, Catalysts and the structure of SiO2 sol–gel films, J. Mater. Sci. 35 (2000) 1835–1841.

[5] Q.Z. Chen, Y. Li, L.Y. Jin, J.M.W. Quinn, P.A. Komesaroff, A new sol–gel process for producing Na2O–containing bioactive glass ceramics, Acta Biomater. 6 (2010) 4143–4153.

[6] J. Faure, R. Drevet, A. Lemelle, N. Ben Jaber, A. Tara, H. El Btaouri, et al., A new sol–gel synthesis of 45S5 bioactive glass using an organic acid as catalyst, Mater. Sci. Eng. C. 47 (2015) 407–412.

[7] L.C. Klein, Sol– gel technology for thin films, fibers, preforms, electronics, and specialty shapes, Noyes Publications, New Jersey, 1987.

[8] R. Roy, Gel route to homogeneous glass preparation:II, Gelling and desiccation, J. Am. Ceram. Soc. 54 (1971) 639–640.

[9] B.A.E. Ben–Arfa, I.M.M. Salvado, J.M.F. Ferreira, R.C. Pullar, Novel route for rapid sol–gel synthesis of hydroxyapatite, avoiding ageing and using fast drying with a 50–fold to 200–fold reduction in process time, Mater. Sci. Eng. C. 70 (2017) 796–804.

[10] S.E. Friberg, J. Yang, A. Amran, J. Sjöblom, G. Farrington, Reaction between copper nitrate hydrate and tetraethoxysilane in methanol. A29Si NMR investigation, J. Phys. Chem. 98 (1994) 13528–13531.

[11] A. Amran, S.E. Friberg, J. Sjöblom, Silicon NMR spectra from the reaction species between tetraethoxysilane and calcium nitrate hydrate, J. Dispers. Sci. Technol. 15

(1994) 621–632.

[12] N.P. Bansal, Influence of several metal ions on the gelation activation energy of silicon tetraethoxide, in: 90th Annu. Meet. Am. Ceram. Soc., 1988: p. 17.

[13] M.H. Selle, F. Fredriksen, J. Sjoblom, A. Christy, S.E. Friberg, Hydrolysis and condensation in systems of silicon alkoxide and hydrated calcium and nickel nitrate in alcohols as followed by means of Fourier–transform infrared spectroscopy, Acta Chem. Scand. 50 (1996) 12–17.

[14] B.Z. Shalumov, A.M. Bessarabov, M. V. Mikheev, Kinetic of autocatalytic hydrolysis of TEOS in the presence of aluminium nitrate, React. Kinet. Catal. Lett. 25 (1984) 177–179.

[15] B.A.E. Ben–Arfa, I.M. Miranda Salvado, J.M.F. Ferreira, R.C. Pullar, A hundred times faster: Novel, rapid sol–gel synthesis of bio–glass nanopowders (Si–Na–Ca–P system, Ca:P = 1.67) without aging, Int. J. Appl. Glas. Sci. 8 (2017) 337–343.

[16] B. Yu, C.A. Turdean–Ionescu, R.A. Martin, R.J. Newport, J. V. Hanna, M.E. Smith, et al., Effect of calcium source on structure and properties of sol–gel derived bioactive glasses, Langmuir. 28 (2012) 17465–17476.

[17] A. Tilocca, Structural models of bioactive glasses from molecular dynamics simulations, Proc. R. Soc. A Math. Phys. Eng. Sci. 465 (2009) 1003–1027.

[18] H.K. Ting, S.J. Page, G. Poologasundarampillai, S. Chen, B. Yu, J. V. Hanna, et al., Phosphate content affects structure and bioactivity of sol–gel silicate bioactive glasses, Int. J. Appl. Glas. Sci. 8 (2017) 372–382.

[19] M. Santoro, F. Gorelli, J. Haines, O. Cambon, C. Levelut, G. Garbarino, Silicon carbonate phase formed from carbon dioxide and silica under pressure, Proc. Natl. Acad. Sci. 108 (2011) 7689–7692.

[20] L. Radev, N. Y. Mostafa, I. Michailova, I. M. M. Salvado, M. H. V. Fernandes, In vitro bioactivity of collagen/Calcium Phosphate Silicate composites, Cross–Linked with Chondroitin Sulfate, Int. J. Mater. Chem. 2 (2012) 1–9.

[21] H. Aguiar, J. Serra, P. González, B. León, Structural study of sol–gel silicate glasses by IR and Raman spectroscopies, J. Non. Cryst. Solids. 355 (2009) 475–480.

[22] R. Catteauxa, F.D. Isabelle Grattepanche–Lebecqa, F. Chai, J.–C. Horneza, S. Hampshirec, C. Follet–Houttemane, Synthesis, characterization and bioactivity of bioglasses in the Na2O–CaO–P2O5–SiO2 system prepared via sol gel processing, Chem. Eng. Res. Des. 596 (2001) 47–54.

[23] P. Innocenzi, Infrared spectroscopy of sol–gel derived silica–based films: a spectra–microstructure overview, J. Non. Cryst. Solids. 316 (2003) 309–319.

[24] E.M.A. Khalil, F.H. ElBatal, Y.M. Hamdy, H.M. Zidan, M.S. Aziz, A.M. Abdelghany, Infrared absorption spectra of transition metals–doped soda lime silica glasses, Phys. B Condens. Matter. 405 (2010) 1294–1300.

[25] A. Lucas–Girot, F.Z. Mezahi, M. Mami, H. Oudadesse, A. Harabi, M. Le Floch, Sol–gel synthesis of a new composition of bioactive glass in the quaternary system SiO2–CaO–Na2O–P2O5: Comparison with melting method, J. Non. Cryst. Solids. 357 (2011) 3322–3327.

Chapter 7

The present chapter was submitted to:
Materials Science & Engineering C;
24 Sebtemper 2018,
ID is MSEC-2018-2814

Cytotoxicity and bioactivity assessments for Cu^{2+} and La^{3+} doped high silica sol–gel derived glasses

Basam A. E. Ben–Arfa [a], Ilaria E. Palamá [b], Isabel M. Miranda Salvado [a]*, José M. F. Ferreira [a] and Robert C. Pullar [a]*.

[a] *Department of Materials and Ceramic Engineering / CICECO – Aveiro Institute of Materials, University of Aveiro, 3810–193 Aveiro, Portugal*

[b] *CNR NANOTEC – Istituto di Nanotecnologia, Campus Ecotekne, Via Monteroni, 73100 Lecce, Italy*

*To whom correspondence should be addressed: isabelmsalvado@ua.pt, rpullar@ua.pt

Keywords: Sol–gel; Bioactive glass; Bioactivity; Cytotoxicity ; Taguchi method; Lanthanum ion; copper ion.

Abstract

The aim of the present work is to show the influence of two doping functional ions (Cu^{2+}, La^{3+}) incorporated in a quaternary (Si, Ca, Na, P) sol–gel derived bioactive glass system on its cytotoxicity, and bioactivity. By doping the parent glass with the two ions in singular or combined forms, sixteen glasses have been prepared by a rapid sol–gel technique. The influence of the combined doping on the cells viability was successfully evaluated by the aid of signal–noise–ratio, using Taguchi analysis. The results reveal that potential synergistic benefits can be obtained by combining the effects on the mean particle size, density, cytotoxicity, and bioactivity of the glasses samples. Cytotoxicity was significantly improved for some doping combinations, while the bioactivity of doped samples was always very similar to that of the parent glass. The improved biocompatibility of the doped glasses makes them promising candidates for biomedical applications.

1. Introduction

Bioactive glasses exhibit surface reactivity when in contact with body fluids, leading to the release of ionic products such as: Si^{4+}, Ca^{2+}, Na^{+}, and P^{5+}, which stimulate various vital mechanisms in the human body, such as gene expression and osteoblast proliferation. Moreover, bioactive glasses might also provide anti–bacterial and anti–inflammatory effects **[1]**. Since the discovery of Hench´s glass **[2]**, a tremendous amount of research work has been done in glass systems containing different mol % of these four main oxide components **[3–5]**. The roles of the related ionic species (Si^{4+}, Ca^{2+} , Na^{+}, P^{5+}) in bone regeneration and soft tissue engineering have been well established and documented **[6–9]**. The focus of the present research is shifting towards exploring the role of different functional ions that, although being present in trace quantities in human body, are essential for good metabolism. Anaemia, and bone abnormalities, can be consequences of copper deficiency and copper is considered as an essential component in gene expression **[10]**. Lanthanum is available in trace amounts in drinking water and food. It is used in the form of lanthanum carbonate as a substitute for calcium–based phosphate binders for patients with chronic kidney disease, and to minimise the risk of death from cardiovascular diseases **[11]**. In patients suffering from osteoporosis, a certain precipitation of lanthanum onto the bones was reported to stimulate osteoblast differentiation and suppression of the bone resorption, which in turn enhanced bone density **[12]**. Doping bioactive glasses with functional ions is important to modify their properties and enhance their interaction with the human body. Nevertheless, in the most cases the doping ions were added separately, and their effects were investigated apart from a parent glass **[13–15]**. No systematic studies of combined doping with multiple elements were found **[16]**. This work is devoted to a systematic study of both the single and combined effects exerted by the two functional ions La^{3+} and Cu^{2+} on the relevant in vitro properties of the parent glass, namely their cytotoxicity and bioactivity behaviours, to enable firmer conclusions to be drawn about their prospective exploitation towards enhancing the bone regeneration performance of the these bone graft materials. To the authors' knowledge, this is the first contribution to systematically study the combined effects of Cu and La ions.

2. Materials and methods

2.1. Glass synthesis

A four–component, high silica sol–gel glass with a composition of $67SiO_2–24CaO–2.5Na_2O–2P_2O_5$, thereafter labelled (HSSGG) was synthesised by employing a rapid sol–gel route, as described previously by the authors **[17]**.

Based on the HSSGG parent glass composition, six doped compositions containing 1, 3, and 5 wt.% of either La^{3+} or Cu^{2+} ions alone were prepared to study the separate influences of the added amounts of copper (Cu^{2+}) and Lanthanum (La^{3+}) ions The sample codes for the resulting compositions are as follows: (Cu1, Cu3, Cu5; and La1, La3, and La5).

Table 7.1: L9 – Taguchi design – 2variables (v), and 3 levels (n)

Levels	Variables (Wt.%)	
	Cu	La
1	1	1
2	3	3
3	5	5

Table 7.2: L9 – Taguchi array, 9 trials, 2 variables and 3 levels

Conditions		
Trial	Cu	La
E1	1	1
E2	1	3
E3	1	5
E4	3	1
E5	3	3
E6	3	5
E7	5	1
E8	5	3
E9	5	5

To distinguish the combined effects of the two ions, a Taguchi orthogonal array (L9)–n3v2 was used to prepare nine pairs of combinations from HSSGG; where: v2 denotes 2 variables, and signifies the doping ions Cu^{2+} and La^{3+}; n3 represents 3 levels for each variable, which are 1, 3 and 5 wt.%, as presented in **Table 7.1**, and **Table 7.2**.

To carry out a study based on the Taguchi array, a further 9 mutual La–Cu doped glasses were also prepared, in addition to the initial 6 individual doped glasses, meaning that 16 glasses in total were prepared starting from the parent glass HSSGG. The batch compositions are presented in wt.% **Table 7.3**, and mol ratio **Table 7.4**.

Table 7.3: Batch compositions of all synthesised glasses in wt.%

Glass	SiO_2	Na_2O	CaO	P_2O_5	CuO	La_2O_3
HSSGG	64.40	2.48	21.53	4.55	–	–
Cu1	63.76	2.46	21.32	4.50	1.00	–
Cu3	62.47	2.41	20.89	4.41	3.00	–
Cu5	61.18	2.36	20.45	4.32	5.00	–
La1	63.76	2.46	21.32	4.50	–	1.00
La3	62.47	2.41	20.89	4.41	–	3.00
La5	61.18	2.36	20.45	4.32	–	5.00
Cu1La1	63.11	2.43	21.10	4.46	1.00	1.00
Cu1La3	61.83	2.38	20.67	4.37	1.00	3.00
Cu1La5	60.54	2.33	20.24	4.28	1.00	5.00
Cu3La1	61.83	2.38	20.67	4.37	3.00	1.00
Cu3La3	60.54	2.33	20.24	4.28	3.00	3.00
Cu3La5	59.25	2.28	19.81	4.19	3.00	5.00
Cu5La1	60.54	2.33	20.24	4.28	5.00	1.00
Cu5La3	59.25	2.28	19.81	4.19	5.00	3.00
Cu5La5	57.96	2.23	19.38	4.09	5.00	5.00

The obtained gels were dried using a roto–evaporator (Buchi 210 Rotavapor with V–850 vacuum controller and V–700 diaphragm vacuum pump), in a 500 mL pear–shaped flask while rotating in a water bath at 55 ºC and under a low pressure of 50 mbar for 30 minutes

[18]. The as–dried gels were heat treated up to 800 ºC according to the schedules presented in **Table 7.5**.

Table 7.4: Batch compositions of all synthesised glasses in mol ratios

Glass	SiO_2	Na_2O	CaO	P_2O_5	CuO	La_2O_3
HSSGG	67.00	2.50	24.00	2.00	–	–
Cu1	66.47	2.48	23.81	1.98	0.79	–
Cu3	65.41	2.44	23.43	1.95	2.37	–
Cu5	64.34	2.4	23.05	1.92	3.97	–
La1	66.87	2.495	23.95	2.00	–	0.19
La3	66.61	2.485	23.86	1.99	–	0.59
La5	66.33	2.475	23.76	1.98	–	1.00
Cu1La1	66.34	2.475	23.76	1.98	0.79	0.19
Cu1La3	66.06	2.465	23.66	1.97	0.81	0.59
Cu1La5	65.78	2.455	23.56	1.96	0.82	1.00
Cu3La1	65.27	2.435	23.38	1.95	2.39	0.19
Cu3La3	64.97	2.425	23.27	1.94	2.43	0.59
Cu3La5	64.67	2.415	23.17	1.93	2.47	1.01
Cu5La1	64.19	2.395	22.99	1.92	4.00	0.20
Cu5La3	63.88	2.385	22.88	1.91	4.07	0.60
Cu5La5	63.55	2.370	22.76	1.90	4.14	1.01

Table 7.5: Details of the three stages of the heat treatment schedule

	1^{st} stage	2^{nd} stage	3^{rd} stage
Starting temperature [ºC]	25	200	400
Target temperature	200	400	800
Heating rate [ºC min^{-1}]	1	2	5
Soaking time [h]	0.5	0.5	2

The heat treated powders were then ball milled. The wet milling was performed using ethanol (EtOH) as milling medium, with an EtOH to powder mass ratio (EPR) = 1.5), balls to powder mass ratio (BPR) = 10, and a milling time of 1 h. The milling was done in a S–series–Fast Mill machine, type S2–1000 (Ceramic Instruments, Sassuolo, Italy), under a rotational speed of 390 rpm, using a sintered alumina jar of 300 cm^3 capacity (Ceramic

instruments Sassuolo, Italy). Yttria–stabilized zirconia balls with 10 mm diameter (Tosoh, Tokyo, Japan) were used as milling medium. After milling, the slurry was separated for drying in an oven at 60 ºC for 24 h. The obtained dry powders were passed through a 63 µm sieve to separate the large agglomerates from the fine powder. The resulting fine powder was characterised using the following techniques.

2.2. Glass Characterization

The average particle sizes (PS) and the particle size distributions (PSD) on a volume basis were determined via a laser diffraction particle size analyser (Coulter LS particle size analyser; Beckman Coulter, CA). Measurements were triplicated to assure confident results.

The specific surface areas (SSA) of the powders were measured using the Brunauer–Emmett–Teller (BET method, Micrometric Gemini M–2380) using N_2 as adsorbate. Samples were degassed at 200 ºC before each measurement.

The skeletal density was assessed by helium pycnometry after drying the powder samples at 60 ºC for 24 h, to eliminate any absorbed humidity and guarantee accuracy of the results.

2.3. In vitro cytotoxicity assays

In vitro cytotoxicity assays for bioactive glass were performed according to the guidelines of the International Organization for Standardisation ((ISO10993–5) **[19]**. The samples were sterilised under UV–radiation prior to performing the cytotoxicity test. Three different cell lines were chosen to execute the test; BJ (ATCC CRL–2522, Human fibroblasts), MG63 (ATCC CRL–1427, Human osteosarcoma), and C13589 (ATCC CRL–2704, Human B lymphoblast). The cells were preserved in Dulbecco's Modified Eagle Medium (DMEM, Sigma Aldrich) supplemented with 10% (v/v) of foetal bovine serum (FBS, Sigma Aldrich), penicillin (100 U mL^{-1} culture medium, Sigma Aldrich), streptomycin (100 µg mL^{-1} culture medium, Sigma Aldrich), L–glutamine (5%, Sigma Aldrich) and sodium pyruvate (5%, Sigma Aldrich). All cell lines were grown in a humidified incubator at 37 ºC, 5% CO_2, and 95% relative humidity.

The cytotoxicity was assessed following MTT assay, by measuring the activity of living cells via mitochondrial dehydrogenase. The key component of MTT is

3–[4,5–dimethylthiazol–2–yl]–2,5–diphenyl tetrazolium bromide. Mitochondrial dehydrogenases of viable cells cleaved the tetrazolium ring, yielding purple MTT formazan crystals which were insoluble in aqueous solutions. The crystals were dissolved in acidified isopropanol and the resulting purple solution was measured using spectrophotometer at wavelength 570 nm and the background absorbance measured at 690 nm subtracted. An increase in cell number results in an increase in the amount of MTT formazan formed and an increase in absorbance.

To determine cell viability when exposed to the bioactive glass samples, cells were seeded into 24 well plates, at $1x10^5$ cells per well, and cultured in cell media supplemented with 0 (CTR) and 0.15 mg mL^{-1} of bioactive glass sample for different periods of time; 24, 48, and 72 h. The control (CTR) being pure culture medium.

The percentage viability was expressed as the relative growth rate (RGR) by the equation:

$$(\%)\mathrm{RGR} = \frac{\mathrm{D_{sample}}}{\mathrm{D_{control}}} \qquad (7.1)$$

Where D_{sample}, and $D_{control}$ represent the Sample and control absorption respectively. Cell viability calculated as a percentage of these control values. Each experiment was done in triplicate (Student's t–test, $P < 0.05$) to ensure better certainty of the acquired data.

2.4. Bioactivity assessment

The bioactivity assessment was performed by immersing 75 mg of each powder sample in 50 mL simulated body fluid solution (SBF) for different periods of time (4 h, 24 h, 72 h, 1 w, 2 w, and 4 w). The SBF was prepared according to the unified approach **[20]**. The powder – SBF mixtures were sealed into plastic flasks and placed in an incubator at 37 ± 0.5 ºC on an orbital shaker set at 120 rpm. After accomplishing each immersion period, the sample was removed from the incubator and the solids were collected through centrifuging the mixture under vacuum at 10,000 rpm for 30 min, using a Beckman model LB–70M ultracentrifuge. The pH of the supernatant solution was measured directly, whereas the separated particles were successively washed with deionised water and acetone to terminate the reaction, followed by centrifuging. The washed particles were then dried at 37 ºC in an oven for 24 h. In order to guarantee accurate results, the experiments were performed in triplicate. The formation of an apatite layer onto the surface of glass particles was followed

by: X–ray diffraction (XRD), (XRD, PANalytical XPERT–PRO Diffractometer system), using Cu–Kα radiation (Kα = 1.540), with 2Θ varying from 6 to 70º in steps of 0.026 s^{-1} and the diffraction patterns were compared with JCPDS standards; Attenuated total reflection Fourier transform infrared spectroscopy (ATR–FTIR, Tensor 27, Brucker, Germany) in the range of 350–4000 cm^{-1}, with 128 Scans and 4 cm^{-1} resolution; pH measurement and Scanning electron microscope (SEM, SU–70, Hitachi, Japan) on samples coated with carbon.

3. Results and discussion

3.1. The effect of doping ion on mean particle size

Fig. 7.1(a) shows the effects of doping the parent HSSGG with copper (Cu–doped glasses), and lanthanum (La–doped glasses) on the mean particle sizes (MPS). The effects of each individual ion on MPS were evaluated at three doping levels (1, 3, and 5 wt.%).

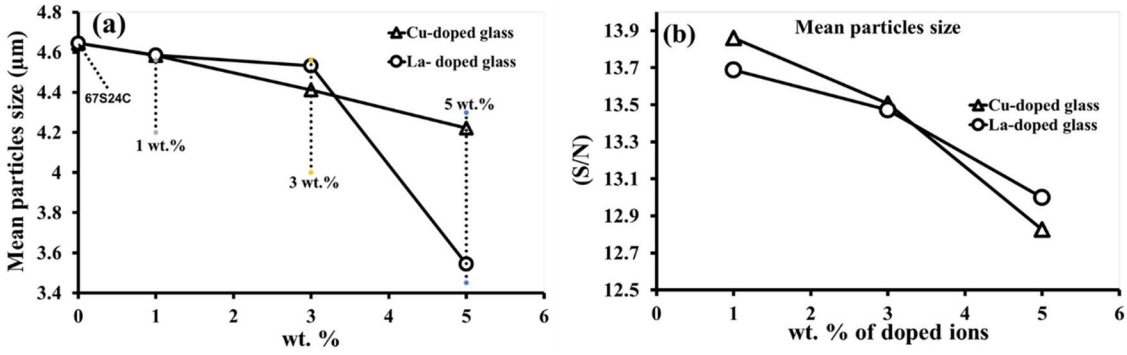

Fig. 7.1: The effects of individual and combined doping on the mean particles sizes of the milled glass powders: (a) individual doping (Cu or La); (b) combined doping (Cu and La).

As can be observed from **Fig. 7.1(a)**, increasing added doping levels induced an almost linear decrease in MPS in the case of Cu^{2+}; while an overall non–linear decreasing trend was also observed for La^{3+} occurring in two successive steps, with a first slow decrease up to 3 wt.%), followed by an abrupt drop for 5 wt.%. Overall, La induces a larger reducing effect on MPS than Cu, particularly at 5 wt.%.

Fig. 7.1(b) represents the effects of doping the parent HSSGG glass with the nine different combinations of the two ions on MPS as reported in **Table 7.1**. Screening the combined effects of the two doping ions for fixed added amounts is not easy. The task becomes even more difficult if several amounts are to be combined. In this context, the Taguchi orthogonal array of nine experiments (L9) reported in **Table 7.1& 7.2** enable this goal to be more easily accomplished. With this purpose, the signal to noise ratio (S/N), defined as the ratio between the desired value, denoted as signal, to the value of undesired variable, denoted as noise **[21]**. (S/N) is a beneficial tool to simplify extracting information about the roles played by these ions in determining the different properties of the synthesised glasses. The higher (S/N) ratio always considered as an optimum result.

The points plotted in **Fig. 7.1(b)** represent the combinations of a given amount of the indicated ion with the different three concentrations of the other investigated ion. For example, the first triangle represents the S/N of 1 wt% Cu with 1 wt%, 3wt% and 5 wt% La. It can be seen that the effect of Cu on MPS predominates at the lowest concentration (a greater S/N value at 1 wt.%), with the opposite being observed at the highest concentration (5 wt.%); while at the intermediate doping level the effects of both ions are almost identical. This suggests that in HSSGG glasses with mixed La–Cu additives, lower amounts of copper and greater amounts of lanthanum ions will result in smaller particles sizes.

3.2. The effect of doping ion on the skeletal density

The individual contributions of Cu and La ions to the skeletal density are presented in **Fig. 7.2(a)**. Density increased with increasing added amounts of both doping ions. This is not surprising considering that both elements have higher atomic numbers the other bioactive glass components, while their ionic radii do not increase proportionally. The effect is more pronounced for the La^{3+}, which can be understood since this is the heaviest element, which had a significantly greater effect on density for the two lower levels of addition, while for 5 wt.% both individual ions exerted similar effects on density. These results suggest that both atomic number and ionic radii will play roles in determining the skeletal density of glasses, resulting in different spatial atomic arrangements.

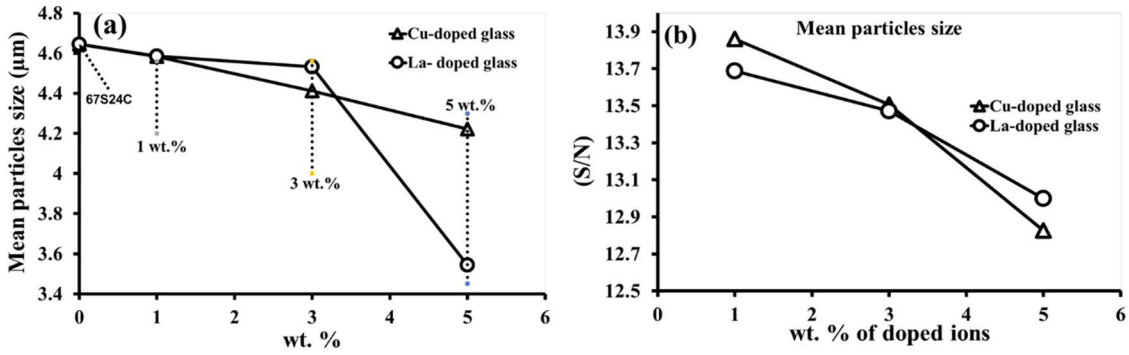

Fig. 7.2: The effects of individual and combined doping on the density of the milled glass powders: (a) individual doping (Cu or La); (b) combined doping (Cu and La).

According to the L9 pairs of experiments reported in **Table 7.1&7.2**, the combined effects of the two doping ions on density displayed in **Fig. 7.2(b)** as S/N values reveal that both contribute for an overall increase in the density. The specific Cu contribution in the combined form seems to predominate within the lower ranges from 1–3 wt.%, being then overcome by that of La with further increasing Cu content to 5 wt.%. The lanthanum contribution appears to be a linear increase, by comparison.

3.3. Cytotoxicity assays

According to ISO 10993–5, the test item is considered non–cytotoxic if the percentage of viable cells is equal to or greater than 70% of the untreated control.

3.3.1. The role of Cu^{2+}, and La^{3+} on viability of C13895 fibroblast cells

The individual and combined effects of doping ions on the viability of C13895 cells, in comparison to the control sample, are reported in **Table 7.6** and displayed in **Fig. 7.3(a)**. Parent glass HSSGG was found to reduce the viability of C13895 cells after 48 and 72 h, but its values were still above the cytotoxicity limits. The reducing effect becomes still slightly more evident for individually doped glass compositions. All showed viabilities below that of the parent glass after 24 h, but all were still above the 70% limit, except for Cu5, which was very slightly cytotoxic at 69.05% viability. However, after 48 and 72 h, all of the individually Cu or La doped glasses showed low levels of cytotoxicity, with values around, or below, the 70% limit, with Cu5 being particularly poor. Cu1 gave the best C13895 cell viabilities of all the individually doped glasses after 24 and 72 h, and increasing amounts of

Cu had greater negative effects on viability. However, the three different amounts of La ions added (La1, La3 and La5) had little differences between their values for all periods, and after 48 and 72 h were superior to Cu3 and Cu5.

Table. 7.6: C13895, BJ and MG63 % cell viability for all synthesised glasses after 24, 48, and 72 h. Bottom line shows the 70% reduction limit from control values for cytotoxicity.

	Cells viability %								
Sample	C13895	C13895	C13895	BJ	BJ	BJ	MG63	MG63	MG63
	24 h	48 h	72 h	24 h	48 h	72 h	24 h	48 h	72 h
CTR	100.00	160.56	218.42	100.00	163.75	174.57	100.00	173.78	193.76
HSSGG	99.51	122.73	157.61	71.04	116.17	123.43	83.70	131.68	169.03
La1	75.82	111.39	135.70	79.06	121.19	143.44	95.11	133.03	189.51
La3	72.49	112.07	123.97	71.79	102.41	112.25	94.19	165.06	198.94
La5	72.38	110.40	125.41	54.66	81.72	93.30	84.05	127.71	173.71
Cu1	97.67	105.86	138.52	75.36	82.51	95.11	103.83	134.44	157.26
Cu3	78.70	96.72	122.77	78.36	91.73	109.98	81.86	148.45	135.36
Cu5	69.05	77.10	88.20	86.48	119.84	139.93	92.20	169.74	171.72
Cu1–La1	92.54	135.78	202.95	79.76	98.89	128.84	93.76	140.82	184.34
Cu1–La3	92.88	144.31	210.99	78.52	97.32	116.41	82.85	149.40	159.96
Cu1–La5	93.49	146.21	211.84	72.49	96.75	109.81	88.52	140.54	148.26
Cu3–La1	94.34	143.42	197.36	83.35	92.60	120.60	89.72	145.92	157.76
Cu3–La3	91.15	140.01	191.92	70.26	86.13	116.73	89.44	142.95	172.79
Cu3–La5	87.26	122.61	165.29	69.95	78.88	113.08	107.87	162.01	193.05
Cu5–La1	67.56	86.23	128.48	64.26	77.18	112.02	77.24	125.80	138.84
Cu5–La3	86.23	104.55	132.90	64.88	71.83	108.53	86.11	137.99	161.23
Cu5–La5	92.68	116.74	138.01	63.61	69.26	90.23	76.51	123.67	174.63

Interestingly, the data reported in **Table 7.6** and **Fig. 7.3(a)** also shows that the combination of the two doping ions (Cu and La) exerts positive effects on cell viability, compared to the individual ions. With the exception of those with 5% Cu, all show greatly improved values over all time periods compared to glasses doped with the individual ions, approaching the values of the control in some cases. Those with 1% Cu were in general slightly better than those with 3% Cu, but all were quite similar, with only Cu3–La5 having significantly lower values after all time periods compared to the rest, although still well above the cytotoxicity limits of cell's viability.

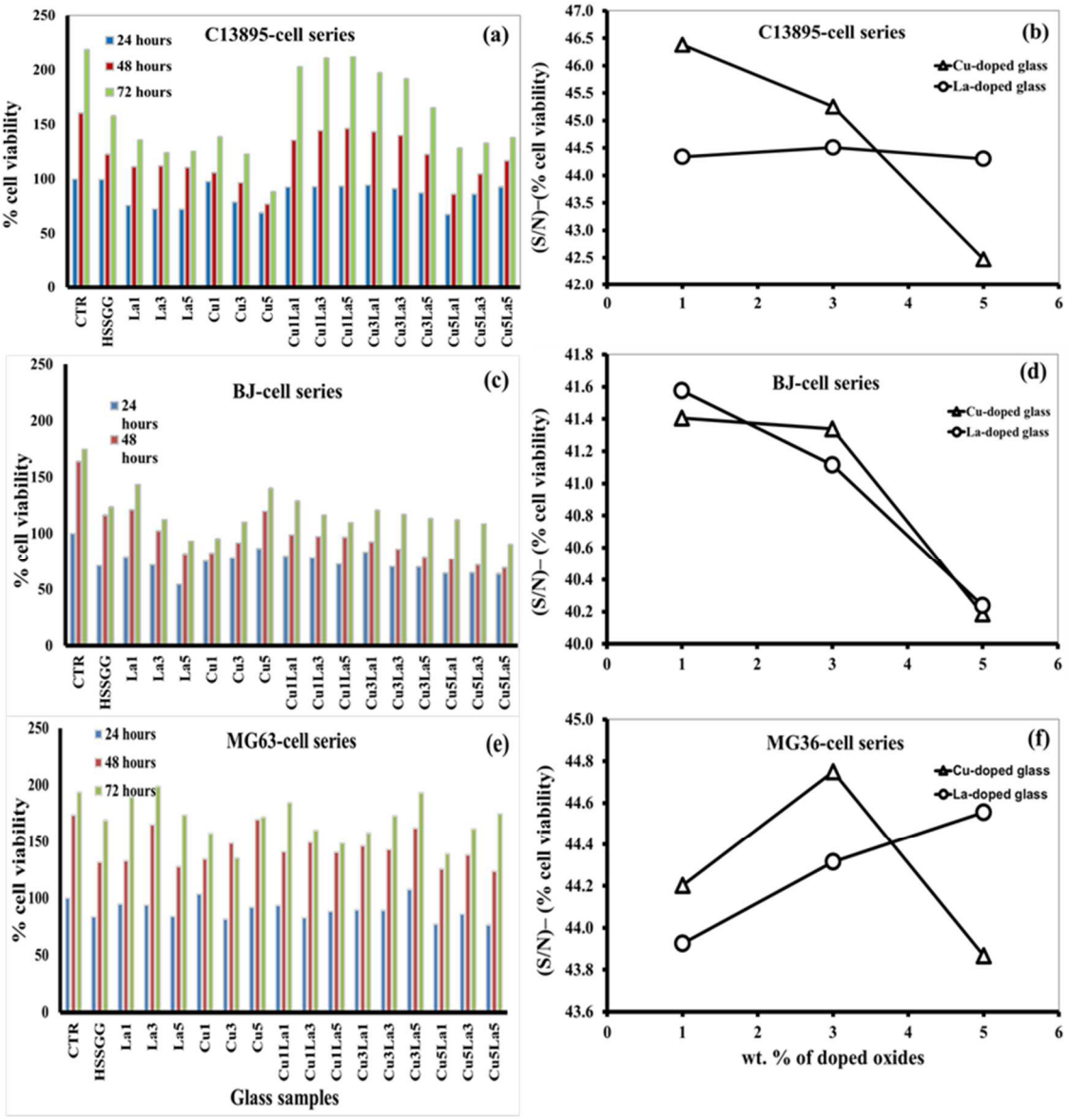

Fig. 7.3: Viability of different types of cells cultured in the presence of the 16 glass compositions: (a, b) C1395–cells; (c, d) BJ–cells. (e, f) MG36–cells; (a, c, e) percentage of cell viability; (b, d, f) Signal to noise ratio (S/N).

The worst sample of all was Cu5–La1, with viability values below the 70% limit for all periods – however, increasing La content improved these values for Cu5–La3 and Cu5–La5. The synergetic effects of this ion combination on cell viability can be better realised when comparing to the non–doped HSSGG. All combined additive glasses with 1% or 3% Cu and all levels of La were superior to the parent glass after 48 and 72 h. The combinations containing 1% Cu (Cu1–La1, Cu1–La3 and Cu1–La5) are especially interesting, displaying cell viability results comparable to the control after 48 and 72 h. Further increasing the Cu

contents in glass compositions (Cu3–Cu5) exerts general negative effects on cell viability. This is particularly noticed for Cu3 combined with concomitant increases in the La content. This is consistent with the variation trend of the S/N displayed in **Fig. 7.3(b)**. Cu definitely plays the most predominant role in determining cell viability, exerting positive and negative effects at the lowest and at highest concentrations, respectively, while La has a constant effect at all levels, as shown in **Fig. 7.3(b)**. When combined with Cu, the intermediate La content seems to be the most favourable for cell

3.3.2. The role of Cu^{2+}, and La^{3+} on viability of BJ lymphoblast cells

The cell viability results gathered for the BJ cell series are also reported in **Table 7.6**, and displayed in **Fig. 7.3(c, d)**. The control and the HSSGG parent glass showed lower cell viability levels for the BJ lymphoblasts, compared to the fibroblasts above. HSSGG showed reduced levels of viability, and was just above the limit for cytoxicity after all periods.

The observed overall effects of individual doping ions are also not the same as those discussed above for the C13895 cells, and some specific differences can be noticed. The incorporation of 1% La in HSSGG enhances BJ cells viability (La1), but there was a clear decreasing trend with further increasing La content (La3 and La5), so that these glasses became cytotoxic. However, an opposite trend in cell viability was observed for Cu–doped, glasses in which increasing added amounts from Cu1 to Cu5 induced positive effects in cell viability, to the extent that while Cu1 and Cu3 were below the 70% cytotoxicity limit after 48 and 72 h, Cu5 was superior to the parent glass, and had values similar to La1.

The combined Cu–La addition was less obviously beneficial with BJ cells, and a general trend of decreasing viability with increasing addition was observed. While all those with 1% and 3% Cu were viable after 24 h. After 48 h, all were cytotoxic, and after 72 h only Cu1–La1 was biocompatible with BJ cells. The combined effects of (Cu–La) doping on BJ cell viability evaluated from the S/N variation trends displayed in **Fig. 7.3(d)** reveal a less straightforward dependence than individual doping, with the overall trends being different to those observed for the C13895 cells **Fig. 7.3(b)**, with increasing La addition having negative effects, and little difference between 1% and 3% Cu addition, attesting to the complex interplay of the combined ions. The best BJ cell viability condition was accomplished for the Cu1–La1 combination. Increasing the level of doping from 1 to 5 wt.%

causes a drastic drop in BJ cell viability to the minimum value for Cu5–La5 as shown in **Fig. 7.3(d)**. From the 16 different glasses, it can be concluded that individual La1 and Cu5 doping levels offer the most compatible environments for BJ cells.

3.3.3. The role of Cu^{2+}, and La^{3+} on viability of MG–63 osteoblast cells

The control showed a viability with MG–63 osteoblasts between that of the other two cell lines above, but the parent HSSGG glass was more cytocompatible with this type of cell, with values well above the 70% viability limit after 48 and 72 h **Fig. 7.3(e)** and **Table 7.6**, and superior to those it had for the C13895 and BJ cells..

The incorporation of La (1–5 wt.%) into the parent glass also improves the MG–36 cell viability, being approximately equal to, or superior to, the parent HSSGG glass in all cases. While La5 showed values similar to those of HSSGG, La1 and La3 had values greater than the glass after all periods, with La3 being particularly good. The addition of copper also lead to a biocompatible glass in all cases, although inferior to that with La additions after 72 h, it was comparable after 48 h. Cu5 was particularly effective, with value close to that of the control after 48 h, and similar to the parent glass after 72 h, as shown in **Fig. 7.3 (e)** and **Table 7.5**.

The mixed La–Cu additive glasses all showed biocompatibility with MG–63 osteoblasts in all cases, sometimes to a very high degree. The best results were seen with Cu3–La5, which had values more or less equal to the control after all time periods, and all three samples with 3% Cu were very good. After 72 h, Cu1–La1, Cu3–La3 and Cu5–La5 also showed very high cytoviabity levels, greater than that of the parent glass.

The concomitant doping with both elements also exerts synergetic effects on the Mg–63 cells viability as deduced from the S/N displayed in **Fig. 7.3(f)**, which was more similar to that seen for the C13895 cells **Fig. 7.3(b**), although with a greater increase with increasing La content. It can be seen that when combined with La, Cu exerts the most stimulating effect on viability of MG–63 cells within the lower concentration regime up to 3% Cu, causing a drastic decrease with further increasing its content to Cu5. It is worth mentioning that these Cu variation trends are exactly the opposite relative to those observed with single Cu doping.

A similar non–straightforward situation, in comparison to individual doping, is also observed for La in the presence of Cu, with the highest level of cell viability being observed for La5 **Fig. 7.3(f)**. Apparently, the presence of Cu may limit the benefits exerted by the lower individual contents of La, as shown in **Fig. 7.3(e)**.

From all the 16 doped glasses, it can be concluded that La3 offers the best cell viability even higher than the control value, followed by the Cu3–La5 glass.

3.4. Bioactivity characterisation

Fig. 7.4(a–d) displays the XRD patterns for the glass powders before (0 h), and after immersion in simulated body fluid (SBF) for different periods of time (4 h, 24 h, 72 h, 1 w, 2 w, and 4 w).

3.4.1. XRD of glass powders before immersion in SBF (0 h)

It was already shown that the parent HSSGG glass preserved its amorphous nature upon heat treating at 550 ºC [**17**]. Increasing the heat treatment temperature to 800 ºC induced the formation of three crystallisation phases: Wollastonite–1A (pdf # 04–011–2265–$CaSiO_3$), Cristobalite, (pdf # 04–007–2134–SiO_2), and Hydroxylapatite; HAp (pdf # 04–013–6615–$Ca_5(PO_4)_3(OH)$) as can be seen from **Fig. 7.4(a)**. All crystallisation phases appear with low intensities, suggesting they are still embedded in an abundant amorphous glassy matrix. However, the incorporation of the highest contents of doping elements, individually (Cu5 or La5), or in a combined manner (Cu5–La5), significantly enhanced the crystallisation tendency of the glass samples, as can be seen in **Figs. 7.4(b, c)** and in the **Fig. 7.4(d)**, respectively. Moreover, the crystallisation seems to be more stimulated by Cu than by La, with the XRD peaks being more intense in the presence of Cu, added individually or in combination with La. This might be attributed to the higher diffusivity of Cu^{2+} due to its smaller ionic radius (0.73 Å) in comparison to that of La^{3+} (1.06 Å) **[22]**.

3.4.2. XRD of glass powders after immersion in SBF

The relative intensities of the XRD peaks in the HSSGG glass sample apparently decreased after 4 h of immersion in SBF, probably due to the formation of an amorphous silica–gel like surface layer. For longer immersion periods, especially beyond 24 h, the intensities of the XRD peaks gradually increased again as a result of crystalline HAp phase precipitation as can be observed in **Fig. 7.4(a)**.

For the glasses doped the highest contents of doping elements, individually (Cu5 or La5), or in a combined manner (Cu5–La5), the intensities of the XRD peaks tended to gradually decrease along the entire period of immersion in SBF as can be seen in **Figs. 7.4(b–d)**.

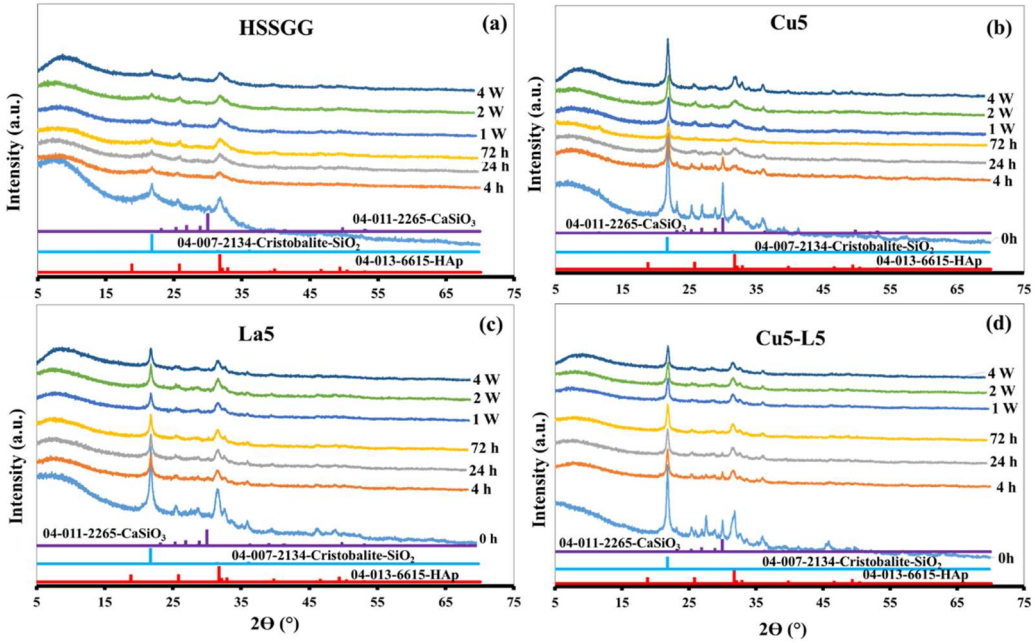

Fig. 7.4: XRD patterns of some selected glass powders before (0 h), and after immersion in SBF for different periods (4 h, 24 h, 72 h, 1 w, 2 w, and 4 w: (a) HSSGG, (b) Cu–5, (c) La–5, (d) Cu5–La5.

These results can be understood considering the hiding effects of the main crystalline phases by: (i) the formation of a silica–gel like surface layer with an amorphous nature; (ii) the gradual precipitation of HAp phase, which starts to be noticed between 4 h – 1 w, becoming more pronounced between 2 – 4 w.

3.4.3. ATR–FTIR before and after immersion in SBF

Figs. 7.5(a–d) present the ATR–FTIR spectra for the selected glass powder samples (HSSGG, Cu5, La5, and Cu5–La5) before (0 h) and after SBF immersion for different time periods. All the samples exhibit a number of common features. The major band observed between 850 cm^{-1}, and 1300 cm^{-1} is ascribed to the asymmetric stretching of the Si–O–Si vibrational mode, and it is composed of a high intensity peak centred at 1020 cm^{-1} with the shoulder at 1220 cm^{-1} which are associated to Si–O–NBO (non–bridging oxygens) **[23]**. Moreover, the peak centred at 1020 cm^{-1} along with the two shoulders at 945 and 1085 cm^{-1} was pointed out as the main characteristic of phosphate group (PO_4^{3-}) **[24]**. The band at ~945 cm^{-1} can be also assigned to Si–O^- stretching vibration **[25]**. The low intensity absorption band at around 875 cm^{-1} is assigned to CO_3^{2-} functional group, suggesting that carbonate is integrated in the formed layer of apatite **[26]**. The peak at 785 cm^{-1} is assigned to the symmetric stretching of Si–O–Si **[27]**. Moreover, two twin peaks at 560 and 603 cm^{-1}, along with the band at 945 cm^{-1}, are associated to the phosphate group, and indicate the precipitation of calcium phosphate, in the form of hydroxyapatite (HAp) **[28]**. Likewise, one of the most common vibrational modes for silica assigned to the rocking vibration for Si–O–Si can be observed at 465 cm^{-1} **[29,30]**. The twin bands at ~560 and ~601 cm^{-1} are clearly less intense before immersion in SBF (0 h). Their intensities gradually increase with extending the immersion period, being well pronounced after 4 w of immersion. Other specific vibrations were detected in the FTIR spectra of doped samples. **Fig. 7.5(b)** shows that the two shoulders at ~945 and 1085 cm^{-1} transformed into two intense peaks. These changes indicate an increase in the degree of crystallisation of (PO_4^{3-}group as HAp, in a good agreement with the XRD results displayed in **Fig. 7.4(b)**.

Two peaks appear at 900 cm^{-1} and 645 cm^{-1} that can be assigned to Si–O–2NBO **[23]**, and are particularly attributed to Ca–Si vibration [**31,32]**, due to the higher degree of crystallisation of calcium silicate. Moreover, the appearance of a peak at ~445 cm^{-1} is a confirmation of the presence of cristobalite **[29]**. The **Figs. 7.5(c–d)** show the incorporation of La5 individually or in a combined manner shifted the vibration bands at 1220, and 945 cm^{-1} to 1200 cm^{-1}, and 930 cm^{-1} respectively. These shifts are assigned to an increase in the number of non–bridging oxygen, confirming that La^{3+} is acting as a modifier for the silica network **[33]**.

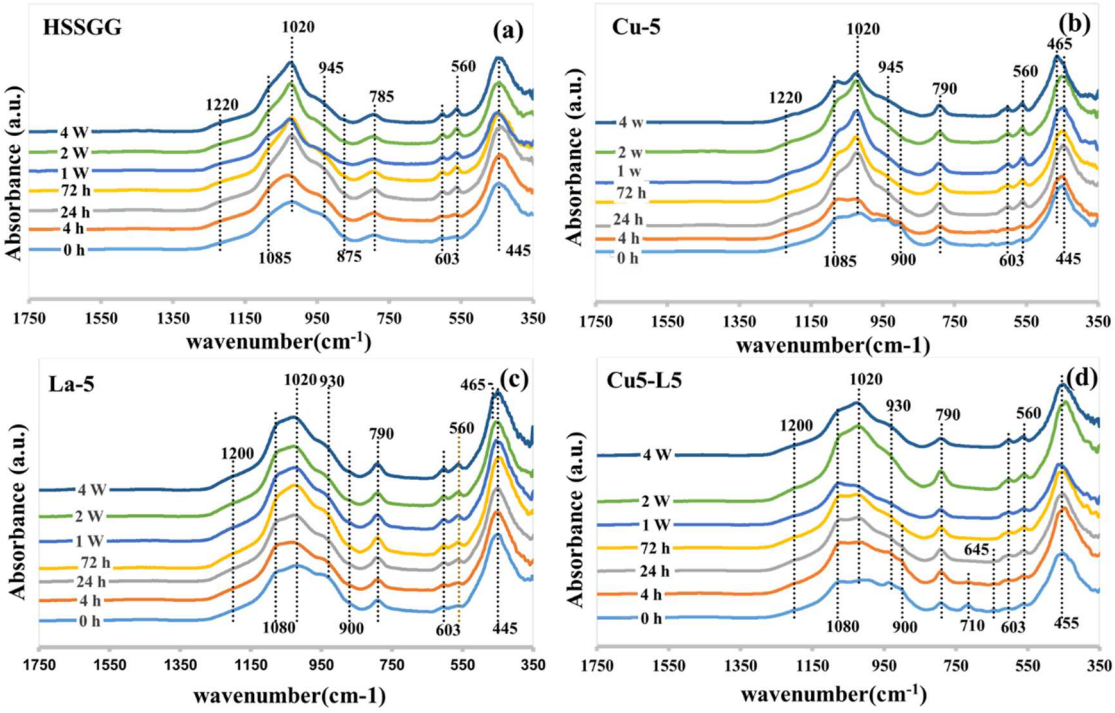

Fig. 7.5: ATR–FTIR spectra of some selected glass powders before (0 h), and after immersion in SBF for different periods (4 h, 24 h, 72 h, 1 w, 2 w, and 4 w: (a) HSSGG, (b) Cu–5, (c) La–5, (d) Cu5–La5.

3.4.4. pH changes undergone along the immersion time in SBF

Fig. 7.6 shows the pH changes in the SBF solution along the entire immersion period of 4 w. Relatively abrupt increases in pH occurred up to 4 h, which were then followed by more gradually increases along the remaining period of immersion. The increase in pH can be attributed to some preferential ionic (Na^+, Ca^{2+}) leaching from the powder, and to an equivalent uptake of H^+ ions by the solid for charge compensation, thus increasing the relative concentration of OH^- in the solution. However it can be seen that doped glasses exhibit significantly higher pH values, suggesting that dissolution of glass powders was enhanced by the incorporation of doping (Cu^{2+} and La^{3+}) ions. These changes further suggest that doping ions are playing the role of glass modifiers, contributing to less polymerised silica networks **[33]**.

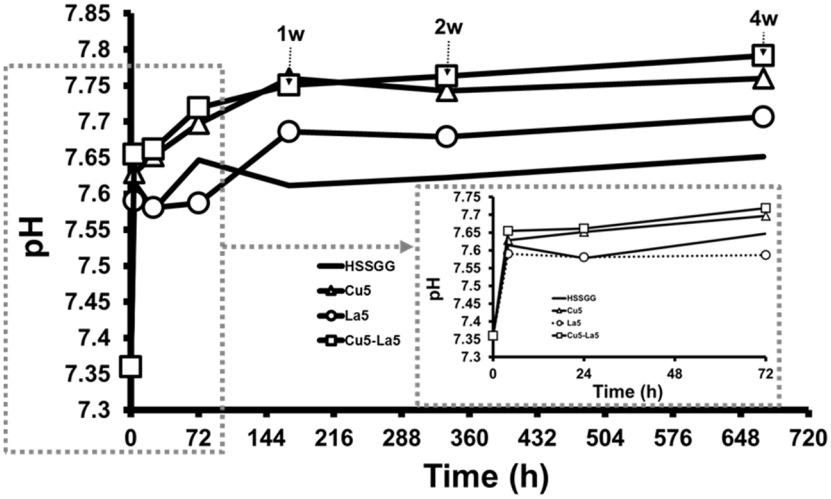

Fig. 7.6: pH changes undergone in the SBF solution when in contact with some selected glass powders (HSSGG, Cu–5, La–5, and Cu5–La5) along the immersion time.

With the gradual supersaturation of the SBF solution, there will be a trend for the excess species to precipitate onto the particles surface. The deposited layer is likely to act as a barrier towards further dissolution, explaining the slow pH increasing rate with extending the immersion period. The apparent near horizontal trend observed between 2–4 w can be attributed to a more effective hindered dissolution due the increased thickness of the deposited surface layer.

3.4.5. Morphological surface changes undergone upon immersion in SBF

Fig. 7.7 presents the SEM micrographs of the selected samples (HSSGG, Cu5, La5, and Cu5–La5) before (0 h) and after immersion in SBF for different time periods. The starting HSSGG powder exhibits a fluffy porous microstructure consisting of clusters in the range of 100–500 nm with uniform shapes, **Fig. 7.7(a)**. Doping with Cu resulted in larger clusters and a dense microstructure, **Fig. 7.7(e)**, while much less noticeable morphological changes were apparently induced by doping with La alone, **Fig. 7.7(i)**. On the other hand, the combined addition of the two doping species induced small changes in the microstructure, in both shape and size of the clusters, with the overall microstructure resembling the features of each individually doped glass as shown in **Fig. 7.7(m)**. Significant morphological changes gradually occurred along the immersion time in SBF. After (72 h – 2 w), both HSSGG and Cu5 glass samples seem to have undergone more extensive surface modifications than La5,

and Cu5–La5, as deduced from the morphological features seen in **Figs. 7.7(b–c)**, and **Figs. 7.7(f–g)**. Assuming that these surface changes are due to the precipitation of HAp, these observations suggest that the HSSGG and Cu5 glasses are more bioactivity up to 2 w immersion time. Upon extending the immersion period in SBF to 4 w, the morphological differences among the samples become mitigated with all glasses without any exception showing extensive formation of HAp.

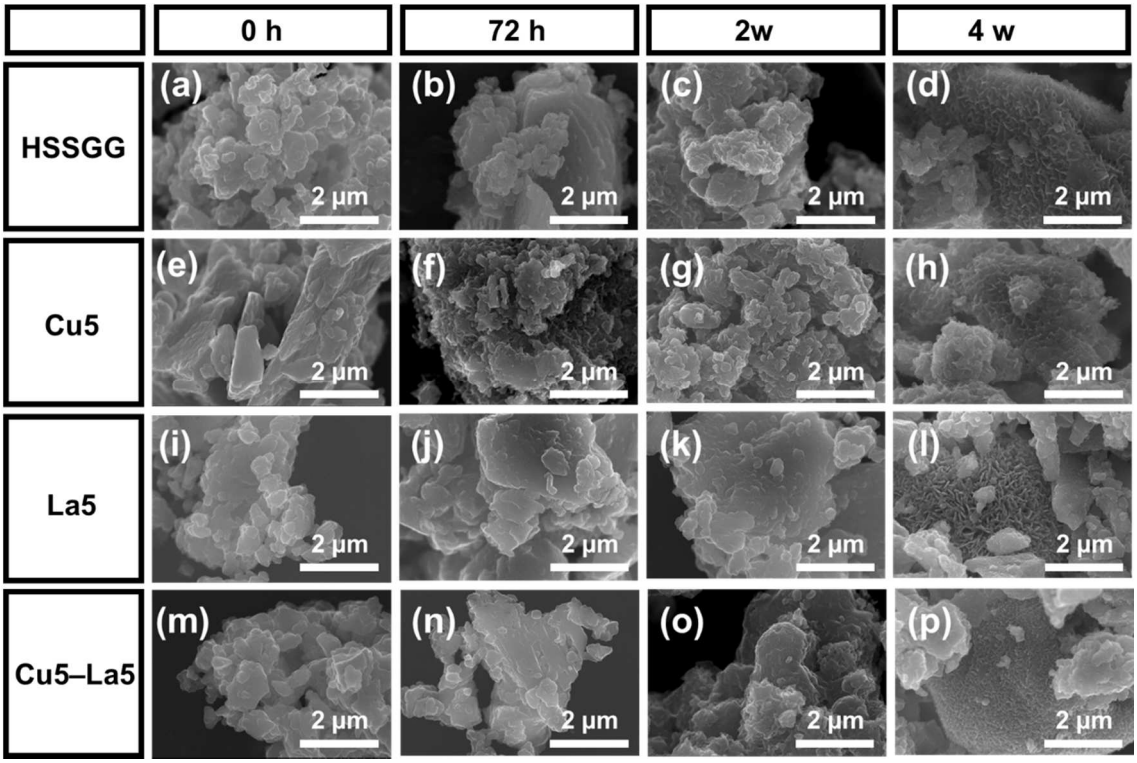

Fig. 7.7: SEM micrographs taken before (0 h), and after immersion in SBF for different time periods (72 h, 2 w, and 4 w) of some selected glass powders: (a–d) HSSGG; (e–h) Cu–5; (i–l) La–5; (m, p) Cu5–La5.

Even though, the images at 4 w **Figs. 7.7(d, h)** tend to confirm the trend observed within the shorter immersion periods pointing to more extensive surface changes in the HSSGG and Cu5 glasses. La–doped glass is apparently less reactive towards the formation of a surface HAp layer as shown in **Fig. 7.7(l)**. The combined doping (Cu5–La5) seems to mitigate the decrease in surface activity due to La as suggested by the micrograph in **Fig. 7.7(p)**.

4. Conclusions

This research was aimed at disclosing the effects of doping a parent sol–gel derived HSSGG glass composition with two ions (Cu^{2+}, and La^{3+}) on the physical properties and the *in vitro* performance. A total of 15 doped glasses containing 1, 3, and 5 wt.% of each individual ion and combinations of both were prepared. From the results presented and discussed above, the following conclusions can be drawn.

i. The individual doping tends to decrease the mean particle size (MPS) of milled powders, with Cu playing the most determining effect, particularly at 5 wt. %. Combined doping induces more complex decreasing effects, with Cu playing again the most determining role at both low and high contents, and similar relevancies for both ions at intermediate concentrations.

ii. The density of glass powders increases with individual doping of both ions, with the heavier one (La) being the most determinant. The same general trends were observed for combined doping mutual, again with higher relevance for La. The influence of individual and combined doping on cells viability strongly depends on the type of cells and on the doping recipe.

iii. The viability of C13895 cells decreases with increases doping amounts of individual ions, particularly in the case of Cu (Cu3, Cu5). But the combined doping highly favours the viability of C13895 cells, especially for doping recipes with lower Cu contents.

iv. The viability BJ cells is slightly stimulated especially by La1 and Cu5, and negatively affected by the other individual doping recipes. The combined recipes containing more than 3 wt.% of each doping ion tend to deteriorate the viability of BJ cells.

v. The viability of the MG–36 cells is significantly improved for La1 – La5 and Cu5, decreasing for Cu1–Cu3. Several combined doping recipes also perform better in comparison to HSSGG.

vi. All the glass compositions have undergone extensive surface modifications upon immersion in SBF for periods up to 4 w, attributed to an early formation of a silica–gel like surface layer followed by the gradual precipitation of HAp with enhanced crystallinity. The surface modifications exert a hiding effect of the

pre–exiting crystalline phases, the XRD peaks of which tend to appear with decreasing intensities.

Acknowledgments

R.C. Pullar wishes to thank the FCT Grant IF/00681/2015 for supporting this work. B. A. E. Ben–Arfa thanks FCT grant BIONANOSCULP PTDC/EPH–PAT/6281/2014 for supporting him during this work. This work was developed in the scope of the project CICECO–Aveiro Institute of Materials (Ref. FCT UID /CTM /50011/2013), financed by national funds through the FCT/MEC and when applicable co–financed by FEDER under the PT2020 Partnership Agreement.

References

[1] O. Leppäranta, M. Vaahtio, T. Peltola, D. Zhang, L. Hupa, M. Hupa, et al., Antibacterial effect of bioactive glasses on clinically important anaerobic bacteria in vitro, J. Mater. Sci. Mater. Med. 19 (2008) 547–551.

[2] L.L. Hench, The story of Bioglass, J. Mater. Sci. Mater. Med. 17 (2006) 967–978.

[3] J.S. Suwandi, R.E.M. Toes, T. Nikolic, B.O. Roep, Inducing tissue specific tolerance in autoimmune disease with tolerogenic dendritic cells, Clin. Exp. Rheumatol. 33 (2015) 97–103.

[4] R. Mathew, B. Stevensson, M. Edén, Na/Ca Intermixing around Silicate and Phosphate Groups in Bioactive Phosphosilicate Glasses Revealed by Heteronuclear Solid–State NMR and Molecular Dynamics Simulations, J. Phys. Chem. B. 119 (2015) 5701–5715.

[5] F.Z. Mezahi, A.L. Girot, H. Oudadesse, A. Harabi, Reactivity kinetics of 52S4 glass in the quaternary system SiO2–CaO–Na2O–P2O5: Influence of the synthesis process: Melting versus sol–gel, J. Non. Cryst. Solids. 361 (2013) 111–118.

[6] A. Boguszewska–Czubara, K. Pasternak, Silicon in medicine and therapy, J. Elem. 16 (2011) 489–497.

[7] P. Pravina, D. Sayaji, M. Avinash, Calcium and its Role in Human Body, Int. J. Res. Pharm. Biomed. Sci. 4 (2013) 659–668.

[8] M. Constantin, I. Alexandru, The role of sodium in the body, Balneo–Research J. 2 (2011) 70–74.

[9] R. Raina, Phosphorus Metabolism, J. Nephrol. Ther. 01 (2012) 1–7.

[10] R. Uauy, M. Olivares, M. Gonzalez, Essentiality of Copper in Humans, Am J Clin Nutr. 67 (1998) 9525–98.

[11] F. Bronner, Metals in Bone. Aluminum, Boron, Cadmium, Chromium, Lanthanum, Lead, Silicon, and Strontium., in: Princ. Bone Biol., 3rd editio, Academic Press, Inc., Farmington, 2008: pp. 515–531.

[12] D.M. Weekes, Lanthanum complexs as therapeutic agents for the treatment of bone resorption disorders, Britsh Colombia, 2016.

[13] E. Wers, H. Oudadesse, B. Lefeuvre, B. Bureau, O. Merdrignac–Conanec, Thermal investigations of Ti and Ag–doped bioactive glasses, Thermochim. Acta. 580 (2014) 79–84.

[14] M. Tylkowski, D.S. Brauer, Mixed alkali effects in Bioglass® 45S5, J. Non. Cryst. Solids. 376 (2013) 175–181.

[15] J. Bejarano, R. Detsch, A.R. Boccaccini, H. Palza, PDLLA scaffolds with Cu– and Zn–doped bioactive glasses having multifunctional properties for bone regeneration, J. Biomed. Mater. Res. – Part A. 105 (2017) 746–756.

[16] P.K. Khan, A. Mahato, B. Kundu, S.K. Nandi, P. Mukherjee, S. Datta, et al., Influence of single and binary doping of strontium and lithium on in vivo biological properties of bioactive glass scaffolds, Sci. Rep. 6 (2016) 1–18.

[17] B.A.E. Ben–arfa, I.M.M. Salvado, J.M.F. Ferreira, R.C. Pullar, Enhanced bioactivity of a rapidly–dried sol–gel derived quaternary bioglass, Mater. Sci. Eng. C. 91 (2018) 36–43.

[18] B.A.E. Ben–arfa, I.M.M. Salvado, R.C. Pullar, A hundred times faster : Novel , rapid sol–gel synthesis of without aging, Int. J. Appl. Glas. Sci. 8 (2016) 337–343.

[19] I.O. for Standardization, International Organization for Standardization (2009) ISO 10993–5. Biological evaluation of medical devices—part 5: tests for in vitro cytotoxicity. , (2009).

[20] A.L.B. Maçon, T.B. Kim, E.M. Valliant, K. Goetschius, R.K. Brow, D.E. Day, et al., A unified in vitro evaluation for apatite–forming ability of bioactive glasses and their variants, J. Mater. Sci. Mater. Med. 26 (2015) 1–10.

[21] Ranjit Roy, A Primer on the Taguchi Method, Van Nostrand Reinhold, New York, 1990.

[22] A.F. Wells, Structural Inorganic Chemistry, 4th ed., Oxford university press, London, 1975.

[23] H. Aguiar, J. Serra, P. González, B. León, Structural study of sol–gel silicate glasses by IR and Raman spectroscopies, J. Non. Cryst. Solids. 355 (2009) 475–480.

[24] J.C. Elliot, Structure and Chemistry of the Apatites and Other Calcium

Orthophosphates, Elsevier B.V, Amsterdam, 1994.

[25] P. Innocenzi, Infrared spectroscopy of sol–gel derived silica–based films: a spectra–microstructure overview, J. Non. Cryst. Solids. 316 (2003) 309–319.

[26] I. Notingher, J.R. Jones, S. Verrier, I. Bisson, P. Embanga, P. Edwards, et al., Application of FTIR and Raman Spectroscopy to Characterisation of Bioactive Materials and Living Cells, Spectrosc. Int. J. 17 (2003) 275–288.

[27] A. Pramanik, K. Bhattacharjee, M. Mitra, A mechanistic study of the initial stage of the sintering of sol–gel derived silica nanoparticles, Int. J. Mod. Eng. Res. 3 (2013) 1066–1070.

[28] P. Sooksaen, N. Pengsuwan, S. Karawatthanaworrakul, S. Pianpraditkul, Formation of porous apatite layer during in vitro study of hydroxyapatite–AW based glass composites, Adv. Condens. Matter Phys. 2015 (2015) 1–10.

[29] M. Zhang, T. Moxon, Infrared absorption spectroscopy of SiO2 –moganite, Am. Mineral. 99 (2014) 671–680.

[30] D.E. Vázquez–valerdi, J.A. Luna–lópez, J. Carrillo–lópez, G. García–salgado, A. Benítez–lara, N.D. Espinosa–torres, Compositional and optical properties of SiO x films and (SiO x / SiO y) junctions deposited by HFCVD, Nanoscale Res. Lett. 9 (2014) 1–8.

[31] D. Eniu, C. Gruian, E. Vanea, L. Patcas, V. Simon, FTIR and EPR spectroscopic investigation of calcium–silicate glasses with iron and dysprosium, J. Mol. Struct. 1084 (2015) 23–27.

[32] M. Horgnies, J.J. Chen, C. Bouillon, Overview about the use of fourier transform infrared spectroscopy to study cementitious materials, WIT Trans. Eng. Sci. 77 (2013) 251–262.

[33] A. Aronne, S. Esposito, P. Pernice, FTIR and DTA study of lanthanum aluminosilicate glasses, Mater. Chem. Phys. 51 (1997) 163–168.

Chapter 8

The present chapter was published on:
Ceramic International;
Volume 106, Issue 2,
Febrauary 2019,
(Online).
Doi: · 10.1016/j.ceramint.2019.02.081

The effects of Cu^{2+} and La^{3+} doping on the sintering ability of sol–gel derived high silica glasses

Basam A. E. Ben–Arfa , Isabel M. Miranda Salvado *, Robert C. Pullar *, and José M. F. Ferreira

Department of Materials and Ceramic Engineering / CICECO – Aveiro Institute of Materials, University of Aveiro, 3810–193 Aveiro, Portugal

Abstract

The aim of this work is to study the hierarchical influence of co–doping (Cu & La) a sol–gel derived quaternary (Si, Ca, Na, P) parent glass on the sintering ability of the resulting bioactive glasses. The mutual effects of Cu & La doping on the density, crystallisation and sintering–ability were investigated by using a (L9)–n3v2–Taguchi orthogonal array (OA) of experiments. The thermal properties of bioactive glasses were assessed by differential thermal analysis (DTA), thermogavometry (TGA), and dilatometry. The evolution of crystallisation phases was monitored by X–ray diffraction. Pellets of ten glass compositions (including the parent glass) were pressed and sintered at two sintering temperatures (800, 900 ºC). The density of the pellets was measured by the Archimedes method. The sintered microstructures were observed by scanning electron microscope (SEM) coupled with energy dispersive X–Ray Spectroscopy (EDS) analysis. The glass structure was analysed by MAS–NMR. The results revealed that Cu promotes early densification enhancing density at lower sintering temperatures. Oppositely, beneficial sintering effects of La might be observed at higher sintering temperature (> 1000ºC). These differences are induced by the distinct roles of doping elements on devitrification upon increasing their concentrations: crystallisation is promoted by Cu and is inhibited by La.

Keywords: Sol–gel; Bioactive glass; density; sintering–ability ;crystallisation; Lanthanum; Copper; Doping.

* *Communicating authors: isabelmsalvado@ua.pt, rpullar@ua.pt*

1. Introduction

Bioactive glasses and glass ceramics deserved particular interest in the last decades **[1,2]**. Bioactive glasses show superior bioactivity properties than bioceramics **[3]**. Moreover, bioactive glasses offer other advantages in the treatment of many disorders and resume normal functionality of several biological systems, such as; Osteomyelitis (destructive bony lesion) **[4,5]**, treating dentin hypersensitivity **[6]**, repair injured Cardiac & Pulmonary tissues **[7]**, treatment of aneurysmal bone cysts (bone tumour) **[8]**. However, bioactive glasses experience poor mechanical properties which limit their use in load bearing devices **[9,10]**. Enormous efforts were done to improve the mechanical properties of bioactive glasses **[11–14]**. The mechanical properties could be improved by increasing the fracture toughness for bioactive glasses. This target can be accomplished by doping a parent glass with some functional ions **[15,16]**, or by impregnating ceramic/metal/polymer particles or fibres in the bioactive glasses matrix to produce composites **[17,18]**. The composites are built from a combination of different components, such as ceramics, metals, and polymers. Accordingly, attention is required to tune the degradation rates between all the constituting composite components **[19]**. Nevertheless, composites are known to exhibit lower bioactivity in comparison to bioactive glasses **[20]**. The difficulty in governing biodegradability, and the low bioactivity of composites prevent their used when a rapid bioactive response with highly controlled biodegradation is required.

The research frontiers are still far from the optimum needed design in terms of mechanical properties and tuned bioactivity. Doping bioactive glasses with some functional ions is likely to give room for enhancing the harmony between the desired levels of bioactivity and mechanical properties **[21]**. In this regard, many investigations were reported on the role of different functional ions in binary **[22,23]**, ternary **[24,25]**, and quaternary glass systems **[25,26]** such as Z^{2+}, Sr^{2+}, T^{3+}, Zr^{4+}, Mg^{2+}, Mn^{2+}, Y^{3+}. Their effects on tuning bioactivity and mechanical properties of bioactive glasses are well documented **[22–27]**. Cu has been extensively reported to significantly enhance the mechanical properties and sintering ability in metal alloys **[28–30]**. It forms a liquid phase that tends to reduce the overall porosity and enhance the diffusion during sintering. Moreover, it enhances the mechanical properties of Ca–Zn–Mg bulk metallic glass **[31]** and of borate glass **[32]**. La was found to increase the density of strontium borate glasses **[33]**. Nevertheless, a literature overview revealed that

very scarce information is available about the effects of these two ions on the density, sintering ability, and crystallisation kinetics of bioactive glasses.

This research paper is dedicated to decode the mutual role of these two ions on the density, crystallisation and sintering ability of a sol–gel derived quaternary parent glass. To the author's knowledge, no such study was assessed to explore the effects of these ions in a glassy matrix.

2. Materials and methods

2.1. Glass synthesis

A quaternary high silica sol–gel bioactive glass with a composition of $67SiO_2$–$24CaO2.5Na_2O$–$2P_2O_5$ [= (67% Si – 24% Ca – 5% Na – 4% P) mol%], hereafter labelled as HSSGG, previously reported by the authors **[34]**, was co–doped with CuO and La_2O_3.

Tetra–ethyl–ortho–silicate (TEOS, $C_8H_{20}O_4Si$, 98%), triethyl phosphate (TEP, $C_6H_{15}O_4P$, ≥99.8%), calcium nitrate tetrahydrate (CaN, $Ca(NO_3)_2{\cdot}4H_2O$, ≥99%), sodium nitrate (NaN, $NaNO_3$, ≥99%), Copper(II) nitrate trihydrate (CuN, $Cu(NO_3)_2{\cdot}3H_2O$, ≥99%), and Lanthanum(III) nitrate hexahydrate (LaN, $La(NO_3)_3{\cdot}6H_2O$, ≥99.9%) were used as precursors. All six precursors were supplied from Sigma–Aldrich. Distilled water (DW) was used as solvent and citric acid monohydrate (CA, $C_6H_8O_7{\cdot}H_2O$, 99.5−102%, Sigma–Aldrich) was added to catalyse the sol–gel hydrolysis and condensation reactions.

Additions of 1, 3 and 5 wt.% of either La or Cu oxides were made to the parent glass (HSSGG) composition following the same experimental approach employed in our earlier investigation **[34]**. The Cu & La precursors were added to the homogeneous sols obtained from the (Si–Ca–Na–P) quaternary system. The doped glass compositions are hereafter labelled as "Cu1–La1, Cu1–La3, Cu1–La5, Cu3–La1, Cu3–La3, Cu3–La5, Cu5–La1, Cu5–La3, and Cu5–La5". The batch compositions (in both wt.% and mol%) are presented in **Table 8.1** & **Table 8.2**.

Table 8.1: Batch compositions of all synthesised glasses in wt.%

Glass	SiO_2	Na_2O	CaO	P_2O_5	CuO	La_2O_3
HSSGG	64.40	2.48	21.53	4.55	–	–
Cu1La1	63.11	2.43	21.10	4.46	1.00	1.00
Cu1La3	61.83	2.38	20.67	4.37	1.00	3.00
Cu1La5	60.54	2.33	20.24	4.28	1.00	5.00
Cu3La1	61.83	2.38	20.67	4.37	3.00	1.00
Cu3La3	60.54	2.33	20.24	4.28	3.00	3.00
Cu3La5	59.25	2.28	19.81	4.19	3.00	5.00
Cu5La1	60.54	2.33	20.24	4.28	5.00	1.00
Cu5La3	59.25	2.28	19.81	4.19	5.00	3.00
Cu5La5	57.96	2.23	19.38	4.09	5.00	5.00

A (L9)–n3v2–Taguchi orthogonal array (OA) comprising nine couples of combinations of the two Cu^{2+} and La^{3+} ions was used to better understand their combined effects when added to the parent HSSGG composition.

Table 8.2: Batch compositions of all synthesised glasses in mol%

Glass	SiO_2	Na_2O	CaO	P_2O_5	CuO	La_2O_3
HSSGG	67.00	2.50	24.00	2.00	–	–
Cu1La1	66.34	2.475	23.76	1.98	0.79	0.19
Cu1La3	66.06	2.465	23.66	1.97	0.81	0.59
Cu1La5	65.78	2.455	23.56	1.96	0.82	1.00
Cu3La1	65.27	2.435	23.38	1.95	2.39	0.19
Cu3La3	64.97	2.425	23.27	1.94	2.43	0.59
Cu3La5	64.67	2.415	23.17	1.93	2.47	1.01
Cu5La1	64.19	2.395	22.99	1.92	4.00	0.20
Cu5La3	63.88	2.385	22.88	1.91	4.07	0.60
Cu5La5	63.55	2.370	22.76	1.90	4.14	1.01

In such OA, v2 denotes 2 variables (Cu and La), and n3 represents 3 levels for each variable, which are 1, 3 and 5 wt. %, as presented in **Table. 8.3**, and **Table. 8.4**.

Table 8.3: L9 – Taguchi design – 2variables (v), and 3 levels (n)

Levels	Variables (Wt.%)	
n	Cu	La
1	1	1
2	3	3
3	5	5

Table 8.4: L9 – Taguchi array, 9 trials, 2 variables and 3 levels

	Conditions	
Trial	Cu	La
E1	1	1
E2	1	3
E3	1	5
E4	3	1
E5	3	3
E6	3	5
E7	5	1
E8	5	3
E9	5	5

The acquired gels were fast dried using a roto–evaporator (Buchi 210 Rotavapor with V–850 vacuum controller and V–700 diaphragm vacuum pump), in a 500 mL pear–shaped flask while rotating in a water bath at 55 ºC, and under a low pressure of 50 mbar for 30 minutes **[35]**. The as–dried gels were heat treated up to 800 ºC, according to the schedules presented in **Table 8.5**.

Table 8.5: Details of the three stages of the heat treatment schedule

	1st stage	2nd stage	3rd stage
Starting temperature [ºC]	25	200	400
Target temperature	200	400	800
Heating rate [ºC min^{-1}]	1	2	5
Soaking time [h]	0.5	0.5	2

The heat treated powders were then ball milled in ethanol (EtOH) using an EtOH to powder mass ratio (EPR) = 1.5), a balls to powder mass ratio (BPR) = 10, and milling time of 1 h. The milling was done in a S–series–Fast Mill machine, type S2–1000 (Ceramic Instruments, Sassuolo, Italy), under a rotational speed of 390 rpm, using a sintered alumina jar of 300 cm^3 capacity (Ceramic instruments Sassuolo, Italy). Yttria–stabilized zirconia balls with 10 mm diameter (Tosoh, Tokyo, Japan) were used as milling medium. After milling, the slurry was separated for drying in an oven at 60 ºC for 24 h. The obtained dry powders were passed through a 63 µm sieve to separate the large agglomerates from the fine powder. The resulting fine powder was used for all characterisation techniques.

2.2. Characterisation of the milled powder

The ^{29}Si MAS–NMR spectra were recorded in a ASX 400 spectrometer (Brucker, Germany) operating at 79.52 MHz (9.4 T), using a 7 mm probe at a spinning rate of 5 kHz. The pulse length was 2 µs with 60 s delay time. The aim was to investigate the silica environments and the degree of condensation in silica network of the stabilised glass samples. Kaolinite was used as a chemical shift reference. ^{29}Si MAS NMR spectra were de–convoluted using dimFit software.

Thermogravimetric and Differential Thermal Analysis (TGA/DTA) were performed. Thermal analysis (TA), including differential thermal analysis (DTA), and thermogravimetric analysis (TGA) of glass powders was carried out in air using TA SDT Q600 equipment, with an air flow rate of 100 ml min^{-1}, from room temperature (RT) to 1000 ºC and a heat ramp of 10 ºC min^{-1}, with calcined α–alumina as reference material. The glass transition temperature (T_g), onset of crystallisation (T_c), and peak temperature of crystallisation (T_p) were obtained from the DTA thermograph. The samples were between 23 and 33 mg in weight, weighed to 0.1 mg with an error of ±0.2 mg, so the maximum overall error in their weight was within the range of 0.61– 0.87%.

X–ray diffraction (XRD) was used to follow–up the evolution of the crystalline phases. The samples were heat treated from RT to three different temperatures; 700 ºC, 900 ºC, 1000 ºC, with a dwell time of 30 min before getting cooled. The XRD patterns were acquired using (XRD, PANalytical XPERT–PRO Diffractometer system), using Cu–Kα radiation (Kα =

1.540), with 2Θ varying from 6 to 70º in steps of 0.026 s^{-1} and the diffraction patterns were compared with JCPDS standards.

The specific surface areas (SSA) of the powders heat treated at 800 ºC were measured using the Brunauer–Emmett–Teller (BET method, Micrometric Gemini M–2380) using N_2 as adsorbate. Samples were degassed at 200 ºC before each measurement.

2.3. Preparation and characterisation of green glass pellets and rods

Ten cylindrical pellets with 13 mm diameter and a thicknesses of ~3 mm were prepared by uniaxial pressing (80 MPa) of dry glass powders in a stainless steel die. The pellets were sintered in air in an electric furnace at heating rate (β) of 10 ºC min^{-1} from 20 ºC up to two different temperatures of 800 and 900 ºC, followed by 30 min soaking time, and ended by natural cooling inside the turned–off furnace. Three pellets for each sample were prepared to assure the accuracy of the results.

Density determination was performed using the buoyancy Archimedes' method by immersing the samples in distilled water, in accordance with European Standard EN 993–1. The bulk density of the glass pellets was calculated via following relation:

$$\rho_b = \frac{m_a}{m_w - m_s} \cdot \rho_w \qquad (8.1)$$

where: ρ_b is the bulk density in (g cm^{-3});

ρ_w is the density of the water, presumed to be 1 g cm^{-3};

m_a is the mass of the dry sintered pellets measured in air;

m_s is the mass of the sintered pellets suspended in water;

m_w is the mass of the sintered pellets saturated in water, measured in air.

Dilatometry measurements (Bahr Thermo Analyse DIL 801 L, Hiillhorst, Germany; heating rate (β) of 5 ºC min^{-1}) were taken for cylindrical rod samples with a diameter of 4 mm by slip casting. A filter paper wrapped around a glass rod with a closed end was inserted in a powder sand mould. The glass rod was carefully removed and the glass slurry was injected

inside using a syringe. The as consolidated green rods with lengths of ~20 mm were used for dilatometry measurements.

The microstructures and morphology of the sintered glass pellets coated with carbon were observed by scanning electron microscope (SEM, SU–70, Hitachi, Tokyo, Japan). Elemental mapping was obtained using energy dispersive spectrometer (EDS), B–U Bruker QUANTAX 400 EDS.

3. Results and discussion

3.1. MAS–NMR spectroscopy analysis

The ^{29}Si MAS–NMR is a useful way to assess the degree of polymerisation of silica–based glasses. Different local environments around the Si nucleus will give rise to different chemical shifts, enabling to extract relevant information about the predominant Q^n species. In this notation, n = 4, 3, 2, 1 and 0, represents the number of bridging oxygens (BOs) bound to other Si tetrahedral units **[36]**. Abundant Q^4 species with Si–O–Si in the 4 corners of the tetrahedral units exist in silicate rich compositions. The gradual replacement of network former by glass modifies leads to less polymerised structural units, Q^3, Q^2, Q^1 in which the silicon is coordinated by 3, 2 and 1 BO respectively. While Q^0 represents isolated silica tetrahedra (silicic acid) **[37,38]**.

Fig. 8.1 displays the MAS–NMR spectra for HSSGG **Fig. 8.1(a)**, Cu1–La1 **Fig. 8.1(b)**, and Cu5–La5 glasses **Fig. 8.1(b)**. It can be observed that all the three glasses exhibit (Q^4, Q^3, Q^2) arrangements and slight modifications in chemical shift (δ) to high negative values with adding increasing concentrations of the two doping elements. This means that Cu and La are acting as glass modifiers, decreasing the degree of polymerisation. The Cu1–La1 sample exhibits slight decreases in δ for the Q^4, Q^3 and Q^2 silica structural units as shown in **Figs. 8.1(a,b)**. Further increasing the concentrations of Cu & La caused more extensive disruptions in the silica network as confirmed by the dislocation of Q^4 and Q^3 to lower chemical shifts, and by increasing the chemical shift of Q^2 at the expense of Q^3 as observed in **Fig. 8.1(c)**. From **Fig. 8.1**, particularly from **Fig. 8.1(d)**, it can be concluded that co–doping the HSSGG with Cu & La oxides induces a general weakening effect of the glass structure.

The depolymerisation extent increases with increasing added amounts glass modifiers. The degree of condensation (D_c), and network connectivity (N_c) for some selected compositions, calculated from the MAS–NMR data **[34]**, are reported in **Table 8.6**. It is perceived that both N_c and D_c steadily decrease with increasing doping levels in the order: HSSGG > Cu1–La1 > Cu5–La5. These results suggest an increasing fraction of non–bridging oxygens (NBO).

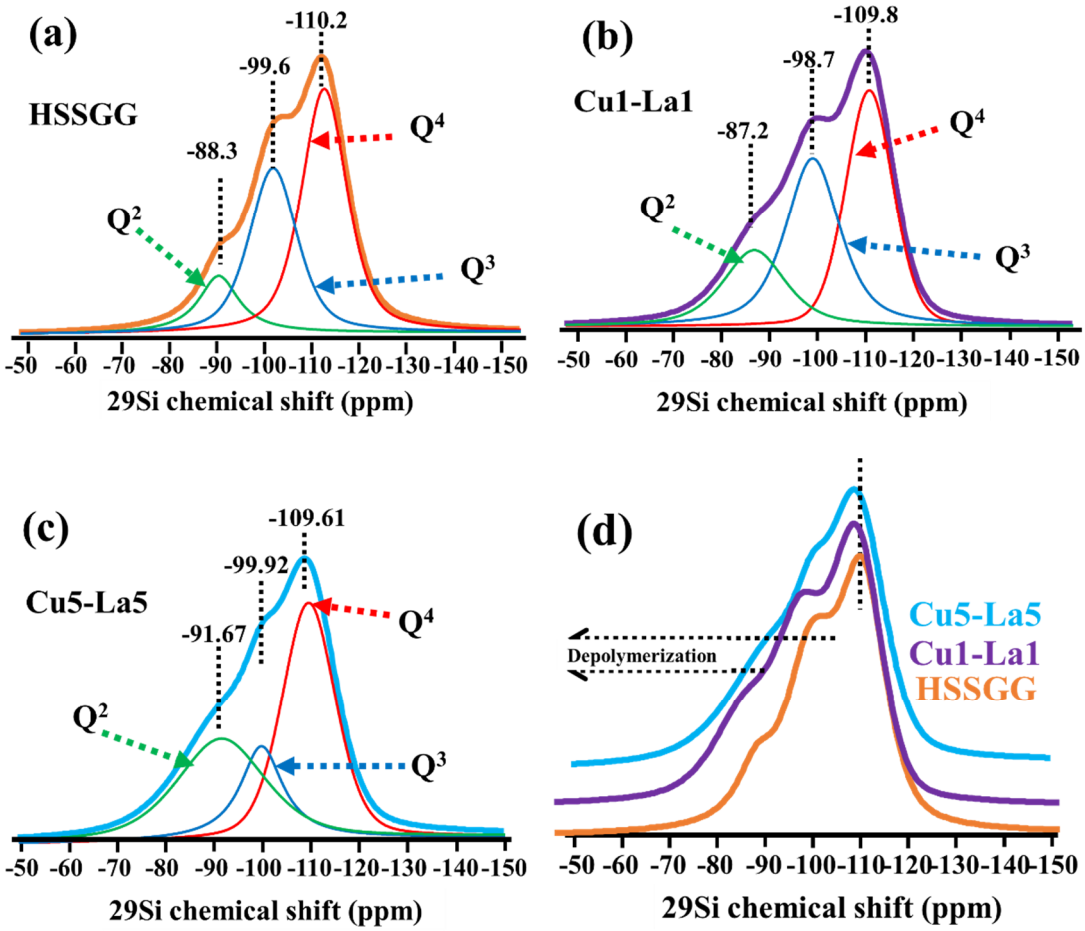

Fig. 8.1: Deconvoluted ^{29}Si MAS–NMR spectra for HSSGG; (a), Cu1–La1; (b), Cu5–La5; (c), and ^{29}Si MAS–NMR spectra in comparison for the three glasses; (d).

Table 8.6: The degree of condensation (Dc), and network connectivity (Nc) for some glass compositions, calculated from the MAS–NMR data.

	Q^n							
	Q^2		Q^3		Q^4			Nc
Sample code	Peak position (ppm)	Integral %	Peak position (ppm)	Integral %	Peak position (ppm)	Integral %	Dc %	From ^{29}Si MAS NMR
HSSGG	–88.3	12.84	–99.6	36.31	–110.2	50.85	84.5	3.38
Cu1–La1	–87.2	20.80	–98.7	39.10	–109.8	40.61	80.1	3.20
Cu5–La5	–91.7	35.29	–99.9	18.92	–109.6	45.79	77.6	3.15

3.2. Thermal analysis

The curves of differential thermal analysis (DTA) and thermogravimetric analysis (TGA) of some selected representative samples (HSSGG, Cu1–La1, and Cu5–La5) are displayed in **Fig. 8.2**. The samples undergo significant total weight losses along the heat treatment schedule as typical for sol–gel derived glasses. The weight losses occur in a step wise way, becoming more accentuated with increasing co–doping levels. The total weight losses undergone by the samples up to 250 ºC vary within ~37–40 %. These significant and continuous weight losses can be assigned to the elimination of residual water and solvents **[39]**, and/or to the extraction of N_2 gas, and are associated with the first endothermic valleys registered from RT to 164 ºC **Fig. 8.2(a)**. These endothermic valleys are slightly deeper for co–doped samples, suggesting the presence of residual nitrates that melt and decompose. $Cu(NO_3)_2 \cdot 3H_2O$ melts at ~115ºC and gradually decomposes to hydroxy copper nitrate **[40]**. Lanthanum (III) nitrate hexahydrate, $La(NO_3)_3 \cdot 6H_2O$ releases hydration water from RT to ~226 ºC **[41]**. The dehydrated metal nitrates are reduced to the respective CuO and La_2O_3 oxides at higher temperatures **[40,41]**. The DTA curves exhibit two main exothermic effects accompanied by abrupt additional weight losses varying within 8–10%. These weight losses associated with the first exothermic effect centred within the range of 295–320 ºC can be attributed to the decomposition of the organic components **[42]** and to the decomposition of metal nitrate residues **[40,41,43]**. The reduction temperature of CuO occurred at ~295 ºC. The total accumulated weight losses up to 320 ºC varied within ~45–50% **Fig. 8.2(a)**. All other metal nitrates are eliminated at ~497 ºC. The second exothermic DTA peak appearing

between 460–540 ºC and centered at ~497 ºC can be attributed to the reduction of all the nitrate salts to their oxides (CaO, Na_2O, and La_2O_3). It is worth noting the first shallow exothermic peaks and the second sharp ones observed for samples HSSGG and Cu1–La1, tend to be reversed with further increasing the co–doping level to Cu5–La5, suggesting that the combined Na, Ca, Cu, and La nitrates tend to decompose at lower temperatures in comparison to their separate individual nitrates copper nitrate to CuO at ~(263–310 ºC) **[43]**, Lanthanum nitrate form La_2O_3 at ~650ºC **[44]**, sodium nitrate form Na_2O at ~ (600–910 ºC) **[45]**, and Calcium nitrates from CaO at (658–678 ºC) **[46]**.

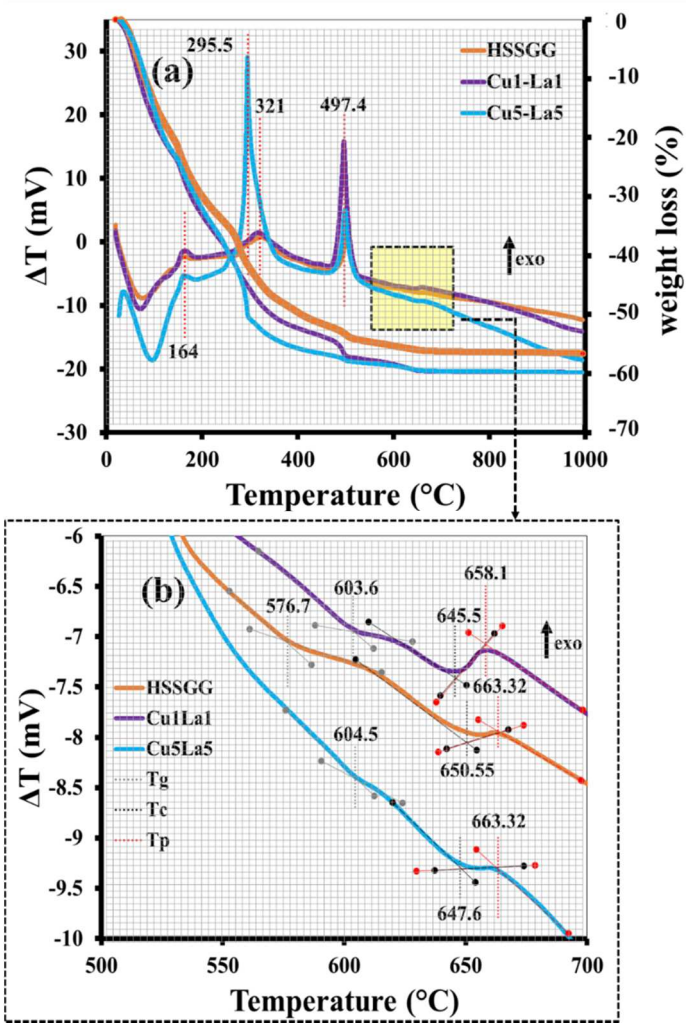

Fig. 8.2: Thermal analysis performed for three representative samples: (a) Differential thermal analysis (DTA) and thermogravimetric analysis (TGA); (b) Zoom of the area indicated in (a) to enable determining the thermal parameters (T_g, T_c & T_p).

The assignment of the second endothermic effect is consistent with the additional weight losses undergone by the samples, totalizing ~54–58% up to about 500 ºC.

The zoomed area indicated in **Fig. 8.2(a)** and replotted in **Fig. 8.2(b)** was used to estimate the thermal parameters, which are reported in **Table 8.7**. The decrease of T_c with co–doping is according to the expectations as Cu atoms promote higher thermal diffusivities and enable the formation of crystalline atomic arrangements **[47]**, as also deduced from the concomitant decrease observed for the peak crystallisation temperature (T_p).

Table 8.7: Thermal parameters including transition temperature (T_g), onset of crystallisation (T_c), peak temperature (T_p), and the sintering window ($\Delta = T_c - T_g$).

Glass	T_g (ºC)	T_c (ºC)	T_p (ºC)	$\Delta = T_c - T_g$ (ºC)
HSSGG	576.7	650.6	663.3	73.9
Cu1–La1	603.6	645.5	658.1	41.9
Cu5–La5	604.5	647.6	663.3	43.1

The changes in thermal parameters tend to firstly narrow the sintering window defined as $\Delta = T_c - T_g$ for the Cu1–La1, followed by as slight broadening effect for Cu5–La5.

Gaddam et al. **[47]** attributed the increased values of the network volume and T_g of La_2O_3 doped $Li_2O–SiO_2$ glasses to the high field strength and size of La^{3+} cation. Their observations could be explained by considering the pure network modifier role of La_2O_3 in the glass compositions and the formation of complex network structural Q^n *(Li)* and Q^n *(La)* units.

3.3. XRD of glass powders; the evolution of crystallisation phases

The X–ray diffraction patterns of the parent glass and of 6 co–doped samples heat treated at different temperatures (700 ºC, 900 ºC, and 1000 ºC) are shown in **Fig. 8.3**. It can be seen that all samples still preserve their amorphous glassy structure at 700 ºC as displayed in **Fig. 8.3(a)**. At 800 ºC all samples exhibit similar XRD patterns with crystalline peaks assigned

to three phases [cristobalite (SiO_2; pdf # 04–008–7639), quartz (SiO_2; pdf # 01–075–8320), pseudo–wollastonite [Ca(SiO_3, pdf # 01–080–9543)].

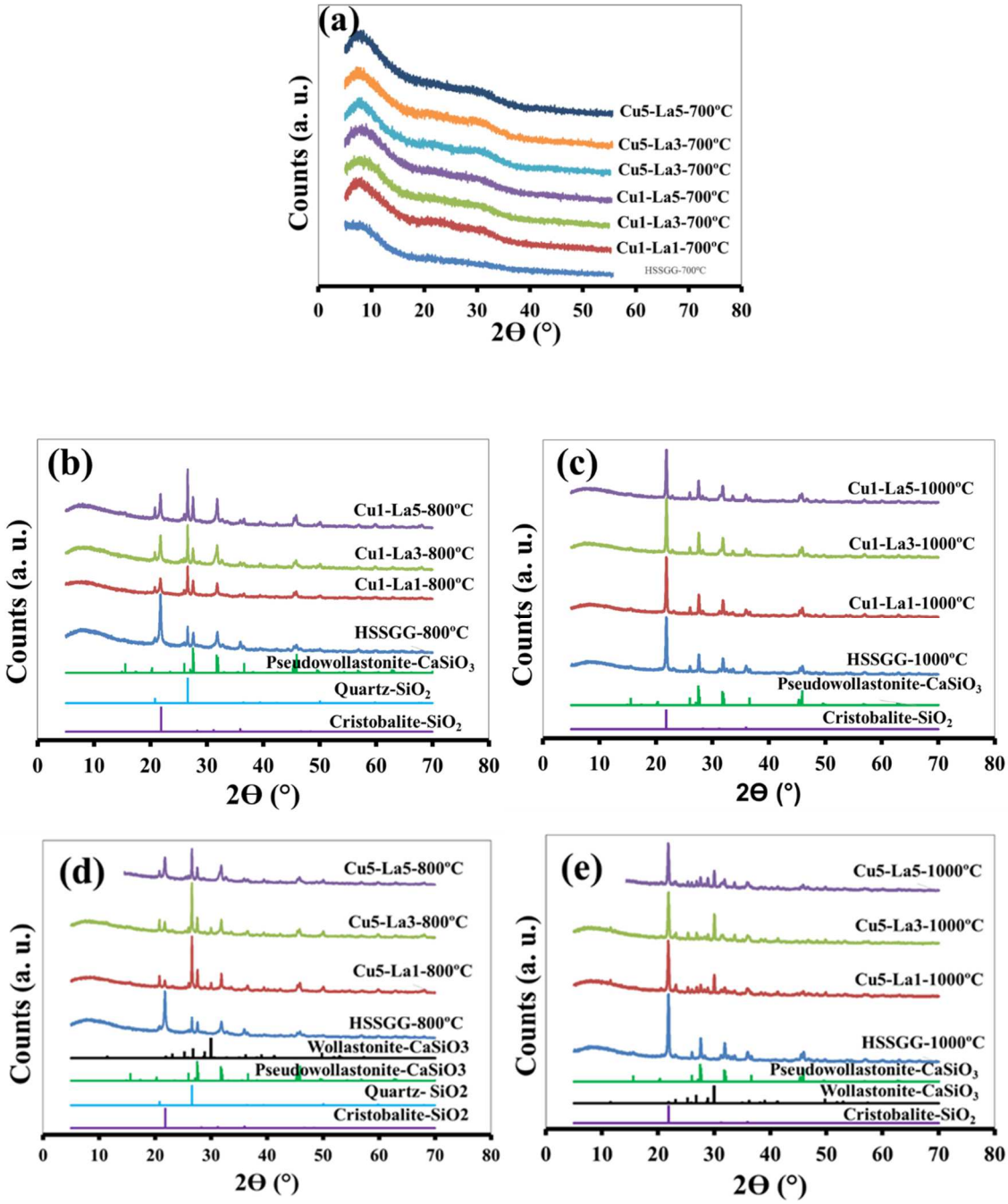

Fig. 8.3: Comparison of the XRD patterns of parent HSSGG composition with the co–doped glasses after being heat treated at different temperatures: (a) 700 ºC; (b) 800 ºC for Cu1–containing samples; (c) 1000 ºC for Cu1–containing samples; (d) 800 ºC for Cu5–containing samples; (e) 1000 ºC for Cu5–containing samples.

Cristobalite is the major crystalline phase formed in HSSGG, followed by pseudo–wollastonite and quartz. Some features common to all the samples include a

significant intensity decrease of XRD peaks of the three crystalline phases identified, and a concomitant intensification of quartz peaks at the expenses of cristobalite ones. The proneness to crystallisation is less noticeable in Cu1–La1, and then gradually increases with increasing the concentration of La (Cu1–La3 & Cu1–La5) as displayed in **Fig. 8.3(b)**.

But with further increasing the heat treatment temperature to 1000 ºC for all these low Cu–containing samples, quartz phase is fading out and cristobalite is strengthened and sharing its abundance with wollastonite [Ca(SiO_3, pdf # 04–016–5569)], a new crystalline phase formed, together with small traces of pseudo–wollastonite as seen in **Fig. 8.3(c)**.

The increase of Cu content from Cu1 to Cu5 strengthened the intensity of quartz peaks at 800 ºC at the expenses of cristobalite, especially for Cu5–La1, with slight decrease in the intensities of pseudo–wollastonite and the evolution of wollastonite as new phase. This trend became gradually less pronounced with increasing La concentrations (Cu5–La3 & Cu5–La5) as shown in **Fig. 8.2(d)**. Again, with further increasing the heat treatment temperature to 1000 ºC, induced the following changes: (i) strengthening significantly the intensity of cristobalite peaks of HSSGG; (ii) the quartz phase preferential formed at 800 ºC in all Cu5–containing samples has been transformed into cristobalite and wollastonite; (iii) the intensity of the peaks is again reduced as the La content gradually increases from Cu5–La1 to Cu5–La3 and Cu5–La5, as observed in **Fig. 8.3(e)**.

These results enable to conclude that Cu promotes the crystallisation of quartz at 800 ºC at the expenses of cristobalite phase. On the other hand, increasing concentrations of La tend to decrease the crystallisation trend. These results are consistent with the effects of co–doping on the thermal properties of the glasses presented and discussed in the previous section.

3.4. The effects of Cu–La co–doping on the BET–SSA and sintered density

The influence of co–doping on the SSA of glass powders heat treated at 800 ºC is displayed in **Fig. 8.4(a)**. It can be seen that the concomitant incorporation of Cu & La in the glassy matrix caused obvious general decreases in the SSA. This trend is less accentuated for systems with La5. To better understand the specific contributions of the two doping ions, the S/N ratio representing the contribution of each ion on the SSA is plotted in **Fig. 8.4(b)**. These

results clearly demonstrate that increasing the concentrations of Cu or La induce opposite effects on the SSA, namely a decreasing and an increasing trend, respectively, in a good agreement with the observations in **Fig. 8.4(a)**.

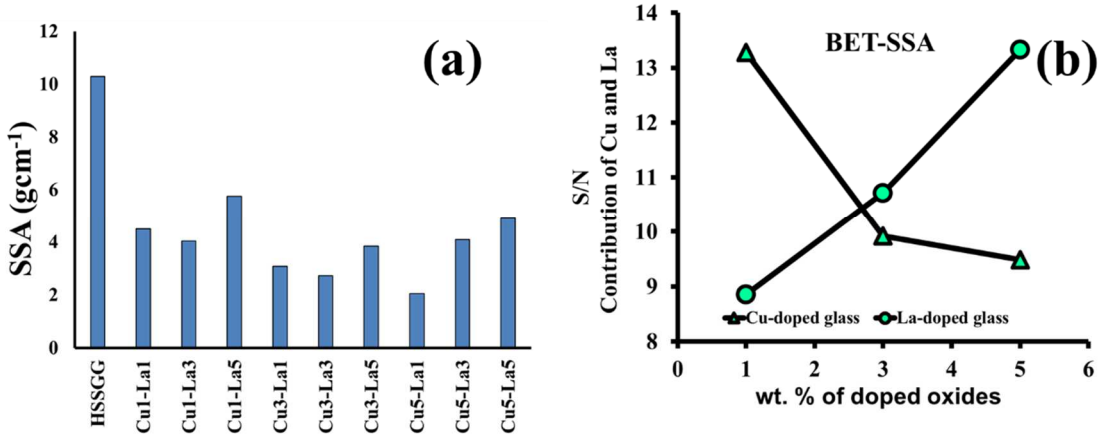

Fig. 8.4: (a) The effects of the nine Cu & La co–doping combinations on the specific area (SSA) of the resulting powders; (b) the specific contributions of the three doping levels (1, 3, 5 wt. %) of Cu & La on the SSA.

All the SSA values of the powders heat treated at 800 ºC are presented in **Table 8.8** together with the density values measured for cylindrical pellets sintered at 800 ºC and at 900 ºC.

Table 8.8: BET–SSA (m^2g^{-1}), and density (ρ)(gcm^{-3})

Nº	Glass labelling	SSA	ρ(800ºC)	ρ(900ºC)
		m^2g^{-1}	gcm^{-3}	gcm^{-3}
1	HSSGG	10.29	1.46±0.031	1.58±0.012
2	Cu1–La1	4.49	1.43±0.190	1.51±0.004
3	Cu1–La3	4.04	1.36±0.006	1.44±0.003
4	Cu1–La5	5.75	1. 22±0.045	1.46±0.001
5	Cu3–La1	3.09	1.39±0.033	1.71±0.009
6	Cu3–La3	2.74	1.35±0.014	1.64±0.002
7	Cu3–La5	3.85	1.30±0.032	1.54±0.003
8	Cu5–La1	2.06	1.42±0.001	1.82±0.017
9	Cu5–La3	4.10	1.40±0.006	1.72±0.013
10	Cu5–La5	4.90	1.35±0.022	1.71±0.008

From **Fig. 8.4** and **Table 8.8** it can be concluded that Cu exerts the most determinant reduction effect on the SSA, probably by promoting bulk diffusion and densification with

an associated decrease of porosity fraction. This is consistent with its positive influence on sintered density as depicted from **Table 8.8** and **Fig. 8.5**.

Co–doping caused an overall decrease in density of all pellets sintered at 800 ºC. The arrows in **Fig. 8.5** indicate clear decreasing trends with increasing La contents for any fixed Cu doping level, followed by a certain recovery upon further increasing the Cu doping level. This descending ramp with raising La contents followed by a step up with a new Cu increment is a common feature also observed for samples sintered at 900 ºC.

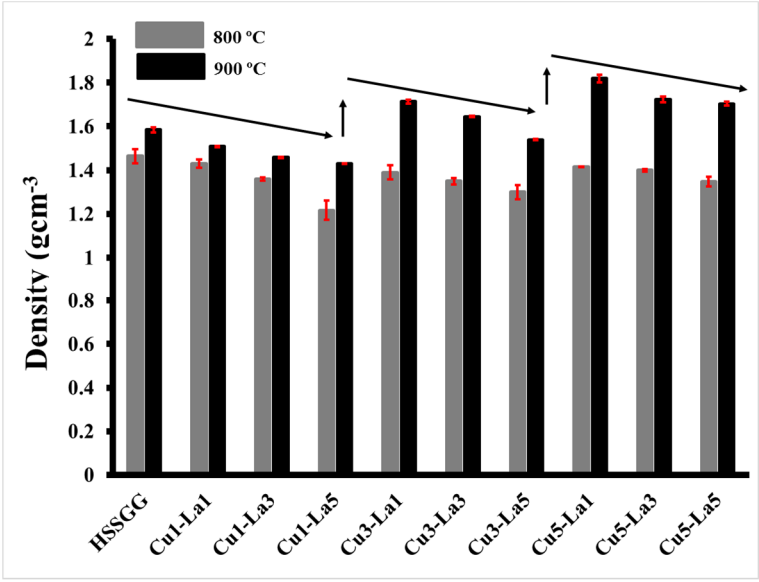

Fig. 8.5: Bulk density of undoped and co–doped samples sintered at 800 ºC and 900 ºC.

These observations enable to conclude that bulk density of samples sintered at 900 ºC is enhanced by increasing both sintering temperature and Cu content, while an opposite effect is exerted by increasing the La content.

Cu–doping was also reported to enhance the density of glasses **[48]**. This effect can be at least partially attributed to the higher atomic weight of the doping elements (Cu = 63.55 g mol^{-1}, La = 138.90 g mol^{-1}) in comparing to those of the remaining constituents of the glass (Na, Ca, Si, P) **[49]**. Moreover, the higher thermal diffusivity of Cu and its positive effect on densification is consistent with its smaller ionic radii (0.73 Å) in comparison to that of La (1.06 Å) **[50]**. This helps explaining the overall sluggish effect of La on densification. In summary, co–doping exerts a direct positive effect on sintered density through the atomic

weight, but the overall effect also depends also on the thermal diffusivity of doping species, as will be further discussed in the next section.

3.5. Dilatometry and densification behaviour assessment

The dilatometry thermograms for samples containing 3–levels of La (La1, La3, and La5) and the lowest Cu content (Cu1–La1, Cu1–La3, and Cu1–La5), are displayed in **Fig. 8.6(a)**. The equivalent results for the highest Cu content (Cu5–La1, Cu5–La3, Cu5–La5) are shown in **Fig. 8.6(b)**. These results aim at shedding further light about the combined effects of different levels of co–doping on the sintering ability, in comparison with HSSGG and are complemented with data reported in **Table 8.9**.

Table 8.9: represents the % shrinkage and the corresponding temperatures

Glass	1st Shrinkage		Plateau	2nd Shrinkage	
	$(T_i - T_f)$ (ºC)	%	$(T_i - T_f)$ (ºC)	$(T_i - T_f)$ (ºC)	%
HSSGG	665 – 825	7.8	825 – 1033	1033 – 1089	9.5
Cu1–La1	665 – 790	8.1	800 – 985	985 – 1095	13.2
Cu1–La3	665 – 755	3.0	760 – 980	980 – 1100	12.5
Cu1–La5	665 – 800	10.0	800 – 993	993 – 1066	11.7
Cu5–La1	625 – 719	1.8	725 – 755	755 – 1073	14.0
Cu5–La3	585 – 705	2.5	–	825 – 1025	13.0
Cu5–La5	590 – 723.5	5.3	736 – 800	800 – 940	11.0

It can be seen that HSSGG starts shrinking at about ~665 ºC and then follows a step wise densification behaviour. The first maximum linear shrinkage of about 7.8 % is reached at ~825ºC, followed by a constant plateau that extends up to ~1066 ºC, where a second shrinkage step starts. This second densification step ends up for a total shrinkage of ~11.7 % achieved at ~1033 ºC.

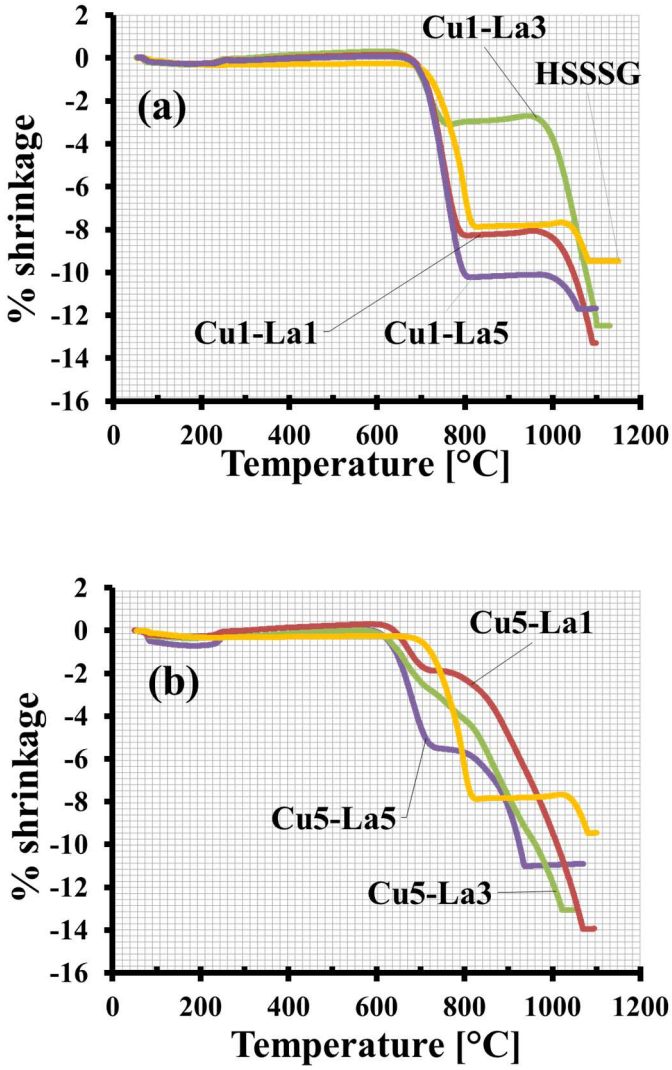

Fig. 8.6: Dilatometry thermogram comparing the shrinkage behaviour of HSSGG with those of co–doped samples for: (a) low Cu content; (b) high Cu content.

Co–doping tends to stimulate early densification, shifting the onset of shrinkage to slightly lower temperatures. The step wise densification behaviour is more evident for the low Cu–content samples (Cu1–La1, Cu1–La3 and Cu1–La5). From RT up to ~700 ºC all these samples exhibit similar behaviour, followed by different shrinkage extents within ~800–900 ºC, and subsequent extended plateaux. A second shrinkage step is then initiated with further increasing the temperature followed by new plateaux. The extent of the 1st stage shrinkage of Cu1–La1 is slightly increased relatively to that of HSSGG, **Fig. 8.6(a)**. But increasing the La content to Cu1–La3 caused a drastic reduction of shrinkage, while a further increase to

Cu1–La5 fostered densification and enhanced the shrinkage extent. These results demonstrate that synergetic complex effects result from co–doping.

The onset of shrinkage for Cu5–containing samples appears at ~600 ºC **Fig. 8.6(b)**, i.e., about 100 ºC below in comparison to HSSGG and the Cu1–containing samples, **Fig. 8.6(a)**. Cu5–La5 exhibits a fast 1st linear shrinkage of about 5.5% up to ~760 ºC followed by an apparent plateau with a not well defined end. The densification kinetics gradually accelerates as temperatures increases and then stops in a plateau at ~940 ºC. The Cu5–La1 exhibits the slowest 1st linear shrinkage rate reaching an extent of only about 1.8% up to ~755 ºC. This is also followed by an apparent short plateau up to ~755 ºC and then by a gradual acceleration up to ~1068 ºC where a new plateau starts. The Cu5–La3 specimen shares the features of both Cu5–La5 and Cu5–La1 sample and reveals intermediate shrinkage behaviour.

The dilatometry curves of Cu5–containing samples also show that high linear shrinkage of 13–14 % could be achieved for Cu5–La1 and Cu5–La3. This suggests that using higher sintering temperatures might be a way to get materials with high densification degrees and enhanced mechanical properties. However, devitrification also increases with sintering temperature and decreases with incremental amounts of La, as shown in **Fig. 8.2**. Considering that bioactivity is affected by devitrification, all these relevant features need to be suitably balanced.

The combined effects of Cu & La on shrinkage and density can also be assessed using the signal to noise ratio (S/N) displayed in **Fig. 8.7(a)**, and **Fig. 8.7(b)**, respectively. The S/N values are calculated by using eq. (8.1) according to the Taguchi method **[51]**:

$$\mathrm{SN} = -10 \log_{10}\left(\frac{1}{n}\sum_{i=1}^{n}\frac{1}{y_i^2}\right) \qquad (8.1)$$

For instance, y_i is the respective value for the density or shrinkage for (n) number of values.The S/N measures the dispersion around the target value. The eq.(8.1) is formulated for the quality characteristic "larger–the–better" , since the larger values of density or shrinkage iare prefferable. The larger the S/N ratio, the smaller will be the dispersion **[52]**.

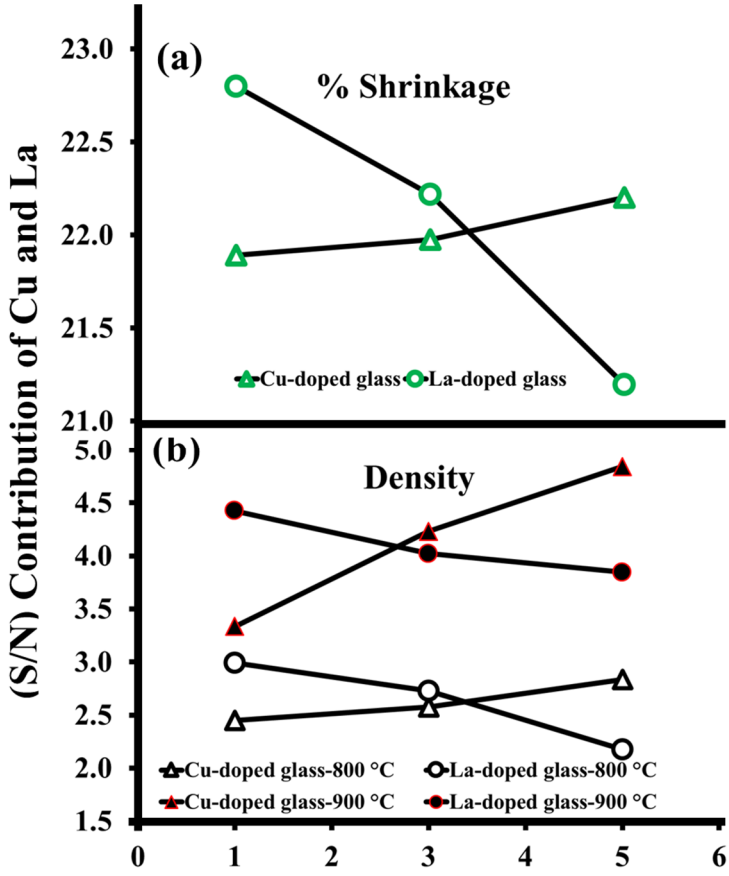

Fig. 8.7: The contribution of Cu & La on the density and % shrinkage

These plots confirm the enhancing effects of increasing the Cu content on shrinkage and density at both sintering temperatures; while an opposite contribution is provided by increasing the La content, especially at the lower sintering temperature (800 ºC).

3.6. SEM and Energy–Dispersive X–Ray Spectroscopy (EDS) analysis

Fig. 8.8 presents the SEM micrographs of fracture surfaces pellets sintered at 800 ºC and at 900 ºC and prepared from some selected representative samples (HSSGG, **Figs. 8.8(a, c, e, g)** and Cu5–La5, **Figs. 8.8(b, d, f, h)**, together with their elemental mappings. The microstructure of HSSGG sintered at 800 ºC **Fig. 8.8(a)** consists of large grains surrounded by clusters of partially fused fine particles with sizes between 0.2–0.3 µm, forming a porous structure with homogeneous elemental distribution **Fig. 8.8(b)**. Increasing the sintering temperature to 900 ºC enhanced neck formation and densification as shown in **Fig. 8.8(c)**.

This is in good agreement with density and dilatometry data discussed in the two previous sections. But the homogeneity of the elemental distribution was maintained as seen in **Fig. 8.8(d)**.

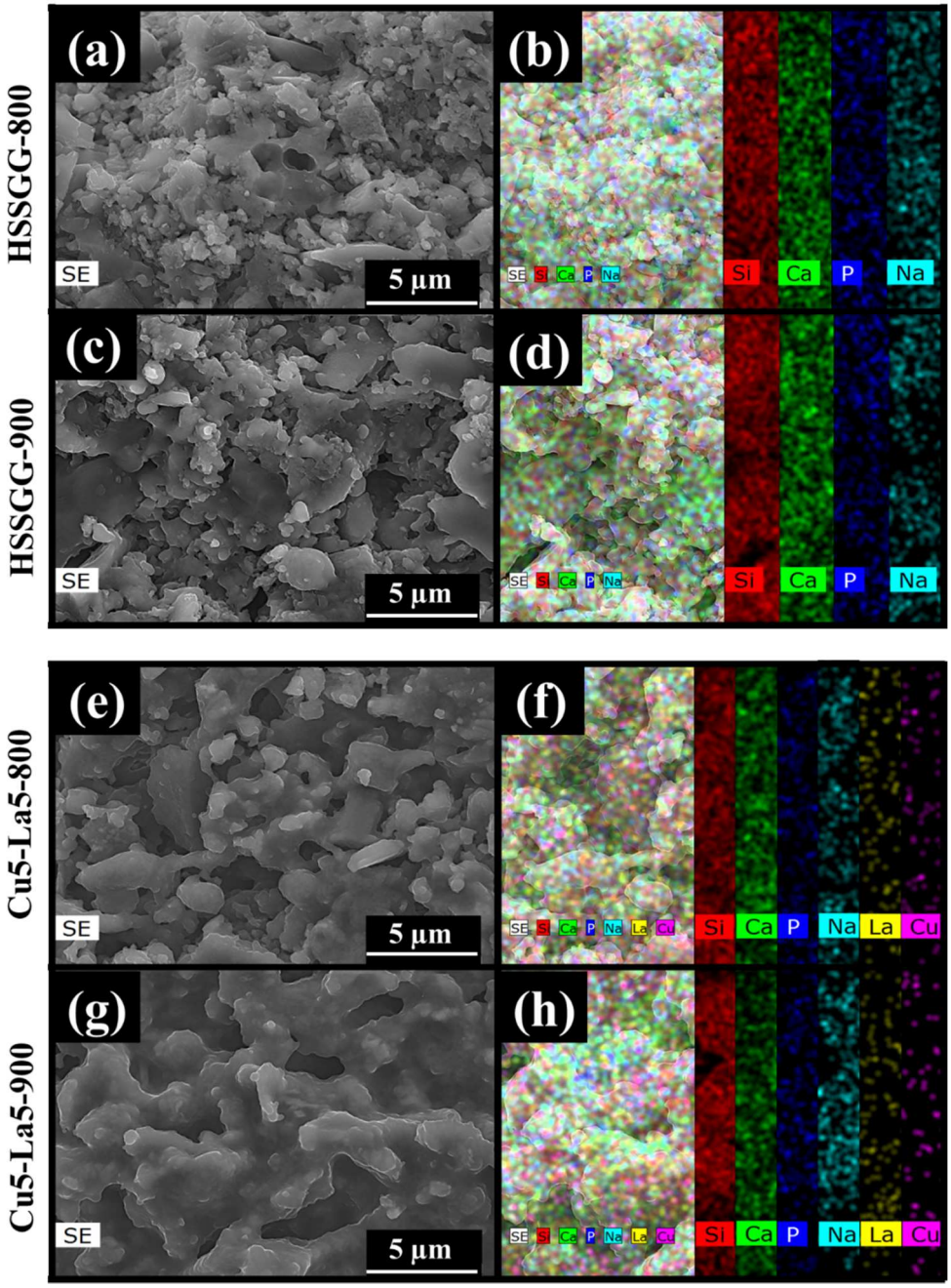

Fig. 8.8: SEM micrographs of pellets of some selected representative samples (HSSGG, and Cu5–La5) sintered at 800 ºC and at 900 ºC: (a–d) HSSGG; (e–h) Cu5–La5; (a–b & e–f) 800 ºC; (c–d & g–h) 900 ºC.

The sample Cu5–La5 sintered at 800ºC exhibits grains well bonded through extensive neck formation as seen in **Fig. 8.8(e)**. This confirms the enhancing effect of co–doping on sintered density for Cu5–containing compositions discussed above. This effect is particularly noticeable upon increasing the sintering temperature to 900 ºC as observed in **Fig. 8.8(g)**. The starting particles joined together to form larger clusters of fused grains, eliminating the fine pores and rounding the large inter–agglomerate ones forming a kind of porous scaffolds. Again, the high degree of homogeneity is preserved in the Cu5–La5 sample sintered at both temperatures as can be seen in **Fig. 8.8(f)** and **Fig. 8.8(h)**.

4. Conclusions

This work intended to disclose the effects of Cu & La co–doping a sol–gel derived quaternary (Si, Ca, Na, P) parent glass on the structure, thermal properties, crystallisation and sintering–ability using a (L9)–n3v2–Taguchi orthogonal array (OA) of experiments. The results presented and discussed above enable the following conclusions to be drawn:

(i) The parent HSSGG glass presents the most polymerised silica network structure with the highest population of Q^4 in comparison co–doped glasses. The doping oxides play the typical roles of glass modifiers.

(ii) The apparent discrepancy between depolymerisation effects on silica network caused by co–doping and the increase in T_g, are likely due to the high field strength and size of La^{3+} cation and to the formation of complex network structural Q^n *(La)* units.

(iii) All glasses heat treated up to 700 ºC preserve their amorphous structure and partially crystallize at 800 ºC into cristobalite, quartz and 2 calcium silicate phases wollastonite, pseudowollastonite. The quartz phase disappears at 1000 ºC and transforms into cristobalite. Increasing Cu contents promote crystallisation, while an opposite tend is observed for La.

(iv) The parent HSSGG glass exhibits highest SSA among all the glass powders heat treated at 800 ºC. Co–doping with CuO and La_2O_3 oxides tends to stimulate atomic diffusion and reduce the exposed surface area. But while increasing Cu contents causes strong decreases in SSA, an opposite effect is observed for La.

(v) None of the HSSGG and Cu1–containing glass green bodies undergoes any shrinkage up to 700 ºC. But the onset of shrinkage is shifted to 600 ºC for Cu5–containing glass compacts. Increasing Cu contents tends to enhance shrinkage and sintered density, while an opposite effect is exerted by La, especially at lower sintering temperatures. At higher temperatures, an increase of La concentration favours the densification behaviour.

Acknowledgments

R.C. Pullar wishes to thank the FCT Grant IF/00681/2015 for supporting this work. B. A. E. Ben–Arfa thanks FCT grant BIONANOSCULP PTDC/EPH–PAT/6281/2014 for supporting him during this work. This work was developed in the scope of the project CICECO–Aveiro Institute of Materials (Ref. FCT UID /CTM /50011/2013), financed by national funds through the FCT/MEC and when applicable co–financed by FEDER under the PT2020 Partnership Agreement.

References

[1] L.L. Hench, N. Roki, M.B. Fenn, Bioactive glasses: Importance of structure and properties in bone regeneration, J. Mol. Struct. 1073 (2014) 24–30.

[2] M.N. Rahamana, D.E. Daya, S. Bal, Q. Fu, S.J. B., L.F. Bonewalde, et al., Bioactive glass in tissue engineering, Acta Biomater. 7 (2011) 2355–2373.

[3] L.L. Hench, Bioceramics: From Concept to Clinic, J. Am. Ceram. Soc. 74 (1991) 1487–1510.

[4] J. McAndrew, C. Efrimescu, E. Sheehan, D. Niall, Through the looking glass; Bioactive glass S53P4 (BonAlive®) in the treatment of chronic osteomyelitis, Ir. J. Med. Sci. 182 (2013) 509–511.

[5] L. Drago, D. Romanò, E. De Vecchi, C. Vassena, N. Logoluso, R. Mattina, et al., Bioactive glass BAG–S53P4 for the adjunctive treatment of chronic osteomyelitis of the long bones: an in vitro and prospective clinical study., BMC Infect. Dis. 13 (2013) 1–8.

[6] C. Tirapelli, H. Panzeri, R.G. Soares, O. Peitl, E.D. Zanotto, A novel bioactive glass–ceramic for treating dentin hypersensitivity., Braz. Oral Res. 24 (2010) 381–7.

[7] S. Kargozar, S. Hamzehlou, F. Baino, Potential of bioactive glasses for cardiac and pulmonary tissue engineering, Materials (Basel). 10 (2017) 1–17.

[8] J. Syvänen, Y. Nietosvaara, I. Kohonen, E. Koskimies, M. Haara, J. Korhonen, et al., Treatment of Aneurysmal Bone Cysts with Bioactive Glass in Children, Scand. J. Surg. 107 (2018) 76–81.

[9] Q. Fu, E. Saiz, M.N. Rahaman, A.P. Tomsia, Bioactive glass scaffolds for bone tissue engineering: state of the art and future perspectives, Mater Sci Eng C Mater Biol Appl. 31 (2012) 1245–1256.

[10] E. Fiume, J. Barberi, E. Verné, F. Baino, Bioactive glasses: From parent 45S5 Composition to Scaffold–Assisted Tissue–Healing Therapies, J. Funct. Biomater. 9 (2018) 1–33.

[11] V.K. Vyas, A.S. Kumar, S. Prasad, S.P. Singh, R. Pyare, Bioactivity and Mechanical behavior of cobalt oxide doped bioactive glass, Bull. Mater. Sci.,. 38 (2015)

957–964.

[12] V.K. Vyas, A. Sampath Kumar, S.P. Singh, R. Pyare, Effect of nickel oxide substitution on bioactivity and mechanical properties of bioactive glass, Bull. Mater. Sci. 39 (2016) 1355–1361.

[13] J.. Wang, C.K.; Ju, C.P.; Chern Lin, Effect of doped bioactive glass on structure and properties of sintered hydroxyapatite, Mater. Chem. Phys. 53 (1998) 138–149.

[14] R. Moonesi Rad, A.Z. Alshemary, Z. Evis, D. Keskin, K. Altunbaş, A. Tezcaner, Structural and biological assessment of boron doped bioactive glass nanoparticles for dental tissue applications, Ceram. Int. 44 (2018) 9854–9864.

[15] B.A.E. Ben–Arfa, I.M. Miranda Salvado, J.M.F. Ferreira, R.C. Pullar, The Influence of Cu2+ and Mn2+ Ions on the Structure and Crystallization of Diopside–Calcium Pyrophosphate Bioglasses, Int. J. Appl. Glas. Sci. 7 (2016) 345–354.

[16] B.A.E. Ben–Arfa, I.M.M. Salvado, J.M.F. Ferreira, R.C. Pullar, The effect of functional ions (Y3+, F−, Ti4+) on the structure, sintering and crystallization of diopside–calcium pyrophosphate bioglasses, J. Non. Cryst. Solids. 443 (2016) 162–171.

[17] I.D. Thompson, L.L. Hcnch, Mechanical properties of bioactive glasses, glass–ceramics and composites, in: Proc. Inst. Mech. Eng. Part H J. Eng. Med., 1998: pp. 127–136.

[18] J.R. Jones, Review of bioactive glass: From Hench to hybrids, Acta Biomater. 9 (2013) 4457–4486.

[19] R.A. Pérez, J. Won, J.C. Knowles, H. Kim, Naturally and synthetic smart composite biomaterials for tissue regeneration ☆, Adv. Drug Deliv. Rev. 65 (2013) 471–496.

[20] M. Par, Z. Tarle, R. Hickel, N. Ilie, Polymerization kinetics of experimental bioactive composites containing bioactive glass, J. Dent. 76 (2018) 83–88.

[21] L.L. Hench, J. Julian, Bioactive Glasses : Frontiers and Challenges, Frontiers (Boulder). 3 (2015) 1–12.

[22] L. Courthéoux, J. Lao, J. Nedelec, E. Jallot, Controlled Bioactivity in Zinc–Doped

Sol – Gel–Derived Binary Bioactive Glasses, J. Phys. Chem. C. 112 (2008) 13663–13667.

[23] J. Soulie, J.M. Nedeleccd, E. Jallot, Influence of Mg doping on the early steps of physico–chemical reactivity of sol – gel derived bioactive glasses in biological medium, Phys. Chem. Chem. Phys. 11 (2009) 10473–10483.

[24] A. Philippart, N. Gómez–cerezo, D. Arcos, A.J. Salinas, E. Boccardi, M. Vallet–regi, et al., Novel ion–doped mesoporous glasses for bone tissue engineering : Study of their structural characteristics in fl uenced by the presence of phosphorous oxide, J. Non. Cryst. Solids. 455 (2017) 90–97.

[25] J. Bejarano, P. Caviedes, H. Palza, Sol–gel synthesis and in vitro bioactivity of copper and zinc–doped silicate bioactive glasses and glass–ceramics, Biomed. Mater. 10 (2015) 1–13.

[26] N.J. Lakhkar, E.A.A. Neel, V. Salih, Strontium oxide doped quaternary glasses : effect on structure , degradation and cytocompatibility, J. Mater. Sci. Mater. Med. 20 (2009) 1339–1346.

[27] W. Nowicki, Synthesis and characterization of a binary system La2O3 – SiO2 prepared by combustion method, J. Sol–Gel Sci. Technol. 82 (2017) 574–580.

[28] W.D. Wong–ángel, L. Téllez–jurado, J.F. Chávez–alcalá, E. Chavira–martínez, V.F. Verduzco–cedeño, Effect of copper on the mechanical properties of alloys formed by powder metallurgy, Mater. Des. 58 (2014) 12–18.

[29] M. Sabzevari, S. Abdolkarim, A. Moloodi, Physical and mechanical properties of porous copper nanocomposite produced by powder metallurgy, Adv. Powder Technol. 27 (2016) 105–111.

[30] M. V Kostina, M.M. Perkas, A.E. Shelest, V.S. Yusupov, Effect of Copper Additions on the Mechanical Properties of Iron 1, Metally. 2011 (2011) 454–458.

[31] Y. Zhao, J. Zhu, L. Chang, J. Song, X. Chen, X. Hui, Influence of Cu content on the mechanical properties and corrosion resistance of Mg−Zn −Ca bulk metallic glasses, Int. Ournal Miner. Metall. Mater. 21 (2014) 487–493.

[32] Z. Yao, P. Houizot, F. Célarié, D. Möncke, L. Wondraczek, T. Rouxel, et al., The

influence of Cu content on the mechanical properties of copper–borate glasses, Key Eng. Mater. 702 (2016) 71–76.

[33] S. V Smiljanic, S.R. Grujic, M.B. Tošic, Vladimir Živanovic, S.D. Matijaševic, J.D. Nikolic, et al., Effect of La2O3 on the structure and the properties of strontium borate glasses, Chem. Ind. Eng. Qual. 22 (2016) 111–115.

[34] B.A.E. Ben–Arfa, I.M.M. Salvado, J.M.F. Ferreira, R.C. Pullar, Enhanced bioactivity of a rapidly–dried sol–gel derived quaternary bioglass, Mater. Sci. Eng. C. 91 (2018) 36–43.

[35] B.A.E. Ben–Arfa, I.M. Miranda Salvado, J.M.F. Ferreira, R.C. Pullar, A hundred times faster: Novel, rapid sol–gel synthesis of bio–glass nanopowders (Si–Na–Ca–P system, Ca:P = 1.67) without aging, Int. J. Appl. Glas. Sci. 8 (2017) 337–343.

[36] H. Maekawa, T. Maekawa, K. Kawamura, T. Yokokawa, The structural groups of alkali silicate glasses determined from 29Si MAS–NMR, J. Non. Cryst. Solids. 127 (1991) 53–64.

[37] J. Machácek, O. Gedeon, Q–Species in Alkali–disilicate glasses, Ceram. – Silikaty. 47 (2003) 45–49.

[38] J. Marchi, Biocompatible Glasses–Advance structured materials V. 53, Springer, Gewerbestrasse, 2016.

[39] G. Gorni, M.J. Pascual, A. Caballero, J.J. Velázquez, J. Mosa, Y. Castro, et al., Crystallization mechanism in sol–gel oxyfluoride glass–ceramics, J. Non. Cryst. Solids. (2018).

[40] S.A.A. Mansour, Thermoanalytical investigation of the decomposition course of copper oxysalts II. Copper(II) nitrate trihydrate, J. Therm. Anal. 45 (1995) 1381–1392.

[41] Z. Guang, Y.U. Jun–xia, X.U. Zhi–gao, Z. Fang, C.H.I. Ru–an, Kinetics of thermal decomposition of lanthanum oxalate hydrate, Trans. Nonferrous Met. Soc. China. 22 (2012) 925–934.

[42] M. Zaharescu, L. Predoana, J. Pandele, Relevance of thermal analysis for sol–gel–derived nanomaterials, J. Sol–Gel Sci. Technol. 86 (2018) 7–23.

[43] S. Ryu, W. Lee, S. Park, Thermal decomposition of hydrated copper nitrate on activated carbon fibers, Carbon Sci. 2004. 5 (2004) 180–185.

[44] S.J. Kim, W.K. Han, S.G. Kang, M.S. Han, Y.H. Cheong, Formation of Lanthanum Hydroxide and Oxide via Precipitation, Solid State Phenom. 135 (2008) 23–26.

[45] E.S. Freeman, The kinetics of the thermal decomposition of sodium nitrate and of the reaction between sodium nitrite and oxygen, J. Am. Chem. Soc. 60 (1956) 14871493.

[46] C. Ettarh, A kinetic and mechanistic study of the thermal decomposition of calcium nitrate, Thermochim. Acta. 288 (1996) 203–219.

[47] A. Gaddam, H.R. Fernandes, D.U. Tulyaganov, J.M. Ferreira, The structural role of lanthanum oxide in silicate glasses (excepted), J. Non–Crystalline Solids. (2018).

[48] I. Kashif, A.A. Soliman, H. Farouk, M. El–Shorpagy, A.M. Sanad, Effect of copper addition on density and magnetic susceptibility of lithium borate glasses, Phys. B Condens. Matter. 403 (2008) 3903–3906.

[49] M.H.M. Zaid, K.A. Matori, S.H. Abdul Aziz, A. Zakaria, M.S.M. Ghazali, Effect of ZnO on the physical properties and optical band gap of soda lime silicate glass, Int. J. Mol. Sci. 13 (2012) 7550–7558.

[50] A.F. Wells, Structural Inorganic Chemistry, 4th ed., Oxford university press, London, 1975.

[51] C.F. Jeffrey Kuo, T.L. Su, P.R. Jhang, C.Y. Huang, C.H. Chiu, Using the Taguchi method and grey relational analysis to optimize the flat–plate collector process with multiple quality characteristics in solar energy collector manufacturing, Energy. 36 (2011) 3554–3562.

[52] Ranjit Roy, A Primer on the Taguchi Method, Van Nostrand Reinhold, New York, 1990.

Chapter 9

The present chapter was published on:
Journal of Ceramics International;
Volume 44, Issue 11,
2018,
Pages 12754-12762.
Doi: 10.1016/j.ceramint.2018.04.080

The influence of processing parameters on morphology and granulometry of a wet comminuted sol–gel glass powder

Basam A. E. Ben–Arfa [a], Isabel M. Miranda Salvado *, José M. F. Ferreira [a] and Robert C. Pullar *.

Department of Materials and Ceramic Engineering / CICECO – Aveiro Institute of Materials, University of Aveiro, 3810–193 Aveiro, Portugal

*To whom correspondence should be addressed: isabelmsalvado@ua.pt, rpullar@ua.pt

Keywords: Powder; Heat treatment temperature; Wet ball milling; Particle size distribution; Nitrogen adsorption isotherms.

Abstract

A quaternary bioactive sol–gel glass of high silica content was heat treated at different temperatures and then wet ball milled under different balls to powder ratios. A total of sixteen experiments were performed to study in detail the effects of both experimental variables on the structure, morphology, particle size distributions and nitrogen adsorption isotherms. The balls to powder ratio exerts a tremendous influence on the final particle size distribution of the powders, while its effects on the pore volume and morphology are minimal. These structural features are mostly governed by the changes in calcination temperature. Therefore, understanding the specific roles of each experimental parameter is of paramount importance towards optimum achieving powders with the desired properties. This work sheds light on the importance of using a suitable combination of these two parameters for tuning the morphology and the granulometry of the sol–gel derived bioactive glass powders.

1. Introduction

Powdered raw materials are widely used to produce ceramics in many industrial sectors [**1**]. The ceramic parts can be shaped either by dry or by wet powder processing routes. The dry processing route includes pressing the powder to form a green body and often requires the addition of processing additives such as binders to assist in the consolidation process and to confer enough strength to the green bodies to enable safe handling and densification behaviour along the subsequent processing steps **[2]**. The wet routes involve mixing the powders with a proper liquid in the required proportions, and adding suitable amounts of processing additives with different roles, which might include dispersants, binders, plasticizers, thickening agents, etc.. The aim is obtaining homogeneous mixtures and to confer them suitable rheological properties for the selected shaping technique. The traditional wet consolidation techniques might start from: (i) relatively concentrated pastes of clayey based materials or of advanced ceramics plasticized with suitable processing additives, and be accomplished by plastic forming (extrusion, roll forming, and jiggering) **[3]**; (ii) fluid suspensions that consolidate upon partially removing the liquid by slip casting **[4]** or pressure casting **[5]**, or by evaporation such as in tape casting **[6]**. However, it was shown that liquid removal driven by the capillary suction exerted by plaster moulds (slip casting), eventually co–adjuvated by an external applied pressure (pressure casting) is prone to lead to particle segregation by a process known as clogging effect **[7]**. This segregation mechanism is particularly favoured when fine particles are enough free to fast move with the liquid under the effects of driving forces, leaving behind the coarser and heavier ones. In other words, all the factors that contribute to lower the viscosity of the medium (high degree of dispersion, decrease in solids loading) enhance the phenomenon. On the other hand, the deposition kinetics also determines the extent of particle segregation. It was shown that the driving force exerted by plaster moulds (about 0.15 MPa) maximized the clogging effect. Lower driving forces favoured segregation by sedimentation, while higher ones did not allow particles to order in highest possible packing arrangements **[8]**. Aiming at overcoming the drawbacks of wet consolidation techniques involving liquid removal and at further exploring the potential advantages of colloidal processing, a number of direct consolidation techniques were developed. The homogeneous suspensions are cast in non–porous moulds and transformed into rigid bodies without liquid removal, thus preserving the homogeneity achieved in the starting suspensions. The consolidation can be achieved through different

setting mechanisms, including, Starch Consolidation **[9]**, Gel Casting **[10]**, Direct Consolidation Casting **[11]**, Hydrolysis–Assisted Solidification **[12]**; Temperature Induced Gelation **[13]**, Epoxy Gel Casting **[14]**, etc.. Direct consolidation techniques enable reducing the number and the size of structural defects, thus enhancing the reliability of the advanced ceramics, and expanding the applications of colloidal processing. To achieve high green density and the desirable final properties **[15]**, particle size (PS), particle size distribution (PSD) and particle morphology of the powders and all the relevant processing parameters need to be optimized. This also applies to the modern additive manufacturing techniques when starting from powders like in 3–D printing **[16]**, or from extrudable pastes like in robocasting **[17]**. All of these reasons justify a renewed emphasis on controlling the properties of the powders involved in the processing of ceramic and glass materials.

The reduction in particle size occurring during milling results from the accumulated stresses inside the particles due to the applied mechanical energy, which induce cracks that propagate, leading to particle breakage **[18]**.

Particles breakage, comminution, pulverizing, and milling, are interchangeably terms, commonly used with apparent identical meanings. The powder milling process may be conducted under dry conditions (dry milling) or in wet environments (wet milling). The later one is more efficient, being commonly recommended when high surface energy induces agglomeration between particles **[19]**.

Many important parameters should be taken into consideration while performing wet ball milling. For example, the liquid to powder ratio (LPR), i.e., the solids loading, the type of milling machine and the speed at it works need to be selected according to the rheological behaviour of the suspension **[20]**. Increasing heat treatment temperatures gradually lead to the formation of hard agglomerates that are difficult to destroy on milling, which strongly affect the microstructure and the properties of the final products. A few examples include power transmission **[20]**, optical properties **[21]**, photocatalytic activity **[22,23]**, drug loading and release **[24]**, phase transformations **[25]**, and sintering ability **[26]**. The effects of balls to powder ratio (BPR) on phase formation and resulting crystallite size have been tackled particularly in works related to mechanochemical synthesis **[27–29]**. However, most of these studies aimed at disclosing some interdependencies between the investigated experimental variables and the measured properties in certain particular applications.

To the best of the author's knowledge, the effects of heat treatment temperature and of the balls to powder ratio on the wet milling performance, granulometry and morphology of the powders are still to be better documented. The aim of this work is to perform a systematic investigation about the effects of these two experimental variables on particle size distributions of the powders, crystalline phase assemblage, pore volume, and morphology of sol–gel derived bioactive glass particles.

2. Materials and methods

2.1. Wet milling procedures

The raw material used in the wet milling experiments was a high–silica–content four–component (SiO_2–CaO–Na_2O–P_2O_5) bioglass system synthesised by employing developed sol–gel method **[30]**. This glass was prepared with a stoichiometry of 75Si–16Ca–5Na–4P (in mol%) as described elsewhere **[31]**. The as dried glasses were calcined in air for a fixed soaking time of 2 h at four different heat treated temperatures (HTT) (550 ºC, 675 ºC, 800 ºC, 925 ºC). The calcination was done in three stages: 1st stage, from room temperature (RT) to 200 ºC, at the heating rate of 1 ºC min^{-1}; 2nd stage, from 200 ºC to 400 ºC, at the heating rate 2 ºC min^{-1}; and the 3rd stage from 400 ºC to the final HTT values (550 ºC, 675 ºC, 800 ºC, 925 ºC) at the heating rate of 5 ºC min^{-1}. Natural cooling to RT followed the soaking time period of 2 h at the maximum HTT values to obtain final glass granules. These glass granules were dry milled for 10 minutes and passed through a 200 µm mesh sieve, and then used as starting powders for all milling experiments. Wet milling in ethanol (EtOH) was carried out in a S–series–Fast mill machine, type S2–1000 (Ceramic instruments Sassuolo–Italy) under a rotational speed of 390 rpm, using sintered alumina jar of 300 cc capacity (Ceramic instruments Sassuolo–Italy) and spherical yttria–stabilized zirconia milling balls with diameters of 10 mm (Tosoh, Tokyo, Japan). The milling experiments were conducted for different periods of time and using different balls to powder mass ratios (BPR) and constant ethanol (EtOH) mass to powder ratio (EPR) as shown in **Table 9.1**. After milling, the balls were removed by using a drainer and the slurry was kept overnight in oven at 60 ºC for drying. The as obtained dry milled powders were passed through a 63 µm mesh sieve to remove large agglomerates and their features were assessed by the characterisation techniques described below.

Table 9.1: The values of experimental parameters set in the 16 milling experiments

	Independent variables			
Trials	BPR	EPR	HTT (ºC)	Milling time (min)
E1	5	2	550	120
E2	5	2	675	120
E3	5	2	800	120
E4	5	2	925	120
E5	10	2	550	120
E6	10	2	675	120
E7	10	2	800	120
E8	10	2	925	120
E9	15	2	550	120
E10	15	2	675	120
E11	15	2	800	120
E12	15	2	925	120
E13	20	2	550	120
E14	20	2	675	120
E15	20	2	800	120
E16	20	2	925	120

2.2. Glass Characterization

Particle size (PS) and particle size distributions (PSD) were measured using a laser diffraction particle size analyser (Coulter LS particle size analyser; Beckman Coulter, CA). All measurements were done in triplicate runs.

The specific surface areas (SSA) and the sorption isotherms of the powders were computed using the Brunauer–Emmett–Teller (BET method, Micrometric Gemini M–2380) using N_2 as adsorbate. Standard pre–treatment conditions were 105 ºC under vacuum for 12 h.

The amorphous and crystalline phases of the samples were identified by X–ray diffraction (XRD, PANalytical XPERT–PRO Diffractometer system) using Cu–Kα radiation (Kα =1.54059 Å), within the 2θ range varying from 6–70º in steps of 0.026 s^{-1}. The diffraction patterns were compared with JCPDS standards.

The microstructure and morphology of the thermally stabilised glasses were observed by scanning electron microscope (SEM, S–4100, Hitachi, Japan) using carbon coated samples.

For density measurements, pellets with 13 mm diameter and ~2 mm thicknesses were prepared in a stainless steel die by uniaxial pressing (60 MPa) from the sixteen milled powders. The pellets were heat–treated in air in an electric furnace at HTT investigated in this work. The heat treatment schedule included three stages: 1st stage from RT to 200 ºC at the heating rate of 1 ºC min^{-1}; 2nd stage from 200 ºC to 400 ºC at the heating rate 2 ºC min^{-1}; and the 3rd stage from 400 ºC to each maximum HTT investigated at the heating rate of 5 ºC min^{-1}. Natural cooling to RT followed the soaking time period of 2 h at 800 ºC. Density determination was performed using the buoyancy (Archimedes') method by immersing the samples in distilled water, in Accordance with European Standard EN 993–1. The bulk density of the glass pellets was calculated via following relation:

$$\rho_b = \frac{m_1}{m_3 - m_2} \cdot \rho_w \qquad (9.1)$$

Where: ρ_b is the bulk density in (g cm^{-3});

ρ_w is the density of the water, assumed to be 1 g cm^{-3};

m_1 is the mass of the dry sintered pellet measured in air;

m_2 is the mass of the sintered pellet suspended in water;

m_3 is the mass of the water saturated pellet measured in air.

3. Results and discussion

3.1. X–ray diffraction (XRD)

Fig. 9.1 shows the sixteen XRD patterns of glass powders heat treated at different temperatures and wet ball milled under different values of BPR (5, 10, 15, and 20). The samples heat treated at 550 ºC **Fig. 9.1(a)**, and at 675 ºC **Fig. 9.1(b)** are essentially amorphous, especially when the lower BPR was used (BPR = 5). With the gradual increasing of BPR, small reflections corresponding to yttrium zirconium oxide (PDF card # 04–016–2117) started appearing with increased intensity. The only possible source of yttrium zirconium oxide is the milling media. Therefore, these results indicate that the more frequent collisions among the balls with increasing BPR enhance the production of wear debris. The change of the HTT from 550 ºC to 675 ºC did not induce noticeable variations in the patterns. Incrementing the HTT to 800 ºC promoted the formation of some poorly

crystalline phases of hydroxylapatite; HAp (PDF card # 01–080–3956) and cristobalite (SiO_2) (PDF card # 04–008–7640) in the sample milled under BPR = 5, as deduced from the broad and relatively low intensity of the main XRD peaks of these two phases displayed in **Fig. 9.1(c)**. With the gradual increase of BPR, the intensities of the peaks corresponding to these two phases tended to steadily fade, while new peaks attributed to yttrium zirconium oxide (PDF card # 04–016–2117) appear with increasing intensities. Further increasing the HTT to 925 ºC resulted in glass ceramics with two new well–developed silicon oxide (SiO_2) phases (PDF card # 01–073–3446), Octadecasil (SiO_2) (PDF card # 00–048–0476), as disclosed in the XRD patterns displayed in **Fig. 9.1(d)**.

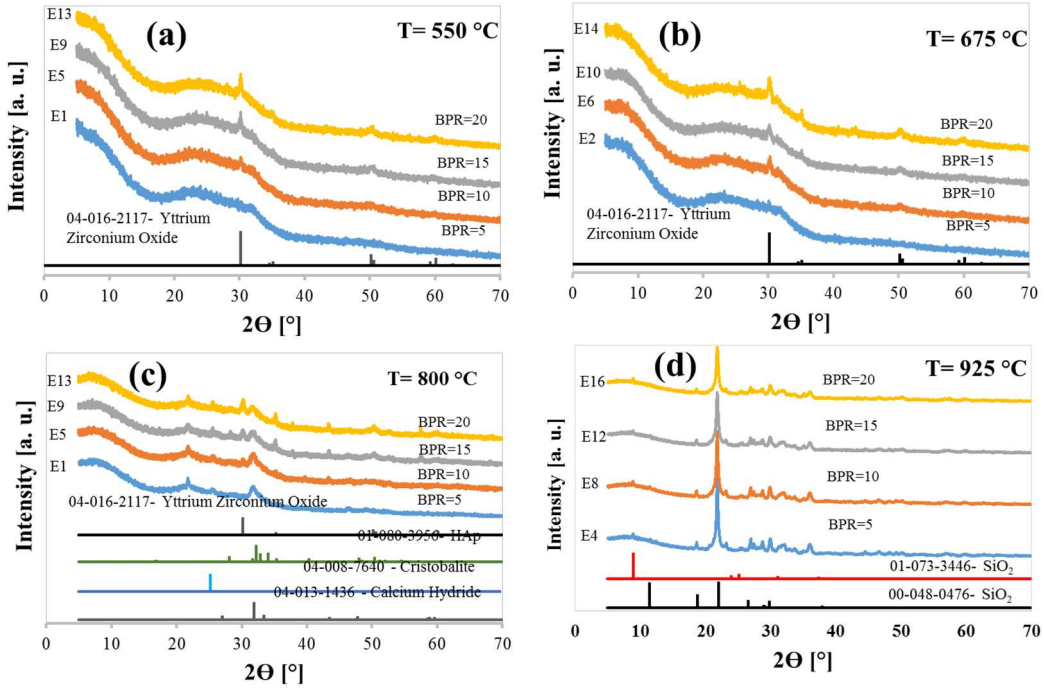

Fig. 9.1: XRD patterns of the bioactive sol–gel glass powders heat treated at different temperatures [a) 550 ºC, b) 675 ºC, c) 800 ºC, d) 925 ºC] followed by wet ball milling in ethanol under four values of BPR (5, 10, 15, 20)

The crystalline phases identified at 800 ºC apparently disappeared. It is likely that the intensities of the corresponding peaks are too low in comparison to the high intensity peaks of the new silica peaks formed at 925 ºC. Concerning the effects of varying the BPR, it is

worth mentioning the steadily reduction of the degree of crystallinity of the samples with increasing values of this experimental variable.

It can be concluded that the higher energetics of the milling process in the presence of higher amounts of balls tend to gradually destroy the crystalline phases formed with the resulting powders becoming progressively amorphous. The same trend was observed for the phases initially formed at 800 ºC.

3.2. Influence of BPR and HTT on the relevant features of powders

3.2.1. Particle size (PS) & particle size distribution (PSD)

Figs. 9.2(a–d) shows the influence of BPR on PS and PSD for the four HTT tested. Almost the same evolution trend can be observed irrespective of the HTT. The increase in BPR tends to decrease the average PS and to reduce the wideness (span) of the PSD, with curves gradually shifting towards the left (small particle sizes) and becoming sharper as BPR increases. In other words, increasing both BPR and HTT led to narrowing the PSD and increasing the volume % of fine particles. But comparing the effects of both these variables on the milling efficiency, it can be clearly concluded that BPR plays the major role and exerts a greater effect in both PS and PSD than HTT.

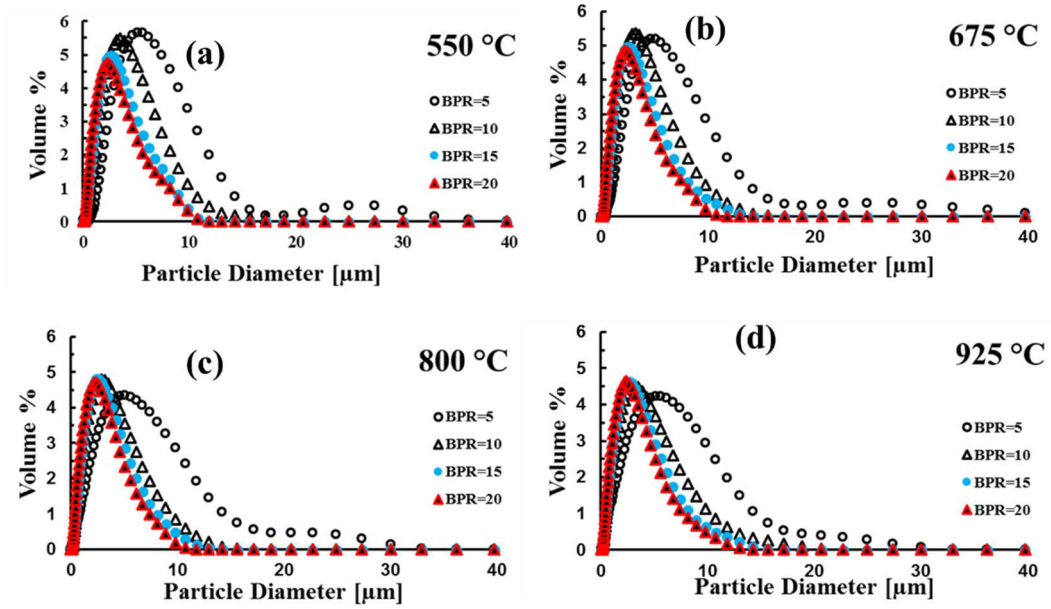

Fig. 9.2: Particle size distributions of the bioactive sol–gel glass powders heat treated at different temperatures [a) 550 ºC, b) 675 ºC, c) 800 ºC, d) 925 ºC] followed by wet ball milling in ethanol under four values of BPR (5, 10, 15, 20).

Figs. 9.3(a–d) also shows the influence of BPR and HTT on PS and PSD but with the series arranged according the HTT tested to facilitate the reading. It can be seen that the lower HTT result in broader PSD. The PSD curves become gradually narrower and almost superimposed with increasing HTT. In other words, the effects of HTT on the PS and PSD are minimised as BPR increases to 15 and 20. This representation of milling data complements the information provided in **Fig. 9.2**.

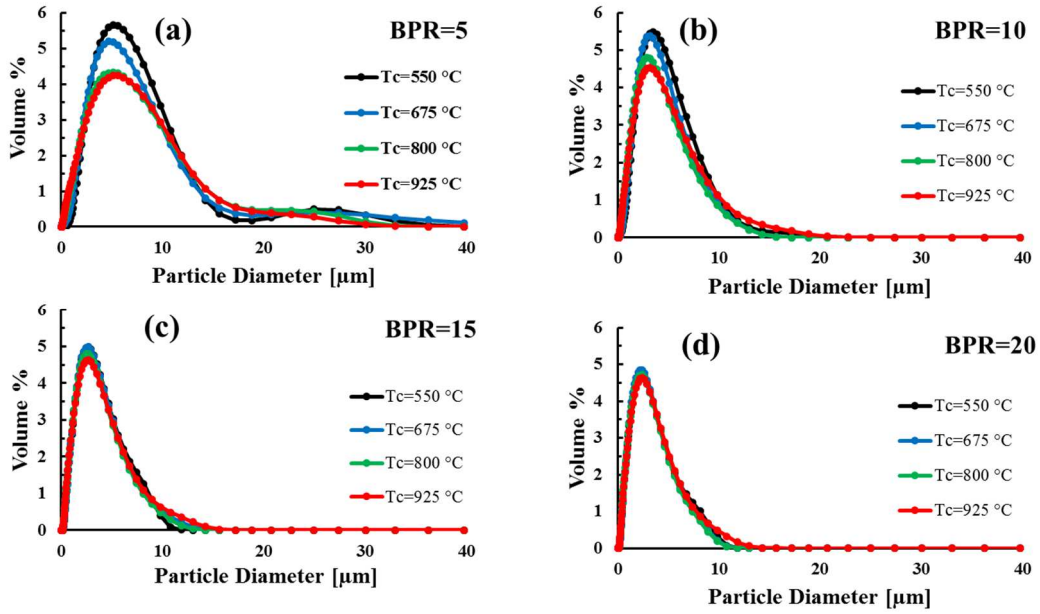

Fig. 9.3: Particle size distributions of the bioactive sol–gel glass powders heat treated at different temperatures followed by wet ball milling in ethanol under given values of BPR: a) 5; b) 10; c) 15; d) 20.

3.2.2. Mean particle size

Fig. 9.4 displays two complementary representations of the evolution of mean particle sizes for all powders as functions of the HTT **Fig. 9.4(a)** and BPR **Fig. 9.4(b)**. From these plots it can be depicted that increasing the HTT up to 800 ºC is accompanied by a small decrease in the mean particle size for all BPR values, suggesting an enhanced milling efficiency. This can be understood considering that the porous structure of the particles/agglomerates makes them less fragile. Therefore, the collisions with the balls are cushioned and milling is less effective. Further increasing the HTT from 800 ºC to 925 ºC reverses this tendency and the material becomes less prone to particle size reduction. This is consistent with the gradual

elimination of porosity and the formation of hard agglomerates that become more difficult to destroy upon milling.

On the other hand, increasing the BPR from 5 to 20 at constant temperature always resulted in a tremendous decrease of mean particle size as can be seen clearly from **Fig. 9.4(b)**. Significant reductions in mean particle size occurred at the lower HTT (550 ºC and 675 ºC) and for BPR values between 5, and 10. At higher values of HTT (800 ºC and 925 ºC) and of BPR (15 and 20), smaller reductions in the mean diameter can be observed. The overall results show that BPR plays the measure role in final particle size. These results are in a good harmony with the particle size distribution curves discussed above.

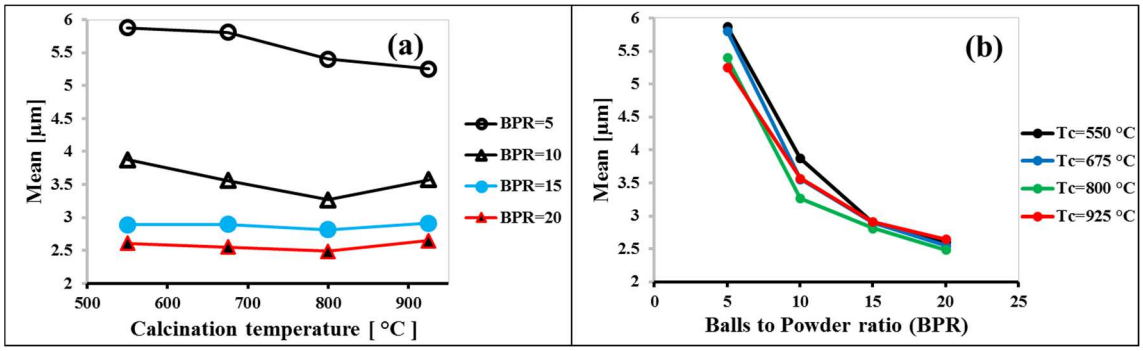

Fig. 9.4: Effects of the processing parameters on the mean particle size of the bioactive sol–gel glass powders: (a) heat treatment temperature (550, 675, 800, 925 ºC); (b) BPR (5, 10, 15, and 20) used in wet ball milling in ethanol.

3.2.3. Specific surface area (BET–SSA) and sorption isotherms

Fig. 9.5 displays two complementary representations of the evolution of the specific surface area of the powders versus HTT **Fig. 9.5**, and as a function of BPR at fixed values of HTT **Fig. 9.5(b)**. It can be seen that incrementing both experimental variables causes drastic reductions in the SSA, especially for the samples heat treated at the lower temperatures (550 ºC and 675 ºC). The noticeable reductions in SSA caused by increasing HTT can easily be understood as micropores in the structures obtained at lower temperatures tend to gradually disappear due to the sintering process **[32]**. All the curves displayed in **Fig. 9.5(a)** tend to converge for temperatures ≥800 ºC. In this elevated temperature range the SSA is practically unaffected by the milling conditions, while at lower HTT (550 ºC and 675 ºC) the BPR also plays a role in determining the SSA, which almost linearly decreases with increasing BPR,

and at decreasing kinetics with increasing HTT. At the first glance these results seem inconsistent as higher values of SSA would be expected when considering the PS decreasing trends inferred from the results displayed in **Figs. 9.2–9.4**. However, sol–gel derived powders usually exhibit complex porous structures, including open pores communicating with the external surface at two ends (through pores), dead–end pores with narrow pore necks (bottleneck pores), and closed pores **[33]**.

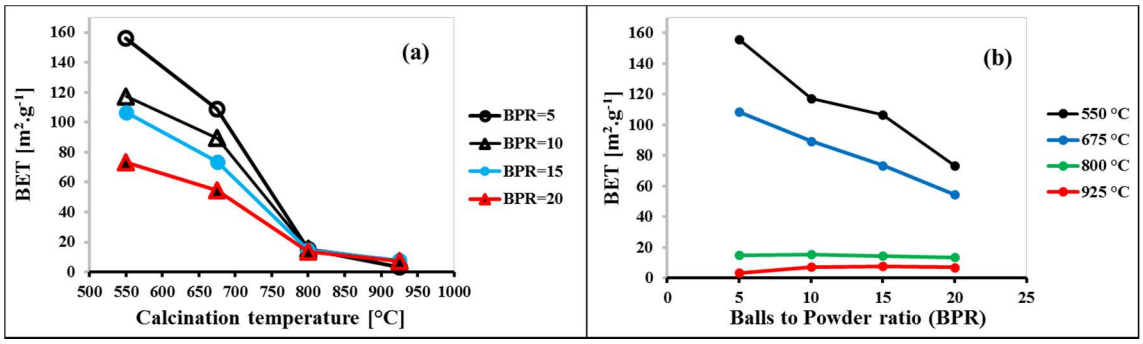

Fig. 9.5: Effects of the processing parameters on the specific surface area of the bioactive sol–gel glass powders: (a) heat treatment temperature (550, 675, 800, 925 ºC); (b) BPR (5, 10, 15, and 20) used in wet ball milling in ethanol.

Closed pores are not associated with adsorption and permeability of molecules, while nitrogen condensation is likely to occur in open pores and be accompanied by hysteresis, depending on the pore size and shape. The nitrogen sorption isotherms of the bioactive sol gel glass powders submitted to different HTT and BPR upon wet milling are displayed in **Fig. 9.6**. All of them are Type IV (a) isotherms, according to the IUPAC classification **[34]**, and capillary condensation is accompanied by hysteresis. For nitrogen adsorption at 77 K, hysteresis starts to occur for pores wider than ~4 nm and when bottleneck type pores are present **[33,34]**.

Fig. 9.6(a) and **Fig. 9.6(b)** compare the nitrogen sorption isotherms of the bioactive sol gel glass samples calcined at all HTT and wet ball milled under the two lower BPR values, while **Fig. 9.6(c)** and **Fig. 9.6(d)** provide similar comparisons for the samples heat treated at 550 ºC and 800 ºC, and milled under all BPR values tested. The highest quantity of adsorbed nitrogen (pore volume) is observed for the sample heat treated at 550 ºC and ball milled under the lower BPR. The amount of adsorbed nitrogen strongly decreases under more

severe milling conditions **Figs. 9.6(b–d)**. This means that a larger volume fraction of pores has collapsed and that the new exposed surfaces, available for nitrogen sorption, do not compensate for the loss in gas sorption storage of the resulting porous structure. This explains the apparent inconsistencies referred above when considering the expected relationship between PS **Figs. 9.2–9.4** and SSA **Fig. 9.5**. The results also show the strong dependence of nitrogen adsorption on the HTT. Drastic decreases are observed with increasing HTT **Figs. 9.6(a–b)**, and pores have been almost eliminated in samples submitted to HTT ≥ 800 ºC **Figs. 9.6(d)** due to the sintering process **[32]**.

The desorption and desorption branches of nitrogen sorption isotherms are not so steep as in the Type models described in literature **[32]**, revealing more complex pore structures with important network effects and larger size distribution of pore diameters and neck widths.

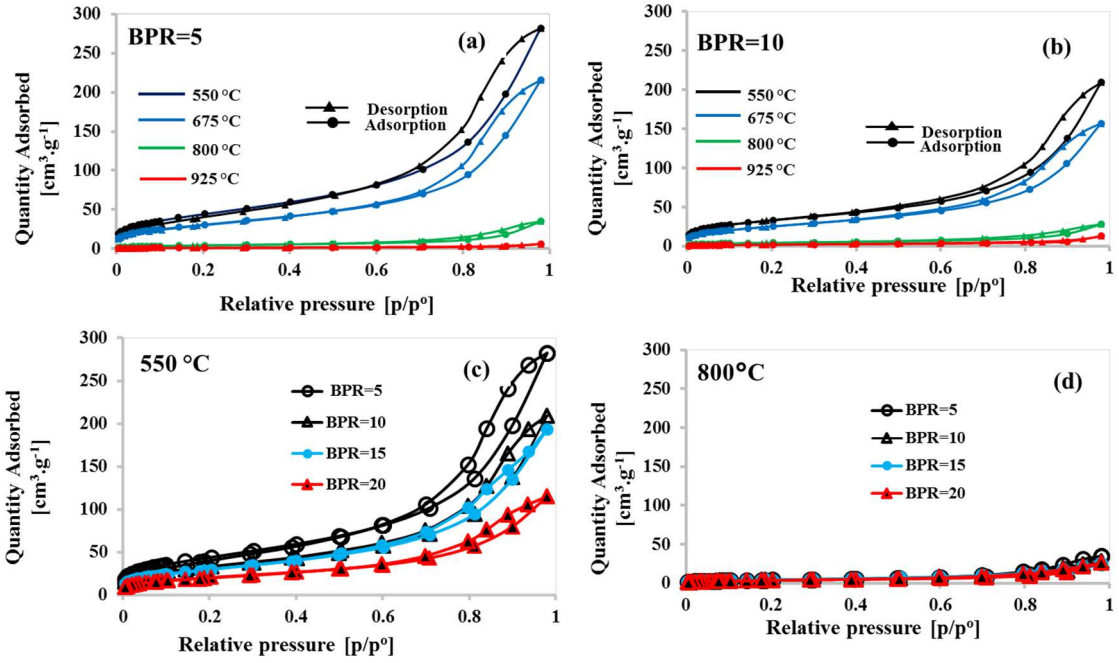

Fig. 9.6: Effects of the processing parameters on the nitrogen sorption isotherms for the bioactive sol–gel glass powders: (a, b) comparison of two BPR (5, 10) used in wet ball milling in ethanol for samples heat treated at different temperatures (550, 675, 800, 925 ºC); (c, d) comparison of two heat treatment temperatures for powders wet ball milling in ethanol under different BPR values (5, 10, 15, 20).

3.2.4. Pore size and density measurements

Pore sizes data extracted from adsorption isotherms are illustrated in **Fig. 9.7**.

Fig. 9.7(a) shows a general increase in mean pore size with increasing HTT up to 800 ºC, followed by a decreasing trend beyond this temperature. These changes are attributed to the sintering effect in which the smaller pores are the first to be readily eliminated, justifying why the mean diameter of the coarser ones increases. It seems that micro porosity is practically eliminated up to 800 ºC. Beyond this temperature, only the larger pores remain open, explaining why the mean pore size increases at 925 ºC. It can also be seen in **Fig. 9.7(a)**, and in **Fig. 9.7(b)** that pore size decreases with increasing BPR. This is consistent with the gradual collapse of the porous structure under more severe milling conditions as referred above. Similar type of pore size information could be extracted from data gathered along the desorption branch of isotherms as shown in **Fig. 9.7(c)**, and in **Fig. 9.7(d)**.

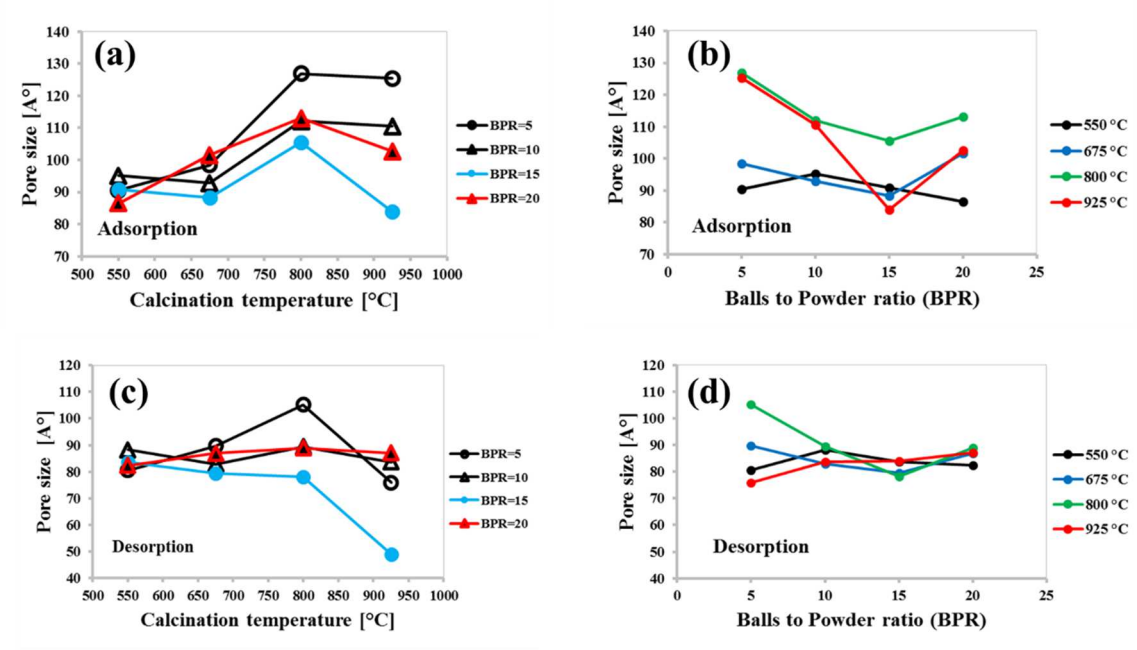

Fig. 9.7: Influence of the heat treatment temperature and of the BPR used in wet ball milling in ethanol on pore size derived from sorption isotherms: (a, b) adsorption branch; (c, d) desorption branch.

The effects of HTT and BPR on density of sintered pellets can be depicted from **Fig. 9.8**. A general increase in density with increasing HTT is observed up to 800 ºC, followed by a reducing trend with further increasing the temperature to 925 ºC. The changes in density as

a function of HTT are less noticeable the sample derived from the powder wet ball milled at the lowest BPR (5). Increasing the BPR to 10 resulted in a general enhancement of density, probably due to a more efficient destruction of particle agglomerates, in good agreement with particle size data plotted in **Figs. 9.2–9.4**. Further increasing the BPR to 15 and 20 resulted in lower values of density in comparison to those observed for BPR = 10. This decreasing trend of density maybe due to two different causes: (i) excessive production of fine particles **Fig. 9.4** with particle packing ability in green state getting worse; (ii) possible deleterious effects on sintering coming from the wear debris of milling media as detected by XRD **Fig. 9.1**.

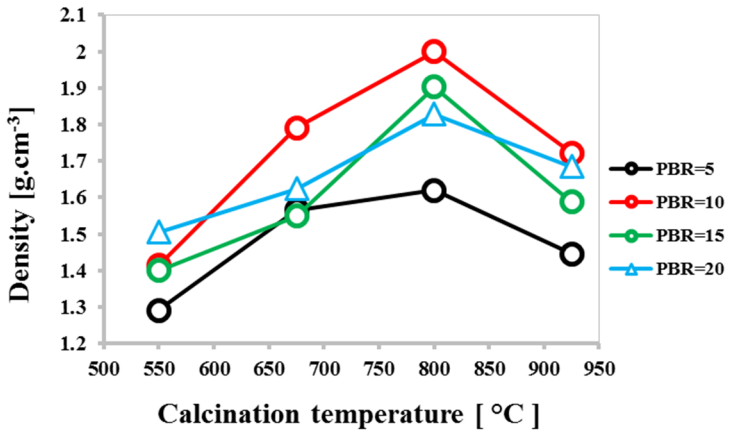

Fig. 9.8: Effects of the processing parameters on the density of cylindrical pellets sintered at 800 ºC.

3.2.5. Morphological features of the glass powders

The morphological features of the glass powders heat treated at two selected temperatures (550 ºC, 800 ºC) and wet ball milled under the extreme values of BPR (5, 20) are presented in the micrographs of **Figs. 9(a–h)**. The powders consist of clusters of primary particles that get together along the condensation step of the sol–gel process forming porous microstructures, which are susceptible of being affected by the changes in the experimental variables investigated. The observed micrographs are consistent with a size reducing of clusters from ~0.3 µm **Fig. 9**(**a**) to ~0.15 µm **Fig. 9**(**b**) as BPR increases from 5 to 20. When observed at higher magnification the clusters at 550 ºC exhibit cauliflower–like shapes built

from primary particles having sizes within the range of ~10–20 nm as depicted from **Figs. 9.9(c–d)**. Obviously, the size of the clusters is reduced from ~ 120 nm **Fig. 9.9**(**c**) to ~ 60 nm in **Fig. 9.9**(**d**).

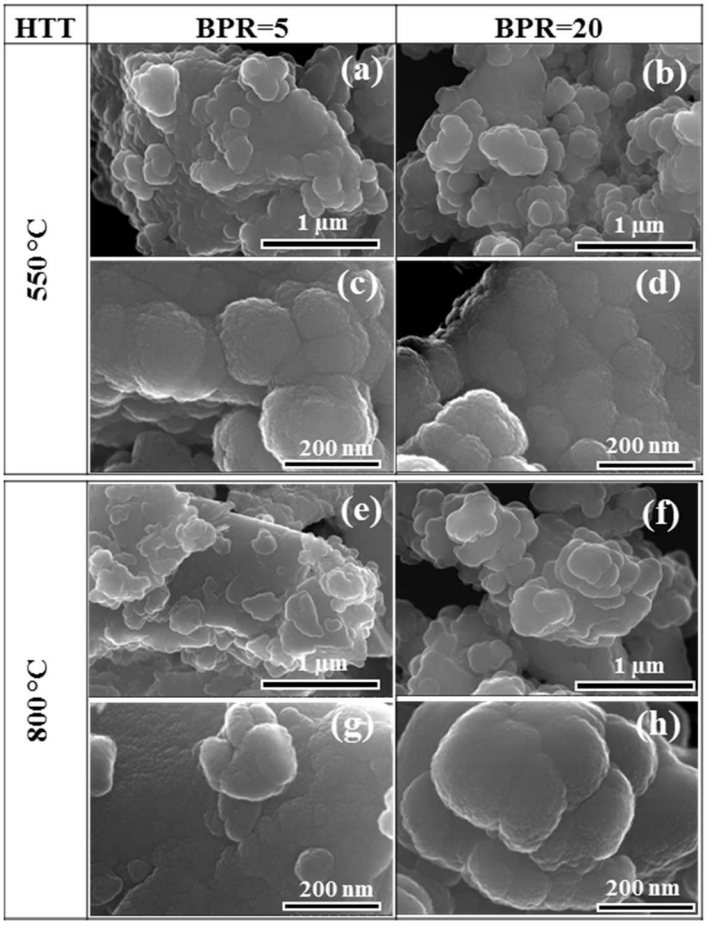

Fig. 9.9: Effects of HTT (550 ºC, 800 ºC) and of BPR (5, 20) on the morphological features of the bioactive sol–gel glass powders observed under two different magnifications: 50x (a, b, e, f) and 200x (c, d, g, h).

With the HTT increasing to 800 ºC, the cluster size decreased from ~0.4 µm **Fig. 9.9**(**e**) to ~0.2 µm **Fig. 9.9**(**f**), while keeping almost the same external morphological features. Although increments in both experimental variables contribute to cluster size reduction, BPR exerts a greater effect.

4. Conclusions

A quaternary (Si–Na–Ca–P) bioactive sol–gel glass was heat treated at different temperatures and fast wet milled under constant conditions of mass ethanol to powder ratio (EPR = 2) and milling time (2 h), and various values of BPR. The characterisation analyses of the resulting sixteen powder samples enable to draw the following conclusions:

1. Crystalline phase assemblages: The sol–gel glass remained essentially amorphous upon heat treating at the lower HTT (550 ºC and 675 ºC). Poorly crystalline phases (HAp, and cristobalite) formed at 800 ºC and could be easily identified in the sample milled under BPR = 5. The intensities of XRD peaks of these two phases tended to steadily fade with increasing BPR, while yttrium zirconium oxide phase gradually appeared, resulting from wear debris of milling media. The increase of HTT to 925 ºC led to the formation of two well crystallized silicon oxide phases and to the apparent disappearance of the poorly crystalline phases formed at 800 ºC, which were masked by the much higher XRD intensity peaks of the new phases.
2. Particle size & size distributions: the BPR played the major role in determining these features, especially at the lower HTT. Particle size decreased and particle size distributions showed a clear narrowing trend with increasing BPR, irrespective of HTT.
3. BET specific surface area, sorption isotherms and pore sizes: The SSA tended to consistently decrease with increasing the HTT. Unexpectedly from the decreasing trend observed for PS, SSA clearly decreased with increasing the BPR, especially for samples heat treated at lower HTT (550 ºC and 675 ºC). This evolution is due to the gradual collapse of the porous structure that decreases its nitrogen storage capacity. For samples heat treated at 800 ºC and 925 ºC, the effect of BPR on SSA was negligible. The gradual elimination of the finer pores due to advancements in the sintering process resulted in less porous structures but consisting of larger mean pore sizes.
4. Sintered density increased with increasing HTT up to 800 ºC, followed by decreasing trends when sintering temperature was further increased to 925 ºC. Density was also enhanced upon increasing BPR from 5 to 10, reaching the highest values. Further increasing the BPR to 15 and 20 enriched the powders in fine particles and wear debris from milling media that accounted for worsening the sintering ability.

Acknowledgments

R.C. Pullar wishes to thank the FCT Grant IF/00681/2015 for supporting this work. B. A. E. Ben–Arfa thanks FCT grant BIONANOSCULP PTDC/EPH–PAT/6281/2014 for supporting him during this work. This work was developed in the scope of the project CICECO–Aveiro Institute of Materials (Ref. FCT UID /CTM /50011/2013), financed by national funds through the FCT/MEC and when applicable co–financed by FEDER under the PT2020 Partnership Agreement.

References

[1] S. Ghosh, M. Das, S. Chakrabarti, S. Ghatak, Development of ceramic tiles from common clay and blast furnace slag, Ceram. Int. 28 (2002) 393–400.

[2] R. Oberacker, Powder Compaction by Dry Pressing, in: Ceram. Sci. Technol., 1st ed., Wiley–VCH Verlag GmbH & Co. KGaA, Verlag, 2013: pp. 1–37.

[3] R. DW., Structure and properties, in: Mod. Ceram. Eng. Prop. Process. Use Des., 2nd ed., Marcel Dekker, inc., New Jersey, 1992.

[4] S.S.Y. Lam, K.L. Petri, A.E. Smith, Prediction and optimization of a ceramic casting process using a hierarchical hybrid system of neural networks and fuzzy logic, IIE Trans. 32 (2000) 83–91.

[5] J.M.F. Ferreira, H.M.M. Diz, Effect of ageing time on pressure slip casting of silicon carbide bodies, J. Eur. Ceram. Soc. 17 (1997) 259–266.

[6] S. Mei, J. Yang, J.M.F. Ferreira, The fabrication and characterisation of low–k cordierite–based glass–ceramics by aqueous tape casting, J. Eur. Ceram. Soc. 24 (2004) 295–300.

[7] J.M.F. Ferreira, Role of the clogging effect in the slip casting process, J. Eur. Ceram. Soc. 18 (1998) 1161–1169.

[8] J.M.F. Lyckfeldt, O.; Ferreira, Processing of Porou s Ceramics by 'Starch Consolidation', J. Eur. Ceram. Soc. 18 (1998) 131–140.

[9] O.O. Omatete, M. a. Janney, S.D. Nunn, Gel casting: From laboratory development toward industrial production, J. Eur. Ceram. Soc. 17 (1997) 407–413.

[10] L.J. Gauckler, T. Graule, F. Baader, Ceramic forming using enzyme catalyzed reactions, Mater. Chem. Phys. 61 (1999) 78–102.

[11] T. Kosmac, S. Novak, M. Sajko, Hydrolysis–assisted solidification (HAS): A new setting concept for ceramic net–shaping, J. Eur. Ceram. Soc. 17 (1997) 427–432.

[12] X. Xu, J.M.F. Ferreira, Temperature–induced gelation of concentrated sialon suspensions, J. Am. Ceram. Soc. 88 (2005) 593–598.

[13] S.M. Olhero, A. Kaushal, P. Antunes, J.M.F. Ferreira, Microfabrication of high

aspect ratio BST pillar arrays by epoxy gel casting from aqueous suspensions with added water soluble epoxy resin, Mater. Res. Bull. 60 (2015) 830–837.

[14] J.M. Torralba, M. Campos, Toward high performance in Powder Metallurgy, 50 (2014).

[15] H.N. Chia, B.M. Wu, Recent advances in 3D printing of biomaterials, J. Biol. Eng. 9 (2015) 1–14.

[16] E. Feilden, E.G.T. Blanca, F. Giuliani, E. Saiz, L. Vandeperre, Robocasting of structural ceramic parts with hydrogel inks, J. Eur. Ceram. Soc. 36 (2016) 2525–2533.

[17] J.E. Field, M. Farhat, S.M. Walley, Comminution limit (CL) of particles and possible implications for pumped storage reservoirs, J. Mater. Sci. 49 (2014) 3780–3784.

[18] Z.H. Loh, A.K. Samanta, P.W. Sia Heng, Overview of milling techniques for improving the solubility of poorly water–soluble drugs, Asian J. Pharm. Sci. 10 (2014) 255–274.

[19] M.F. Ferreira, M.I.L.L. Oliveira, K. Chen, Influence of the deagglomeration procedure on aqueous dispersion , slip casting and sintering of Si 3 N 4 –based ceramics, J. Eur. Ceram. Soc. 22 (2002) 1601–1607.

[20] M.D. Bentzon, L.O. Andersen, J. Goul, P. Bodin, P. Vase, Influence of the Powder Calcination Temperature on the Microstructure in Bi (Pb) –2223 Tapes, IEEE Trans. Appl. Supercond. 7 (1997) 1411–1414.

[21] B. Ma, T. Lu, N. Wei, Z. Lu, F. Li, X. Chen, et al., Effect of powder calcination temperature and ceramic post–treatment on the optical properties of Nd:YAG ceramics, Int. J. Appl. Ceram. Technol. 12 (2015) 1230–1238.

[22] Y. Chen, D.D. Dionysiou, Effect of calcination temperature on the photocatalytic activity and adhesion of TiO2films prepared by the P–25 powder–modified sol–gel method, J. Mol. Catal. A Chem. 244 (2006) 73–82.

[23] J. Cai, W. Xin, G. Liu, D. Lin, D. Zhu, Effect of calcination temperature on structural properties and photocatalytic activity of Mn–C–codoped TiO2, Mater.

Res. 19 (2016) 401–407.

[24] A.J. Melville, L.M. Rodríguez–Lorenzo, J.S. Forsythe, Effects of calcination temperature on the drug delivery behaviour of Ibuprofen from hydroxyapatite powders, J. Mater. Sci. Mater. Med. 19 (2008) 1187–1195.

[25] S. Sun, Q. Xu, Effect of Calcination Temperature on Phase Transformation and Microstructure of Al2O3/GdAl3Compound Powder Prepared by Co–Precipitation Method, Key Eng. Mater. 512–515 (2012) 535–538.

[26] H. Juang, Effect of calcination on sintering of hydroxyapatite, Biomaterials. 17 (1996) 2059–2064.

[27] M. Zakeri, M. Ramezani, A. Nazari, Effect of ball to powder weight ratio on the mechanochemical synthesis of MoSi2–TiC nanocomposite powder, Mater. Res. 15 (2012) 891–897.

[28] S.M. Salili, A. Ataie, Z. Sadighi, Effect of ball size and ball to powder ratio variation on crystallite size and formation of nanocrystalline materials in planetary ball mill, AIP Conf. Proc. 1400 (2011) 127–130.

[29] Y.J. Lv, J. Su, Y.F. Long, X.R. Cui, X.Y. Lv, Y.X. Wen, Effects of ball–to–powder weight ratio on the performance of LiFePO4/C prepared by wet–milling assisted carbothermal reduction, Powder Technol. 253 (2014) 467–473.

[30] B.A.E. Ben–Arfa, I.M. Miranda Salvado, J.M.F. Ferreira, R.C. Pullar, A hundred times faster: Novel, rapid sol–gel synthesis of bio–glass nanopowders (Si–Na–Ca–P system, Ca:P = 1.67) without aging, Int. J. Appl. Glas. Sci. 8 (2017) 337–343.

[31] B.A.E. Ben–Arfa, H.R. Fernandes, I.M.M. Salvado, J.M.F. Ferreira, R.C. Pullar, Effects of catalysts on polymerization and microstructure of sol–gel derived bioglasses, J. Am. Ceram. Soc. 101 (2018) 2831–2839.

[32] M. Nogami, Y. Moriya, Glass formation through hydrolysis of Si(OC2H5)4 with NH4OH and HCl Solution, J. Non. Cryst. Solids. 37 (1980) 191–201.

[33] B.D. Zdravkov, J.J. Čermák, M. Šefara, J. Janků, Pore classification in the characterization of porous materials: A perspective, Cent. Eur. J. Chem. 5 (2007) 385–395.

[34] M. Thommes, K. Kaneko, A. Neimark, J. Olivier, F. Rodriguez–Reinoso, Physisorption of gases, with special reference to the evaluation of surface area and pore size distribution (IUPAC Technical Report), 2015.

Chapter 10

The present chapter was published on:
Journal of the American Ceramic Society;
Volume -, Issue -,
19 September 2018,
Pages -.
Doi: 10.1111/jace.16092

Robocasting: prediction of ink printability in sol–gel bioactive glass

Basam A. E. Ben–Arfa, Ana S. Neto, Isabel M. Miranda Salvado*, Robert C. Pullar* and José M. F. Ferreira,

Department of Materials and Ceramic Engineering / CICECO – Aveiro Institute of Materials, University of Aveiro, 3810–193 Aveiro, Portugal

*To whom correspondence should be addressed: isabelmsalvado@ua.pt, rpullar@ua.pt

Keywords: Calcination temperature; Balls to powder ratio; Solid loading; Suspension rheology; Robocasting, Scaffolds.

Abstract

Bioactive glass powders synthesised by sol–gel are usually porous and exhibit high specific surface areas, conferring them poor ability for scaffolds fabrication using colloidal processing approaches. The difficulties assocciated with colloidal processing of sol–gel glass have hindered so far the processing of 3–D scaffolds by robocasting. This research paper investigates the importance of calcination temperature (CT) and balls to powder ratio (BPR) used upon wet milling on the maximum achivable solid loading in aqueous media. The effects of CT, BPR, and solid loading on the flow behaviour and viscoelastic properties of the suspensions/pastes were evaluated in this preliminary work. The aim is to disclose the sets of experimental variables that are most promising for the formulation of printable inks, and open the way for the future fabrication of porous scaffolds by robocasting and other 3D additive manufacturing techniques.

1. Introduction

Robocasting started to be used about two decades ago as a revolutionary tool to produce complex shaped ceramic and composite components **[1]**. The technique is based on the extrusion of a paste (ink) throughout a nozzle, and its deposition in a layer–by–layer fashion to build the final desired shape according to a CAD (computer aided design) model. The ink is made by mixing a powder with water and small percentages of processing additives, including dispersants, binders, thickening agents and coagulants, in order to obtain the desired rheological properties. A suitable ink for robocasting should steadily flow under the applied shear stress without clogging the nozzle. It should become thinner under shear (i.e., have a shear thinning flow behaviour) to facilitate extrusion, and then exhibit a fast recovering of the internal structure for shape retention, while offering mechanical support to the subsequent layers **[2]**. This is to say that setting the suitable viscoelastic behaviour of pastes for Robocasting is a challenging process, as it depends on many experimental factors.

The most relevant factors determining the rheological behaviour of the starting suspensions include: solid loading size (PS) and particle size distributions (PSD) **[3–5]**, particle shape and density **[6]**, and the interfacial solid/liquid interactions **[7,8]**. Maximising the solid loading is an important issue for minimising the dimensional variations of the constructs during the drying and sintering steps **[7,9]**. However, an obvious consequence of incrementing the dispersed solids volume fraction of a given powder is the increase in viscosity of the resulting suspension **[7–14]**. Therefore, the optimal solids volume fraction has to be a balance achieved between these two desirable, but incompatible, features: a maximum solid loading, and a relatively low viscosity that determines the easiness of preparation, handling and casting of the suspensions **[8,9]**.

Repulsive interparticle forces are required for overcoming the attractive Van der Walls forces and preparing dense and homogeneous suspensions with good flow properties for colloidal processing **[7–11,15–18]**. Repulsive forces can be of electrostatic origin, or be created by steric hindrance of polymeric species specifically adsorbed at the surface of the particles, or be achieved by a mixed electrosteric stabilisation mechanism when polyelectrolytes are used as dispersants **[3,15,16]**. The solid/liquid interactions can be manipulated by selecting suitable processing additives for the specific system **[7,10]**.

Particle size determines the balance between buoyancy and sedimentation trends for individual particles, as well as the apparent increase in solids volume fraction due to the

hydrated surface layer thickness (δ) formed around each dispersed particle, according to Eq. (10.1):

$$\emptyset_{eff} = \emptyset\left(1 + \frac{\delta}{a}\right)^3 \qquad (10.1)$$

Where ϕ and ϕ_{eff} are the true and the effective solids volume fractions, and a is the real particle radius. Considering that δ depends essentially on the pair dispersion conditions/material, and therefore can be considered independent on the particles diameter. An obvious consequence of Eq. (10.1) is a drastic decreasing trend of the maximum achievable solids loading when processing finer and finer nanoparticles **[17]**.

The particle packing density can be greatly improved by mixing proper volume fractions of different particle sizes having adequate mean size ratios to fit the Furnas model **[18]**. Filling the interstitial spaces left between the coarser and finer particles has a further advantage of releasing dispersion media from those interstices, which becomes available for flow, lowering the viscosity and enabling further increments in solids loading. Although significant gains can be obtained when dealing with mortars **[18]**, coarse particles in ceramic green bodies tend to form a kind of skeletal framework that hinders densification upon sintering, annulling the advantages of using higher solid loadings and the ability to achieve high green densities **[8]**.

Hard agglomerates tend to confer poor flow properties (shear thickening behaviour) to the suspensions, implying the use of low shear rate deagglomeration processes **[19]**. The efficient destruction of hard agglomerates is of outstanding importance for improving the flow behaviour of the suspensions, the homogeneity and the sintering ability of the green bodies. The homogeneity of green bodies (small particles and pore sizes that shorten the diffusion paths), enabling full densification and sub–micrometre grain sizes and transparent ceramics to be achieved at relatively low sintering temperatures, is the best proof of this concept **[20–22]**.

It is likely that any new colloidal system requires a specific systematic approach for disclosing the experimental variables that have stronger impacts on the rheology, and the malleability of the suspensions/pastes prepared thereof. The intrinsic porosity of a sol–gel derived bioactive glass powder is a new critical feature, the effects of which need to be addressed. Direct ink writting of melt–quenching glasses was already studied and is reasonably well documented **[23–27]**. To the best of the authors' knowledge, the processing of sol–gel glasses by robocasting was not yet investigated so far. A literature survey revealed

that almost no work has been done to demonstrate the combined effects of porosity and particle/agglomerate size on the rheological properties of the suspensions prepared from sol–gel derived bioactive glass powders. This is particularly true in the case of fabrication of porous scaffolds by robocasting from sol–gel derived bioactive glass pastes. Therefore, the purpose of this study is to disclose how the changes in calcination temperature (CT), the balls to powder ratio (BPR), and in solids loading affect the flow properties of the suspensions/pastes, and the subsequent ease of additive manufacturing.

A quaternary glass composition synthesised by a unique rapid sol–gel process already developed by the authors **[28,29]** was used as starting raw material for the formulation of suitable inks for robocasting. The selected composition revealed to be biocompatabile and highly bioactive, leading to the formation of a HAp layer onto the surface of the particles upon in–vitro tests in SBF for periods up to one month **[30]**.

2. Materials and methods

2.1. Wet milling procedures

A four–component (SiO_2–CaO–Na_2O–P_2O_5) bioactive glass with a stoichiometric composition of 75Si–16Ca–5Na–4P (at.%) **[28]** was synthesised by employing a sol–gel route, as described previously by the authors **[31]**. The as–dried glass was calcined in air at various temperatures (600, 800 and 1000 ºC), and used as the raw material for wet ball milling experiments under different balls to powder ratio (BPR) values (5, 10 and 15) in a total of nine experimental trials. The trials, the corresponding experimental conditions used (CT and BPR) and some results obtained are summarised in **Table 10.1** (See Results and Discussion). The calcination was performed in three stages: 1st stage, from room temperature (RT) to 200 ºC, at the heating rate of 1 ºC min^{-1}; 2nd stage, from 200 ºC to 400 ºC, at the heating rate 2 ºC min^{-1}; and the 3rd stage, from 400 ºC to the final calcination temperature (CT) value (600 ºC, 800 ºC, 1000 ºC), at the heating rate of 5 ºC min^{-1}, followed by 2 h soaking time for all glasses to produce glass granules.

The glass granules were firstly dry milled for 10 minutes, passed through a 200 µm mesh sieve, and then used as starting powders for the designed experiments. Nine wet milling operations were performed under a constant ethanol (EtOH) to powder mass ratio (EPR = 1.5), and fixed milling time of 1 h.

Table 10.1: Dependence of PSD parameters (mean size, D10, D50, D90) and features (skewness, size span) on the history of the powders (TC, BPR).

Trial	CT	BPR	Diameters (µm)				skewness	Span
	(ºC)		mean	D_{10}	D_{50}	D_{90}		
E1	600	5	7.61	2.39	6.26	14.06	2.05	1.86
E2	800	5	7.83	1.40	6.00	16.64	1.61	2.54
E3	1000	5	7.58	1.04	6.04	16.26	1.34	2.52
E4	600	10	5.74	1.57	4.34	11.10	2.33	2.19
E5	800	10	4.89	1.05	3.57	10.14	2.26	2.54
E6	1000	10	4.51	0.84	3.44	9.70	1.52	2.58
E7	600	15	4.76	1.21	3.56	9.84	1.91	2.42
E8	800	15	3.93	0.87	2.94	8.15	2.03	2.47
E9	1000	15	3.74	0.77	2.86	7.95	1.65	2.51

The milling was done in a S–series–Fast Mill machine, type S2–1000 (Ceramic instruments Sassuolo, Italy) under a rotational speed of 390 rpm, using a sintered alumina jar of 300 cm^3 capacity (Ceramic instruments Sassuolo, Italy) and spherical yttria–stabilized zirconia milling balls with 10 mm diameter (Tosoh, Tokyo, Japan). After milling, the slurry was separated from the balls and kept overnight in the oven at 60 ºC for drying. The obtained dry powders were passed through a 63 µm mesh sieve to take out the large agglomerates, and their features were assessed by the characterisation techniques described below.

2.2. Characterisation of the milled powders

The average particle sizes (PS) and the particle size distributions (PSD) of the milled powders, in a volume basis, were determined using a laser diffraction particle size analyser (Coulter LS particle size analyser; Beckman Coulter, CA). Measurements were done in triplicated runs.

The specific surface areas (SSA) and the sorption isotherms of the powders were measureded using the Brunauer–Emmett–Teller (BET method, Micrometric Gemini M–2380) using N_2 as adsorbate. Samples were degassed at 200 °C before the measurment.

Zeta–potential measurements were performed in both the acidic and the alkaline regions at several pH values to evaluate particles' surface charges for all the nine trials, using a Malvern

Zeta sizer Nano ZS (Malvern Instruments, Worcestershire, UK). The measurement was carried out after dispersing the powders in a background 10^{-3} M KCl electrolyte solution under sonication for ~10 min, and gradually shifting the pH into both acidic and basic conditions by using HCl and NaOH, respectively.

2.3. Suspension preparation

For studying the rheological and printability behaviours of the inks, several suspensions containing different solid loadings between (25–45 vol.%) were prepared from the powder samples reported in **Table 10.1**. The powders were dispersed in de–ionised water in the presence of 1.1 wt.% carboxymethyl cellulose (CMC) (M_w = 250,000, Lamberti Iberia s.a.u., Castellón, Spain) as a multifunctional processing additive (dispersant, binder and gelation agent) **[32]**. The powders were gradually added in small dosages to the dispersing solution by mixing in a planetary centrifugal mixer (ARE–250, Thinky Corp., Tokyo, Japan) to ensure homogeneous suspensions were obtained.

2.4. Rheological characterisation of suspensions and pastes

The rheological properties of the suspensions and pastes were assessed using a Kinexus Pro$^+$ Rheometer (Malvern Instruments, USA). The viscometry mode was used to measure the apparent viscosity of the tested samples, using the cone (4º/40 mm) and plate sensor system with a 150 µm gap size. The viscoelastic properties of the pastes were assessed using the oscillatory mode of the rheometer equipped with plate & plate sensor (20 mm), with 1 mm gap size. In all rheological measurements, a metal ring with di–ionised water as solvent trap was used to prevent water evaporation from the samples while testing.

3. Results and Discussion

3.1. Influence of BPR and CT on the relevant features of powders

3.1.1. Particle size (PS), size span (SS) & particle size distribution (PSD)

The effects of the thermal history (CT) and wet ball milling conditions (BPR) on the experimental data related with PSD (mean size, D_{10}, D_{50}, D_{90}, skewness, size span) are

disclosed in **Table 10.1**. The following general tendencies can clearly be observed from **Table 10.1**: the skewness decreases with increasing CT, while the size span shows the opposite trend, in agreement with data plotted in **Fig. 10.1**.

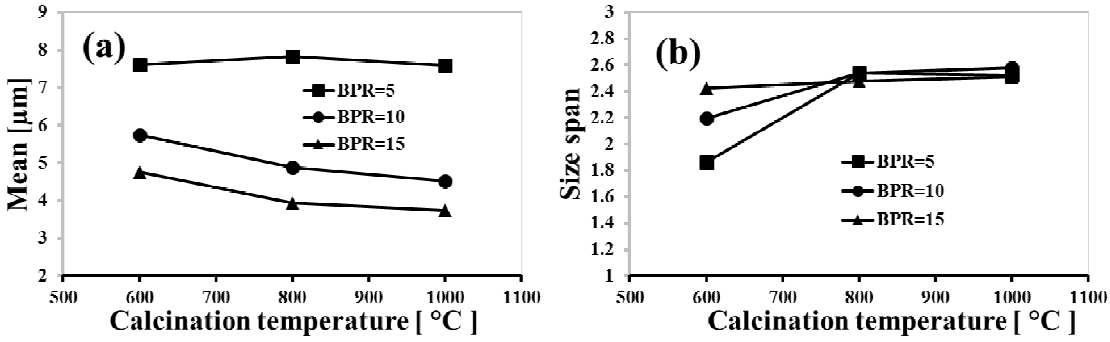

Fig. 10.1: Effects of CT and BPR on the PSD features after wet milling for 1 h under a constant (EtOH) to powder mass ratio (EPR = 1.5): (a) mean particles size; (b) particle size span.

Fig. 10.1(a) shows the dependence of the mean size profiles as a function of CT for three values of BPR. At BPR=5, the mean particle size slightly increases with increasing CT from 600 to 800 ºC, to be followed by an opposite trend with a further rise in CT to 1000 ºC. Similar, but continuous, reduction trends of the mean particle sizes can be observed at both BPR=10 and BPR=15 with increasing CT. However, the most accentuated mean particle size reduction is obtained at BPR=15. **Fig. 10.1(b)** shows the width of PSD, which can be represented by the size span (SS) according to the following formula **[33]**:

$$SS = \frac{(D_{90} - D_{10})}{D_{50}} \qquad (10.2)$$

In Eq. (10.2), the parameters D_{90}, D_{50}, and D_{10} stand for equivalent particle diameters below which there are percentages of 90%, 50% and 10% of the overall distribution. From these results it can be concluded that BPR has a significant effect on SS for the powders calcined at 600 ºC and milled at BPR=5. The differences in SS are mitigated when increasing BPR to 10–15, and become negligible for powders calcined at 800–1000 ºC. These results show that mean PS and SS can be manipulated by changing CT and/or BPR.

Considering the overall PSD of a milled powder as comprising small, intermediate and large size ranges, its matematical description is likely to be suitably achieved by using a multi–parameter Weibull distribution, which is governed by a generic formula:

$$f = f_{1,o}\left(\frac{k_1}{\lambda_{1,o}}\right)\left(\frac{D_i}{\lambda_{1,o}}\right)^{k_1-1} exp\left[-\left(\frac{D_i}{\lambda_{1,o}}\right)^{k_1}\right] + f_{2,o}\left(\frac{k_2}{\lambda_{2,o}}\right)\left(\frac{D_i}{\lambda_{2,o}}\right)^{k_2-1} exp\left[-\left(\frac{D_i}{\lambda_{2,o}}\right)^{k_2}\right] + f_{3,o}\left(\frac{k_3}{\lambda_{3,o}}\right)\left(\frac{D_i}{\lambda_{3,o}}\right)^{k_3-1} exp\left[-\left(\frac{D_i}{\lambda_{3,o}}\right)^{k_3}\right] \quad (10.3)$$

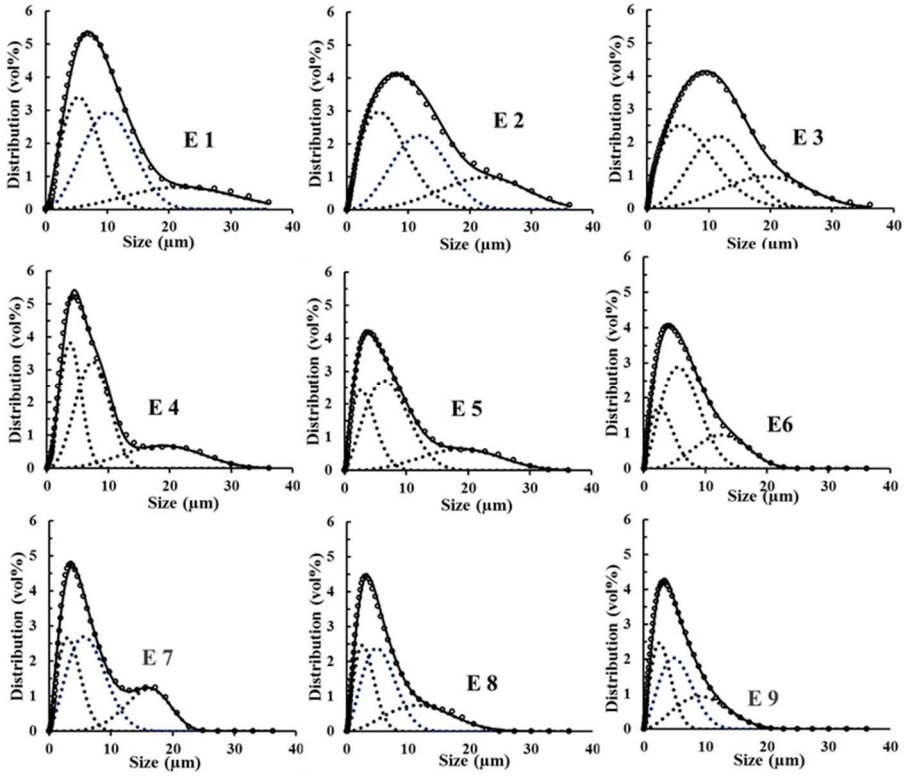

Fig. 10.2: Experimental (thick solid line) and modelled volume particle size distributions (PSD) and their Weibull deconvolutions represented by three dotted contribution curves.

In this Weibull distribution, D_i is the differential diameter, $f_{j,o}$ denotes the relative contribution of component j to the overall PSD, with j within the range of 1–3. $\lambda_{j,o}$ is the mean size of the specific distribution component, and k_j is its Weibull parameter. The calculated particle volume distribution curves for each size range component of each

experimental PSD curve are shown in **Fig. 10.2**. The definitions of E1–9 are shown in **Table 10.1**.

3.1.2. Specific surface area and pore volume

Fig. 10.3 reports on the dependence of BET specific surface area (SSA) and pore volume (PV) on the calcination temperature and of the balls to powder ratio used in wet ball milling. At 600 ºC, the SSA and PV vary between ~100–130 $m^2.g^{-1}$ and 0.34–0.48 $cm^3.g^{-1}$, respectively, with the lowest values being measured for the highest BPR=15, and the mid values being registered for the intermediate BPR=10. With increasing CT, both SSA and PV drastically decrease, and tend to be practically overlapped for all BPR values tested. These data show that: (i) BPR exerts a secondary role in determining both SSA and PV features, but only at 600 ºC, becoming completely irrelevant as calcination temperature further increases to 800–1000 ºC; (ii) Accordingly, CT is the main factor affecting both SSA and PV, as shown in **Fig. 10.3(a)** and **Fig. 10.3(b)**, respectively.

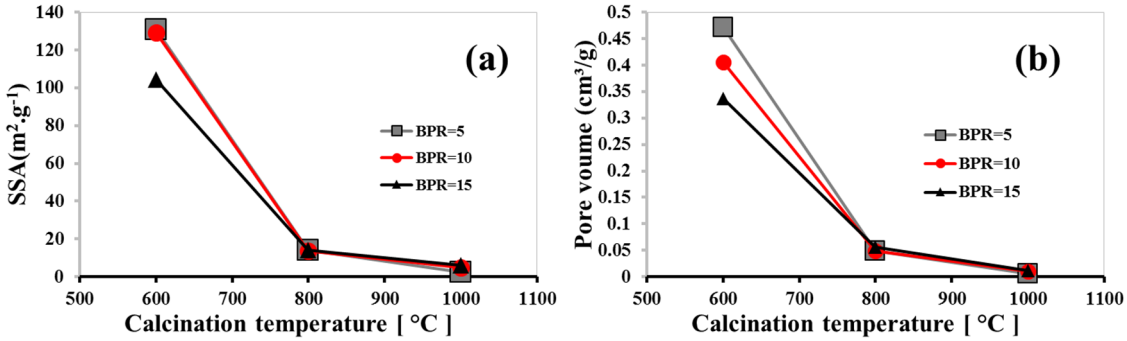

Fig. 10.3: Effects of CT and BPR on the microstructural features of the powders after wet milling for 1 h under a constant EPR = 1.5 and different values of BPR: (a) Specific surface area; (b) Pore volume.

With increasing CT, the smaller pores will be the first to be eliminated, being the main contributors for an overall decrease of pore volume fraction. The mechanical stresses applied upon milling tend to gradually destroy such porous structures, which is expected to break down preferentially through the larger pores. Accordingly, there is a good consistency between the concomitant decreases observed in PV **Fig. 10.3(b)** and mean diameters in **Table 10.1**. Oppositely, the observed decrease in SSA with increasing BPR, which is

accompanied by a clear particle size reduction trend **Table 10.1** seems counterintuitive, as milling is expected to expose new surfaces where adsorption should take place. This counterintuitive observation suggests that nitrogen condensation has already occurred in some pores with smaller radii at the maximum P/P_0=0.35 used. In such a condition, the total apparent amount of "adsorbate" will somewhat exceed the required amount for a monolayer formation, leading to an overestimation of the SSA. As the porous structure is gradually destroyed upon milling, some of the smaller pores become exposed, and nitrogen condensation cannot occur within such partially destroyed pores. These pores will not account anymore for the excess of nitrogen apparently adsorbed, which is translated into a lower apparent observed SSA. In other words, the values of SSA measured for the more extensively milled powders (BPR=10−15) calcined at 600 ºC **Fig. 10.3(a)** should be more realistic than those registered for the same powder milled under BPR=5. Moreover, the apparent reductions in SSA **Fig. 10.3(a)** with decreasing mean particle sizes **Fig. 10.1**, **Table 10.1** observed for the powder calcined at 600 ºC suggest that the incremental adsorption by the newly created surfaces upon milling is much less relevant that the decrease in nitrogen condensation within the smaller pores, explaining the counter intuitiveness of the results obtained.

The elimination of the smaller pores with further increasing of CT to 800−1000 ºC offsets the nitrogen pore condensation problem. As a matter of fact, there was a tremendous reduction in SSA to ~18 $m^2.g^{-1}$ with CT changing from 600 to 800 ºC, with further decreases to about one half of that for CT = 1000 ºC **Fig. 10.3(a)**. A similar tendency was observed for PV as a function of CT **Fig. 10.3(b)**.

3.1.3. Zeta potential (ζ)

Zeta potential (ζ) is used to assess the interaction forces amongst the particles. A value of zeta potential higher than ± 30 mV is often considered to be sufficient for obtaining stable suspension **[34,35]** . Although measurements have been made for powders samples derived from the nine trials, only data corresponding to different CTs (600, 800, and 1000 ºC) and milled under the two extreme BPR values (5, 15) will be reported here. **Fig. 10.4** plots the zeta potential ζ results gathered over a broad pH range for the selected powders (E1–3 and

E7–9). It can be seen that all the samples exhibit acidic isoelectric points converging to pH ~2 (pH_{iso} ~2), which are similar to that reported for silica **[36]**. This is particularly true for the samples calcined at the higher temperatures (800, 1000 ºC). With pH increasing, the ζ values become gradually more negative, with absolute values reaching approximate zeta potentials plateaux of 35–50 mV within the pH range from 6–12.

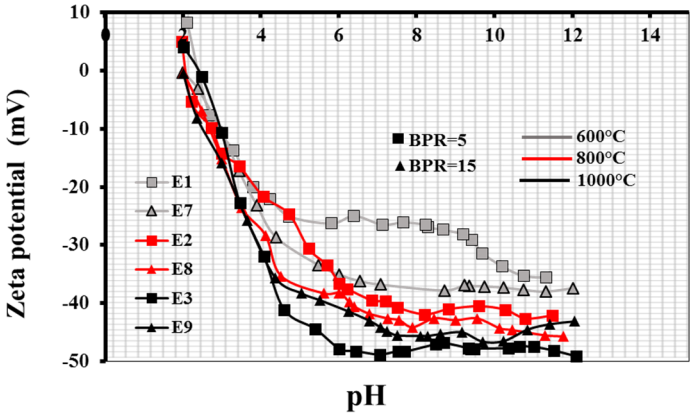

Fig. 10.4: Effects of calcination temperature (CT) and of BPR on the zeta potential of the bioactive glass particles: 600 ºC; (grey lines), 800 ºC; (red lines), 1000 ºC (black lines).

It is clear that the negative polarity of the particles' surface becomes gradually better defined as CT increases, leading to higher absolute ζ values. Accordingly, the most and the least negative ζ values are observed for CT=1000 ºC and CT=600 ºC, with intermediate values being registered at CT=800 ºC. Therefore, a higher CT is expected to favour electrostatic stabilisation **[37]**. The powder treated at 600 ºC exhibits a more porous structure, as seen from **Fig. 10.3**, and is prone to undergo a more extensive surface hydration process. With increasing CT, the tendency for surface hydration decreases, leading to higher ζ values. The ζ profiles obtained are in good harmony with the results acquired above for both mean particle size **Fig. 10.1(a)** and pore volumes **Fig. 10.3(b)**.

The BPR has a much more secondary role in determining interfacial solid/liquid interactions, meaning that zeta potential is essentially dependent on the surface polarity **[38]**. Despite this, particle size is likely to somewhat affect the electrophoretic mobility, as gravity lends a vertical component to the motion that becomes more significant for large particles. The observed dependence of ζ on particle size is in a good agreement with the results for a range

of different particle types found by Liu et al. **[39]**, Kazi et al. **[34]**, and Lelievre et al. **[40]**. Oppositely, it contrasts with the results reported by Vasconcellos et al. **[41]** for carbon black particles, who did not find any dependency between particle size and ζ.

3.2. Influence of the powders' features and solid loading on the rheological properties of the suspensions

All the relevant features of the powders ζ potential **[3]**, particle size and PSD profiles **[8–13]**, porous structure **[38]**, etc.), influence their dispersing ability. Higher values of ζ potential lead to stronger electrostatic forces among the particles. They start feeling the presence of other neighbouring particles at larger distances due to the consequent increment in their apparent size, as established by Eq. (10.1). This explains why the electrostatic stabilisation mechanism often limits the maximum solids loading, in comparison to steric or electrosteric stabilisation mechanisms **[3]**.

Porous particles derived from the powder calcined at 600 ºC absorb a portion of the dispersion liquid, which is no longer available to contribute to flowing. Moreover, such particles are more reactive towards water and develop lower absolute ζ potential values **Fig. 10.4**. The changes in the overall powder features with increasing CT tend to favour an aqueous dispersion. The maximum achievable solid loadings with the powders derived from the nine experiments are reported in **Fig. 10.5**.

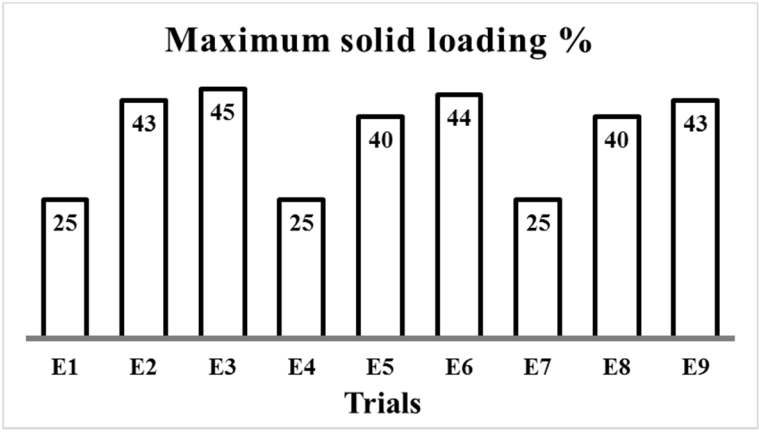

Fig. 10.5: Maximum achievable solid volume fractions with the powders derived from the nine experiments.

From the considerations above, it is not surprising the lower values of maximum solid loadings (25 vol.%) are obtained for the lowest CT. Increasing the CT to 800–1000 ºC enables significant increments in solid volume fractions. On the other hand, the maximum achievable solid loadings show an almost negligible dependence on the BPR (and the associated PSD features reported in **Fig. 10.2** and **Table 10.1**.

3.2.1. Apparent Viscosity

The flow properties of the suspensions were assessed in the ratational mode. The apparent viscosity curves *versus* shear rate of the bioactive glass slurries are displayed in **Fig. 10.6**. The comparison of the flow behaviour of suspensions prepared from all the powders could only be performed at 25 vol.% solid loading, the maximum achivable for the powder heat treated at 600 ºC. The flow curves displayed in **Fig. 10.6(a)** exhibit the following interesting features: (i) an initial increase in apparent viscosity at the lowest shear rates up to a maximum point, or plateau. This is often called Zero–Shear–Viscosity (ZSV, or η_0), being commonly oberved in gelled systems exhibiting yield stress; (ii) a branch of decreasing viscosity along the remaining shear rate range. This shear thinning behaviour is an essential requirement for extrusion, especially through fine nozzles.

The flow curves could be roughly divided into two sets depending on CT: one at 600 ºC, and the other at 800–1000 ºC. The curves of the first set are more irregular, and the apparent viscosity levels are about 3 orders of magnitude higher in comparison to the other systems, especially up to ~100 s^{-1}. The BPR has a less notiable effect on the flow properties in comparison to CT. However, there is a clear general trend, also visible in **Fig. 10.6(b)**, for the apparent viscosity to increase with particle size reduction, as expected. The increase of CT to 1000 ºC resulted in slightly lower apparent viscosity in comparison to systems derived from powders calcined at 800 ºC. This can be attributed to a further decrease of pore size and pore volume fraction **Fig. 10.3**, and to an increase of ζ potential **Fig. 10.4** associated with a less hydrated particle surface **[42]**. The associated changes in PS and PSD are also likely to account for the flow properties **[43]**. Although the flow curves for CT = 600 ºC at 25 vol.% solid loading in **Fig. 10.6(a)** exhibit similar, or even slighly higher, levels of apparent viscosity than those with CT = 800–1000 ºC at 40 vol.% loading shown in **Fig. 10.6(b)**, and printability is also likely under those conditions, the low solids loading (25

vol%) of the first case would imply a greater degree of shrinkage upon the drying and sintering steps. In this regard, the increases in both CT and BPR were revealed to be crucial for achieving a higher solid loadings, favouring the formulation of more promising inks for robocasting.

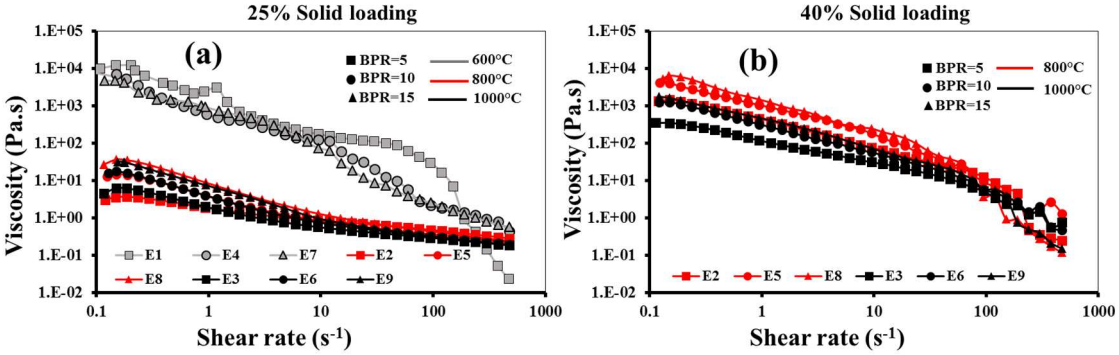

Fig. 10.6: Effects of CT and BPR on the apparent viscosity as a function of shear rate at different solid loadings: (a) 25 vol.%; (b) 40 vol.%.

3.2.2. Viscoelastic Properties

The viscoelastic properties of the formulated inks were assessed by rheological measuremments under the oscillatory mode. **Figs. 10.7(a–c)** displays the elastic modulus (G´) as a function of complex shear stress for sytems containing 25 and 40 vol.% solids. In **Fig. 10.7(a)** it can be seen that sufficiently high G´values for printing (G´~1 MPa) could be achieved for pastes with 25 vol.% loading derived from the powder calcined at 600 ºC and ball milled under BPR of 5−10 (E1 and E4). Further increasing of BPR to 15 caused a drop in G´ of about one order of magnitude, suggesting that the fluidification effect of the liquid released from the smaller pores that have been more extensively destroyed upon milling overcame the thickning effect expected from the reduction in PS. Furthermore, the pastes (inks) derived from the powder calcined at 600 ºC exhibit continuous linear viscoelastic regions (LVR) that extend beyond 100 Pa. The extensive LVR combined with the high values of G´ suggest that these pastes are promising for printing and shape retention **[32,44]** . Oppositely, the pastes containing 25 vol.% powder calcined at higher temperatures (800−1000 ºC) exhibit extremely low G´ values, and show a much narrower LVR that forbids easy printability.

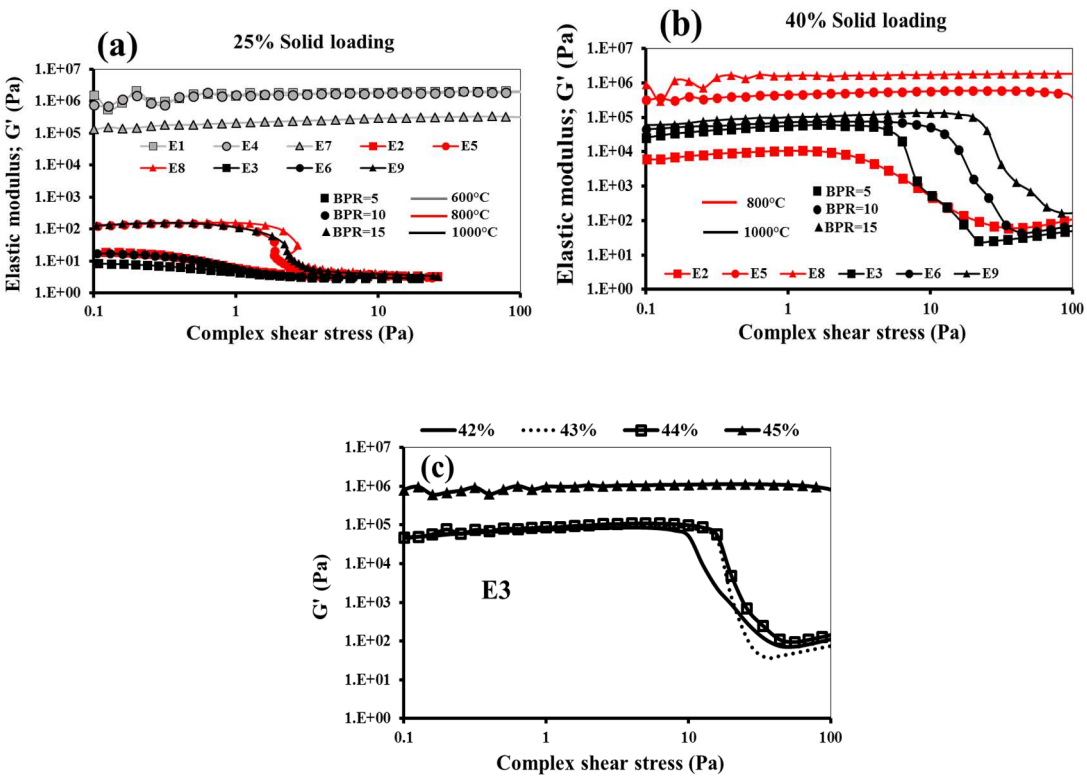

Fig. 10.7: Effects of CT and BPR on the Elastic modulus (G´) and the extent of LVR as a function of complex shear stress at different solid loadings: (a) 25 vol.%; (b) 40 vol.%; (c) 42–45 vol.% of E3 powder.

The increase of solid loading to 40 vol.% **Fig. 10.7(b)** enabled us to obtain pastes from the finer powders (BPR=10 and BPR=15) with promising viscoelastic properties for printing, especially in the case of the powder calcined at 800 ºC (E5 and E8). Such viscoelastic properties are similar to those of the pastes containing 25 vol.% of the powder calcined at 600 ºC **Fig.10.7(a)**. The system prepared from the ~~coaser~~ coarser powder (BPR=5) is insufficiently stiff for printing. With a further increase in CT to 1000 ºC, the pastes became even less stiff, resulting in noticeable decreases in the G´ magnitude and in the extent of LVR **Fig. 10.7(b)**. These features show a clear gradual decresing trend when moving from BPR=15 to BPR=5, with the last one being too soft and hardly printable.

Considering the lesser thickning effect caused by the highest CT and the coarser particle size (BPR=5); and the decreasing shrinkage undergone by structures deposited from pastes with increasing solids loading, the powder derived from experiment E3 was further explored in an attempt to maximise the solids volume fraction. The curves displayed in **Fig. 10.7(c)** show that a solids loading of 45 vol.% is required to achieve a G´ ~1 MPa, which also resulted in

a long LVR, conferring to the resulting paste a good printing potential. Further, with this E3 powder, the solids loading becomes a very critical parameter, as a small variation from 45 to 44 vol.% caused a significant decrease in G´ greater that one order of magnitude, and a narrowing of the LVR to about one fifth (~20 Pa). Such trends become exacerbated with further decreases in the solids loading, compromising the printing ability of the pastes. Therefore, although 45 vol.% of the powder derived from the highest CT and the lowest value of BPR (E3) enables the highest achivable solid loading among all the experiments, the printable window, in terms of other processing conditions, becomes too narrow. Playing with PSD, namely further reducing PS, is likely to give more room for optimal processing conditions.

4. Conclusions

Nine suspensions were prepared from high silica bioactive glass to assess their potential as inks for robocasting. The results presented and discussed above enable us to draw the following conclusions:

1) The CT negatively affects the porosity fraction and the SSA, and tends to extend the span of PSD, while the reduction in mean particle size is particularly favoured by the increase in BPR.
2) The surface polarity (charge density) of the high silica bioactive glass particles was shown to depend essentially on the heat treatment temperature, gradually increasing when CT increased from 600−1000 ºC. The BPR was revealed to exert only a secondary effect through its small influence on particle size.
3) The apparent viscosity, the elastic modulus, and the extent of LVR are strongly dictated by a set of interdependent factors determined by the CT, BPR, PS, PSD, and solids loading. For a given CT, the viscoelasticity is enhanced by increasing the solid loading and decreasing the mean particle size. The values of elastic modulus within the range of 10^5–10^6 Pa, combined with extensive of LVR with shear stress values to over 100 Pa measured for a number of inks, enable us to predict good printing ability. Such promising rheological properties can be obtained at a solid loading as low as 25 vol.% for CT=600 ºC. However, considering the benefits of higher solid loadings in terms of dimenssional control along the entire process, similar

viscoelestic properties can be achieved at solid loading >40 vol.% by suitably adjusting all the relevant process variables, especially for CT = 800 ºC and BPR = 10–15.

Acknowledgments

R.C. Pullar wishes to thank the FCT Grant IF/00681/2015 for supporting this work. B. A. E. Ben–Arfa thanks FCT grant BIONANOSCULP PTDC/EPH–PAT/6281/2014 for supporting him during this work. This work was developed in the scope of the project CICECO–Aveiro Institute of Materials (Ref. FCT UID /CTM /50011/2013), financed by national funds through the FCT/MEC and when applicable co–financed by FEDER under the PT2020 Partnership Agreement.

References

[1] J. Cesarano III, A Review of Robocasting Technology, in: MRS Proc., 1998: pp. 133–139.

[2] S. Eqtesadi, A. Motealleh, P. Miranda, A. Pajares, A. Lemos, J.M.F. Ferreira, Robocasting of 45S5 bioactive glass scaffolds for bone tissue engineering, J. Eur. Ceram. Soc. 34 (2014) 107–118.

[3] G. Tarì, J.M.F. Ferreira, A.T. Fonseca, O. Lyckfeldt, Influence of particle size distribution on colloidal processing of alumina, J. Eur. Ceram. Soc. 18 (1998) 249–253.

[4] S.M. Olhero, J.M.F. Ferreira, Influence of particle size distribution on rheology and particle packing of silica–based suspensions, Powder Metall. 139 (2004) 69–75.

[5] G. Tari, J.M.F. Ferreira, A.T. Fonseca, Infuence of particle size and particle size distribution on drying–shrinkage behaviour of alumina slip cast bodies, Ceram. Int. 25 (1999) 577–580.

[6] J.V. Milewski, Efficient Use of Whiskers in the Reinforcement of Ceramics, Adv. Ceram. Mater. 1 (1986) 36–41.

[7] G. Tarì, J.M.F. Ferreira, O. Lyckfeldt, Influence of the Stabilising Mechanism and Solid Loading on Slip Casting of Alumina, J. Eur. Ceram. Soc. 18 (1998) 479–486.

[8] A. Kaushal, S.M. Olhero, J.M.F. Ferreira, Lead–free 0.5Ba(Zr0.2Ti0.8)O3–0.5(Ba0.7Ca0.3)TiO3 powder surface treated against hydrolysis – a key for a successful aqueous processing, J. Mater. Chem. C. 1 (2013) 4846–4853.

[9] J.M.F. Ferreira, O. SM, Drying Induced Forming from Highly Concentrated Alumina Slips, Am. Ceram. Soc. 112 (2001) 483–488.

[10] G. Tarì, J.M.F. Ferreira, Influence of Solid Loading on Drying–Shrinkage Behaviour of Slip Cast Bodies, J. Eur. Ceram. Soc. 18 (1998) 487–493.

[11] J.M.F. Ferreira, H.M.M. Diz, Effect of Solids Loading on Slip–Casting Performance of Silicon Carbide Slurries, J. Am. Ceram. Soc. 82 (2004) 1993–2000.

[12] Z. Yuan, Y. Zhang, Y. Zhou, S. Dong, Effect of solid loading on properties of reaction bonded silicon carbide ceramics by gelcasting, RSC Adv. 4 (2014) 50386–

50392.

[13] L.F.G. Setz, L. Koshimizu, S.R.H. de Mello–Castanho, M.R. Morelli, Rheological Analysis of Ceramics Suspensions with High Solids Loading, Mater. Sci. Forum. 727–728 (2012) 646–651.

[14] R. Kyrpal, I. Dulina, A. Ragulya, Effect of BaTiO3 nanopowder concentration on rheological behaviour of ceramic inkjet inks, J. Phys. Conf. Ser. 602 (2015) 1–6.

[15] B. V. Velamakanni, F.F. Lange, Effect of Interparticle Potentials and Sedimentation on Particle Packing Density of Bimodal Particle Distributions During Pressure Filtration, J. Am. Ceram. Soc. 74 (1991) 166–172.

[16] Pugh, R. J. & Bergstrom, L., Surface and colloid chemistry in advanced ceramic processing, Surfactant science series vol. 51, Marcel Dekker, New York, 1994.

[17] C.T. Nguyen, F. Desgranges, G. Roy, N. Galanis, T. Maré, S. Boucher, et al., Temperature and particle–size dependent viscosity data for water–based nanofluids – Hysteresis phenomenon, Int. J. Heat Fluid Flow. 28 (2007) 1492–1506.

[18] C. Furnas, The relation between specific volume, voids and size composition in systems of broken solids of mixed sizes, Dep. of commerce, Bureau of mines, RI 2894, 1928.

[19] M.I.L.L. Oliveira, K. Chen, J.M.F. Ferreira, Influence of the deagglomeration procedure on aqueous dispersion , slip casting and sintering of Si3N4 –based ceramics, J. Eur. Ceram. Soc. 22 (2002) 1601–1607.

[20] A. Krell, P. Blank, M. Honggwei, T. Hutzler, Transparent Sintered Corundum with High Hardness and Strength, J. Am. Ceram. Soc. 86 (2003) 12–18.

[21] A. Krell, J. Klimke, Effects of the homogeneity of particle coordination on solid–state sintering of transparent alumina, J. Am. Ceram. Soc. 89 (2006) 1985–1992.

[22] A. Krell, J. Klimke, T. Hutzler, Advanced spinel and sub–µm Al2O3for transparent armour applications, J. Eur. Ceram. Soc. 29 (2009) 275–281.

[23] Q. Fu, E. Saiz, Tomsia, A. P., Direct ink writing of highly porous and strong glass scaffolds for load–bearing bone defects repair and regeneration, Acta Biomater. 7

(2011) 3547–3554 .

[24] Q. Fu, E. Saiz, M.N. Rahaman, Toward Strong and Tough Glass and Ceramic Scaffolds for Bone Repair, Adv. Funct. Mater. 23 (2013) 5461–5476 .

[25] X. Liu, M.N.. Rahaman, Q. Fu, Bone regeneration in strong porous bioactive glass (13–93) scaffolds with an oriented microstructure implanted in rat calvarial defects, Acta Biomater. 9 (2013) 4889–4898 .

[26] A. Nommeots–Nomm, P.D. Lee, J.R. Jones, Direct ink writing of highly bioactive glasses, J. Eur. Ceram. Soc. 38 (2018) 837–844.

[27] S.M. Olhero, H.R. Fernandes, C.F. Marques, B.C.G. Silva, J.M.F. Ferreira, Additive manufacturing of 3D porous alkali–free bioactive glass scaffolds for healthcare applications, J. Mater. Sci. 52 (2017) 12079–12088.

[28] B.A.E. Ben–Arfa, I.M. Miranda Salvado, J.M.F. Ferreira, R.C. Pullar, A hundred times faster: Novel, rapid sol–gel synthesis of bio–glass nanopowders (Si–Na–Ca–P system, Ca:P = 1.67) without aging, Int. J. Appl. Glas. Sci. 8 (2017) 337–343.

[29] B.A.E. Ben–Arfa, H.R. Fernandes, I.M. Miranda Salvado, J.M.F. Ferreira, R.C. Pullar, Synthesis and bioactivity assessment of high silica content quaternary glasses with Ca: P ratios of 1.5 and 1.67, made by a rapid sol–gel process, J. Biomed. Mater. Res. – Part A. 106 (2018) 510–520.

[30] B.A.E. Ben–Arfa, I.M.M. Salvado, J.M.F. Ferreira, R.C. Pullar, Enhanced bioactivity of a rapidly–dried sol–gel derived quaternary bioglass, Mater. Sci. Eng. C. 91 (2018) 36–43.

[31] B.A.E. Ben–Arfa, H.R. Fernandes, I.M.M. Salvado, J.M.F. Ferreira, R.C. Pullar, Effects of catalysts on polymerization and microstructure of sol–gel derived bioglasses, J. Am. Ceram. Soc. 101 (2018) 2831–2839.

[32] S. Eqtesadi, A. Motealleh, P. Miranda, A. Lemos, A. Rebelo, J.M.F. Ferreira, A simple recipe for direct writing complex 45S5 Bioglass®3D scaffolds, Mater. Lett. 93 (2013) 68–71.

[33] S. He, Y. Qin, E. Walid, L. Li, J. Cui, Y. Ma, Effect of ball–milling on the physicochemical properties of maize starch, Biotechnol. Reports. 3 (2014) 54–59.

[34] S.N. Kazi, A. Badarudin, M.N.M. Zubir, H.N. Ming, M. Misran, E. Sadeghinezhad, et al., Investigation on the use of graphene oxide as novel surfactant to stabilize weakly charged graphene nanoplatelets, Nanoscale Res. Lett. 10 (2015) 1–15.

[35] D. Sun, S. Kang, C. Liu, Q. Lu, L. Cui, B. Hu, Effect of Zeta Potential and Particle Size on the Stability of SiO2 Nanospheres as Carrier for Ultrasound Imaging Contrast Agents, Int. J. Electrochem. Sci. 11 (2016) 8520–8529.

[36] R.K. Iler, The chemistry of silica solubility, polymerization, colloid and surface properties, and biochemistry, John Wiley & sons, Toronto, 1978.

[37] M. Larsson, A. Hill, J. Duffy, Suspension stability : Why particle size , zeta potential and rheology are important, Annu. Trans. Nord. Rheol. Soc. 20 (2012) 209–214.

[38] J. Vinogradov, M.D. Jackson, Zeta potential in intact natural sandstones at elevated temperatures, Geophys. Res. Lett. 42 (2015) 6287–6294.

[39] X. Liu, T. Yu, Q. Wei, Z. Yu, X. Xu, Enhanced diamond nucleation on copper substrates by employing an electrostatic self–assembly seeding process with modified nanodiamond particles, Colloids Surfaces A Physicochem. Eng. Asp. 412 (2012) 82–89.

[40] F. Lelievre, D. Bernache–Assollant, T. Chartier, Influence of powder characteristics on the rheological behaviour of hydroxyapatite slurries, J. Mater. Sci. Mater. Med. 7 (1996) 489–494.

[41] S.R. Vasconcellos, J.J. Kosman, R.L. Rowell, A.I. Medalia, The relationship between zeta potential and particle size in non–aqueous carbon–black dispersions, J. Dispers. Sci. Technol. 4 (1983) 409–413.

[42] S. Padilla, R. García–Carrodeguas, M. Vallet–Regí, Hydroxyapatite suspensions as precursors of pieces obtained by gelcasting method, J. Eur. Ceram. Soc. 24 (2004) 2223–2232.

[43] T. Huber, M. Misra, A.K. Mohanty, The effect of particle size on the rheological properties of polyamide 6/biochar composites, in: AIP Conf. Proc., 2015: pp. 6–10.

[44] E. Feilden, E. Blanca, F. Giuliani, E. Saiz, L. Vandeperre, Robocasting of structural

ceramic parts with hydrogel inks, J. Eur. Ceram. Soc. 36 (2016) 2525–2533.

Chapter 11

The present chapter was published on:
Journal of the European Ceramic Society;
Volume 39, Issue 4,
2019,
Pages 1625-1634.
Doi: 10.1016/j.jeurceramsoc.2018.11.019

Robocasting of ceramic glass scaffolds: Sol–gel glass, new horizons

Basam A. E. Ben–Arfa [a], Ana S. Neto [a], Ilaria E. Palamá [b], Isabel M. Miranda Salvado [a] *, Robert C. Pullar [a]* and José M. F. Ferreira.[a]

[a] *Department of Materials and Ceramic Engineering / CICECO – Aveiro Institute of Materials, University of Aveiro, 3810–193 Aveiro, Portugal*

[b] *CNR NANOTEC – Istituto di Nanotecnologia, Campus Ecotekne, Via Monteroni, 73100 Lecce, Italy*

*To whom correspondence should be addressed: isabelmsalvado@ua.pt, rpullar@ua.pt

Keywords: Sol–gel; Bioactive glass; Suspension rheology; Robocasting 3D scaffolds; Cytotoxicity.

Abstract

Sol–gel derived bioactive glass powders usually exhibit high volume fractions of meso– and micro–porosities that make them inappropriate for colloidal processing, as a significant portion of the dispersing medium is absorbed by the porous structure and will not be available for a good dispersion and flow. Here, we report for the first time how to circumvent these practical difficulties to achieve pastes with high solids loading and appropriate rheological properties for the extrusion through fine nozzles in a robocasting process. A novel and rapid sol–gel approach that reduces the time required for the synthesis and drying processes to just 2 h was used to prepare a high silica glass. The dried product was calcined and milled to obtain powders with particle size distributions and other powder features suitable for colloidal processing. Scaffolds with different macro–pore sizes could be produced by robocasting from optimal pastes with solid loadings up to 40 vol.%. The sintered (800 ºC, 2 h) scaffolds exhibited compressive strength within the range of (2.5–4.8 MPa), the formation of a hydroxyapatite surface layer after 72 h of immersion in SBF, the absence of cytotoxic effects and a considerable MG63 cells viability rate. These features make the scaffolds promising candidates for tissue engineering applications and worthy for further *in vivo* investigations.

1. Introduction

The firstly developed biomaterials were intended as bio–inert and to induce minimal responses from the surrounding tissues. The paradigm changed in the late 1960s with the discovery of bioactive glasses (BGs) by Hench and collaborators in their pioneering work **[1]**. Bioactive glasses elicit special responses when in contact with biological fluids that lead to the formation of a bone–like hydroxyapatite (HAp) layer at the surface of BGs *in vivo* and to their strong bonding to the host living tissues and might be resorbable. Besides being non–cytotoxic and either resorbable or bioactive, modern bone graft biomaterials are aimed at combining other added features to stimulate gene activation and potentiate their performances *in vitro* and *in vivo* including: (i) Non–genotoxicity (causing no damage to genes within a cell or DNA mutations); (ii) Osteo conductive (bone readily grows on its surface); (iii) Osteoinduction (ability to recruit immature cells and to stimulate them towards developing into pre–osteoblasts, essential in any bone healing process); (iv) Osseo integration (establish a stable implant anchorage through its direct bone–to–implant contact) **[2]**. In this regard, bioactive glasses commonly present several advantages over bioceramics, playing important roles in tissue engineering constructs and inducing bone regeneration **[3]**.

The first bioactive glasses were synthesised by the conventional melt–quenching technique **[1]**. Nevertheless this technique has several disadvantages in comparison to sol–gel route, including: (i) relatively high melting temperatures that may led to the partially volatilisation of some constituents as the case of P_2O_5, energy consumption and an increase of production costs **[4]**; (ii) less porous and bioactive materials for a given composition; (iii) may undergo liquid–liquid phase separation, nucleation and crystallization upon cooling, degrading the molecular level homogeneity. Therefore, the sol–gel preparation route is considered to be a better choice for synthesizing homogeneous and highly bioactive glasses and a good strategy to get rid of the above mentioned disadvantages **[5]**.

Tissue engineering (regenerative medicine) is a multidisciplinary research field that began in 1980's **[6]** to combine engineering and life science to develop a new methods tissue replacement with better functionality. This includes, harvesting cells from the body and seeding them in an implantable scaffold *in vitro*. The scaffold is a three dimensional (3–D) structure constructed to be a temporary implant, to act as a template for new cell growth, and which degrades during/after the healing process, while the seeded cells grow and proliferate

to regenerate a new tissue **[7]**. Scaffolds need to meet particular morphological requirements to accomplish their function in regenerative tissue. The scaffolds need to have a large interconnected pores, and a hierarchical degree of porosity. They require macro–pore sizes >50 µm, to enable the cells to easily penetrate the scaffold structure, and micro pores sizes within the range of (1–50 µm) to facilitate cell anchorage and proliferation. They must also exhibit a moderate mechanical strength in such a manner that resist the applied loads while avoiding the effect of stress shielding that can result in bone loss **[8,9]**. A scaffold with high macro–sized interconnectivity is a crucial element for the cells to be able to migrate into to the centre of the scaffold, and to allow a sufficient supply of nutrient for the cells to grow **[9]**. Many techniques have been used to build scaffolds, such as replica templating **[10]**, foaming **[11]**, starch consolidation **[12]**, freeze casting **[13]**, and robocasting [**14–17**]. Among these methods, robocasting offers a better control on the macro–pores´ shape and size, as well as the possibility to produce tailored, shaped implants for an individual patient. The robotic control of the ink deposition enables the synthesis of specific predesigned complex shapes and morphologies to enable substitution of the defect part of the bone in a very precise manner, using a CAD–CAM model **[18]**.

Many materials have been used to build scaffolds for tissue engineering by robocasting including, calcium phosphate (CP), and its derivatives [**19–21**], and ceramic/polymer composites **[22,23]**. However, the fabrication of bioactive glass scaffolds by robocasting has proven to be more complicated, even from less porous melt–quenching glass frits. The typical porous features of sol–gel derived bioactive glass powders bring further processing difficulties, as the dispersing liquid portion absorbedby the porous structure will not be available for flowing. This explains why the fabrication of bioactive glass scaffolds by robocasting has been scarcely reported and only for glass compositions prepared by melt–quenching **[24]**. The most important requirements for successful fabricating scaffold by robocasting include the easiness of ink preparation and the aptitude of the glass composition for sintering **[24]**. These requirements are not satisfactorily met by the most popular 45S5 Bioglass® composition. The excessive leaching of Na^+ and the concomitant increase in pH hinder an efficient dispersion. The ink preparation challenge could only be overcome for the first time when a new recipe using carboxyl methyl cellulose (CMC) as single processing additive was adopted Ferreira *et al*. **[17,24]**. However, the sintered scaffolds exhibited poor densification due to the narrow sintering window, defined

as the difference (ΔT) between the onset of crystallization temperature (T_c ~600 ºC) and the first glass transition temperature (T_g ~560 ºC), ($\Delta T = T_c - T_g$ ~40 ºC) **[17]**. Therefore, in the additive manufacturing of scaffolds by robocasting, preference has been given to less soluble glasses exhibiting broader sintering windows such as the (13–93) composition **[25]**. But the enhanced sintering ability and the gains in mechanical properties are in this case achieved at the expenses of lower bio–mineralization and degradation rates, as expected from the relatively high network connectivity of the (13–93) glass **[26]**.

Nevertheless, there is still a lack of bioactive sol–gel glasses suitable for formulating inks for robocasting. This can be attributed to their high specific surface area and porous structure responsible for up–taking a significant portion of the dispersing liquid. Although these features of sol–gel derived glasses are advantageous in terms of bioactivity, such features supposedly constitute the main barriers towards using these powders in robocasting. This issue was recently tackled by the authors in an attempt to overcome these constrains in the formulation of ink and predicting ink printability **[27]**. It was shown that significant progresses could be made by playing with the calcination temperature and with the milling conditions, which determine the particle size (PS), particle size distribution (PSD) and porous fraction of the synthesised powder. These features, in turn, determine the packing ability and the flow behaviour of the inks.

Powder milling is a critical step in deciding the ink printing ability. This task has been accomplished by using sophisticated equipment such as attrition mill **[25]** and planetary milling **[21]** for different time periods up to 4 h. The milling efficiency strongly depends on the milling conditions, namely on the rotation speed and the balls to powder ratio (BPR). A suitable control of these variables was shown to enable shortening the milling time of our sol–gel bioactive glasses to 1 h using a simple equipment **[27]**. Following the same strategy used here is likely to open new research avenues for the fabrication of sol–gel derived bioactive glass scaffolds by robocasting.

2. Materials and methods

2.1. Wet milling procedures

A four–component high silica sol–gel glass (HSSGG) composition reported in **Table 11.1** was synthesised by the sol–gel route as previously described by the authors **[28]**. The as–dried gel was calcined in air according to the following three stages heat treatment schedule: 1st stage, from room temperature (RT) to 200 ºC at the heating rate of 1 ºC min^{-1}; 2nd stage, from 200 ºC to 400 ºC, at the heating rate 2 ºC min^{-1}; and the 3rd stage, from 400 ºC to 800 ºC, at the heating rate of 5 ºC min^{-1}, 2 h dwell time at 800 ºC, followed by natural cooling.

Table 11.1: Comparison our HSSGG composition (and other relevant features), with bioactive glasses prepared by melt quenching that have been already used in the fabrication of scaffolds by robocasting.

Sample code	Composition in wt. %							Network connectivity	Thermal parameters (ºC)		
	SiO_2	Na_2O	CaO	P_2O_5	K_2O	MgO	CaF_2	(NC)*	T_g	T_c	ΔT
HSSGG	64.40	4.90	21.53	9.09	–	–	–	3 $_{(NMR)}$ [28]	621	723	102
13–93	53.00	6.00	20.00	4.00	12.00	5.00	–	2.6 [47]	592 [47]	932	340
45S5	54.00	24.50	24.50	6.00	–	–	–	2.1 [47]	560 [47]	600	40
FastOs®BG	38.84	–	33.98	13.37	–	13.03	0.77	1.94 [48]	750 [48]	875	125

*Network connectivity was calculated from NMR data (Eq. 11.1), or based on the molar concentrations of the oxide components (Eq. 11.2):

$$N_c(NMR) = 4\left[\frac{Q^4}{100}\right] + 3\left[\frac{Q^3}{100}\right] + 2\left[\frac{Q^2}{100}\right] + \left[\frac{Q^1}{100}\right] \quad (11.1)$$

$$\mathrm{N_c} = \frac{4[\mathrm{SiO_2}] - 2[\mathrm{M_2^I O} + \mathrm{M^{II} O}] + 6[\mathrm{P_2O_5}]}{[\mathrm{SiO_2}]} \quad (11.2)$$

The calcined material was wet ball milled for 1 h in ethanol (EtOH) using a mass ethanol to powder ratio (EPR = 1.5), and a balls to powder ratio (BPR) = 10. The milling was done in

a S–series–Fast Mill machine, type S2–1000 (Ceramic instruments Sassuolo, Italy) under a rotational speed of 390 rpm, using a sintered alumina jar of 300 cm^3 capacity (Ceramic instruments Sassuolo, Italy) and spherical yttria–stabilized zirconia milling balls with 10 mm diameter (Tosoh, Tokyo, Japan). After milling, the slurry was separated and dried in an oven at 60 ºC for 24 h for drying. The dry powders were passed through a 63 µm mesh sieve to retain the large agglomerates. The features of the fine powder fraction were assessed by the characterisation techniques described below.

2.2. Characterisation of the milled powder

The average particle size (PS) and the particle size distribution (PSD) of the milled powder, on a volume basis, was determined using a laser diffraction particle size analyser (Coulter LS particle size analyser; Beckman Coulter, CA) through triplicate measurements.

The specific surface areas (SSA) of the powders were measured using the Brunauer–Emmett–Teller (BET method, Micrometric Gemini M–2380) using N_2 as adsorbate. Samples were degassed at 200 ºC before the measurement. The adsorption/desorption isotherms were measured, specific surface area (SSA) was calculated by the BET method. The BJH method was used to estimate the meso– and macroporous (17–3000 Å) SSA, as well as absolute meso/macropore volumes and areas from both adsorption and desorption isotherms. The BJH pore size (w) distribution was calculated by plotting dV/dlog(w) and dA/dlog(w) for pore volume (PV) and pore area (PA), respectively, with the area under the graph representing the distribution between two pore width values.

Zeta–potential measurements were performed in both the acidic and the alkaline regions at several pH values to evaluate the particles' surface charges, using a Malvern Zeta sizer Nano ZS (Malvern Instruments, Worcestershire, UK). The measurements were carried out after dispersing the powders in a background 10^{-3} M KCl electrolyte solution under sonication for ~10 min, and gradually shifting the pH into both acidic and basic conditions by using HCl and NaOH, respectively.

2.3. Suspension preparation

For studying the effects of solid loading on the rheological properties and printability of the inks, suspensions containing three different solid volume fractions (30, 35, and 40 vol.%) were prepared. The powder was dispersed in de–ionised water in the presence of 1.1 wt.% carboxymethyl cellulose (CMC) (Mw = 250,000, Lamberti Iberia s.a.u., Castellón, Spain) as a multifunctional processing additive (dispersant, binder and gelation agent) **[24]**. The powder was gradually added to the dispersing solution in small dosages, followed by mixing in a planetary centrifugal mixer (ARE–250, Thinky Corp. Tokyo, Japan) to ensure a homogeneous suspension.

2.4. Rheological characterisation of suspensions and pastes

The rheological properties of the suspensions were assessed using a Kinexus Pro+ Rheometer (Malvern Instruments, USA). The viscometry mode was used to measure the apparent viscosity of the tested samples, using the cone (4º/40 mm) and plate sensor system with a 150 µm gap size. The viscoelastic properties of the pastes were assessed using the oscillatory mode of the rheometer equipped with plate & plate sensor (20 mm), with 1 mm gap size. In all rheological measurements, a metal ring with di–ionised water as solvent trap was used to prevent water evaporation from the samples while testing.

2.5. Fabrication of scaffolds by robocasting

The bioactive glass scaffolds were deposited layer–by–layer using a robocasting equipment (3–D Inks, Stillwater, OK, USA). The paste was extruded through a nozzle with a diameter of 410 µm and using a printing speed of 10 mm s^{-1}. The designed scaffold consisted of a 3D structure made of 12 layers, each one consisting of 5 parallel rods, with the next layer being rotated around 90º in the plane of the rods. Scaffolds were printed in groups contain nine scaffolds with three different pore sizes (the distance between the rods) of 300, 400 and 500 µm, all with dimensions of (3x3x4) mm. The deposition was carried out in a reservoir containing paraffin oil to allow a uniform drying of the green scaffolds. Once printing was finished, the scaffolds were removed from the oil and dried at room temperature for 24 h,

followed by sintering at 800 ºC for 2 h, using a heating rate of 1ºC min^{-1} to ensure a complete removal of the residual organics.

2.6. Compressive strength evaluation

The compressive strength of sintered scaffolds was determined under uniaxial tests using 10 samples of each pore size series (300, 400, and 500 μm). The tests were carried on a universal testing machine (AG–IS10kN, Shimadzu, Kyoto, Japan) at a constant speed of 0.5 mm min^{-1} in the perpendicular direction to the printing plane. The compression–displacement relationship was obtained from the tests.

2.7. In vitro cytotoxicity assays

In vitro cytotoxicity assays for bioactive glass scaffolds were performed according to the International Organization for Standardization (ISO) guidelines (ISO 10993–5) (International Organization for Standardization 2009) **[29]**. MG63 cell line (ATCC CRL–1427, Human osteosarcoma) was used to determine the materials cytotoxicity through the MTT assay. MG63 cells were conserved in Dulbecco's Modified Eagle Medium (DMEM, Sigma Aldrich) supplemented with 10% (v/v) of foetal bovine serum (FBS, Sigma Aldrich), penicillin (100 U/mL culture medium, Sigma Aldrich), streptomycin (100 μg ml^{-1} culture medium, Sigma Aldrich), L–glutamine (5%, Sigma Aldrich) and sodium pyruvate (5%, Sigma Aldrich). The cells were grown in a humidified incubator at 37 ºC, 5% CO_2, and 95% relative humidity. The samples were prepared by cutting each scaffold in two halves, each half weighing ~12 mg. The scaffolds were sterilized by UV–radiation prior being tested in cell cultures. Measuring the activity of living cells via mitochondrial dehydrogenase activity whose key component is 3–[4,5–dimethylthiazol–2–yl]–2,5–diphenyl tetrazolium bromide. Mitochondrial dehydrogenases of viable cells cleaved the tetrazolium ring, yielding purple MTT formazan crystals which were insoluble in aqueous solutions. The crystals were dissolved in acidified isopropanol and the resulting purple solution was spectrophotometrically measured. An increase in cell number results in an increase in the amount of MTT formazan formed and an increase in absorbance.

MG63 osteoblasts were seeded (5,000 cells/ml) on scaffolds of the three different pore size series and incubated at 37 ºC in 5% CO_2, 95% relative humidity for 7 days. The culture medium was changed every 2 days. The control (CTR) was a complete culture medium. The absorbance was spectrophotometrically measured at 570 nm wavelength, and the background absorbance measured at 690 nm.

The percentage of viability was expressed as the relative growth rate (RGR) by eq. (11.3):

$$\mathrm{RGR}(\%) = \frac{\mathrm{D_{scaffold}}}{\mathrm{D_{control}}} \times 100 \qquad (11.3)$$

Where $D_{scaffold}$ and $D_{control}$ stand for the absorbance of the testing sample and of the negative control, respectively. Each experiment was done in triplicate (Student's t–test, $P < 0.05$) to ensure better certainty of the acquired data.

2.8. Bioactivity assessment

The scaffolds of the 300 µm pore size series sintered at 800 ºC were selected for bioactivity assessment. The test was done by immersing the scaffold in 6 ml of simulated body fluid (SBF), for different periods of time (4 h, 24 h, 72 h, 1 w, 2 w, and 4 w). The SBF was prepared according to the unified approach proposed elsewhere **[30]**, and the test was triplicated for each period of time. After each immersion period, the scaffolds were collected from the SBF solution, washed using distilled water several times, and then kept to dry at 60 ºC overnight in an oven. The pH of the solution after each immersion was recorded. The precipitation of hydroxyapatite (HAp) phase was monitored by scanning electron microscope (SEM). The scaffolds were crushed to evaluate the evolution of HAp phase using X–ray diffraction (XRD), (XRD, PANalytical XPERT–PRO Diffractometer system), using Cu–Kα radiation (Kα = 1.540 Å), with 2Θ varying from 6 to 70º in steps of 0.026 s^{-1}. The diffraction patterns were compared with JCPDS standards. Attenuated total reflection Fourier transform infrared spectroscopy (ATR–FTIR), (Tensor 27, Brucker, Germany) in the range of 350–4000 cm^{-1}, with 128 Scans and 4 cm^{-1} resolution was also performed.

3. Results and Discussion

3.1. Powder milling outcomes

The powder calcined at 800 ºC and milled for 1 h exhibited a mean particle size of 4.9 µm, a BET SSA of 13.83 m^2 g^{-1}, and its density measured by helium pycnometry was 2.248 g cm^{-3}. The BET isotherm is shown in **Fig. 11.1(a),** and it presents a type IV isotherm typical of a porous material, with a narrow hysteresis loop as we would expect.

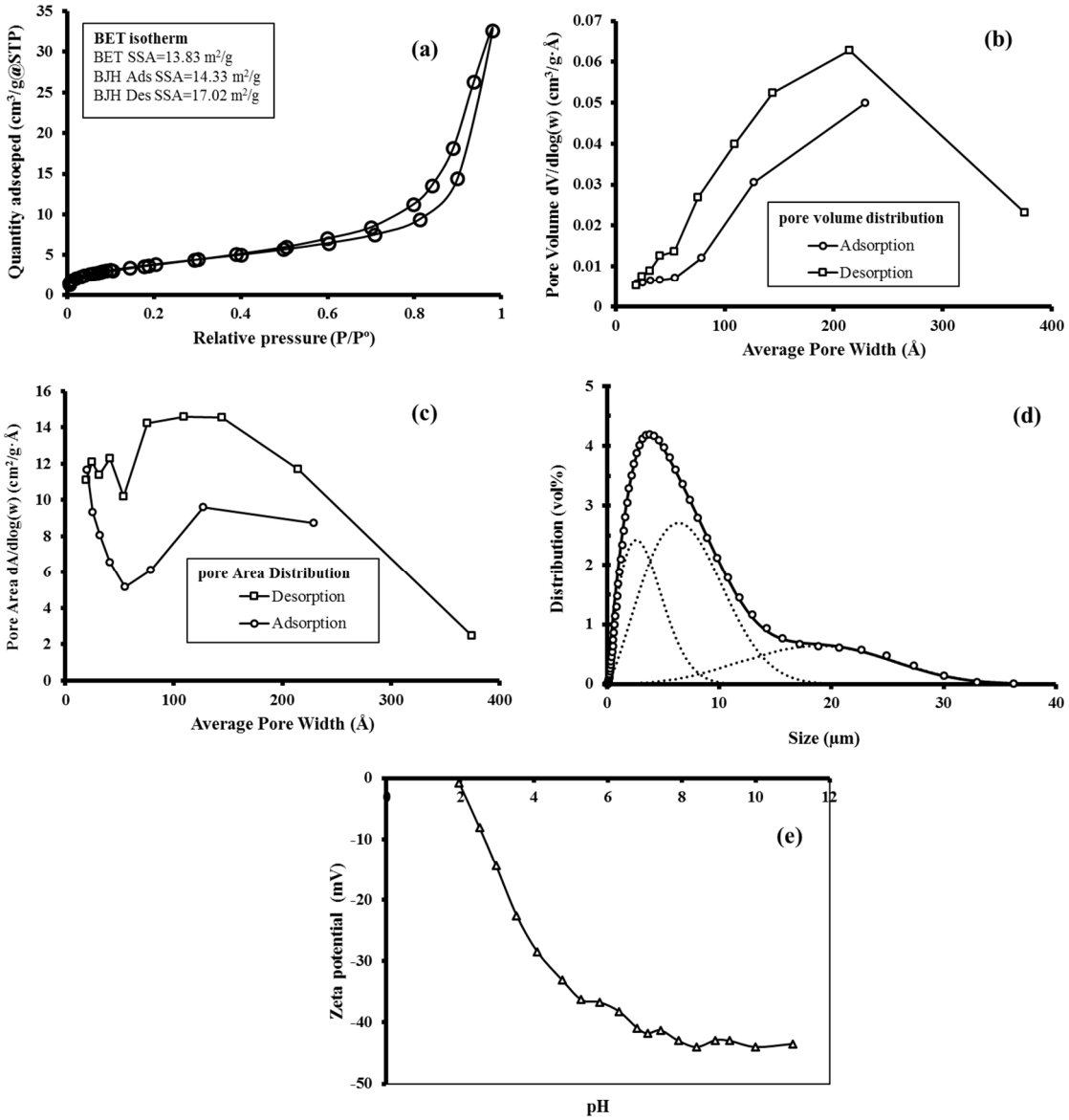

Fig. 11.1: Features of the starting milled powder: (a) BET isotherm and SSA values, (b) BJH mesopore volue distribution, (c) BJH mesopore area distribution, (d), particle size distribution in vol.%; (c) zeta potential.

This shows a small amount of monolayer coverage in the initial increase until it levels out at ~4 cm^3/g, followed by subsequent multilayer coverage, with the hysteresis loop being caused by capillary condensation in mesopores (between 20 and 500 Å, according to IUPAC). The BJH method can be used to extract information on meso– and macroporosity, and the BJH SSA values of 14.33 (adsorption) and 17.02 (desorption) m^2/g are approximately equal to the BET values.There is a difference between the adsorption and desorption values due to the hysteresis caused by capillary condensation in these pores. The calculated average meso/macropore size is 135.5 Å for adsorption and 115.9 Å for desorption, but much more information can be extracted from the BJH adsorption and desorption plots of pore volume and area.

The plot of pore volume distribution shows that the majority of the mesopore volume originates from pores between 50–380 Å in diameter **Fig. 11.1(b)**. However, an analysis of the pore area distribution **Fig. 11.1 (c)** indicates that while mesopores between ~50–300 Å contribute the bulk of the mesopore area, the smaller mesopores <50 Å also contribute a significant amount of the mesopore area, about 25% according to the cumulative pore area data. Such a fine pore distribution (<30 nm) will aid in the reduction of fluid uptake in the resulting glass paste for robocasting.

The powder density was used to calculate the solid loading (vol.%). For instance, a powder volume of 0.8 cm^3 (1.7984 g) will be required to prepare 2 ml of a paste containing 40 vol.%. The preparation of the inks and optimisation procedures were performed according to the outputs of our systematic previous study **[27]**.

The particle size distribution (PSD) for the powder after milling for 1 h is presented in **Fig. 11.1(d)**. It consists of a trimodal distribution, which is expected to enhance the powder packing ability in the suspension thereafter.

3.2. Rheological characterisation of suspensions and pastes

3.2.1. Zeta potential (ζ)

Zeta potential (ζ) is used to assess the electro kinetic forces between the particles at specific pH values. A zeta potential value greater than ± 30 mV is often deemed to be adequate for

obtaining a stable suspension **[31,32]**. The isoelectric point of the suspensions prepared from the powder was found to be near to pH ~2 as shown in **Fig. 11.1(e)**, which is complementary to the value disclosed for silica **[33]**. Further, it can be seen that increasing pH gradually enhances the electrostatic repulsion between the particles with absolute ζ values of ~ –44 mv within pH range between 8–11. The CMC molecules were reported to dissociate at pH >5.5 [**24**]. This means that at the natural pH of the concentrated suspensions (pH ~10.7) the specific adsorption of dissociated CMC species will enhance the intensity of electrostatic interactions.

3.2.2. Apparent Viscosity

The flow behaviour of the suspensions was determined in the rotational mode. The apparent viscosity curves *versus* shear rate of the suspensions with the different solid loadings (30, 35, and 40 vol.%) are presented in **Fig. 11.2(a)**. For all the systems, the apparent viscosity decreases with the increase in shear rate. This shear thinning behaviour is an imperative requirement for extrusion through fine nozzles. The high apparent viscosity values measured within the low shear rate range can be attributed to the structuring role of the dissolved and entangled CMC species significantly increase the intrinsic viscosity of the dispersing liquid. Such internal structures tend to gradually break down as shear rate increases. However, an increasing trend of apparent viscosity can be observed within the lowest shear rate range (0.1–0.2 s^{-1}) up to maximum values, particularly evident for the most concentrated suspension.

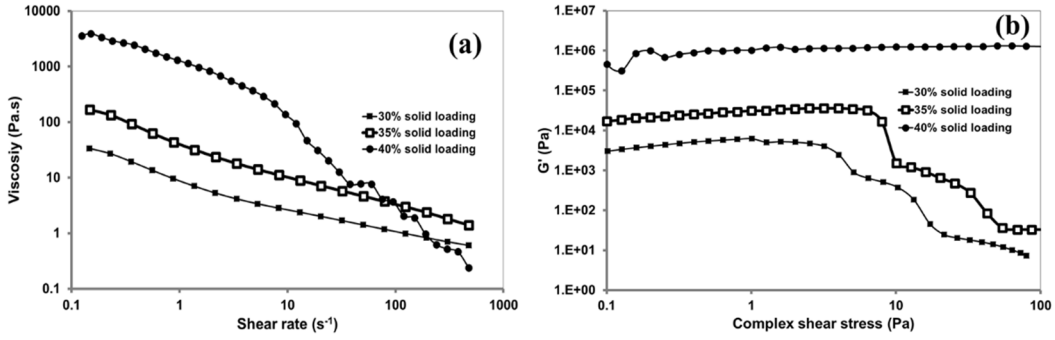

Fig. 11.2: Viscoelastic properties of the robocasting pastes with different solid loadings (30, 35, and 40 vol.%): (a) flow curves; (b) elastic modulus (G´) and extent of LVR as a function of complex shear stress.

This feature is typical of systems with yield stress, being a manifestation of the elastic component and commonly described as Zero–Shear–Viscosity (ZSV, or η_0). The shear thinning behaviour and the more accentuated elastic modulus of the ink with 40 vol.% suggest it as being the most suitable for printing.

3.2.3. Viscoelastic Properties

Rheological measurements under the oscillatory mode were used to assess the viscoelastic features of the inks containing different solid loading, and **Fig. 11.2(b)** displays their elastic modulus (G') as a function of complex shear stress. It can be seen that G' values sufficiently high for printing (G´~1 MPa) could be obtained for the most concentrated paste. Decreasing the solid loading from 40 to 35 vol.% caused a drop in G' of more than one order of magnitude. A further decrease to 30 vol.% led to an even greater decrease in G´ that became about 2.5 orders of magnitude lower in comparison to the most concentrated paste. Moreover, the 40 vol.% paste exhibits a continuous linear viscoelastic region (LVR) that expands beyond 100 Pa. The broad LVR, coupled with the high values of G´, are the main features required for ink printability **[18,24]**.

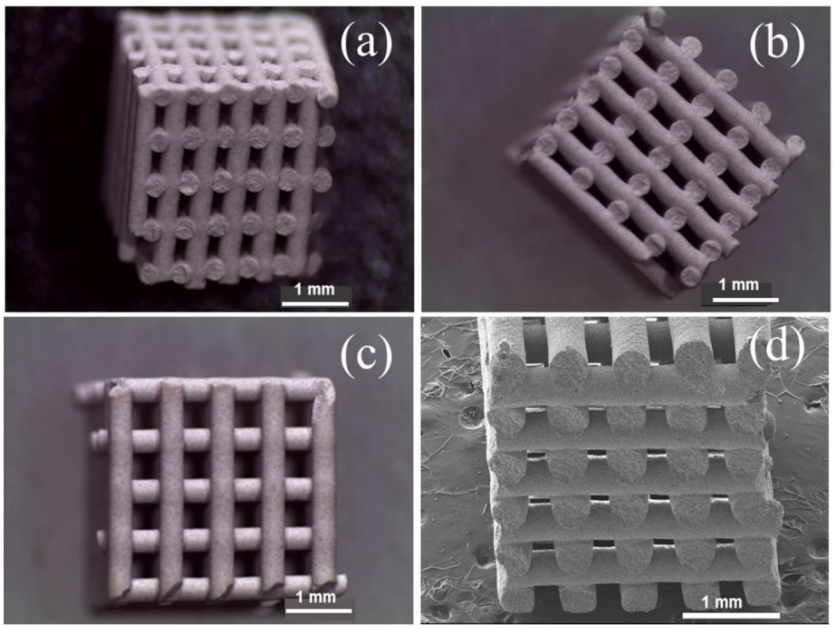

Fig. 11.3: Images of scaffolds with 300 µm macro pore size after sintering at 800 ºC. The images were captured by Leica optical microscope (a, b, c); and by SEM (d).

This means that the dissolved and entangled CMC species together with solid loading provide to the paste the stiffness and the viscoelastic properties required for extrusion and shape retention of the filaments during the robocasting process. Accordingly, scaffolds could be successfully printed from the most concentrated paste as illustrated in **Fig. 11.3**.

3.2.4 Sintering of scaffolds and dimensional changes

The dimensional variations of scaffolds upon drying and sintering could be estimated from the SEM micrographs. **Figs. 11.4(a–e)** displays some views of scaffolds with 300 μm pore size. The average diameter of the rods after sintering was reduced to ~383 μm (when considering the horizontal and vertical directions, see arrows in **Fig. 11.4**. Considering the inner nozzle diameter of 410 μm, there was an apparent overall shrinkage of about 6.6 %. On the other hand, the horizontal distances between rods seem to have decreased from the planned value in the CAD model (300 μm) to ~271.4 μm, corresponding to an apparent total shrinkage of 9.5 % **Fig. 11.4(b)**. This value might be overestimated as the rods' cross sections seem to have undergone small deviations from the normal circular shape, becoming somewhat elliptical with the main axis being in the horizontal direction. This vertical abatement is likely to be mostly driven by the layers' overlapping imposed in the CAD model, forcing layer beneath to slightly deform **Fig. 11.4(c)**, although some vertical creep due to the weight of the whole structure cannot be discarded. This hypothesis is supported by the overall height variations undergone by the 12 layers scaffold, which changed from ~3.850 mm after deposition to 3.419 mm after sintering, a reduction of ~11.2 % **Fig. 11.4(d)**. This compares with the overall width variations of the scaffold that changed from ~3.079 mm to ~2.872 mm, a reduction of only ~6.71 %. **Fig. 11.4(e)**. This reduction can only be attributed to shrinkage upon sintering. Therefore, the dimensions of scaffolds upon sintering changed from 3.08 x 3.08 x 3.85 mm (36.52 mm^3) to 2.87 x 2.87 x 3.42 mm (28.17 mm^3), an overall volume reduction of 22.9 %, corresponding to an average linear shrinkage of ~7.6 %. Considering that the depositing ink contains 40 vol.% solids, a total volume shrinkage of 60 vol.% would be expected if full densification has occurred and the stating material did not undergo any phase change upon sintering. This last hypothesis is reasonable as the temperature level was the same upon calcination the starting powder and sintering of the scaffolds. Based on these assumptions, a total micro–porosity volume fraction of ~37 %

would be expected in the sintered rods. When the Archimedes method was used to determine the apparent porosity of the sintered scaffolds, the average valued of six measurements was 46.70 ± 1.80%, i.e., ~10% above the maximum theoretical expected value. This means that excess water was left inside the scaffolds probably forming menisci between the macro–pores, misrepresenting their apparent porosity. Accordingly, bulky portions of the ink were let to dry, and then submitted to the same sintering schedule and to the same apparent porosity measurements as the scaffolds. The samples without any macro–pores exhibited an average apparent porosity of 36.10 ± 0.50%. This value is only slightly below to the theoretical expected one, meaning that only a small fraction of closed micro pores was left in the sintered scaffolds. This is an interesting feature as open micro pores also play important roles in biological activity **[34]**.

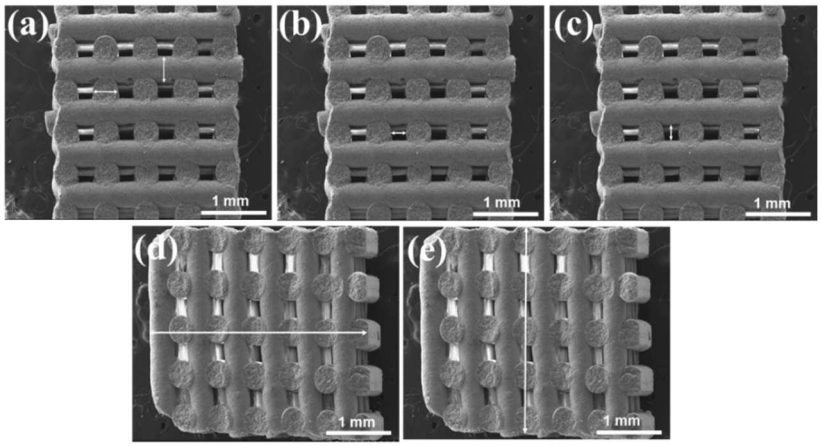

Fig. 11.4: SEM images of scaffolds with 300 µm macro pore size after sintering at 800 ºC, in which various measurements were made for: rod diameter (a); inter–rod diatances in both directions, horizontal (b) and vertical (c); overall height (d) and, the overall width of scaffold (e).

3.3. Mechanical Properties

Fig. 11.5 displays the compressive strength of the scaffolds with the three pore sizes (300, 400, and 500 µm), showing an expected decreasing trend as the pore size increases from 300 to 500 µm. The compressive strength for all the scaffolds varied between the limits of 2.45–4.95 MPa, which are within the range reported for human cancellous (trabecular) bone (2–12 MPa) **[35]**, with the lowest and the highest values being registered for the largest (500 µm) and smallest (300 µm) pore sizes, respectively. The compressive strength value of 4.95 MPa is superior to that reported for 45S5 scaffold (~4.5 MPa) with 300 µm pore size, after

sintering at 800 ºC **[17]**. However, for scaffolds with the same macro–pore size fabricated from FastOs® BG, an alkali–free bioactive glass composition prepared by melt quenching **Table 11.1**. In that case, the measured compressive strength for the same pore size (300 μm) was more than 5 time higher (~28 MPa) **[36]**. A fast bio–mineralization rate (with the formation of a surface hydroxyapatite layer being detected by XRD after immersion in SBF for 1 h) coupled with a full densification upon sintering at 800 ºC for 1 h, were other remarkable features of FastOs®BG. These features are certainly related to its lower network connectivity (Nc=1.94) **[37] Table 11.1**. Even significantly higher and seemingly exaggerated compressive strength values (~86 MPa) have been reported for scaffolds produced from the 13–39 glass with similar macro–pore size (300 μm) and sintered for 1 h at 700 ºC **[25]**. But in this case, the gains in mechanical properties are achieved in detriment of the bio–mineralization and degradation rates, consequences that are expected from the relatively high network connectivity (Nc=2.6) of the (13–93) glass **Table 11.1 [30]**.

3.4. Cytotoxicity assays

MTT cytotoxicity was evaluated for 7 days after seeding the MG63 cells onto scaffolds of the three different pore sizes (300, 400 and 500 μm). The results displayed in **Fig. 11.5(b)**, reveal that within the pore size range tested, pore size does not exert any significant influence on cell viability. The dashed line represents the cut–off of 30% of reduction of cell viability – according to ISO 10993–5, the test item is considered non–cytotoxic if the percentage of viable cells is equal to or greater than 70% of the untreated control **[28]**. Therefore, all of these scaffolds can be considered to be fully biocompatible with osteoblasts.

Similar results have been reported for other bioactive glass compositions presented in **Table 11.1**. The absence of cytotoxity towards MC3T3 osteoblasts was a common feature reported for scaffolds made from the Hench 45S5 Bioglass [38,39]; (13–93) when tested up to 144 h (6 days) in the presence of osteoblasts **[40]**; and Biosilicate® tested in the presence of osteoblasts up to 120 h **[41]**. However, to the authors' knowledge, no previous biocompatibility tests have been reported so far for scaffolds made of high silica/low sodium glasses as the one reported in this work.

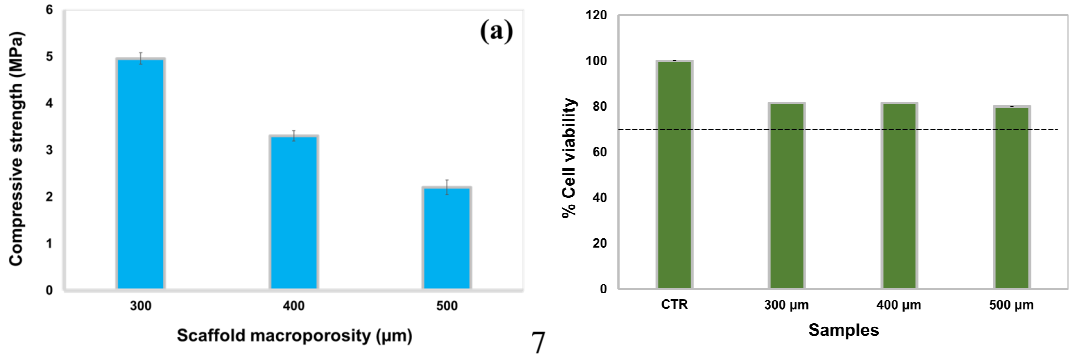

Fig. 11.5: Properties of the scaffolds with different macro pore sizes (300, 400, and 500 µm) sintered at 800 ºC: (a) Compressive strength; (b) In–vitro cell viability with MG63 osteoblasts after 7 days in comparison to the control. The dashed line shows the 70% limit for cytocompatibility.

3.5. Bio–mineralisation activity

As no significant difference in biocompatibility could be detected among the scaffolds of the three pore sizes, only the 300 µm ones were used in the bio–mineralization activity tests. **Fig. 11.6(a)** shows the pH changes along the entire 4 w immersion time period, which can roughly be divided in 4 stages (I–IV).

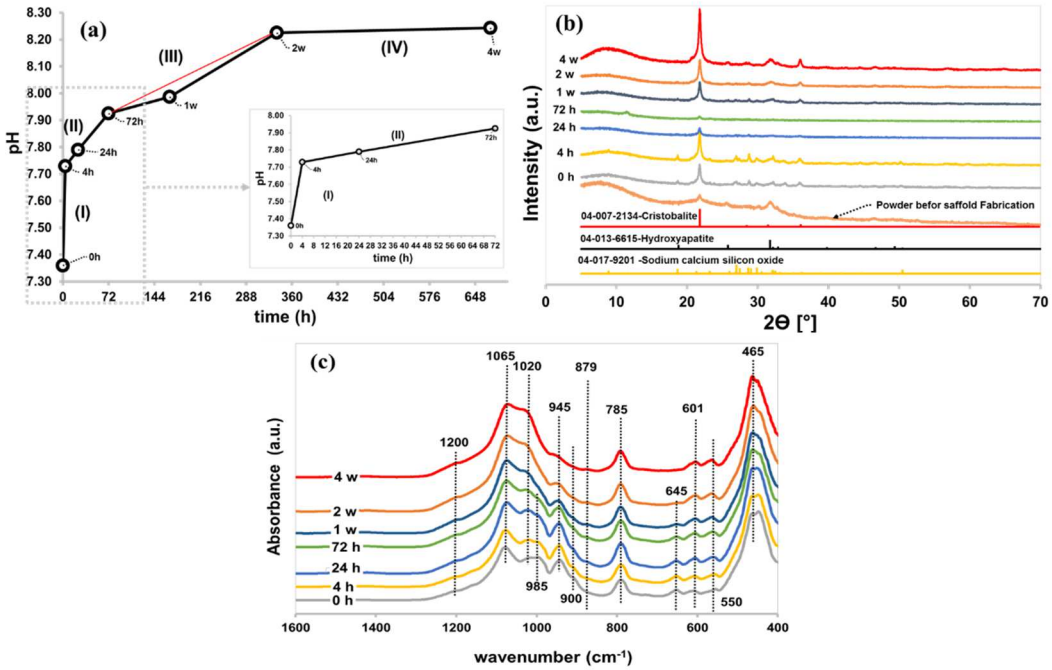

Fig. 11.6: Changes undergone in the SBF solution and at the surface of the scaffolds over the entire immersion period: (a) Evolution of pH through four stages; (b) XRD difractograms of the samples at different time points; (c) ATR–FTIR spectra at different time points.

A relatively sharp increase in pH occurred up to 4 h (stage I), which was then followed by gradually less steep paces along the remaining period of immersion. The pH variation rates (the change in pH divided by the elapsed time within each stage) over the stages I–IV were 1.93, 0.116, 0.031, and 0.024, respectively.

The increase in pH can be attributed to some preferential ionic (Na^+, Ca^{2+}) leaching from the scaffolds and to an equivalent uptake of H^+ ions by the solid for charge compensation, thus increasing the relative concentration of OH^- in the solution. With the gradual supersaturation of the SBF solution, there will be a trend for the excess species to precipitate onto the surface of the scaffolds. The deposited layer is likely to act as a barrier towards further dissolution, explaining the overall pH increasing rate with extending the immersion period. The apparent near horizontal trend observed between 2–4 w can be attributed to a more effective hindered dissolution due the increased thickness of deposited surface layer and to the partial depletion of the periphery of the particles in the more easily leachable species. **Fig. 11.6 (b)** displays the XRD patterns of the calcined powder and of the scaffolds before (0 h), and after being immersed in SBF for different periods of time.

The only difference observed between the calcined powder and the as sintered scaffolds is a small change in the peaks intensity, attributed to doubling the overall heat treatment time.

When calcined at 550 ºC, the same sol–gel powder revealed that an amorphous but high porosity structure **[28]**. However, such relatively high porosity hindered to prepare inks with solids loading higher than 25 vol.% **[28]**. To circumvent this shortcoming and get a good control over the suspension rheology, the sol–gel powder was here calcined at higher temperature (800 ºC), which induced the formation of 3 crystalline phases: sodium calcium silicate (PDF card # 04–012–6691), hydroxyapatite (PDF card # 04–013–6615) and silicon oxide (crystobalite) (PDF card # 04–007–2134). The relative intensities of the XRD peaks of these phases seemingly decreased after 24 h – 72 h of immersion in SBF. This can be attributed to their partial dissolution and most probably to the hiding effect exerted by the HAp layer precipitated onto the scaffolds' surface, which could be clearly identified after 2 weeks of immersion. With extending the immersion time to 4 w, the intensity of the peaks of cristobalite and HAp increased again, likely due to a gradual enhancement of layer thickness and or of their crystallinity.

Fig. 11.6 (c) presents the ATR–FTIR spectra for the scaffolds before (0 h) and after SBF immersion for different time periods. The major band observed between 850 cm^{-1}, and 1300 cm^{-1} is ascribed to the asymmetric stretching of the Si–O–Si vibrational mode **[42]**, composed of a high intensity peak centred at 1065 cm^{-1}, with shoulders at 1020 and 1200 cm^{-1}. The peak at 1065 cm^{-1} is assigned to a Si–O–Si stretching mode, and the two shoulders at 1020 cm^{-1} and 1200 cm^{-1} that are associated with Si–O–NBO (non–bridging oxygens) are also present in the spectra. Furthermore, the band at around 985 cm^{-1}, assigned to the asymmetric stretching of all NBOs, is also present **[43]** . The bands at 900–945 cm^{-1} can be assigned to Si–O–2NBO **[42]**. The low intensity absorption band at around 880 cm^{-1} is due to the formation of CO_3^{2-} functional group. The peak at 785 cm^{-1} is assigned to the Si–O– end group vibration **[44]**, and an additional peak observed at 645 cm^{-1} is attributed to a Si–H wagging vibrational mode **[45]**. Likewise, one of the most common vibrational modes for silica assigned to the rocking vibration for Si–O–Si **[45]** can be observed at 465 cm^{-1}. Moreover, two twin peaks at 550 and 601 cm^{-1}, along with the band at 945 cm^{-1}, are associated to the phosphate group. These three last bands confirm that calcium phosphate precipitation has occurred. This finding supports the formation of crystalline hydroxyapatite (HAp) **[46]**. The twin bands at 550 and 601 cm^{-1} are clearly less intense before immersion in SBF (0 h). Their intensity gradually increases with extending the immersion period, being well pronounced after 4 w of immersion.

Fig. 11.7 shows SEM images of the scaffolds taken before (0 h) and after immersion in SBF for different periods of time (72 h, 2 w, and 4 w). The printed and sintered scaffolds display a reasonable shape retention regarding the circular cross–sectional shape of the rods as displayed in **Figs. 11.7(a, b)**. Upon observing the surface of the rods under a higher magnification, their highly microporous structure is revealed, **Figs. 11.7(c, d)**. This incomplete densification can be attributed to some concurrent factors including the eventual presence of clusters of particles/agglomerates, consistent with a broad overall PSD **Fig. 11.1(a)**; and the partial crystallisation of the starting powder **Fig. 11.6(a)**. The atoms are less mobile when in the crystalline state, therefore less prone to bulk diffusion to promote densification. These results are very consistent with the apparent porosity data reported and discussed above.

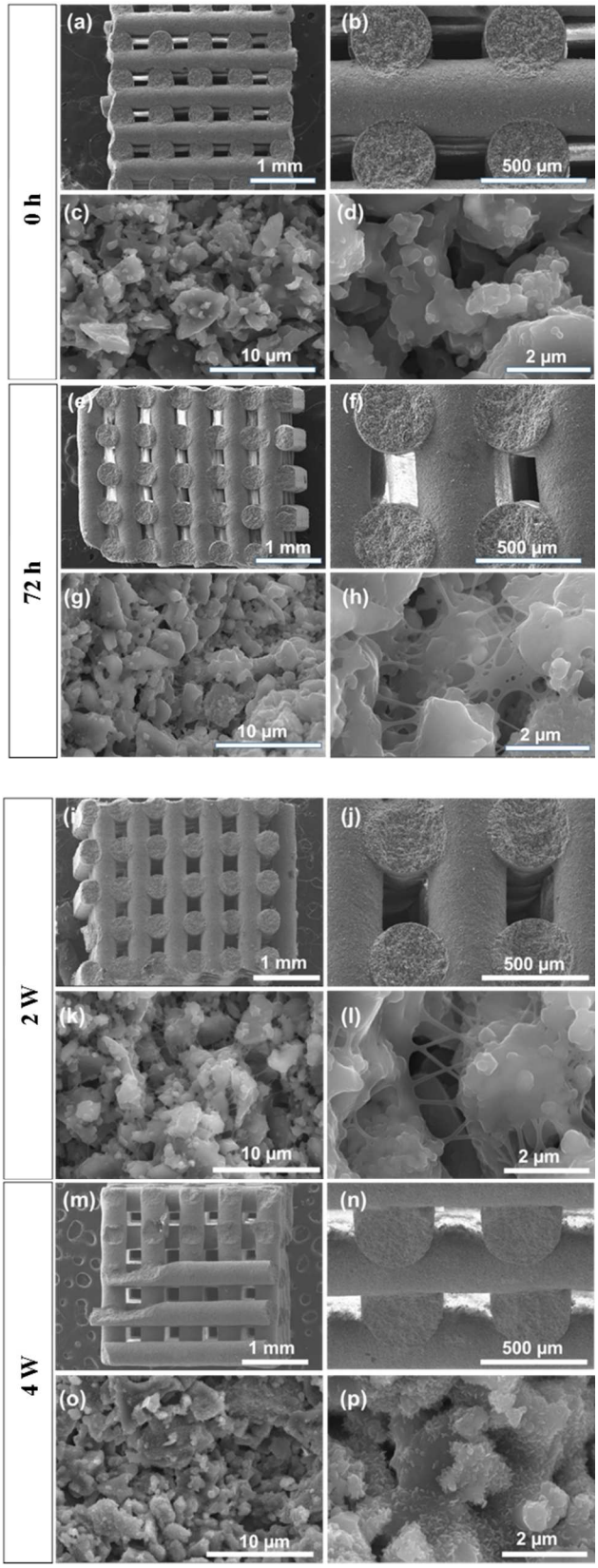

Fig.11.7: Structural and morphological features of the scaffolds with 300 µm macro pore size, before (a–d), and after immersion in SBF for different time periods: (e–h) 72 h; (i–l) 2 w; (m–p) 4 w.

Evident morphological surface modifications can be clearly observed after 72 h of immersion in SBF, **Figs. 11.7(g, h)**. The surface layer looks like a spider web when seen under the highest magnification, **Figs. 11.7(h)**, probably consisting of a mixed of silica gel and HAp. These features become more pronounced after 2 w of immersion, as shown in **Figs. 11.7(k, l**). With further extending the immersion period up to 4 w, the density of the formed clusters increased and their morphology becomes gradually more consistent with an enrichment in HAp hiding the previously formed formation spider web structures, **Figs. 11.7(o, p)**.

4. Conclusions

The fabrication of 3D scaffolds from sol–gel derived glass is here reported for the first time. An easy fast sol–gel synthesis and drying route was followed, which takes only 1.5 h for overall procedure, plus 1 h for milling, after calcination. The results presented and discussed enable the following conclusions to be drawn:

1. A calcination temperature of 800 ºC is required for obtaining a powder with a small fraction of fine pores (mesopores <30 nm) to reduce the uptake of the dispersing liquid and prevent an exaggerated specific surface area to be exposed to the liquid media, and achieve a relatively high solids loading in the printing inks;
2. Another important requirement is the achievement of a suitable particle size distribution upon milling to facilitate the particles' packing in the suspensions/pastes prepared thereof. This requirement was accomplished by using a simple milling equipment within just 1 h, a much shorter time period in comparison to those reported in other works about the milling of powders using sophisticated milling facilities;
3. The sol–gel derived glass powder undergoes partial crystallization upon the overall heat treatment (calcination and sintering schedules) that hinders extensive densification to occur upon sintering; leaving an expressive fraction (~36%) of open micro–porosity in the sintered rods. Although such micro–porosity level limits the compressive strength of the scaffolds (~5 MPa for the 300 μm macro–pore size), it is likely enhance the *in vitro* and *in vivo* performances of the constructs in bone regeneration and tissue engineering applications;
4. The *in vitro* bioactivity assessment by immersion in SBF revealed the occurrence of extensive surface transformations illustrated by: (i) pH changes through four successive stages but at gradually lower rates with time increasing; (ii) the appearance of a spider web–like surface layer after 72 h, likely formed by a mixed silica–gel and HAp composition, the thickness of which increased and its morphology changed with further extending the immersion time;
5. The scaffolds did not show any cytotoxicity towards osteoblasts, making them promising candidates for bone regeneration and tissue engineering applications.

Acknowledgments

R.C. Pullar wishes to thank the FCT Grant IF/00681/2015 for supporting this work. B. A. E. Ben–Arfa thanks FCT grant BIONANOSCULP PTDC/EPH–PAT/6281/2014 for supporting him during this work. This work was developed in the scope of the project CICECO–Aveiro Institute of Materials (Ref. FCT UID /CTM /50011/2013), financed by national funds through the FCT/MEC and when applicable co–financed by FEDER under the PT2020 Partnership Agreement.

References

[1] L.L. Hench, The story of Bioglass, J. Mater. Sci. Mater. Med. 17 (2006) 967–978.

[2] J.M.F. Ferreira, The key Features expected from a Perfect Bioactive Glass –How Far we still are from an Ideal Composition?, Biomed. J. Sci. Tech. Res. 1 (2017) 4–7.

[3] J.R. Jones, Review of bioactive glass : From Hench to hybrids, Acta Biomater. 9 (2013) 4457–4486.

[4] S.Y. Moustafa, M.R. Sahar, S.K. Ghoshal, Comprehensive thermal and structural characterization of antimony–phosphate glass, Results Phys. 7 (2017) 1396–1411.

[5] R. Li, A.E. Clark, L.L. Hench, An Investigation of Bioactive Glass Powders by Sol–Gel Processing, J. Appl. Biomater. 2 (1991) 231–239.

[6] B.P. Chan, K.W. Leong, Scaffolding in tissue engineering : general approaches and tissue–specific considerations, Eur. Spine J. 17 (2008) S467–S479.

[7] F.J. O'Brien, Biomaterials & scaffolds for tissue engineering, Mater. Today. 14 (2011) 88–95.

[8] M. Houmard, Q. Fu, E. Saiz, A.P. Tomsia, Sol – gel method to fabricate CaP scaffolds by robocasting for tissue engineering, J. Mater Sci Mater Med. 23 (2012) 921–930.

[9] J.M. Karp, P.D. Dalton, M.S. Shoichet, F. Cahn, Scaffolds for tissue engineering, clinical use of porous scaffolds for tissue engineering of skin, MRS Bull. (2003) 301–306.

[10] P.S. Lui, G.F. Chen, Porous materials, Elsevier Inc., Oxford, 2014.

[11] A. Barbetta, A. Carrino, M. Costantini, M. Dentini, Polysaccharide based scaffolds obtained by freezing the external phase of gas–in–liquid foams, Soft Matter. 6 (2010) 5213.

[12] L.M. Rodrıguez–Lorenzo, M. Vallet–Regı, J.M.F. Ferreira, Fabrication of porous hydroxyapatite bodies by a new direct consolidation method : starch consolidation, J. Biomed. Mater. Res. 60 (2002) 232–240.

[13] S. Deville, E. Saiz, A.P. Tomsia, Freeze casting of hydroxyapatite scaffolds for bone tissue engineering, Biomaterials. 27 (2006) 5480–5489.

[14] S.–I. Roohani–Esfahani, P. Newman, H. Zreiqat, Design and Fabrication of 3D printed Scaffolds with a Mechanical Strength Comparable to Cortical Bone to Repair Large Bone Defects, Sci. Rep. 6 (2016) 1–8.

[15] F.J. Martínez–Vázquez, P. Miranda, F. Guiberteau, A. Pajares, Reinforcing bioceramic scaffolds with in situ synthesized ε–polycaprolactone coatings, J. Biomed. Mater. Res. – Part A. 101A (2013) 3551–3559.

[16] R.C. Richard, R.N. Oliveira, G.D.A. Soares, R.M.S.M. Thir??, Direct–write assembly of 3D scaffolds using colloidal calcium phosphates inks, Rev. Mater. 19 (2014) 61–67.

[17] S. Eqtesadi, A. Motealleh, P. Miranda, A. Pajares, A. Lemos, J.M.F. Ferreira, Robocasting of 45S5 bioactive glass scaffolds for bone tissue engineering, J. Eur. Ceram. Soc. 34 (2014) 107–118.

[18] E. Feilden, E. García–tu, F. Giuliani, E. Saiz, L. Vandeperre, Robocasting of structural ceramic parts with hydrogel inks, J. Eur. Ceram. Soc. 36 (2016) 2525–2533.

[19] P. Miranda, A. Pajares, E. Saiz, A.P. Tomsia, F. Guiberteau, Mechanical properties of calcium phosphate scaffolds fabricated by robocasting, J. Biomed. Res. Part A. 85 (2008) 218–227.

[20] R.C. Richard, M.S. Sader, J. Dai, R.M.S.M. Thiré, G.D.A. Soares, Beta–type calcium phosphates with and without magnesium: From hydrolysis of brushite powder to robocasting of periodic scaffolds, J. Biomed. Mater. Res. – Part A. 102 (2014) 3685–3692.

[21] Y. Maazouz, E.B. Montufar, J. Guillem–Marti, I. Fleps, C. Öhman, C. Persson, et al., Robocasting of biomimetic hydroxyapatite scaffolds using self–setting inks, J. Mater. Chem. B. 2 (2014) 5378–5386.

[22] E. Feilden, C. Ferraro, Q. Zhang, E. García–Tuñón, E. D'Elia, F. Giuliani, et al., 3D Printing Bioinspired Ceramic Composites, Sci. Rep. 7 (2017) 1–9.

[23] A.P.T. J. Russias, E. Saiz, S. Deville, K. Gryn, G. Liu, R.K. Nalla, Fabrication and in vitro characterization of three– dimensional organic/inorganic scaffolds by robocasting, J. Biomed. Mater. Res. Part A. 38A (2006) 434–445.

[24] S. Eqtesadi, A. Motealleh, P. Miranda, A. Lemos, A. Rebelo, J.M.F. Ferreira, A simple recipe for direct writing complex 45S5 Bioglass®3D scaffolds, Mater. Lett. 93 (2013) 68–71.

[25] X. Liu, M.N. Rahaman, G.E. Hilmas, B.S. Bal, Mechanical properties of bioactive glass (13–93) scaffolds fabricated by robotic deposition for structural bone repair, Acta Biomater. 9 (2013) 7025–7034.

[26] A.A. Nommeots–nomm, P.D. Lee, R. Julian, Direct ink writing of highly bioactive glasses, J. Eur. Ceram. Soc. 38 (2018) 837–844.

[27] B.A.E. Ben–arfa, A.S. Neto, I.M.M. Salvado, R.C. Pullar, J.M.F. Ferreira, Robocasting : Prediction of ink printability in solgel bioactive glass, Accepted (2018) 1–11.

[28] B.A.E. Ben–arfa, I.M.M. Salvado, J.M.F. Ferreira, R.C. Pullar, Enhanced bioactivity of a rapidly–dried sol–gel derived quaternary bioglass, Mater. Sci. Eng. C. 91 (2018) 36–43.

[29] International Organization for Standardization, International Organization for Standardization (2009) ISO 10993–5. Biological evaluation of medical devices— part 5: tests for in vitro cytotoxicity. ISO, Geneve, 2009.

[30] A.L.B. Maçon, T.B. Kim, E.M. Valliant, K. Goetschius, R.K. Brow, D.E. Day, et al., A unified in vitro evaluation for apatite–forming ability of bioactive glasses and their variants, J. Mater. Sci. Mater. Med. 26 (2015) 1–10.

[31] S.N. Kazi, A. Badarudin, M. Nashrul, M. Zubir, H.N. Ming, M. Misran, Investigation on the use of graphene oxide as novel surfactant to stabilize weakly charged graphene nanoplatelets, Nanoscale Res. Lett. 10 (2015) 1–15.

[32] D. Sun, S. Kang, C. Liu, Q. Lu, L. Cui, B. Hu, Effect of Zeta Potential and Particle Size on the Stability of SiO 2 Nanospheres as Carrier for Ultrasound Imaging Contrast Agents, Int. J. Electrochem. Sci. 11 (2016) 8520–8529.

[33] R.K. Iler, The chemistry of silica solubility, polymerization, colloid and surface properties, and biochemistry, John Wiley & sons, Toronto, 1978.

[34] K. Zhang, Y. Fan, N. Dunne, X. Li, Effect of microporosity on scaffolds for bone tissue engineering, Regen. Biomater. (2018) 115–124.

[35] D.R. Carter, G.H. Schwab, D.M. Spengler, Tensile fracture of cancellous bone, Acta Orthop. Scand. 51 (1980) 733–741.

[36] S.M. Olhero, H.R. Fernandes, C.F. Marques, B.C.G. Silva, J.M.F. Ferreira, Additive manufacturing of 3D porous alkali–free bioactive glass scaffolds for healthcare applications, J. Mater. Sci. 52 (2017) 12079–12088.

[37] A. Goel, S. Kapoor, A. Tilocca, R. Rajagopal, Structural role of zinc in biodegradation of alkali–free bioactive glasses, J. Mater. Chem. B. 1 (2013) 3073–3082.

[38] L.L. Hench, I.D. Xynos, J.M. Polak, Bioactive glasses for in situ tissue regeneration, J. Biomater. Sci. Polym. Ed. 15 (2004) 543–562.

[39] P.S.P. Poh, D.W. Hutmacher, M.M. Stevens, M.A. Woodruff, Corrigendum: Fabrication and in vitro characterization of bioactive glass composite scaffolds for bone regeneration, Biofabrication. 6 (2014) 029501.

[40] P.R. Gabbai–Armelin, M.T. Souza, H.W. Kido, C.R. Tim, P.S. Bossini, K.R. Fernandes, et al., Characterization and biocompatibility of a fibrous glassy scaffold, J. Tissue Eng. Regen. Med. 11 (2017) 1141–1151.

[41] H.W. Kido, P. Oliveira, N.A. Parizotto, M.C. Crovace, E.D. Zanotto, O. Peitl–Filho, et al., Histopathological, cytotoxicity and genotoxicity evaluation of Biosilicate® glass–ceramic scaffolds, J. Biomed. Mater. Res. – Part A. 101 A (2013) 667–673.

[42] H. Aguiar, J. Serra, P. González, B. León, Structural study of sol–gel silicate glasses by IR and Raman spectroscopies, J. Non. Cryst. Solids. 355 (2009) 475–480.

[43] N. Zotov, M. Marinov, L. Konstantinov, Degree of structural disorder in sodium metasilicate glass: Model for Raman spectra, J. Non. Cryst. Solids. 197 (1996) 179–191.

[44] C. Gautam, A.K. Yadav, A.K. Singh, A Review on Infrared Spectroscopy of Borate Glasses with Effects of Different Additives, ISRN Ceram. 2012 (2012) 1–17.

[45] D.E. Vázquez–valerdi, J.A. Luna–lópez, J. Carrillo–lópez, G. García–salgado, A. Benítez–lara, N.D. Espinosa–torres, Compositional and optical properties of SiO x films and (SiO x / SiO y) junctions deposited by HFCVD, Nanoscale Res. Lett. 9 (2014) 1–8.

[46] P. Sooksaen, N. Pengsuwan, S. Karawatthanaworrakul, S. Pianpraditkul, Formation of porous apatite layer during in vitro study of hydroxyapatite–AW based glass composites, Adv. Condens. Matter Phys. 2015 (2015) 1–10.

[47] D. Groh, F. Döhler, D.S. Brauer, Bioactive glasses with improved processing . Part 1 . Thermal properties , ion release and apatite formation, Acta Biomater. 10 (2014) 4465–4473.

[48] A. Goel, S. Kapoor, R. Raman, M.J. Pascual, H. Kim, J.M.F. Ferreira, Alkali–free bioactive glasses for bone tissue engineering : A preliminary investigation, Acta Biomater. 8 (2012) 361–372.

Chapter 12

The present chapter was published on:
Acta Biomaterialia;
2019,
(Online)
Doi: 10.1016/j.actbio.2019.01.048

Robocasting of Cu^{2+} & La^{3+} doped sol–gel glass scaffolds with enhanced mechanical properties

Basam A. E. Ben–Arfa , Sofia Neto, Isabel M. Miranda Salvado *, Robert C. Pullar *, and José M. F. Ferreira [a]

Department of Materials and Ceramic Engineering / CICECO – Aveiro Institute of Materials, University of Aveiro, 3810–193 Aveiro, Portugal

*To whom correspondence should be addressed: isabelmsalvado@ua.pt, rpullar@ua.pt

Keywords: Sol–gel; Sol–gel; Bioactive glass; Compressive strength; Particle size ; Particle size distribution; Lanthanum ions; Copper ions.

Abstract

This research details the successful fabrication of scaffolds by robocasting from sol–gel high silica glass doped with Cu^{2+} or La^{3+}. The parent glass was doped with 5 wt.% of Cu^{2+} or La^{3+} (Cu5 and La5). The paper sheds light on the importance of Cu^{2+} and La^{3+} in improving the mechanical properties of the 3D printed scaffolds. 1 h wet milling was sufficient to obtain a glass powder ready to be used in the preparation a 40 vol.% solid loading paste suitable for printing. Moreover, Cu5 glass showed a small reduction in the mean particle size, while La5 glass exhibited a greater reduction, compared with the parent glass. Scaffolds with macroporosity between 300–500 µm were successfully printed by robocasting, and then sintered at 800 ºC. A small improvement in the compressive strength (7–18%) over the parent glass) accompanied the addition of La. However, a much greater improvement in the compressive strength was observed in Cu5 up to 221% greater than the parent glass, with compressive strength values of up to ~14 MPa. This enhancement in compressive strength, approaching the upper limit registered for human cancellous bones, supports the potential use of this material in biomedical applications.

Keywords: Sol–gel; Bioactive glass; Compressive strength; Particle size ; Particle size distribution; Lanthanum ions; Copper ions.

** Communicating authors: isabelmsalvado@ua.pt, rpullar@ua.pt*

1. Introduction

Bioactive glasses demonstrate high degrees of rapid response to body fluids and encourage new cell growth, both *in–vitro* and *in–vivo*. However, they also typically have weak mechanical properties **[1]**. There exist many functional ions that although existing in trace quantities in human body play important different roles and are vital for a good body metabolism. Doping a bioactive glass with some of these functional ions in trace quantities has also been shown to improve their properties **[2]**.

Copper (Cu) is found throughout the tissues of the human body in total trace quantities of ~75–100 mg. Of this quantity, 50% of the Cu is stored in the muscles and bones **[3]**. Cu is also a vital component in gene–expression **[4]**, and since it serves as a cofactor **[5]**, Cu aids about 30 enzymes to provide the proper function **[6]**. Cu works as an antioxidant preventing free radicals from damaging the walls of cells. Moreover, Cu is an essential element for keeping blood vessels, connective tissues and skin in a healthy condition **[6]**. Cu deficiency may lead to inappropriate bone formation, as well as fracture of the bones, particularly in children. In patients with bone fractures, it is found that Cu–supplements reduce the healing time **[7]**. Much work has been carried out on doping Cu in bioactive glasses and composites for biomedical applications. For example, in a composite of poly methyl methacrylate (PMMA) and Cu–doped glass, the system showed good bioactivity, and antibacterial action towards staphylococcus epidermidis **[2]** and Escherichia coli **[8]**. Borate glass doped with copper showed promising results in healing full–thickness skin wounds **[9]**, and it was found that, the inclusion of Cu in bioactive glass increases vascularisation and augments bone formation **[10]**.

Lanthanum (La) is a rare earth element, which has no biological role in humans, and its bioavailability in the human body is extremely low, at 0.00127% (± 0.00080%) **[11]**. Commonly La does not exist in the animal and plants tissue; nevertheless, it is found in traces in drinking water **[12]**, and in elevated quantities (up to 16 times higher than nonexposed controls), with amounts (~0.5 μg g^{-1}) in bones and lungs of refinery and smeltery workers **[13]**. Despite this, it has a wide range of applications in treatments to repair disorders in the human body, such as playing an important role in treating atherosclerotic cardiovascular disease when taken as a lanthanum chloride supplement **[14]**. Furthermore, if taken as supplement in the form of lanthanum carbonate it can partially replace the

calcium–based phosphate which occurs in hypercalcemia, leading to cardiovascular calcification **[12]**, or the case of hyperphosphatemia in patients with end stage renal disease (ESRD) **[15]**.

Adding trace amounts of La to 45S5 glass (up to 0.5 wt.%) resulted in improved bioactivity, while beyond this value La retarded the bioactivity of bioglass® **[16]**. There is much evidence to suggest that lanthanum tends to deposit in bone, and addition of La^{3+} ions demonstrated a pronounced enhancement of *in–vitro* osteoblast differentiation **[17]**. Treatment of titanium surfaces with La, implanted in both rats and rabbits, led to increases in protein adsorption, resulting in an improved healing response of the bone **[18]**, and in hydroxyapatite (HAp)–La composites, better mechanical properties were observed than when using pure HAp in bone implants **[19]**.

Therefore, it is interesting to look at the effects of these two additives on sol–gel derived bioglasses, and fabricated glass or glass–ceramic scaffolds. Literature review reveals that no Cu and/or La doped glasses have been used so far as precursors to produce 3–D scaffolds by robocasting. Sol–gel derived glasses have many advantages (lower sintering temperatures, more intimate mixing of components, greater porosity), but the inherent porosity of sol–gel derived glass powders causes problems during preparation of robocasting pastes, as their high level of porosity can adsorb liquid from the pastes affecting viscosity and flow behaviour during printing. The authors have addressed the problem previously in a Ca–Si–P–Na based 4 component sol–gel glass system **[20]**.

A scaffold is a 3–D structure constructed to be a temporary implant, acting as a template for new cell growth, and which degrades during/after the healing process, while the seeded cells grow and proliferate to regenerate new tissue **[21]**. Scaffolds need to meet particular morphological requirements: they need to have large interconnected pores and a hierarchical degree of porosity, requiring macro–pore sizes >50 μm to enable cells to easily penetrate the scaffold structure, and micro pore sizes <50 μm to facilitate cell anchorage and proliferation. They must also exhibit moderate mechanical strength to resist any applied loads, while avoiding the effect of stress shielding that can result in bone loss **[22,23]**. A large degree of macro–sized interconnectivity is a crucial element to enable cells to migrate into to the centre of the scaffold, and to allow a sufficient supply of nutrients for cell growth **[23]**. Robocasting offers a better control of the macro–pore shape and size, as well as the

possibility to produce customized implants for an individual patient. The robotic control of the ink deposition also enables the assembling of specific predesigned complex shapes and morphologies to replace the defect part of a bone in a very precise manner, using CAD–CAM technology **[24]**.

Very little work has been carried out regarding the robocasting of bioactive glass fabricated by melt–quenching method for 3–D scaffolds **[25,26]**, while the use of sol–gel glass is still a new field for robocasting, the author's being pioneers in this area. To the authors' knowledge, there have been no previous investigations into the use of doped sol–gel bioactive glass as precursors to fabricate 3–D scaffolds by robocasting. This work is devoted to improving the mechanical properties, with copper or lanthanum additives, of quaternary–system, high–silica content bioactive sol–gel derived glass scaffolds made by robocasting.

2. Materials and methods

2.1. Sol–gel glass synthesis

A four–component high silica sol–gel bioactive glass with a composition of $67SiO_2$–$24CaO$–$5Na_2O$–$2P_2O_5$ [= (67% Si – 24% Ca – 5% Na – 4% P) mol%], thereafter labelled HSSGG, was synthesized by employing a rapid sol–gel route, as described previously by the authors **[27]**.

Tetra–ethyl–ortho–silicate (TEOS, $C_8H_{20}O_4Si$, 98%), triethyl phosphate (TEP, $C_6H_{15}O_4P$, ≥99.8%), calcium nitrate tetrahydrate (CaN, $Ca(NO_3)_2{\cdot}4H_2O$, ≥99%), sodium nitrate (NaN, $NaNO_3$, ≥99%), Copper(II) nitrate trihydrate (CuN, $Cu(NO_3)_2{\cdot}3H_2O$, ≥99%), and Lanthanum(III) nitrate hexahydrate (LaN, $La(NO_3)_3{\cdot}6H_2O$, ≥99.9%) were used as precursors. All six precursors were supplied from Sigma–Aldrich. Distilled water was used as solvent and citric acid monohydrate (CA, $C_6H_8O_7{\cdot}H_2O$, 99.5–102%, Sigma–Aldrich) was added to catalyse the sol–gel hydration and polymerization reactions.

The two doped glasses containing 5 wt.% each of either La^{3+} or Cu^{2+} ions were prepared based on the parent (HSSGG) glass composition following the synthesis methods employed in our previous work. The Cu or La precursors were added to the homogeneous sols obtained according to the procedures described previously by the authors **[27]** to study their separate

influence on the scaffold printing ability, and on the corresponding mechanical properties of the sintered scaffolds. The doped glass compositions are hereafter designated as Cu5 and La5. The batch compositions (in both wt.% and mol%) are presented in **Table 12.1**.

Table 12.1: Batch compositions of all synthesized glasses in mol %, and wt.%

Glass	Si		Na		Ca		P		Cu		La	
	wt.%	mol %	wt.%	mol %	wt.%	mol%	wt.%	mol%	wt.%	mol%	wt.%	mol%
HSSGGG	67.00	64.40	5	4.97	24.00	21.53	4.00	9.10	0.00	0.00	0.00	0
Cu5	64.34	61.18	4.80	4.72	23.05	20.45	3.84	8.64	3.97	5.00	0.00	0
La5	66.33	61.18	4.95	4.72	23.76	20.45	3.96	8.64	0.00	0.00	1	5.00

2.2. Wet milling procedure

The acquired gels were dried by means of roto–evaporator (Buchi 210 Rotavapor with V–850 vacuum controller and V–700 diaphragm vacuum pump), in a 500 mL pear–shaped flask while rotating in a water bath at 55 ºC and under a low pressure of 50 mbar for 30 minutes. The as–dried gels were heat treated up to 800 ºC using the following regime: From room temperature to 200 ºC with heating rate of 1 ºC min^{-1} and soaking time of 30 min; followed by increasing the temperature to 400 ºC with a heating rate of 2 ºC min^{-1} and soaking time of 30 min; and from 400 to 800 ºC with heating rate of 5 ºC, and soaking time of 2 h, to be followed by natural cooling to room temperature.

The heat treated powders were pulverized using wet ball milling. Ethanol (EtOH) served as a milling medium, EtOH to powder mass ratio (EPR) = 1.5, balls to powder mass ratio (BPR) = 10, and 1 h milling time. The milling was performed in a S–series–Fast Mill machine, type S2–1000 (Ceramic Instruments, Sassuolo, Italy), with a rotational speed of 390 rpm, using 300 cm^3 capacity alumina jar (Ceramic instruments Sassuolo, Italy). 10 mm diameter Yttria–stabilized zirconia balls (Tosoh, Tokyo, Japan), were used as milling medium. After milling, the obtained slurry was separated for drying in an oven at 60 ºC for 24 h. The dry powders were passed through a 63 µm sieve to separate the large agglomerates from the fine powder. The fine powder was characterized using the following techniques:

2.3. Characterization of the milled powder

Particle size (PS) and the particle size volume distribution (PSD) were investigated using a laser diffraction particle size analyser (Coulter LS particle size analyser; Beckman Coulter, CA). Measurements were triplicated to guarantee accurate results. The effects of ion doping on the polymerization silica networks were assessed by magic angle spinning–magnetic nuclear resonance (MAS–NMR) for ^{29}Si NMR environment.

2.4. Suspension preparation

To study the effects of the dopants on the rheological properties and printability of the inks, suspensions were prepared from the three glass powders at a solid loading fraction of (40 vol.%). The powder was dispersed in de–ionized water in the presence of 1.1 wt.% carboxymethyl cellulose (CMC) (Mw = 250,000, Lamberti Iberia s.a.u., Castellón, Spain). CMC serves as a multipurpose processing additive (dispersant, binder and gelation agent) **[28]**. The powder was added in small dosages, followed by mixing in a planetary centrifugal mixer (ARE–250, Thinky Corp. Tokyo, Japan) to assure a homogeneous suspension.

2.5. Rheological characterisation of suspensions and pastes

The rheological properties of the suspensions were evaluated using a Kinexus Pro+ Rheometer (Malvern Instruments). The viscometry mode was used to measure the apparent viscosity of the tested samples, using the cone (4°/40 mm) and plate sensor system with a 150 µm gap size. The viscoelastic properties of the pastes were measured using the oscillatory mode of the rheometer equipped with plate & plate sensor (20 mm), with 1 mm gap size. In all rheological measurements, a metal ring with deionized water as solvent trap was used to prevent water evaporation from the samples while testing.

2.6. Fabrication of scaffolds by robocasting

The bioactive glass scaffolds were deposited layer–by–layer using robocasting equipment (3D Inks, Stillwater, OK). The paste was extruded through a 410 µm diameter nozzle using a printing speed of 10 mm s^{-1}. The designed scaffold was constructed from 12 deposited

layers, each layer consisting of 5 parallel rods, and with the next layer perpendicular to the plane of the rods. The porous structures were printed in assemblies containing nine scaffolds, with three different pore sizes (the distance between the rods) of 300, 400 and 500 μm, all with dimensions of (3*x*3*x*4) mm. The deposition was carried out in a reservoir containing paraffin oil to allow a uniform drying of the green scaffolds. After printing completion, the scaffolds were removed from the oil and dried at room temperature for 24 h, followed by sintering at 800 ºC for 2 h, using a heating rate of 1ºC min^{-1} for the entire heating cycle, to ensure a complete removal of residual organics.

2.7. Compressive strength evaluation

The compressive strength of sintered scaffolds was determined under uniaxial tests using 10 samples of each pore size series (300, 400, and 500 μm). The tests were carried on a universal testing machine (AG–IS10kN, Shimadzu, Kyoto, Japan) at a constant speed of 0.5 mm min^{-1} in the perpendicular direction to the printing plane.

3. Results and Discussion

3.1. The effects of ion doping on particle size distribution

Figs. 12.1(a,b,c) show particle sizes distributions for HSSGG, Cu5 and La5 glasses, respectively. The effects of each individual doping ion on PSD were evaluated. As can be observed from **Fig. 12.1**, all PSDs exhibit 3–modal profiles. HSSGG shows larger particle sizes **Fig. 12.1(a)** than the two doped glasses. A decrease in the particle size was observed for Cu5 **Fig. 12.1(b)**, and a further decrease in particle size was observed in La5 **Fig. 12.1(c)**. Moreover, the area of the 3rd fitted peak in PSD, representing the coarser fraction is getting gradually smaller and the modal sizes gradually shift from ~19 μm to ~14 μm (Cu5) and to ~11 μm (La5). The ionic radius of Cu (0.73 Å) is much smaller than that of La (1.06 Å) **[29]**.

The difference in ionic radii of metal (M) cations is likely to affect the average coordination number with oxygen atoms and the M–O bond length and strength, even in an amorphous structure that is more compliant than a crystalline one. This is to say that the possible role of ionic radius on the easiness of particle size reduction cannot be discarded, although data shedding light on this issue could not be found in the available literature.

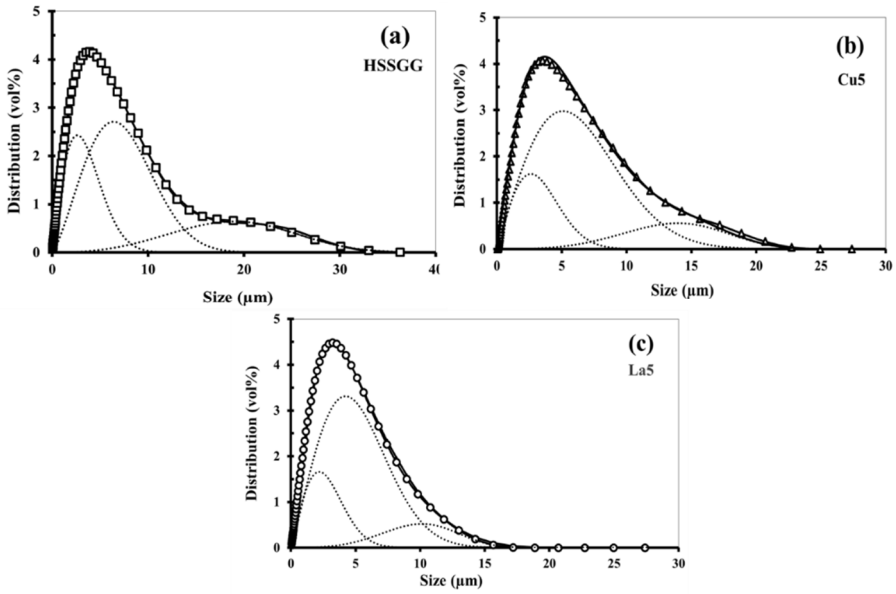

Fig. 12.1: The ion doping effects on the particles size distributions of the wet–milled glass powders: (a) HSSGG, (b) Cu5 and (c) La5.

But both Cu and La are well–known to act as glass modifiers leading to less polymerized silica–networks. This is confirmed by the ^{29}Si NMR spectra of the three glasses displayed in **Fig. 12.2**. The parent glass (HSSGG) exhibits the highest degree of network polymerization.

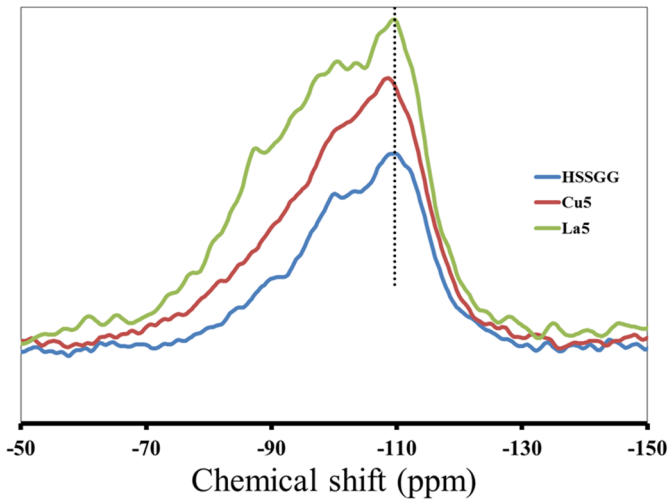

Fig. 12.2: ^{29}Si NMR for HSSGG (blue line), Cu5 (brown line), and La (green line) doped glasses.

The Cu5 glass shows a somewhat less polymerized structure, while a more extensive disruption in the silica–network is observed for the La5 glass. Experimental evidences about the network modifier role of La_2O_3 in silicate glasses were recently reported **[30]**. All these results support the hypothesis that the less polymerized networks of doped glasses facilitate breakage of the particles into smaller sizes.

3.2. Rheological characterization of suspensions and pastes

3.2.1. Apparent Viscosity

The apparent viscosity curves *versus* shear rate for the suspensions prepared from the HSSGG, Cu5 and La5 powders are presented in **Fig. 12.3**. In all cases, the apparent viscosity decreases with the increase in shear rate in a similar manner. This shear thinning behavior is an essential prerequisite for ink extrusion through fine nozzles. Within the range of low shear rate, the high apparent viscosity values measured can be assigned to the role played by the entangled CMC species, which led to a significant increase in the intrinsic viscosity of the suspension. As a result of increasing the shear rate, the CMC species are likely to align in the flow direction and the internal structure will gradually break down decreasing the apparent viscosity. In the region 0.1–10 s^{-1} HSSGG exhibits the highest apparent viscosity level followed by Cu5, and La5, respectively. However, in the region from 10–100 s^{-1}, HSSGG maintains the same behavior, while Cu5 and La5 show a slight increase in comparison. The sequence of flow curves in terms of apparent viscosity levels within the region from 10–100 s^{-1} coincides with the order of the three glass powders in terms of average particle size and broadness of PSD. This suggests that the differences observed in apparent viscosity are likely due to the physical features of the starting powders. The internal network structure promoted by the CMC species is likely less disturbed at lower shear rates when the particles are coarser since larger interstices are left among them in comparison to a finer powder. At the higher shear rates where hydrodynamic interactions prevail over the intermolecular ones, all the three different suspensions behave more similarly, with a continuous reduction of apparent viscosity.

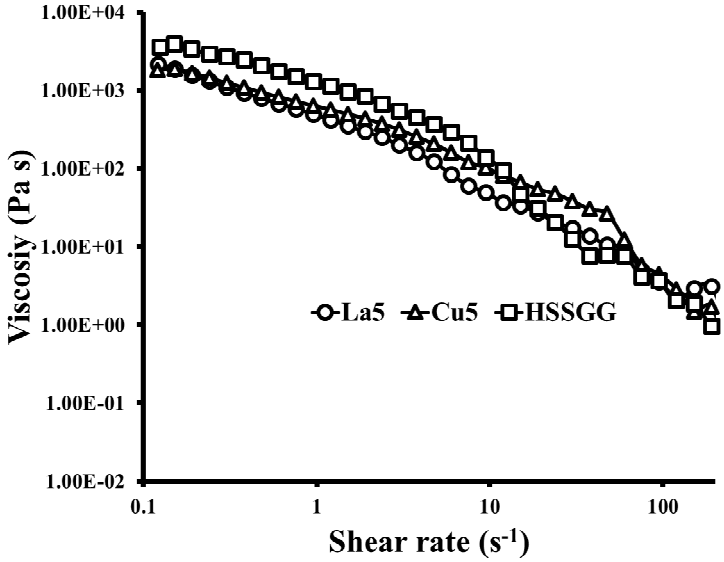

Fig. 12.3: Comparison of the flow properties of suspensions prepared from HSSGG, Cu5 and La5 glass powders.

3.2.2. Viscoelastic Properties

Fig. 12.4 displays the elastic modulus (G') of the three glass inks as a function of complex shear stress. It can be seen that the measured G' values are sufficiently high for printing (G´ ~1 x 10^5 – 1 x 10^6 Pa) for all three glass pastes with a solid loading of 40 vol.%. Interestingly, the order of the G' curves is the same observed for apparent viscosity curves plotted in **Fig. 12.3**. Cu–doping caused a small drop in G', and La–doping caused a further and more accentuated drop in the stiffness of the paste. Moreover, all pastes exhibit a continuous linear viscoelastic region (LVR) that extends nearly to 100 Pa for HSSGG system, becoming gradually narrower for the Cu5, and La5 pastes. These results support the hypothesis admitted above that internal network structure promoted by the CMC species is likely less disturbed under low deformations as those prevailing within the LVR.

Broad LVR coupled with the high values of G´ are the main features required for ink printability **[24,28]**.

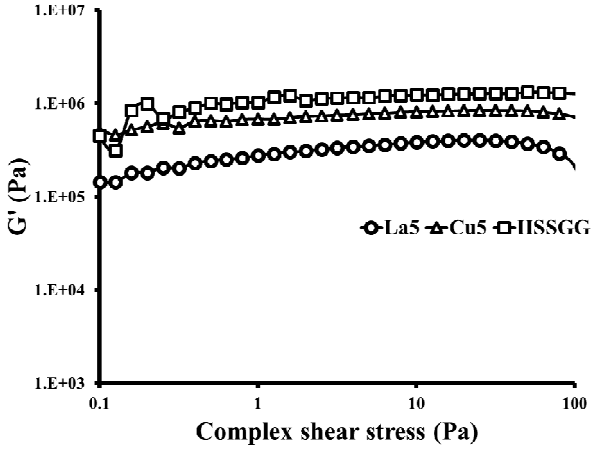

Fig. 12.4: Elastic modulus (G´) and extent of LVR as a f□n□tion ofcomplex shear stress of suspensions/pastes prepared from HSSGG, Cu5 and La5 glass powders.

This means that the dissolved and entangled CMC species, together with 40 vol.% solid loading, confer to the paste the stiffness and the viscoelastic properties essential for extrusion and shape preservation of the filaments during the robocasting process. Therefore, these pastes are eminently suitable for robocasting. This is confirmed by the good shape retention observed in the SEM micrographs of sintered scaffolds presented in **Figs. 12.5(a–d)**. The general overviews **Figs. 12.5(a,b)** reveal that the successive layers were successfully printed without disturbing the layers beneath, and the detailed views, **Figs. 12.5(c,b)**, show that good densification levels have been achieved.

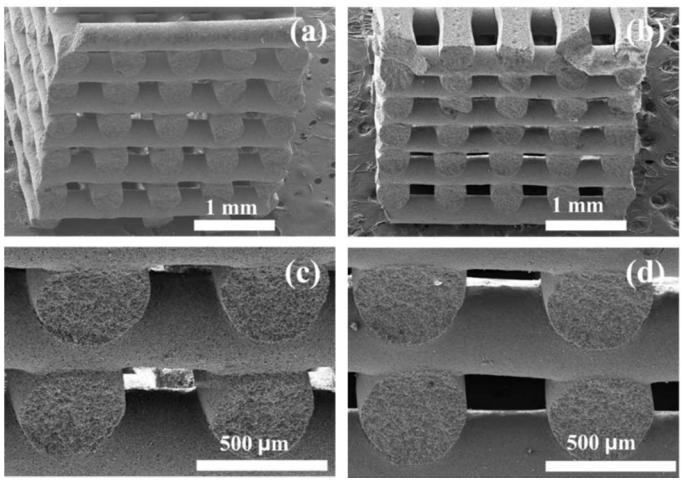

Fig. 12.5: Scaffolds printed from pastes of ion doped glasses: (a, c) Cu5; (b, d) La5.

3.3. Compressive strength

All compressive strength values measured for the sintered scaffolds with the three pore sizes (300, 400 and 500 μm) are reported in **Table 12.2**. **Fig. 12.6** also displays the variations trends. A predictable decrease in the compressive strength values with incremental pore sizes from 300 to 500 μm is observed for all the glass compositions. The compressive strength for HSSGG scaffolds varied between the limits of 2.20±0.12 – 4.96±15 MPa, which are within the range reported for human cancellous (trabecular) bone (2 – 12 MPa) **[31]**, with the lowest and the highest values being registered for the largest (500 μm) and smallest (300 μm) pore sizes, respectively. A slight improvement in mechanical properties was registered for La5, where the compressive strength value was between the limits of 2.60±0.35 MPa (500 μm) and 5.41±30 MPa (300 μm). This means increments between 9 – 18% over that measured for HSSGG. However, great and impressive improvements in mechanical properties were observed for the Cu5 glass, with compressive strength values varying between 4.97±0.28 MPa (500 μm) and 13.96±0.28 MPa (300 μm), which are 125–181% greater than those obtained for HSSGG. The greatest increase 221% in compressive strength (221% over HSSGG) was measured for the scaffold with 400 μm pores. The higher enhancement of Cu5 comparing to La5 can be attributed to the differences ionic radii. The much smaller ionic radius of Cu (0.73 Å) [in comparison to that of La (1.06 Å)] **[29]**, and its lower valence confer to Cu a higher thermal diffusivity upon sintering the scaffolds. This enables Cu to act as an effective sintering aid, enhancing densification and the mechanical properties as reported in **Table 12.2** and **Fig. 12.6**. This fluxing role of Cu has been already explored to prepare mullite whiskers from kaolinite **[32]**.

Table 12.2: The corresponding compressive strength for sintered scaffolds with 300, 400 and 500 μm macropores for HSSGG, La5 and Cu5 glasses.

Macropores (μm)	Compressive strength (MPa)		
	HSSGG	La5	Cu5
300	4.96±0.12	5.41±0.34	13.96±0.28
400	3.30±0.11	3.54±0.26	10.60±0.29
500	2.21±0.29	2.60±0.30	4.97±0.29

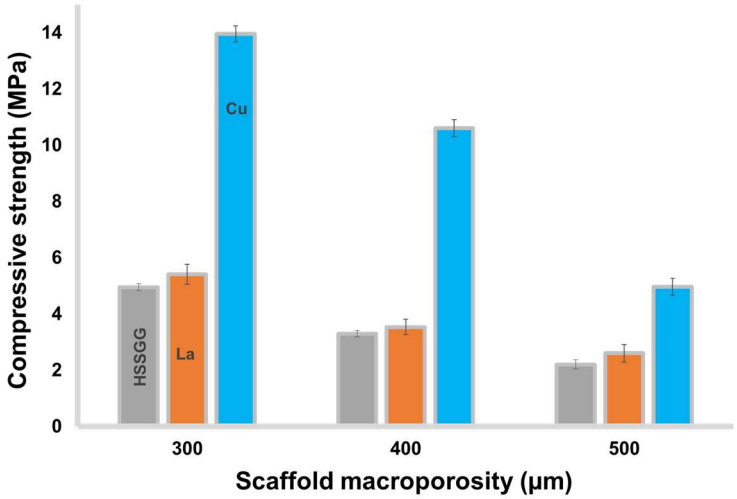

Fig. 12.6: Compressive strength of the scaffolds, fabricated from HSSGG, Cu5 and La5 glasses, with different macro–pore sizes (300, 400 and 500 µm) sintered at 800 ºC.

Therefore, doping the parent HSSGG glass with Cu exerts a remarkable improvement in the mechanical properties. It is suggested that doping HSSGG is a good option towards tailoring the mechanical properties for specific applications. Considering that individual La and Cu doping led to slight and accentuated increases in the compressive strength, their combined effects in different quantities are likely to be explored in future studies aiming at widening the range of potential applications for the implants.

3.4. Influences of ion doping on morphological surface features of scaffolds

Fig. 12.7 displays the SEM micrographs of HSSGG, (a, b), Cu5 (c, d) and La5 (e, f). The observation of these samples enables to conclude that the parent HSSGG composition is the less prone to densification with a higher intrinsic porosity fraction left in the sintered microstructures with large pores exhibiting non–uniform shapes.

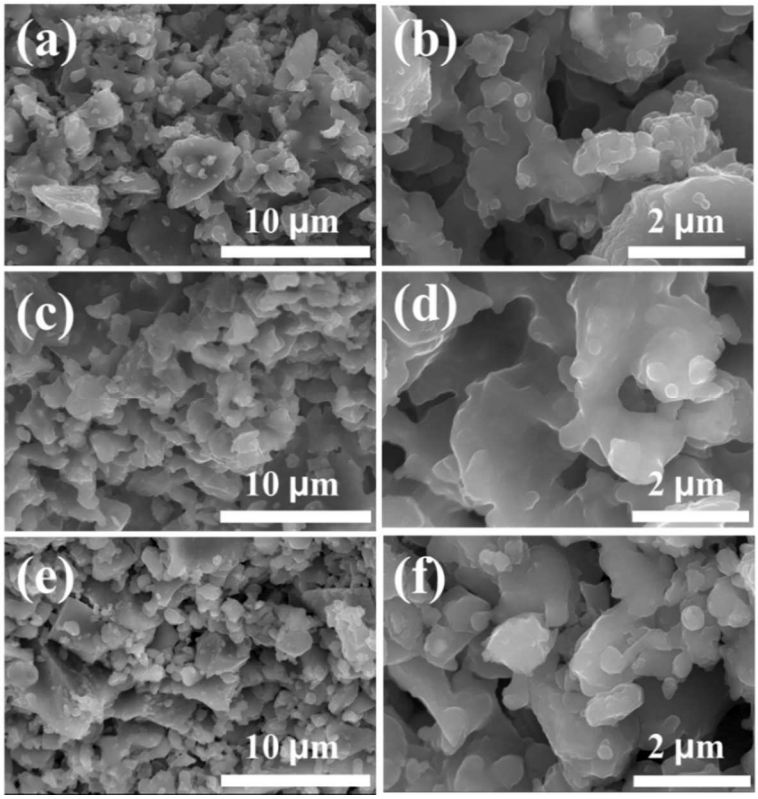

Fig. 12.7: Microstructural features of sintered scaffolds fabricated from the different glasses: (a, b) HSSGG; (c, d) Cu5; (e, f) La5.

Moreover, the necks formed among the particles are less extensive for the HSSGG sample in comparison to the doped ones. The most extensive necks' formation is observed for the Cu5 particles, which become strongly bonded together.

This is consistent with the hither compressive strength values measured for Cu5 glass scaffolds as discussed in the previous section. In the case of La5 glass, doping also enhanced the formation of necks among the particles upon sintering in comparison to parent glass, but in a less extensive manner in comparison to Cu5. These results suggest that doping ions are acting as sintering aids, favoring the bulk material diffusion process upon sintering. The differences between the two doping ions can be attributed to their different thermal diffusivities due to dissimilar ionic radii and valences **[29]**. The active fluxing agent role of Cu has been already demonstrated **[32]**. Moreover, CuO has a lower melting point 1325 ºC **[33]** in comparison to La_2O_3 (2313 ºC) **[34]**, permitting earlier diffusion. It is also likely that the morphologies of sintered microstructures somehow reflect the particle sizes, PSD and packing ability of the starting glass powders displayed in **Fig. 12.1**.

4. Conclusions

The aim of this research work was to disclose the effects of ion (Cu^{2+} and La^{3+}) doping on the printability of sol–gel derived glass pastes for robocasting, and on the mechanical properties of the resulting sintered scaffolds. The results revealed that doping tends to decrease the mean particle size of the milled powders, an effect that was more evident for La5 than for Cu5. The rheological properties of the 40 vol.% solid loaded inks were also affected by doping the parent glass with 5 wt.% of Cu or La. With doping, the pastes became gradually less stiff and the LVR were less extended in comparison to that of HSSGG, which exhibited the highest G'~1 MPa, and the more extended LVR up to ~100 Pa. Nevertheless, the small differences in rheological properties did neither affect the printability of all the pastes nor the shape retention of the printed scaffolds. Although all scaffolds exhibited compressive strength values that fit well within the range reported for human cancellous bone (2 – 12 MPa), doping significantly enhanced their mechanical properties. This was particularly true in the case of Cu5, with increments up to 221% in comparison to those made of HSSGG. In the case of La5, only modest increments in compressive strength of 9 – 18% were registered. These results here obtained confirm that glass doping is an important avenue to explore with the potential to greatly enhance the mechanical properties of the scaffolds.

Acknowledgments

R.C. Pullar wishes to thank the FCT Grant IF/00681/2015 for supporting this work. B. A. E. Ben–Arfa thanks FCT grant BIONANOSCULP PTDC/EPH–PAT/6281/2014 for supporting him during this work. This work was developed in the scope of the project CICECO–Aveiro Institute of Materials (Ref. FCT UID /CTM /50011/2013), financed by national funds through the FCT/MEC and when applicable co–financed by FEDER under the PT2020 Partnership Agreement.

References

[1] I.D. Thompson, L.L. Hcnch, Mechanical properties of bioactive glasses, glass–ceramics and composites, in: Proc. Inst. Mech. Eng. Part H J. Eng. Med., 1998: pp. 127–136.

[2] M. Miola, A. Cochis, A. Kumar, C.R. Arciola, L. Rimondini, E. Verné, Copper–doped bioactive glass as filler for PMMA–based bone cements: Morphological, mechanical, reactivity, and preliminary antibacterial characterization, Materials (Basel). 11 (2018).

[3] M. Angelova, S. Asenova, V. Nedkova, Copper in the human organism, Trakia J. Sci. 9 (2011) 88–98.

[4] R. Uauy, M. Olivares, M. Gonzalez, Essentiality of Copper in Humans, Am J Clin Nutr. 67 (1998) 9525–98.

[5] V. Culotta, Cell Biology of copper, J. Biol. Inorg. Chem. 15 (2010) 1–2.

[6] J. Osredkar, N. Sustar, Copper and Zinc, Biological Role and Significance of Copper/Zinc Imbalance, J. Clin. Toxicol. s3 (2011) 1–18.

[7] H.H.A. Dollwet, J.R.J. Sorenson, Roles of copper in bone maintenance and healing, Biol. Trace Elem. Res. 18 (1988) 39–48.

[8] S. Soltani–Dehnavi, M. Mehdikhani–Nahrkhalaji, M. Rafienia, A. Doostmohammadi, Copper–doped and copper–free bioactive glass nanopowders cytotoxicity and antibacterial activity assessment, Sci. Iran. 24 (2017) 1706–1716.

[9] S. Zhao, L. Li, H. Wang, Y. Zhang, X. Cheng, N. Zhou, et al., Wound dressings composed of copper–doped borate bioactive glass microfibers stimulate angiogenesis and heal full–thickness skin defects in a rodent model, Biomaterials. 53 (2015) 379–391.

[10] L. Weng, S.K. Boda, M.J. Teusink, F.D. Shuler, X. Li, J. Xie, Binary Doping of Strontium and Copper Enhancing Osteogenesis and Angiogenesis of Bioactive Glass Nanofibers while Suppressing Osteoclast Activity, ACS Appl. Mater. Interfaces. 9 (2017) 24484–24496.

[11] D.M. Taylor, R.W. Leggett, A generic biokinetic model for predicting the behaviour of the lanthanide elements in the human body. (vol 105, pg 193, 2003), Radiat. Prot. Dosimetry. 106 (2003) 281.

[12] F. Bronner, Metals in Bone. Aluminum, Boron, Cadmium, Chromium, Lanthanum, Lead, Silicon, and Strontium., in: Princ. Bone Biol., 3rd editio, Academic Press, Inc., Farmington, 2008: pp. 515–531.

[13] T. Das, A. Sharma, G. Talukder, Effects of lanthanum in cellular systems – A review, Biol. Trace Elem. Res. 18 (1988) 201–228.

[14] D.M. Kramsch, A.J. Aspen, C.S. Apstein, Suppression of experimental atherosclerosis by the Ca++–antagonist lanthanum. Possible role of calcium in atherogenesis, J. Clin. Invest. 65 (1980) 967–981.

[15] D.M. Weekes, Lanthanum Complexes As Therapeutic Agents for the Treatment, Britsh Columbia, 2016.

[16] M. Ershad, V.K. Vyas, S. Prasad, A. Ali, R. Pyare, Synthesis and characterization of cerium– and lanthanum containing bioactive glass, Key Eng. Mater. 751 (2017) 617–628.

[17] X. Wang, L. Yuan, J. Huang, T.L. Zhang, K. Wang, Lanthanum enhances in vitro osteoblast differentiation via pertussis toxin–sensitive Gi protein and ERK signaling pathway, J. Cell. Biochem. 105 (2008) 1307–1315.

[18] J.E. Ellingsen, E.M. Pinholt, Pretreatment of titanium implants with lanthanum ions alters the bone reaction, J. Mater. Sci. Mater. Med. 6 (1995) 125–129.

[19] C.R. Gautam, S. Kumar, V.K. Mishra, S. Biradar, Synthesis, structural and 3–D architecture of lanthanum oxide added hydroxyapatite composites for bone implant applications: Enhanced microstructural and mechanical properties, Ceram. Int. 43 (2017) 14114–14121.

[20] B.A.E. Ben–arfa, A.S. Neto, I.M.M. Salvado, R.C. Pullar, J.M.F. Ferreira, Robocasting : Prediction of ink printability in solgel bioactive glass, J. Am. Ceram. Soc. Accepted (2018) 1–11.

[21] F.J. O'Brien, Biomaterials & scaffolds for tissue engineering, Mater. Today. 14 (2011) 88–95.

[22] M. Houmard, Q. Fu, E. Saiz, A.P. Tomsia, Sol–gel method to fabricate CaP scaffolds by robocasting for tissue engineering, J. Mater. Sci. Mater. Med. 23 (2012) 921–930.

[23] J.M. Karp, P.D. Dalton, M.S. Shoichet, Scaffolds for Tissue Engineering, MRS Bull. (2003) 301–306.

[24] E. Feilden, E.G.T. Blanca, F. Giuliani, E. Saiz, L. Vandeperre, Robocasting of structural ceramic parts with hydrogel inks, J. Eur. Ceram. Soc. 36 (2016) 2525–2533.

[25] S. Eqtesadi, A. Motealleh, P. Miranda, A. Pajares, A. Lemos, J.M.F. Ferreira, Robocasting of 45S5 bioactive glass scaffolds for bone tissue engineering, J. Eur. Ceram. Soc. 34 (2014) 107–118.

[26] S.M. Olhero, H.R. Fernandes, C.F. Marques, B.C.G. Silva, J.M.F. Ferreira, Additive manufacturing of 3D porous alkali–free bioactive glass scaffolds for healthcare applications, J. Mater. Sci. 52 (2017) 12079–12088.

[27] B.A.E. Ben–Arfa, I.M.M. Salvado, J.M.F. Ferreira, R.C. Pullar, Enhanced bioactivity of a rapidly–dried sol–gel derived quaternary bioglass, Mater. Sci. Eng. C. 91 (2018) 36–43.

[28] S. Eqtesadi, A. Motealleh, P. Miranda, A. Lemos, A. Rebelo, J.M.F. Ferreira, A simple recipe for direct writing complex 45S5 Bioglass®3D scaffolds, Mater. Lett. 93 (2013) 68–71.

[29] A.F. Wells, Structural Inorganic Chemistry, 4th ed., Oxford university press, London, 1975.

[30] N. Gaddama, H.R. Fernandes, D.U. Tulyaganov, J.M.F. Ferreira., The structural role of lanthanum oxide in silicate glasses (submitted). Manuscript number: NOC–D–18–01218. , (2018).

[31] D.R. Carter, G.H. Schwab, D.M. Spengler, Tensile Fracture of Cancellous Bone,

Acta Orthop. Scand. 51 (1980) 733–741.

[32] S. Agathopoulos, H.R. Fernandes, D. Tulyaganov, J.M.F. Ferreira, Preparation of mullite whiskers from kaolinite using CuSO4 as fluxing agent, Mater. Sci. Forum. 455–456 (2004) 818–821.

[33] H.S. Roberts, H. Smyth, System copper: cupric oxide: oxygen., J. Am. Chem. Soc. 43 (1921) 1061–1079.

[34] O. Polyakov, Technology of Ferroalloys with Rare–Earth Metals, in: Handb. Ferroalloys, Twelfth Ed, Elsevier Ltd, 2013: pp. 459–469.

Chapter 13

General conclusions

New glasses were designed in a quaternary system (Si, Na, Ca, P) with high silica, and low Na and P contents to overcome the problems of low mechanical properties and high dissolution rates associated with Hench's glass. It is known that the increase of silica content enhances the mechanical properties of the glasses to the detriment of their bioactivity. As the bio–mineralisation activity is a surface process, an increase in the exposed surface area/porosity is a good solution towards enhancing the bioactivity of the high silica glasses. This justified the selection of the sol–gel method for synthesis of high porosity glasses instead of the traditional melt–quenching method. Sodium is known to promote early crystallisation in glasses. Therefore, the preparation of sodium– containing glasses by the sol–gel method is a big challenge. Furthermore, in sol–gel, aging is known to promote segregation that in turn induces early crystallisation. To overcome all the above challenges, a novel sol–gel fast drying (FD) process, avoid aging, was developed for the first time. In the FD the as–obtained sol is immediately dried directly without aging using a rotary evaporator. The major part of the liquid is extracted under vacuum at 55 ºC. This process enables the successful sol–gel preparation of the novel quaternary high silica sodium–containing glass (HSSGG) in just 1 h, reducing the processing time by two orders of magnitude (at least 100 times shorter) compared to the conventional sol–gel glass (CD), while minimising/suppressing the early crystallisation.

A full comparison and assessment study between the FD and CD glasses was made. The result showed very similar microstructures of the glasses prepared by the two methods. Moreover, FD glass exhibited lower network connectivity which led to improved bioactivity in comparison to the CD glass.

The effect of two different orbital agitation rates (60 rpm and 120 rpm) on the bioactivity of the glass powder immersed in SBF was also evaluated. The results reveal that, the bioactivity is favoured by at higher orbital agitation rate (120 rpm).

The influences of the Ca/P ratios, and of the Ca–content, on bioactivity and biocompatibility were investigated for glass powders prepared with two different metal salts (acetates and nitrates) for both Na and Ca. The obtained results consolidated the preferred use of nitrates rather than acetates, since the nitrates precursors offer enhanced homogeneity, an amorphous glass structure with a higher degree of polymerisation, higher values of density and SSA,

and improved bioactivity. The acetate–derived glasses are less homogeneous with some nitrate residues remaining in the heat treated samples, and tend to undergo early crystallisation. The moderate increase in Ca content as well as Ca/P ratio enhanced the bioactivity compared with high silica glass, whereas higher proportions of both Ca and Ca/P facilitated the precipitation of a calcium carbonate crystalline phase (calcite). On the other hand, biocompatibility was favoured by low Ca content samples, and the high silica content glass showed the best biocompatibility amongst all prepared glasses.

The type of catalyst (citric or nitric acid) and its concentration (zero to a relatively high amounts), and type of metal salts (acetate or nitrate) were investigated. The results confirm the results suggested above, that the use of citric acid with nitrate metal salts, rather than acetate salts with nitric acid as catalyst, is preferred

The possibility of preparing bioactive glass by sol–gel without catalyst was demonstrated here for the first time. The main drawback of this approach is the significant amount of residual nitrates remaining after the heat treatment. The 2nd highest residual nitrate levels were observed in the acetate salt glass samples catalysed with nitric acid, probably due to the high amounts of HNO_3 catalyst required. The combination of a relatively lower concentration (0.15 M L^{-1}) of citric acid catalyst with nitrate metal salts enables the obtaining of glasses almost free of residual nitrates, and with lower values of network connectivity. Therefore, changing the concentration and type of catalyst is a very powerful approach to tailor the bioactivity without changing the composition.

The general properties were modified by doping HSSGG with (Cu^{2+}, La^{3+}). For instance, the cytotoxicity was significantly improved for some doping combinations, while the bioactivity of doped samples was always very similar to that of HSSGG. Cu promotes crystallisation, decreases SSA, and enhances the density, shrinkage and sinterability, while La played an opposite role.

In powder milling, the ball to powder ratio (BPR) exerts a tremendous influence on the final particle size distribution of the powders, while its effect on volume and morphology is negligible.

The sol–gel glass remained amorphous upon heating to 700 ºC. Heat treating the glass at 800 ºC induced the incipient crystallisation of phases such as HAp and cristobalite. These crystalline phases tended to steadily fade with increasing BPR, while a yttrium zirconium oxide crystalline phase gradually appeared, resulting from wear debris of the milling media. Particle size (PS) and SSA decreased, while particle size distribution (PSD) showed a clear narrowing trend with increasing BPR, irrespective of heat treatment temperature (HTT). The SSA tended to consistently decrease with increasing HTT.

In rheology and prediction of ink printability, the apparent viscosity, the elastic modulus, and the extent of the linear viscosity range (LVR) are strongly dictated by a set of interdependent factors, determined by the HTT, BPR, PS, PSD and solids loading. For a given HTT, the viscoelasticity is enhanced by increasing the solid loading and decreasing the mean particle size. The high values of elastic modulus within the range of 10^5–10^6 Pa, combined with extension of the LVR up to shear stress values over 100 Pa, were measured for a number of inks, enabling the prediction of good printing ability.

A calcination temperature of 800 ºC is required to obtain a powder with a small fraction of fine pores (mesopores <30 nm), to reduce the uptake of the dispersing liquid and prevent an exaggerated specific surface area to be exposed to the liquid media, and achieve a relatively high solids loading in the printing inks.

For the first time, the practical difficulties in achieving sol–gel derived pastes with high solids loading, and appropriate rheological properties for the robocasting process, were circumvented. Scaffolds with different macro–pore sizes were produced by robocasting from optimal pastes with solid loadings up to 40 vol.%.

The scaffolds were found to exhibit a good bioactivity, illustrated by the appearance of a spider web–like layer formed of mixed silica gel and HAp after just 72 h of immersion. The scaffolds did not show any cytotoxicity towards osteoblasts, making them promising candidates for bone regeneration and tissue engineering applications. The scaffolds exhibited slightly improved compressive strength (5 MPa) compared with bioglass®.

Following the same approach, 40 vol.% solid loading paste could be prepared from the Cu^{2+} & La^{3+} doped sol–gel glasses, and successfully used to fabricate scaffolds with improved compressive strength (5 – ~14 MPa) that was up to 221% greater than that of undoped HSSGG.

Future plan

The successful development of the fast novel sol–gel approach enables the easy and fast synthesis of several sol–gel derived glasses with different silica contents and Ca/P ratios. This new approach has been only partially explored in the frame of this PhD Thesis, and plenty of future research work can be planned, benefiting from the advantages it offers in comparison to the traditional sol–gel approach. On the other hand, several other findings reported along this PhD Thesis open the way for future research directions for more deeply exploring the following issues:

1. Tuning the ratio between citric acid and metal nitrates to enable a more efficient extraction of nitrate residues at the minimum possible temperature in the same or in newly designed glass compositions, and also to promote the entrance of Ca into the silica network at lower temperatures.
2. Doping sol–gel derived bioactive glasses with other relevant functional ions with potential antiseptic and/or antibacterial activities and evaluating their effects on the overall properties of the synthesised materials.
3. Deeply explore the synthesis of magnetic bioactive glasses for hyperthermia (bone cancer cure therapy). The following approaches are suggested:
    a. Mixing the glasses with magnetic particles in different percentages using dry ball milling, wet ball milling, and during the sol preparation and evaluate the consequences in terms of intimacy of the mixtures and the difference in magnetic properties.
    b. Doping the glass directly with iron ions:
        i. Using Fe(II) only;
        ii. Using Fe(III);
        iii. Using both Fe(II) and Fe(III).
4. Perform full assessment of the magnetic properties for parent and doped glasses, including the measurements of the dissipated heat from the glasses/glass ceramics. Since the hyperthermia cancer therapy approach uses a temperature around ~45ºC to kill the cancerous cells, tuning the magnetic properties is essential to control the heat dissipated during the hyperthermia treatment for do not exceeding that temperature limit.

For the scaffolds fabricated by robocasting some issues need to be addressed as following:

5. The fabrication of scaffolds in the frame of this PhD Thesis explored mostly the use of pastes with high solid loadings to enhance the dimensional control over the entire process. With this purpose, the typically high intrinsic porosity of sol–gel derived glasses had to be drastically reduced, losing this interesting feature in the final scaffolds, i.e. large population of the pores need to be eliminated to be able to print the scaffold. Therefore, future work needs to be undertaken towards exploring the printing ability of lower solid loading pastes prepared from porous sol–gel derived glasses to take full advantages of this high porosity feature in terms of bioactivity and capacity of storage and in situ release of therapeutic drugs. The expected decrease in the mechanical properties of the more porous structures needs to be compensated by complementary studies aiming at enhancing the mechanical performance of the scaffolds.
6. Surface modifications studies with biopolymers and their influence on wettability and the *in vitro* performance using suitable cell lines are required for broadening the potential applications of the scaffolds.
7. *In vivo* studies are also required to test the suitability of the scaffolds for the intended applications in bone regeneration and tissue engineering.